

INFORMATION TO USERS

This manuscript has been reproduced from the microfilm master. UMI films the text directly from the original or copy submitted. Thus, some thesis and dissertation copies are in typewriter face, while others may be from any type of computer printer.

The quality of this reproduction is dependent upon the quality of the copy submitted. Broken or indistinct print, colored or poor quality illustrations and photographs, print bleedthrough, substandard margins, and improper alignment can adversely affect reproduction.

In the unlikely event that the author did not send UMI a complete manuscript and there are missing pages, these will be noted. Also, if unauthorized copyright material had to be removed, a note will indicate the deletion.

Oversize materials (e.g., maps, drawings, charts) are reproduced by sectioning the original, beginning at the upper left-hand corner and continuing from left to right in equal sections with small overlaps. Each original is also photographed in one exposure and is included in reduced form at the back of the book.

Photographs included in the original manuscript have been reproduced xerographically in this copy. Higher quality 6" x 9" black and white photographic prints are available for any photographs or illustrations appearing in this copy for an additional charge. Contact UMI directly to order.

U·M·I

University Microfilms International
A Bell & Howell Information Company
300 North Zeeb Road, Ann Arbor, MI 48106-1346 USA
313/761-4700 800/521-0600

Order Number 9410173

**The morphology and electrodynamics of the boreal polar winter
cusp**

McHarg, Matthew G., Ph.D.

University of Alaska Fairbanks, 1993

U·M·I
300 N. Zeeb Rd.
Ann Arbor, MI 48106

**THE MORPHOLOGY AND ELECTRODYNAMICS
OF THE BOREAL POLAR WINTER CUSP**

**A
THESIS**

**Presented to the Faculty of the University of Alaska Fairbanks
in Partial Fulfillment of the Requirements
for the Degree of**

DOCTOR OF PHILOSOPHY

**By
Matthew G. McHarg, B.S., M.S.**

Fairbanks, Alaska

September 1993

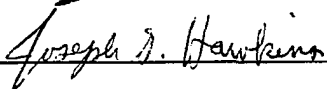
THE MORPHOLOGY AND ELECTRODYNAMICS
OF THE BOREAL POLAR WINTER CUSP

By

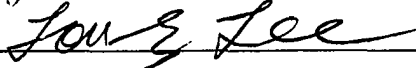
Matthew G. McHarg

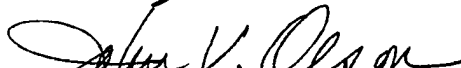
RECOMMENDED:












J.V. Olson, Advisory Committee Chair



J.L. Morack, Head, Physics Department

APPROVED:



Dean, College of Natural Sciences



Chancellor's Faculty Associate Graduate Studies



Date

ABSTRACT

The major result of this thesis is the determination of the magnetic signatures of the dayside cusp region. These signatures were determined by comparing the magnetic observations to optical observations of different energy particle precipitation regions observed in the cusp. In this thesis, the cusp is defined as the location of most direct entry of magnetosheath particles into the ionosphere. Optical observations show that the observing station rotates daily beneath regions of different incident energy particles. Typically, the station passes from a region in the morning of high energy particles into a region near magnetic noon of very low energy precipitation, and then returns to a region of high energy precipitation after magnetic noon. A tentative identification of the cusp is made on the basis of these observations. The optical observations also are used to determine the upward field aligned current density, which is found to be most intense in the region identified as the cusp. The magnetic field measurements are found to correlate with the optical measurements. When the characteristic energy is high, the spectrogram shows large amplitude broad band signals. The Pc5 component of these oscillations is right hand polarized in the morning, and left hand polarized in the afternoon. During the time the optics detect precipitation with a minimum characteristic energy, the magnetic spectrogram shows a unique narrow band tone at 3-5 mHz. The occurrence statistics of the magnetic oscillations are compared to DMSP satellite observations of the cusp and low latitude boundary layer. The pulses that make the narrow band tone are found to come in wave trains that are phase coherent. These trains of coherent pulses are found to be separated by phase jumps from adjacent wave trains. These jumps in phase occur when a new field aligned current appears on the equatorward edge of the cusp. This combination of phase coherent wave trains associated with poleward propagating auroral forms which are shown to contain intense field aligned currents may be the signature of newly reconnected flux tubes in the ionosphere.

which are shown to contain intense field aligned currents may be the signature of newly reconnected flux tubes in the ionosphere.

TABLE OF CONTENTS

	Page
List of Figures	viii
List of Tables	xii
Preface	xiii
1 Introduction	1
1.1 Early observations of the cusp	3
1.2 Satellite observations of the cusp	4
1.2.1 <i>Particles</i>	4
1.2.2 <i>Fields</i>	10
1.2.3 <i>Optical Emissions</i>	16
1.3 Ground Based Magnetic Observations of the Cusp	17
1.4 Ground Based Optical Observations of the Cusp	23
1.5 Conceptual Overview	26
2 Optical observations of the cusp	31
2.1 Description of Meridian Scanning Photometer	32
2.2 Use of Spectral Ratios for Cusp Observations	35
2.3 Mapping of MSP scan angle to latitude	39
2.3.1 <i>Manufacturing Synthetic MSP Data</i>	40
2.3.2 <i>Analysis of Synthetic MSP Data</i>	47
2.3.3 <i>Flat Mapping Scan Angle to Latitude</i>	51
2.3.4 <i>Eather Mapping of Scan Angle to Latitude</i>	54
2.4 Ground based optical observations of the cusp	63
2.5 Identification of Boundary Regions and Central Cusp	83
3 Magnetic observations of the cusp	85

3.1	Introduction to magnetic pulsation observations of the cusp	86
3.2	Identification of cusp and boundary region signature using ULF magnetic observations	89
3.3	Statistical occurrence of cusp and boundary region signatures	91
3.3.1	<i>Ground-based ULF signature of the boundary regions and cusp</i>	93
3.3.2	<i>Comparison of ground based signature to satellite based signatures of the LLBL and cusp</i>	94
3.4	Spectral categories observed in magnetic ULF observations	100
3.5	IMF correlations with spectral categories seen in magnetic ULF observations	107
3.6	Discussion	119
4	Analysis of cusp magnetic observations	124
4.1	Study of cusp ULF power spectra	125
4.2	Estimation of cusp current system parameters	138
4.3	Time series of magnetic perturbations	140
4.4	Temporal coherence length of cusp pulsations	142
4.5	Possible sources of cusp pulsations	152
4.5.1	<i>Boundary Region Phenomena</i>	152
4.5.2	<i>Central Cusp Phenomena</i>	158
4.6	Summary	166
5	Review and recommendations for future work	169
5.1	Review	169
5.2	Recommendations for future work	174
A1	Ground magnetic fields caused by field aligned currents	176
A1.1	Assumptions and governing equations	176
A1.2	Derivation of Potential Equation	178

A1.3 Determining the surface currents and the magnetic field	179
A2 Emission height determination in the Eather map	182
References	183

LIST OF FIGURES

Figure	Page
1.1 Magnetic field topology of magnetosphere	2
1.2 Ionospheric map of the cusp/cleft	6
1.3 Map of particle precipitation regions in the ionosphere	8
1.4 Position of Region 1, Region2, and Cusp field aligned current systems as a function of B_y	12
1.5 Observables and source regions in the cusp	14
1.6 Conceptual view of the ground based observations of the ionospheric cusp	27
2.1 Relative transmission of 6300 Å Filter	33
2.2 Geometry of the flat latitude map	40
2.3 Geometry of the Eather Map	41
2.4 Emission Profile of 6300 Å and 4278 Å from 1.3 keV particles	42
2.5 Geometry of integration	44
2.6 Background emission profiles for 6300 Å and 4278 Å	46
2.7 Background intensity versus scan angle	47
2.8 Background plus arc intensity versus scan angle	48
2.9 Map of actual characteristic energy and energy flux of precipitating particles	49
2.10 Keogram of 6300 Å and 4278 Å emission versus scan angle	50
2.11 Flat map of 4278 Å and 6300 Å emission	52
2.12 Map of characteristic energy and energy flux of precipitating particles inferred from flat map	53

2.13	Difference of inferred characteristic energy of precipitating particles using flat map from input	55
2.14	Inferred emission altitude for one scan using Eather method	56
2.15	Inferred latitude for one scan using Eather method	57
2.16	One 6300 Å scan mapped to latitude using Eather method	58
2.17	Comparison of Eather map and flat map for one 6300 Å scan	59
2.18	Keogram of 4278 Å and 6300 Å emissions using Eather map	60
2.19	Plot of the inferred characteristic energy and energy flux of precipitating particles using the Eather map	62
2.20	Comparison of Eather map of 6300 Å emission with high and low background	63
2.21	Keogram of 6300 Å and 5577 Å emission from 9 Jan 1991	65
2.22	Universal time of magnetic local noon at Nordlysstasjonen from September 1990 to March 1991	66
2.23	Inferred characteristic energy of precipitating particles for 9 Jan 1991	68
2.24	Inferred characteristic energy flux of precipitating particles for 9 Jan 1991	69
2.25	Schematic of magnetospheric source of ionospheric precipitation from <i>Newell et al.</i> [1991a]	72
2.26	Inferred characteristic energy of precipitating particles for 7 Jan 1992	75
2.27	Inferred field aligned current density for 9 January 1991	77
2.28	Inferred field aligned current density for 7 January 1992	79
2.29	Inferred height Integrated Hall and Pederson Conductivity for 9 January 1991	81
2.30	Inferred height Integrated Hall and Pederson Conductivity for 7 January 1992	82
3.1	Frequency time spectrogram for ULF pulsations on 9 Jan 1991	87

3.2	Comparison of the Optical MSP and Magnetic Pulsation data for 9 January 1991	90
3.3	Pc-5 integrated spectra from 9 January 1991	92
3.4	Probability of observing cusp and boundary region signatures	93
3.5	Probability distribution function in magnetic latitude versus magnetic time of the cusp and low latitude boundary region (LLBL) as observed by satellite measurement	95
3.6	Latitude integrated probability distribution of LLBL and cusp	97
3.7	Comparison of ground based ULF signatures and satellite signatures	99
3.8	Example of Category 1 spectrogram	101
3.9	Example of Category 2 spectrogram	102
3.10	Example of Category 3 spectrogram	103
3.11	Distribution of cusp occurrences by spectral category	105
3.12	Ratio of the power in the pre-noon to post-noon boundary region	106
3.13	IMF GSM Component Histogram for total data set	111
3.14	IMF GSE Angle Histogram for total data set	112
3.15	IMF GSM Component Histogram for Category 1	114
3.16	IMF GSM Component Histogram for Category 2	115
3.17	IMF GSM Component Histogram for Category 3	117
3.18	GSE IMF Angle Histogram for Categories 1-3	118
3.19	IMF GSM Component Histogram for Category 4	120
3.20	IMF GSM Component Histogram for Category 5	121
4.1	Example of power spectral density and power law fit	126
4.2	Geometry for relation between Solar Depression and Solar Zenith Angle	128
4.3	Spectral index, variance, and photoionization rates versus solar depression angle for entire data set	129

4.4	Spectral index and variance versus solar depression angle for Category 1	133
4.5	Spectral index and variance versus solar depression angle for Category 2	134
4.6	Spectral index and variance versus solar depression angle for Category 3	135
4.7	Topology of magnetic field and bow shock location for winter solstice in GSM coordinates	137
4.8	Time series for magnetometer on 9 Jan 1991	141
4.9	Fluxgate x component phase diagram, 9 January 1991	144
4.10	Fluxgate X component phase diagram, 8 November 1990	146
4.11	Fluxgate Y component phase diagram, 22 December 1990	148
4.12	Inferred component of field aligned current carried by downward flowing electrons on 9 January 1991	149
4.13	Comparison of Latitude Integrated FAC's and magnetometer phase jumps	151
4.14	Multiple X Line Reconnection Geometry	159
4.15	Field Aligned currents associated with multiple X line reconnection	161
4.16	Geometry of ULF waves due to multiple X line reconnection	163
A1.1	Geometry for ionospheric slab with arbitrary conductance and field aligned current	177
A1.2	Integration geometry for Biot-Savart Law	180

LIST OF TABLES

Table		Page
2.1	Relative Transmission of 6300 Å filter at different wavelengths.	34
2.2	Emissions Observed with MSP.	35
3.1	Occurrence Statistics of Spectral Categories.	104
3.2	Cusp signature and Pc3 Statistics, Percent Relative to Category.	104
3.3	IMF Coverage broken down by ground-based spectral category .	110
3.4	IMF time selection criteria for ground-based spectral category.	110

Preface

In January 1991 I had the great good fortune to observe firsthand dayside aurora at the Nordlysstasjonen in the Svalbard islands of Norway. The visual difference between day and night side aurora was immediately obvious to me, and the rather naive question of why this difference occurs started me down the path that led to this thesis. I was able to participate in these observations through the support of my advisor Professor John Olson, and I lay my interest in dayside phenomena squarely at his feet. The three years I spent working on this topic have been the most rewarding of my professional career. John provided a unique mixture of mentor, teacher, academic advisor and friend that resulted in an exciting atmosphere in which to work. A simple "thanks John" seems rather inadequate, but is certainly heartfelt. I would also like to thank my wife Sabrina. Going back to school in midlife can be trying, and Sabrina helped me realize it was not only possible, but can actually be fun. I would be remiss if I failed to thank my good friend J.T.B., whose constant banter always helped me keep my sense of perspective while writing this thesis.

CHAPTER 1

Introduction

Since the 1930's, the interaction of the solar wind with the terrestrial dipolar magnetic field has been shown to result in a current carrying layer that surrounds the earth. This layer of current, called the magnetopause, serves as the boundary across which mass, energy and magnetic flux gain entry into the earth's magnetosphere. *Chapman and Ferraro*, [1931] point out that in the simplifying case of a plane current sheet oriented perpendicular to the solar wind velocity that the current layer has two points where the magnetic field is perpendicular to the magnetopause. This causes the magnetic field pressure to be zero at these points and, in principle, allows entry of magnetosheath plasma to the ionosphere. This is the simplest explanation of the cusp; a region where magnetosheath plasma is allowed entry to ionospheric levels due to the magnetic field geometry.

Figure 1.1 shows the resulting magnetic field topology based on the empirical model of *Tsyganenko* [1989]. In this figure the magnetic field lines are shown for winter solstice and a K_p disturbance level of 6 at 12:00 universal time (UT). Notice the dayside portion of the magnetosphere is compressed due to the solar wind, while the night side is stretched out into a tail. This figure shows that at high latitudes the field lines stop closing on the dayside, and start closing on the nightside. While the model is based on a closed magnetosphere, it still indicates that some latitude exists where there will be access to the ionosphere of magnetosheath particles, and is the general location of the cusp. Such a model can only be used in a general sense however because it does not include the dayside current systems which modify the dayside magnetic field.

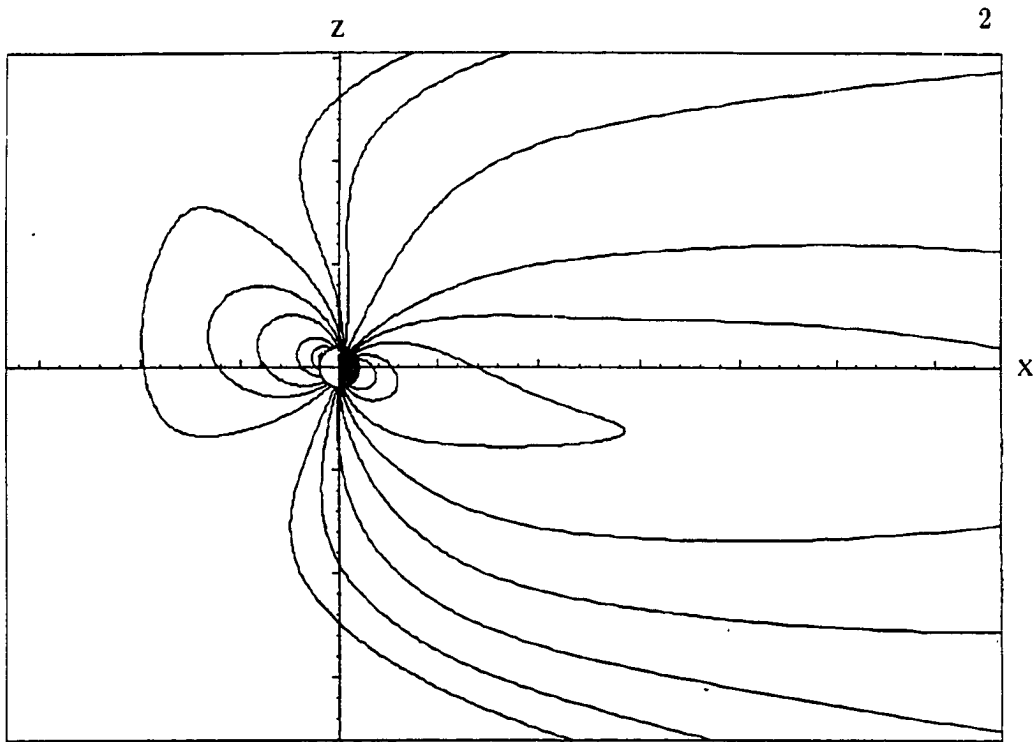


Figure 1.1. Magnetic field topology of magnetosphere using the model field of *Tsyganenko* [1989]. The magnetic field is shown in the noon midnight meridian plane for winter solstice. Note the fieldlines at high latitude change from closing on the dayside to the nightside, and this is in general the latitude of the cusps. Note that the summer cusp is sunlit while the winter cusp is not sunlit.

From its original inception then the concept of the magnetospheric cusp has at least two important different ideas associated with it. First is the magnetic field topology that results from the interaction of the solar wind and the terrestrial magnetic field. The second is the resulting plasma entry due to this topology and the implications of this plasma entry into the ionosphere. Since the cusp represents different ideas to different people, the literature surrounding this broad topic reflects this dichotomy. Some authors concentrate on the magnetic topology of the region, see for instance *Spreiter and Summers*, [1967], *Dungey*, [1958], while

others concentrate on the plasma characteristics observed at ionospheric heights, see *Heikkila and Winningham* [1971]. This introductory chapter is a blend of these two ideas, with the emphasis being given to the latter, that is the observational effects of the magnetosheath plasma gaining entry through the cusp into the ionosphere. After this brief introduction to the literature I present the basic conceptual framework for the analysis and discussion that follows in the body of the thesis.

1.1 Early observations of the cusp

Airborne optical observations made by *Eather and Mende*, [1971] showed that a region of low energy precipitating particles existed poleward of the of the auroral oval near the midday meridian. These particles had electron energies of 100-200 eV and *Eather and Mende*, [1971] postulated that these particles came from the magnetosheath. The cusp has been identified at least since the 1960's as a source of large amplitude ULF fluctuations in the Earth's magnetic field. *Feldstein and Zaitzev* [1968], report data taken during the IGY that show the "...polar electrojet with westward current is located at $\phi \sim 65^\circ$ at midnight and $\phi \sim 76^\circ$ at midday ...". *Zmuda et al.* [1970] report crossings of the high latitude dayside by satellite, and show large transverse magnetic field fluctuations centered on magnetic noon and falling between 77° and 80° invariant latitude. *Zmuda et al.* [1970] attributed these fluctuations to passage of the satellite through currents flowing along the field lines. *Burch* [1968] and *Heikkila and Winningham* [1971] show that the high latitude dayside region is the area of direct access of magnetosheath like plasma to low altitudes. According to *Heikkila and Winningham* [1971] this plasma "...flux is related to a number of geophysical phenomena, including magnetospheric surface currents, daytime auroras, VLF and LF emissions, ionospheric irregularities, and geomagnetic fluctuations." These early papers show the basic division of observations of the cusp with both ground and satellite observations playing an important

role. However all reinforce the idea that the cusp is the a region of enhanced electromagnetic turbulence and particle entry into the dayside ionosphere. This idea is presented by *Heikkila et al.* [1972] in one of the first attempts to combine optical observations made in aircraft, with particle measurements made by satellite.

1.2 Satellite observations of the cusp

This section deals with the satellite observations of the cusp, and is arranged into three main areas by the type of observation. The first subsection studies the observed precipitating particles in the cusp, while the second studies the magnetic and electric fields associated with currents and waves in the cusp region. The third studies the optical emission resulting the interaction of the first two with the ionospheric plasma. These three differing measurements tend to complement each other, and yield different types of information. The particle measurements have been the major discriminant used in morphological determinations because they map locations of plasma with similar characteristics. In this vein the measurement of field aligned currents also yield morphological results. In general the particle and current measurements give a macroscopic view of cusp physics. The field measurements yield insight into source mechanisms, and tend to give a more microscopic view of the cusp physics. The optical measurements are something of a combination, having been used for both morphological exploration of the dayside and also being used to determine such microphysical details as the cusp temperature.

1.2.1 Particles

Along with *Heikkila and Winningham* [1971] early particle measurements were carried out by *Burch* [1968], *Frank and Ackerson* [1971], and *Frank* [1971]. All these papers indicate that a region of low energy electron precipitation exists at latitudes higher than the typical auroral zone, and that these particles are indicative of

magnetosheath like parameters. *Frank* [1971] and *Heikkila and Winningham* [1971] both attribute these particles directly to entry of magnetosheathlike characteristics.

McDiarmid et al. [1976,1975,1972] report on particle precipitation in the high latitudes. These measurements do not distinguish between particles in the cusp and those in the boundary layers. Rather they treat the entire ensemble as one entity with a wide distribution in local magnetic time and geomagnetic latitude, which they call the cleft. *McDiarmid et al* [1976] gives a statistical argument to show a difference in the particle energy spectrum before and after magnetic local noon. Due to this, and the fact that they make no distinction between the boundary layer particles and the central cusp, *McDiarmid et al.* [1976] argue for the cleft particles to be on closed field lines.

The question of whether particles originating in the magnetosheath penetrate to the ionosphere is fundamental given our definition of the cusp. *Reiff et al.* [1977] and *Shelly et al.* [1976] show that the observations of ions at mid altitudes are consistent with injection of magnetosheath plasma at the equatorward edge of the cusp. Due to a constant $\vec{E} \times \vec{B}$ drift as the ions propagate down the field lines there will be a dispersion on parallel energies with latitude. The higher energy ions will penetrate faster, and hence be convected poleward a shorter distance. *Reiff et al.* [1977] and *Shelly et al.* [1976] show that this is the case for most of the measurements made of the mid-altitude cusp. *Burch et al.* [1982] use ion energy measurements from the DE-1 satellite and a model of the expected ion energy pitch angle distribution to estimate that cusp ions seen at DE-1 had their injection point at distances of 8 earth radii (R_E). This again shows that the cusp ions have a magnetosheath origin. All these studies are based on a relatively few satellite crossings, and hence do not allow a detailed mapping of the the cusp with latitude and magnetic local time. However they do seem to show that indeed magnetosheath

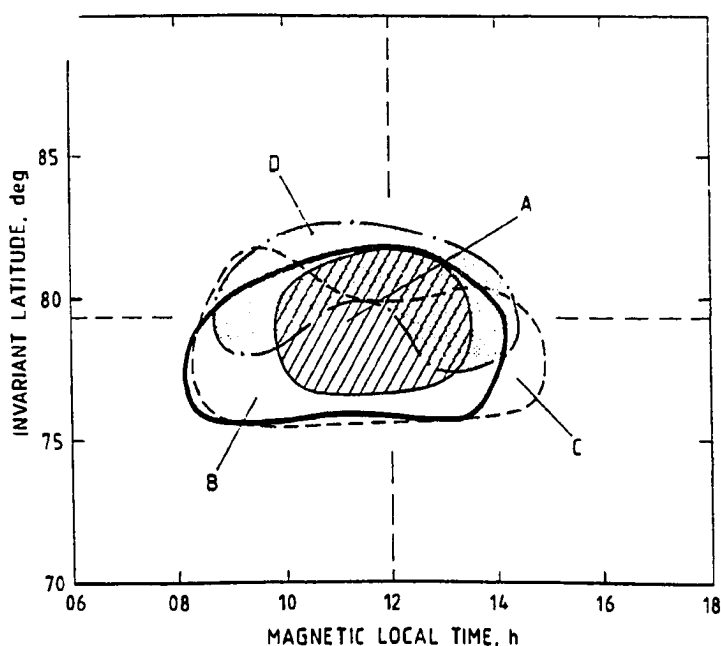


Figure 1.2. Ionospheric map of the cusp/cleft from Figure 12 of *Kremser and Lundin* [1990]. The plot shows outlines of four regions of precipitation as determined by the Viking satellite. Region A is the cusp proper, region B is the entry layer, region C is the low latitude boundary layer, and region D is the plasma mantle.

ions penetrate to ionospheric levels, and are consistent with intermittent injections at the equatorward boundary of the cusp.

Kremser and Lundin [1990] address the statistical question of where the cusp maps in the ionosphere, and the results are shown in Figure 1.2. Using the Viking satellite which orbits at mid-altitudes from 817 km to 13,530 km they distinguish between four regions in the cusp/cleft system. They define the central cusp as a region with magnetosheath like ion characteristics containing no accelerated electron events. Connected to the equatorward edge of this central cusp is the entry layer, which contains both magnetosheath-like ions, and accelerated electrons. *Kremser*

and Lundin [1990] consider both the entry layer and the central cusp to be part of the cusp, but separate them with the distinction that the entry layer shows signs of electron acceleration. Equatorward of the central cusp is the low-latitude boundary layer which they feel maps to the magnetospheric boundary layer. Finally poleward of the central cusp is the mantle, which has strong antisunward flows and has its origin in the magnetosheath.

Using the energy flux and energy spectral measurements of precipitating particles on the dayside ionosphere Newell and Meng [1992] have characterized the populations of the cusp and boundary layer region in the lower ionosphere. These measurements are made on the Defense Meteorological Support Program (DMSP) and are detailed over a series of articles; see Newell *et al.* [1991a;c], Newell and Meng [1989], and Newell and Meng [1988]. In these papers the authors use the average energy and energy flux of the ions and electrons as parameters to distinguish between different particle precipitation regions in the dayside ionosphere. The seven different regions defined in these papers are, following Newell and Meng [1992], polar rain, mantle, cusp, low latitude boundary layer (LLBL), boundary plasma sheet (BPS), central plasma sheet (CPS), and regions void of significant particle fluxes. These definitions were applied along the track of each orbit and statistics kept on the location of the differing particle precipitation regions. Comparing to the Viking data we see that the DMSP measurements have added additional categories in terms of the CPS and BPS, while not distinguishing between the central cusp and entry layer as did Kremser and Lundin [1990].

Figure 1.3 reviews the results reported by Newell and Meng [1992], and is figure 2 of that paper. Figure 1.3 displays a typical statistical mapping of the particle populations to the DMSP altitude of 835 km. These results are the average of approximately 60,000 crossings of the dayside ionosphere over both poles. The display is in magnetic coordinates using the PACE model for magnetic local times

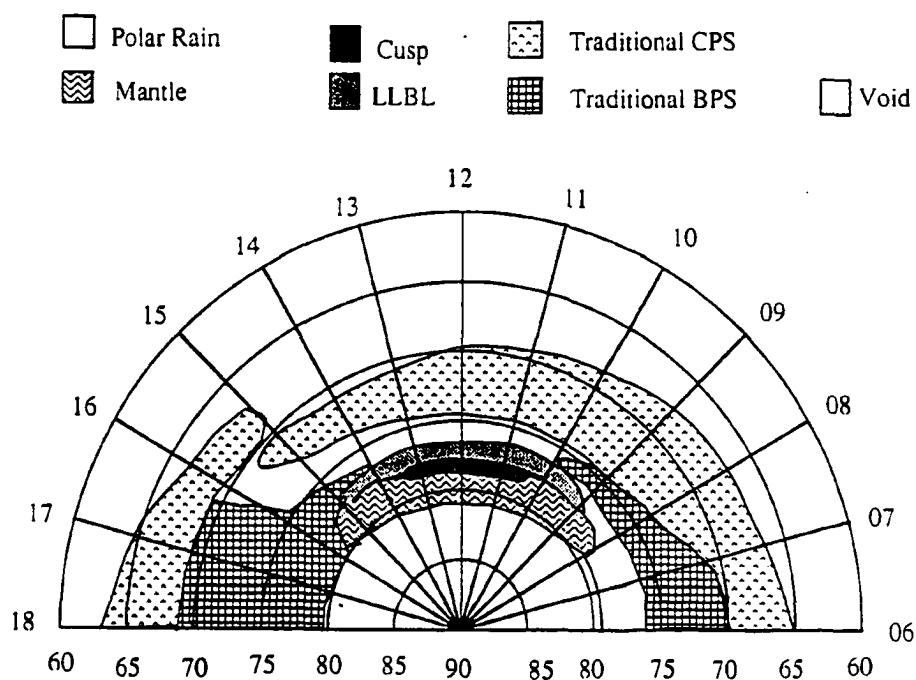


Figure 1.3. Map of particle precipitation regions in the ionosphere. From *Newell and Meng* [1992], their Figure 2. This is a statistical view of the dayside precipitation regions, note that the cusp is seen at about 78-79 °magnetic latitude from about 10:30 MLT to 13:30 MLT.

and latitudes, *Baker and Wing* [1989]. As can be seen the cusp at this altitude is detected over some 2.5 hours in local time, and is located at about 78 degrees magnetic latitude. Equatorward of the cusp is the region of the low latitude boundary layer, and poleward of the cusp is the mantle region. Poleward of the mantle is the region of polar rain, while the CPS and BPS intrude around the flanks of the dayside regions. While representing no individual day this statistical picture is still a good overview of the differing precipitation regions, and is in good general agreement with that found by *Kremser and Lundin* [1990].

In addition to determining the mapping of these different regions to the ionosphere, the DMSP work has looked at effects of the interplanetary magnetic field on the location of these plasma boundaries. *Newell et al.* [1989], *Burch et al.* [1986] and *Carbary and Meng* [1986] show that the cusp position shifts equatorward with increasing negative B_z , while *Newell et al.* [1989a] also shows that cusp latitude has little dependence on the magnitude of northward B_z . Thus the cusp responds nonuniformly to changes in B_z . *Newell et al.* [1989] also show that the component of B_y is important only when the B_z component is negative. When B_z is negative and B_y is positive, then the cusp moves towards dusk in the northern hemisphere, and when B_z is negative and B_y is negative the cusp moves toward dawn in the northern hemisphere. *Carbary and Meng* [1986] also show a pronounced movement of the cusp with B_z and also correlate this movement with the AE index, [see *Mayaud*, 1980]. They note that the poleward edge of the cusp shows a higher correlation coefficient with both B_z and AE than the equatorward edge of the cusp.

In two companion papers *Newell and Meng* [1988b,1989b] show a distinct asymmetry in cusp latitude and particle precipitation characteristics with dipole tilt angle. *Newell and Meng* [1988b] show that when the cusp is toward the sun the ion energy flux increases by 61 ± 11 percent over the cusp that is away from the sun. They also find that the average energy decreases in the summer hemisphere.

The winter cusp has a higher energy because the tailward flowing ions have accelerated to a higher velocity by the time they get to the cusp. They believe that only the higher energy ions and electrons can then penetrate the stagnation region surrounding the cusp. *Newell and Meng* [1989b] show statistically that the position of the cusp in latitude changes with dipole tilt angle, and hence season. They find that between solstices the cusp will move in latitude by about four degrees of magnetic latitude, with the cusp being furthest equatorward in the winter solstice. They also find in this paper that the low-latitude boundary layer does not show as pronounced a shift due to dipole tilt angle, and its average seasonal dependence is only about 2 degrees.

1.2.2 Fields

In addition to the particle precipitation data there have been many studies of the electromagnetic field measurements in the cusp region. Magnetic field measurements can be used to determine locations of field aligned currents into and out of the cusp ionosphere. *Sugiura and Potemra* [1976] show that net currents indeed flow along field lines into and out of the ionosphere. *Iijima and Potemra* [1976a] show that these field aligned currents are in two basic regions, the poleward one called region 1 and the equatorward called region 2. They also show that the sense of current flow to the ionosphere is opposite for the two regions, with the region 1 currents flowing into the ionosphere before magnetic noon, and out of the ionosphere after magnetic local noon. *Iijima and Potemra* [1976a] also point out that the region 1 currents seem to be a permanent feature, and continue to exist for very small disturbance levels.

Erlanson et al. [1988] show that while the Region 1 current flows into the ionosphere before "noon", and away from the ionosphere after "noon", the line demarking "noon" actually moves in magnetic local time in response to the sign of

the IMF B_y component. If B_y is positive the line moves towards dusk, and if B_y is negative the line demarking "noon" moves towards dawn. This movement with the IMF B_y component is the same as found for the cusp as shown by *Newell et al.* [1989], and it is tempting to conclude that the Region 1 currents are divided on the dayside by the cusp.

The Region 2 currents on the other hand seem to be well correlated with the nightside westward electrojet, and disappear during very low disturbance levels. *Iijima and Potemra* [1976a] find the largest Region 1 current density is between 0700 and 0800 MLT, and that at this time the Region 1 field aligned current is at about 75 degrees magnetic latitude. *Iijima and Potemra* [1976a] speculate that the source of the region 1 current is the dayside magnetospheric boundary layer. This view is supported by *Bythrow et al.* [1981] who use combined magnetometer and particle precipitation measurements to determine that the region 1 currents arise in the boundary layer of the magnetosphere. *Potemra et al.* [1987] also come to this conclusion using Viking satellite measurements.

Iijima and Potemra [1976b] discuss the field aligned currents associated with the cusp. These currents are found poleward of the region 1 current system, and generally have the opposite sense of direction from the region 1 currents, that is the cusp currents are out of the ionosphere in the morning and into the ionosphere in the afternoon. *Bythrow et al.* [1988] show that these cusp currents are associated with the mantle precipitation regions, that is they are poleward of the cusp as defined by particle precipitation. A summary of the Birkeland current systems associated with the dayside ionosphere is shown in Figure 1.4, taken from *Erlanson et al.* [1988]. Figure 1.4 shows the relative position of the Region 1, Region 2 and Cusp Current systems with respect to local time and magnetic latitude for positive and negative B_y orientations. Also shown are the DPY currents, which are zonal Hall currents that flow in between the Region 1 and Cusp current system. It is

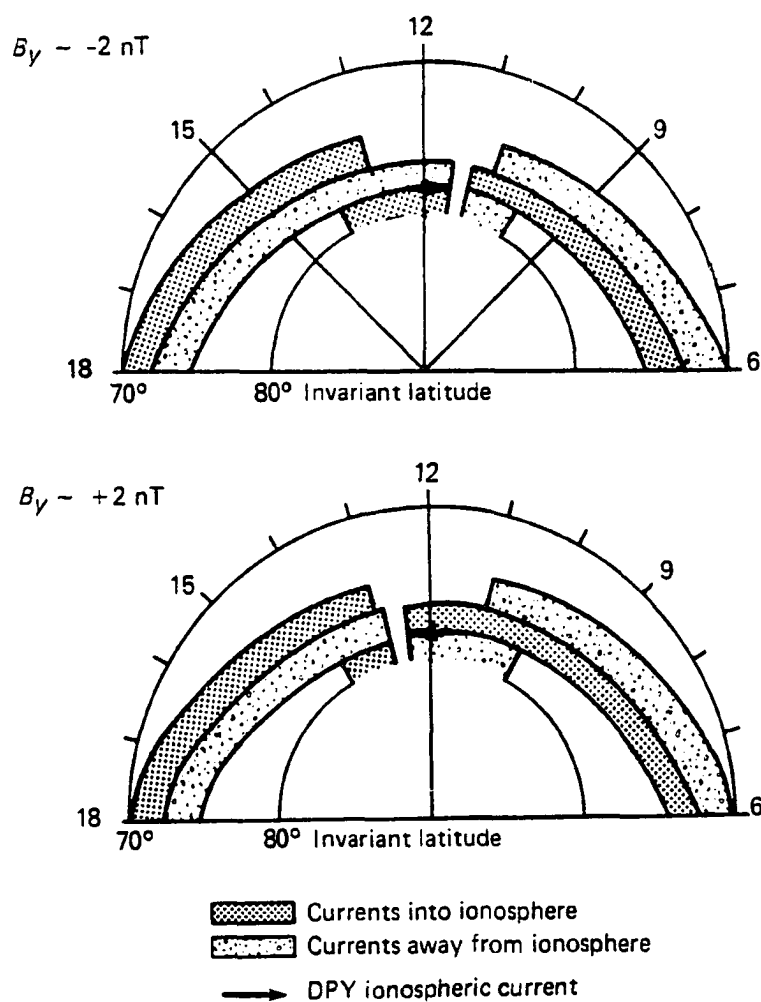


Figure 1.4. Position of Region 1, Region 2, and Cusp field aligned current systems as a function of B_y , taken from *Erlandson et al.* [1988]. Notice that the line demarking where the Region 1 currents flow into and out of the ionosphere is not fixed, but follows B_y .

consistent with the statistical data of *Newell and Meng* [1989] to put the cusp as defined by the particle precipitation data in the gap between the Region 1 currents systems in this figure.

Measurements onboard satellites can also be used to look for areas of rapidly changing magnetic and electric fields at the magnetopause, magnetosphere, or in the ionosphere. At the magnetopause *Russell et al.* [1971], *Scarf et al.* [1972], *Fredricks and Russell* [1973] and *Fredricks et al.* [1973] use satellite data from OGO 5 during the very disturbed day ($K_p = 8+$) of 1 November 1968 to show that the boundary layers of the cusp are rich in ULF fluctuations and plasma wave energy, specifically ion cyclotron wave modes. *D'Angelo* [1973] revisit this data set, and interpret the observations in terms of a Kelvin-Helmholtz instability. *D'Angelo et al.* [1974] discuss measurements made with the HEOS 2 satellite of 20 crossings of the cusp and its boundary. Again *D'Angelo et al.* [1974] favor the Kelvin-Helmholtz instability when describing the observed results. *D'Angelo et al.* [1974] also point out that magnetic field fluctuations are common on one or both of the boundaries of the cusp. *Tsurutani et al.* [1981] shows that at the boundary layer just inside the magnetopause, electrons and ions with kilovolt energies are observed.

The upstream bow shock has been noted to be turbulent when the angle the IMF makes with the normal to the bow shock becomes small, [*Greenstadt* 1972]. This orientation can lead to the generation of ULF pulsations in the upstream region, and flood the magnetosheath with ULF noise, see *Russell et al* [1983]. *Engebretson et al.* [1987] and *Luhmann et al.* [1986] verify that the Earth's magnetosphere is flooded with Pc3-4 pulsations when the IMF cone angle is small. *Engebretson et al.* [1987] shows further that these pulsations happen in two main categories, the first is broad band compressional wave power centered around magnetic noon, and the second are more monochromatic with periods identical to that seen in the solar wind upstream of the bow shock. *Engebretson et al.* [1987] find

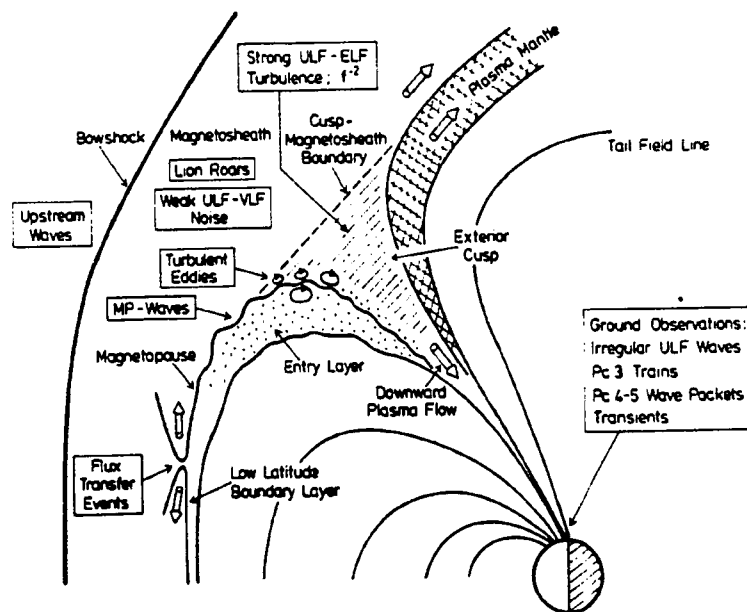


Figure 1.5. Observables and source regions in the cusp, taken from figure 1.4 of *Glassmeier* [1989].

that the narrow band pulsations are seen at higher latitudes. All this leads *Engebretson et al.* [1987] to conclude that upstream wave power can leak into the cusp via compressional waves and serve as a source for Pc3 pulsations at lower latitudes. *Engebretson et al.* [1991] feel that the source of this coupling may be that the ionospheric conductivity is modified by particle precipitation that occurs at the frequency of the compressional wave that penetrates the cusp. This modified conductivity causes the ionospheric currents to be modulated, which in turn can modulate the Region 2 field aligned currents. This modulation of the ionospheric currents causes a modulation of the Region 2 currents and is proposed as the source of the coupling of upstream wave energy into the lower latitudes.

Erlandson et al. [1987] also report that the equatorward side of the cusp is a site of intense electrostatic waves with frequencies between the electron plasma and cyclotron frequency. They find a strong correlation between this region and the downward flowing region 1 current system. This has also been reported by *Maynard et al.* [1991] who also show that the equatorward side of the cusp has intense field aligned currents associated with it, with current densities of $10 \mu\text{amps} \cdot \text{m}^{-2}$. *Maynard et al.* [1991] attribute these intense field aligned currents to an Alfvén wave packet of finite dimensions, which is at the equatorward side of the cusp.

A summary of the observables in the cusp and the possible source regions of these observables is given by *Glassmeier* [1989], and reproduced here as Figure 1.5. This figure reinforces the idea that the cusp/boundary layer system is an area with both accelerated particles, and large amplitude wave fields that arise in both local and remote locations.

1.2.3 Optical Emissions

The final type of observations that are relevant to this section are optical emissions detected from satellite. Among the first satellite photos of the aurorae were those taken by the DMSP satellite. The DMSP does not actually take a two dimensional image rather the satellite scans from side to side along the flight path. The intensity in a filtered photometer is recorded for each scan angle, and the image is built in this method. *Rogers and Nelson* [1974] report that the DMSP spectral response peaks in the near IR at $0.80 \mu\text{m}$, and falls to 50 percent of the maximum by 0.59 and $1.01 \mu\text{m}$. This response thus integrates over the forbidden O I lines of 5577 \AA , the O I allowed 8446 \AA , and the 6300 6364 \AA doublet, as well as a majority of the N_2 first positive, OH, and N_2^+ Meinel system, [*Chamberlain*, 1961]. *Snyder and Akasofu* [1976] showed that the midday oval was different from the rest of the auroral oval, with distinct arcs that terminate around local noon, instead of a continuous band of arcs across local noon. *Dandekar and Pike* [1978] give this observation the title of the midday gap, and explain it in terms of a lack of discrete arcs seen through the midday time. *Dandekar* [1979] show this gap is seen two thirds of the time. *Dandekar* [1979] feels that the appearance of discrete arcs in the dayside gap is connected to to the the IMF Bz component and to substorm phase. The question of whether the night side substorm and dayside aurora are linked is very interesting, and *Meng and Lundin* [1986] argue that there is no correlation between the two. They also use DMSP imagery to come to this conclusion. Their conclusion is that the dayside arcs that are seen around the central midday gap are connected to the low-latitude boundary layer, which means that the two systems are unconnected.

Meng [1981] uses both optical and particle precipitation data from the DMSP to look at the midday gap in the oval. He reports on one instance when the midday gap is determined to be the cusp using particle precipitation data. A more recent

article by *Newell et al.* [1992] using particle data from DMSP and imaging data from the Polar Bear satellite reveals that the arcs seen on the dayside oval are found to map to the interfaces of the distinct plasma regions as identified by the DMSP particle data.

The ISIS-II spacecraft carried photometers with filters centered around the 6300, 5577 and 3914 Å lines. *Shepherd and Thirkettle* [1973] report that the cusp has enhanced emissions in the 6300 Å band compared to the rest of the auroral oval. This is consistent with low energy electron precipitation, [e.g. *Shepherd et al.*, 1976]. *Shepherd et al.* [1976] show that during a pass at 13.1 hours local magnetic time the ratio of the red to green (6300 to 5577 Å) forbidden lines intensity was about 8. This points out that the midday gap is not really a lack of all emissions, but rather a distinct decrease in the structured green arcs that are caused by the higher energy electron precipitation, which is normally lacking in the cusp. They also report that in the cusp itself the electron temperatures were about 3500 °K, while the ion temperature rose to almost 7000 °K somewhat poleward of the cusp, and the peak in the F region electron density was about $2.0 \times 10^5 \text{ cm}^{-3}$. *Cogger et al.* [1977] reports that the N_2^+ 3914 Å band is observed to decrease as well during the midday gap, but does not totally disappear. *Shepherd* [1979] reviews these and other articles and summarizes the state of the measurements at the end of the 1970's.

1.3 Ground Based Magnetic Observations of the Cusp

The ambient magnetic field at cusp latitudes has an inclination angle of about 10 degrees from the vertical. The total field is about 53,000 nT, with only about 7500 nT in the horizontal component of the field. Thus a large perturbations of 75 nT in horizontal plane is only a 1 percent fluctuation of the total horizontal

component. With this introduction to the ambient field the fluctuations observed in this ambient field are now reviewed.

As mentioned, ground based observations of the magnetic field fluctuations in the high latitude dayside have a long history. Using a chain of fluxgate magnetometers in Canada, *Samson et al.* [1971] report on the latitudinal variation of long period magnetic field fluctuations. They find that the polarization of the magnetic perturbation vector has a distinct variation with latitude and magnetic local time. *Samson et al.* [1971] find that at geomagnetic latitude 75° the polarization of the 5 mHz signals are right handed in the morning sector, and switch to left handed about 1300 hours MLT. They suggest that this reversal in polarization again be explained by a Kelvin-Helmholtz instability driven vortex caused by the shear flow of the solar wind around the magnetopause. This causes perturbations in a counterclockwise (as viewed looking along the field) - or left hand sense in the morning hours, and this sense switches to right after magnetic local noon. They note however that the latitudinal variations of polarization seen in their results do not fit with this simple explanation. The Kelvin - Helmholtz instability driven idea is further developed by many authors in terms of resonant oscillations of the geomagnetic field in response to an input of energy onto the field lines. *Chen and Hasegawa* [1974], and *Southwood* [1974] show that the polarization changes observed by *Samson et al.* [1971] can be explained by this field line resonance model.

Lee et al. [1981] show the inner edge of the magnetopause is unstable to the Kelvin-Helmholtz instability. They also show the inner edge of the magnetopause will have a right handed polarization in the morning and a left handed polarization in the afternoon, while the magnetosheath side of the magnetopause will be of opposite handedness. Both authors also confirm that a latitudinal change of the polarization as observed on the ground could be due to this instability. *Rostoker et*

al. [1972] allude to such a switch in polarization with latitude as the demarcation line on the ground for cusp latitude fluctuations.

Bol'shakova and Troitskaya [1977] also report on ground observations at high latitudes and find a latitudinally dependent time of maximum power of long period (3 -7 minutes) oscillations. They call these oscillations ipcl: long period irregular pulsations. In this paper they suggest that the latitude of the cusp can be found by measuring this maximum occurrence time at a single station, and comparing it to the results from a known line of stations. *Kleyменова et al.* [1982], report on use of the Greenland chain of magnetometers to define an empirical fit to the offset in time of the maximum of the ipcl's from magnetic noon to find the latitude of the cusp. *Troitskaya and Bol'shakova* [1977] report on the diurnal variation of the latitude of the cusp with U.T. time as derived from this method. *Troitskaya* [1985] explains this effect in terms of the angle between the magnetic pole and the earth-sun line. She finds this daily variation is on the order of 5° . *Stasiewicz* [1991] uses the Tsyganenko field models, version 1987 and 1989 *Tsyganenko* [1987,1989], to look at the cusp latitude and reports a similar diurnal variation. However *Stasiewicz* [1991] concludes that this variation is an artifact of the coordinate system used to report the data, and shows that use of corrected magnetic coordinates reduces this diurnal variation to approximately $\pm 1^\circ$. The variation shown by *Troitskaya* [1985] is similar in nature to but larger in magnitude with a slightly offset peak in UT time from the results found by using the invariant coordinate system as seen in Figure 7 of *Stasiewicz* [1991]. Thus it is not yet clear if the diurnal variations reported by *Troitskaya* [1985] are totally explained by the the coordinate system used for reporting the results, or if indeed there exists a residual diurnal variation of the current systems on the dayside with UT time.

Lanzerotti et al. [1986,1987] report on cusp latitude pulsations caused by hydro-magnetic waves. They find large amplitude, (100 nT), low frequency (2 mHz) single

cycle pulsations. The polarization of these events is predominantly right handed, with linear polarization at the time of occurrence of the maximum amplitude of the event. *Lanzerotti et al.* [1990] examine magnetic data from cusp latitude ground stations at the South Pole and a conjugate site in Iqaluit, Northwest Territories. In this report they again focus on the large amplitude, low frequency events with large perturbations in the vertical direction. They interpret these events as a single cycle of an odd mode Alfvén wave. This work is followed by *Lanzerotti et al.* [1991] which is a statistical study of such events. The selection criteria for each event are that it has to be present within an 8 minute window at both conjugate sites, and the perturbation in the vertical direction has to be greater than 50 nT, while the perturbations in the horizontal plane have to be larger than 40 nT. Statistical results from this report show such events occur more often at local magnetic times away from noon. Specifically peaks of the occurrence distributions at Iqaluit occur at 0830 MLT and at 1330 MLT. A strong minimum in occurrence of these impulsive signals is seen around local noon. *Lanzerotti et al.* [1991] also show that such signals occur more frequently during the solstice periods. Again these signals are interpreted as the ground observations of single cycle odd mode Alfvén wave along a near magnetopause flux tube. No source mechanism for the Alfvén wave is mentioned. In contrast to their earlier work, no general trend in the polarization state is seen in these events.

Other cusp latitude magnetic studies are carried out using the Greenland Magnetometer Array. Using meridional chains of magnetometers on the East and West coast of Greenland, *Friis-Christensen et al.* [1988] find the ionospheric signature of a pair of tailward convecting vortices. These vortices are found to move toward the midnight sector in the ionosphere at constant magnetic latitude. These vortices are interpreted in terms of a pair of field-aligned current systems. They find the line joining the two field-aligned currents is roughly parallel to the direction

of convection. This alignment is used to argue that the field-aligned currents are being caused by a readjustment of the magnetopause due to changes in the solar wind pressure.

McHenry et al. [1990a] show that these vortices can come in multiple sets of events. The peak amplitudes of the associated disturbances are found to be at approximately 75 degrees invariant latitude. Simultaneous observations with the Sondrestrom radar indicate to *McHenry et al.* [1990a] that the vortices fall close to the convection reversal boundary. They also find, using simultaneous DMSP overpasses, that the vortices are on field lines that are associated with plasma from the low latitude boundary layer, and they place the vortices on the inner edge of the boundary layer. All these indications lead *McHenry et al.* [1990a] to conclude that the probable source mechanism of these vortices was the Kelvin-Helmholtz instability on the inner edge of the boundary layer.

McHenry et al. [1990b] then follow with a statistical study of these traveling ionospheric vortices. They find no correlation between the IMF and solar wind pressure and occurrence of the vortices. They find a slight increase in occurrence of vortices with slow solar wind speed. They also report a larger percentage of occurrence for the post local magnetic noon time periods rather than the pre noon time periods. They note that the last two facts seem counter to their explanation of the Kelvin-Helmholtz instability. They state however that they are biased due to experimental constraints to detecting large slow moving vortices, and this may explain why they see larger numbers in the post noon sector. They also note that geometry effects may play an important role in determining when they can observe the vortices. The Greenland chain of magnetometers is tilted approximately 20 degrees with respect to the lines of constant invariant latitude, and this may make detecting vortices in the afternoon easier than detecting them in the morning.

The auroral zone signatures of traveling vortices are reported by *Glassmeier et al.* [1989]. The auroral zone measurements show the centers of the vortices to be at approximately 73 degrees invariant latitude, in good agreement with the Greenland Array data. In contrast to the higher latitude studies, *Glassmeier et al.* [1989] find a pronounced peak in the probability of occurrence for the 0800 MLT time period. *Glassmeier* [1992] and *Glassmeier and Heppner* [1992] continue to study the twin vortex structure. They model the vortices as a pair of field aligned currents driven by Alfvén waves launched from a moving partial compression in the dayside magnetopause. While this theory is very attractive it seems to contradict the findings of *McHenry et al.* [1990b] who show no particular increase in occurrence in vortices with solar wind pressure. It is possible that the pressure perturbations involved are spatially localized in nature, and the sparse coverage of solar wind parameters do not measure these localized changes in pressure. The careful studies by *McHenry et al.* [1990a and 1990b], and *Glassmeier et al.* [1989], *Glassmeier* [1992], and *Glassmeier and Heppner* [1992], seem to indicate that even when a meridional chain of magnetometers is used, sorting out the resulting signals can be a daunting task.

Olson [1989] shows that as well as moving zonally that current filaments can propagate poleward. Using magnetometers at two stations in Cape Parry and Sachs Harbor, N.W.T. which are positioned approximately along a line of constant magnetic longitude, *Olson* [1989] was able to track individual large amplitude pulses from the southern station to the northern station. Using a sliding cross-correlation analysis, *Olson* [1989] determined that the correlation was maximized between the two time series when the two stations were offset by approximately 60 seconds, yielding an apparent poleward speed of 2 - 5 km · s⁻¹. These pulsations were found to be large in amplitude, 20 - 50 nT, and uncorrelated with each other.

Engebretson et al. [1986,1989] show that the South Pole Station cusp site is an area of intense Pc3 pulsations. They show that these Pc3 pulsations are associated with small IMF cone angles, suggesting an upstream source for these waves in the bow shock region. *Engebretson et al.* [1990] also show that the Pc3 pulsations present in the magnetic data are associated with pulsations in the optical emissions. *Engebretson et al.* [1990] believe that this indicates that the incoming precipitation modifies the conductivity of the darkened ionosphere, and this causes horizontal currents to flow, resulting in the magnetic pulsations observed on the ground. This paper demonstrates that inclusion of optical information derived from the same location can be crucial in interpreting the magnetometer observations.

1.4 Ground Based Optical Observations of the Cusp

Observations of the high latitude dayside using optical techniques from ground or airborne platforms date back at least to the airborne observations of Eather in 1968 and the NASA Airborne Auroral expedition of 1969, *Eather* [1969] and *Eather and Mende* [1971]. *Eather* [1969] report that a zone of soft electron precipitation exists poleward of the normal auroral zone. *Eather and Mende* [1971] extend this work, and show that the energy of the precipitating particles decreases with increasing latitude. *Eather and Mende* [1971] also identify these precipitating particles as coming from the magnetosheath. *Sivjee and Hultqvist* [1975] report on a comparison of particle precipitation energies as determined by using ratios of optical emissions and as obtained from satellite observations. During the 1969 NASA Airborne Auroral expedition the jet flew along the same path as the ESRO IA satellite. *Sivjee and Hultqvist* [1975] compare the results for the derive energy and energy flux of the precipitating particles and show good agreement between the two platforms. *Sivjee and Hultqvist* [1975] used the ratios of the two forbidden O I lines of 6300 Å and 5577 Å and the N₂⁺ 1NG (0,1) band of 4278 Å, as described

in *Rees and Luckey* [1974] to determine the energy and energy flux of the particles from the aircraft observations. Since the satellite orbital speed is large compared to the aircraft the two were over the same point only at 08:27 UT on 13 December 1969. However the particle precipitation energy as a function of latitude agrees very well between the two observations, and the assumption is that the incoming particle precipitation characteristics did not substantially change in the time it took the aircraft to fly the same ground track as the satellite.

Deehr et al. [1980] report on the multinational campaign in Svalbard, Norway to observe the dayside cusp using optical techniques. They report that scattered sunlight is a very important contributor to the N_2^+ 4278 Å band, so that the use of the 6300 Å to 5577 Å ratio is warranted in the dayside. They found significant contributions to the N_2^+ 4278 Å band from solar resonance even with solar depression angles of 22.5°. Since the solar shadow height is roughly given in kilometers by the square of the solar depression angle in degrees, this means that some of the 4278 Å emission had to be coming from past the solar shadow height of 400 km. Using triangulation techniques they found the lower borders of the 5577 Å arcs at 140 km and the lower borders of some 6300 Å and 4278 Å arcs as high as 220 km. *Deehr et al.* [1980] point out that the midday gap is really a paucity of 5577 Å emissions during the midday due to the low energy of incoming particles. They do find localized injections of high energy particles, even during the midday gap, but on the main the midday lacks the higher energy particles that give rise to the green 5577 Å emissions.

Stamnes et al. [1985] calculate the effect of solar extreme ultraviolet (EUV) radiation for different solar zenith angles. They find that at solar zenith angles of 104° the EUV radiation has little impact on photoionization. They do find however that solar fluorescence of the N_2^+ is the dominant source of 4278 Å emissions even at these large solar zenith angles. *Stamnes et al.* [1985] conclude by saying that the

4278 Å band should not be used on the dayside for energy input measurements because of this solar fluorescence problem. This conclusion is somewhat at odds with that of *Sivjee* [1976] who calculates that the effect of solar fluorescence is 20 %. The differences in the two calculations seems to be in the calculation of the N_2^+ column density since the g factors used in the fluorescence are almost equal. In any event, use of the 4278 Å band in calculating energy flux must be viewed with caution on the dayside where solar fluorescence can play a role. *Stamnes et al.* [1985], and *Sivjee et al.* [1982] suggest that the use of the O II 7320 Å doublet would be more appropriate for the dayside since it does not undergo solar resonance.

Eather et al. [1979] present a statistical summary of the dayside oval morphology using results from a ground based meridian scanning photometer similar to that used in the airborne experiments described above. *Eather et al.* [1979] find that the dayside oval position is in good agreement with oval positions predicted by *Starkov* [1969]. The main topic of this paper is whether the dayside oval responds more to substorm activity or shifts in Bz. *Eather et al.* [1979] take pains to point out that they can find instances where the oval position responds to Bz, but that statistically the position is better correlated with the AE index, a general measure of substorm activity. Using Meridian scanning photometer and all sky camera data, *Sandholt et al.* [1983] counter this conclusion with individual examples where a substorm occurs on the night side with little or no effect on the dayside aurora. *Sandholt et al.* [1983] feel that these observations indicate that the dayside auroral oval is influenced by both IMF Bz changes and night side activity, with the most important factor being the IMF Bz contributions. This is also supported by *Meng* [1983] who report on the cusp position using particle precipitation data during selected large geomagnetic storms. *Meng* [1983] finds that the cusp latitude is determined by the IMF Bz component, and is not closely associated with substorm activity. More ground based case studies are provided by *Sandholt et al.* [1985,1986a], to again

demonstrate correlation between the IMF Bz and the cusp latitude. *Sandholt et al.* [1985] also show that a distinct By effect can be seen in the ground based magnetometer data in the near field of the cusp. A single example is shown where the amplitude of the local magnetometers seems to correlate “by eye” to the By component of the IMF. Thus it appears that there is some confusion as to how strongly the dayside auroral oval position is dictated by either the IMF or some measure of nightside activity such as the AE index.

1.5 Conceptual Overview

The data for this study have all been taken at the Nordlysstasjonen in Svalbard Norway. The Nordlysstasjonen (literally Northern Lights Station) is located outside the town of Longyearbyen on the West Spitsbergen Island in the Svalbard archipelago, and has taken measurements of the dayside cusp aurorae since December of 1978, see *Deehr et al* [1980]. The station is located at geographic north latitude 78.2 degrees, and east longitude of 15.4 degrees. This corresponds to magnetic latitude 75.0, longitude 114.5 using the PACE system of *Baker and Wing* [1989], with magnetic local noon occurring at approximately 0830-0900 hours (UT). At this magnetic latitude the station is normally equatorward of the cusp, which *Newell and Meng* [1992] show is found at magnetic latitudes of 78-79 degrees in the PACE system. *McHarg and Olson* [1992] show a correlation between the ratio of the integrated 6300 Å and 5577 Å emission, and the spectrogram of the induction magnetometer at this station.

Figure 1.6 is shown to introduce the overall relationship between the ground based observations and the ionospheric footprint of the cusp. Several important observational facts are presented without proof in this overview. The right panel of Figure 1.6 is a schematic illustration portraying the station at Svalbard rotating underneath the cusp/boundary layers. As shown, the normal position of the

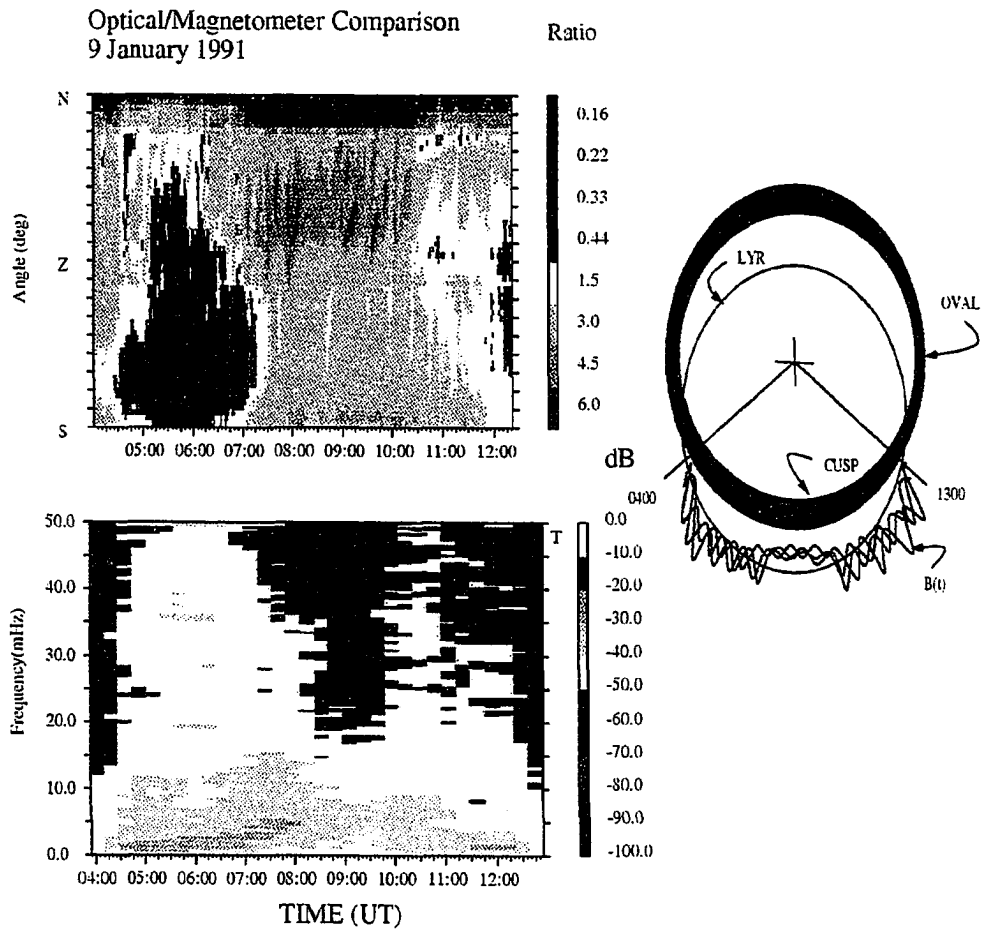


Figure 1.6. Conceptual view of the ground based observations of the ionospheric cusp, see text for details.

cusps/boundary layers is North of our station at magnetic noon. Nevertheless it should be noted that variations in the activity level will place the cusp/boundary layer system directly overhead, and sometimes south of our station. The optical data from the MSP is particularly useful in tracking the position of the cusp/boundary layer system in latitude on a daily basis. The left panel of Figure 1.6 compares the optical and magnetic signals for 9 January 1991, with the optical data displayed above the magnetic data. The optical data are presented with the ordinate showing the scan angle in degrees with North to the top of the figure, and South to the bottom. Universal Time (UT) in hours is shown on the abscissa, and the ratio of the intensities of the 6300 Å to 5577 Å emission are color coded in the image displayed. Such diagrams are called keograms “... derived from the Eskimo word ‘keoeit’ for aurora”, and were first used by *Eather et al.* [1976]. The magnetic data are presented below the optical data, in a color contoured spectrogram format with 50 mHz being the Nyquist frequency of our system. On this particular day the northern hemispheric cusp is poleward of the terminator, and the southern hemispheric cusp is sunlit.

Looking at the optical observations we see what appears to be the boundary regions, characterized by high energy particles precipitating in discrete auroral arcs. This can be seen by the low red to green ratio lasting from 0430 - 0730 before magnetic noon, and from 1030 - 1230 after magnetic noon. Such a low ratio is indicative of high energy particles. The boundary regions are known to be associated with high energy particles, and are an area of discrete arcs, see *Hansen et al.* [1992], *Tsurutani et al.* [1981], *Sandholt* [1990], *Newell and Meng* [1992]. *Newell et al.* [1992] specifically show that the interfaces are sites of discrete auroral arcs.

The optical central cusp is seen in Figure 1.6 as an area with a relative increase in the red to green ratio by a factor of 2 and is north of the zenith, lasting from approximately 0730- 1030 (UT). This patch of large red to green ratio is the lower

energy particles precipitating directly into the ionosphere from the magnetosheath. While individual arcs cannot be seen in this figure, inspection of the data from 6300 Å and 5577 Å channels show that the periods identified as boundary regions are rich in structured arcs. The period of the optical central cusp is seen in the 6300 Å channel to as having some structure, which shows in this figure as the enhanced red to green ratios in the central cusp.

The magnetic spectrogram also shows a distinct difference between the periods identified as boundary regions and the central cusp. The time period of 0430 - 0730, identified as the boundary layer in the optical data, shows a broad band increase in power in the spectrogram above 20 mHz. This time period also shows an intense narrow bandwidth polarized signal in the Pc5 band. This broad band increase of power corresponding to the boundary regions is seen to repeat in the afternoon sector between 1030 - 1230 (UT). During the period of 0730 - 1030, which the optics identify as the central cusp, the spectrogram shows a marked decrease in power above 20 mHz. A narrow band tone is seen at approximately 5 mHz, and the frequency of this tone seems to rise and then fall during this period. This feature is referred to as the "arch" due to its rising and falling tendency in frequency. The low frequency narrow band tone which starts at the beginning of the boundary layer, rises and continues through the central cusp period, and then falls in frequency again in the post noon boundary layer has a substantial polarized component. Polarization information not shown here reveals that the narrow band tone is right hand polarized before magnetic noon, and left hand polarized after magnetic noon.

The overall temporal correspondence between the optical and magnetic data is striking. Figure 1.6 is representative of the data, and another example will be presented later in the thesis. When the optical data indicate high energy particles the magnetic data show a broad band increase in power. When the optical data

show low energy particles in a confined area the arch is present in the magnetic data. This correspondence leads me to postulate that on a daily basis as the station rotates beneath the dayside oval, it first passes underneath the boundary regions, then passes the cusp, and finally exits out the afternoon side through the afternoon boundary layer.

The observations described are a common occurrence. In Chapter 2 the optical data are discussed in detail, and I find that the particle precipitation energy associated with the area identified as cusp in Figure 1.6 is in good agreement with the energies of incident particles into the cusp as described by *Newell and Meng [1992]*. The magnetic data are discussed in Chapter 3, where it is shown that the magnetic data are so repeatable that only three major variations of the example spectrogram shown for 9 January 1991 are found. The data taken within each of these three major categories are found to have common IMF orientations. Chapter 4 discusses the coherence length of the pulses found in the boundary regions and central cusp, as well as the possible sources of the observations seen in both the magnetic and optical data. Chapter 5 concludes and recommends further avenues of cusp research using the unique combination of optical and magnetic data available from the Svalbard site.

CHAPTER 2

Optical observations of the cusp

Use of optical observations in cusp latitudes is necessarily restricted to the dark winter months. This limited period of coverage is made up for by the rich nature of material that can be gleaned from the optical observations. All the measurements were made at the Nordlysstasjonen in Svalbard, Norway. The four major forms of optical observations carried out are the all-sky television (ASC), meridian scanning photometer (MSP), Fabry-Perot interferometer (FPI), and spectrometer. These instruments combine to give information on the spectral, temporal, and spatial nature of the optical emissions from the dayside aurorae. The ASC gives the most dynamic information because of its two-dimensional, large field of view coverage combined with a 30 frames/second data rate. The ASC is currently an analog device, which makes using digital analysis techniques difficult due to the prohibitive expense of digitization of large amounts of data. Further, the ASC collects white light which maximizes the signal but prohibits gathering spectral information. The FPI and spectrometers gather spectral information over a narrow bandwidth, but currently offer poor spatial and temporal coverage of the sky.

The MSP is something of a compromise offering a large one-dimensional field of view, moderate time resolution, while also providing moderate spectral information. The MSP uses filtered photometers to digitally record the intensity of light in five narrow optical passbands. This chapter describes the use of the MSP in observations of the dayside aurorae associated with the cusp. The first section describes the MSP operation, while the second section shows how intensity ratios between several of the observed emissions can be used to infer the energy and energy flux

of the electrons incident on the ionosphere. The third section details how the data taken from the MSP can be mapped to latitude, and the last section describes actual MSP data taken from the cusp Svalbard location and its interpretation.

2.1 Description of Meridian Scanning Photometer

The meridian scanning photometer used in Svalbard is described by *Deehr et al.* [1980]. The MSP consists of a rotating flat mirror and a set of five filtered photometers, each with a 1 degree wide field of view. The MSP scans along a meridional line 45 degrees west of geographic north, which corresponds approximately to the geomagnetic meridian at our station. The filters on the photometers restrict the wavelength of light reaching the photometer to a passband of about 3 Å centered on the wavelength of choice called the peak wavelength. The filters are tilted so the passband wavelength is off the peak wavelength every other pass to record the background light level. The corrected brightness measurement is equal to the difference between the peak and background measurement. The mirror rotates once every 4 seconds, and 2 peak scans and 2 background scans are averaged to produce a complete peak minus background scan. The effective data rate is one complete peak minus background scan every 16 seconds. Calibration of the MSP is achieved through the use of a calibrated lamp. The lamp output falls on two lambertian screens to diffuse the light and to reduce the intensity recorded at the photometer to intensities comparable to the aurorae. Knowing the spectral intensity of the calibration lamp and the filter characteristics allows computation of the amount of light in the passband falling on the photometer, which, in conjunction with the number of counts recorded at this time, allows calibration for each photometer.

Figure 2.1 shows the transmitted intensity of the 6300 Å filter as a function of wavelength at different tilt angles. This measurement was taken at the Geophysical Institute with the help of Joe Minow and Duane Bostow. It is obvious that, as the

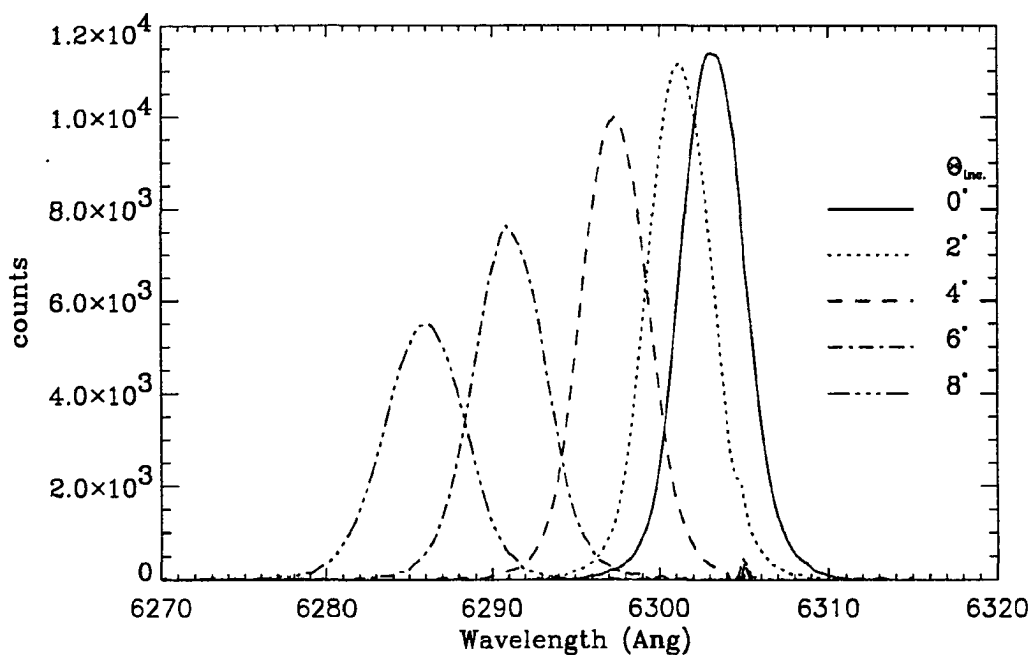


Figure 2.1. Relative transmission of 6300 Å Filter. Note that as the filter is tilted with respect to the light path the center of the passband moves to shorter wavelength, and the peak of the transmission curve decreases.

filter is tilted the center of the transmission curve moves to shorter wavelengths, the peak of the transmission curve decreases, and the width of the transmission curve increases. Table 1 shows the area under the curves normalized to the case of normal incidence.

Figure 2.1 demonstrates why the filter is tilted: as the tilt angle increases the peak of the transmission curve moves off the emission feature under observation to a region of continuum, which provides the background continuum measurement. This type of tilting filter arrangement is described in greater detail by *Eather and Reasoner* [1969], who show that the change in the center of the passband wavelength

TABLE 2.1. Relative Transmission of 6300 Å filter at different wavelengths

Angle Off Normal (degrees)	Integrated Fraction of Normal	Center Passband Wavelength (Å)
Normal	1.	6303.
2	0.99	6301.
4	0.93	6297.
6	0.78	6290.
8	0.63	6285.

is proportional to the square of the change in the angle off the normal. The data in Table 2.1 are in substantial agreement with this prediction.

The emission features commonly observed in dayside aurorae are summarized in Table 2.2 along with the respective spectroscopic information and lifetime of the states. Following *Chamberlain* [1961] the lower energy level is specified first in atomic spectra, and the higher energy level is specified first in molecular spectra. Emissions from the two forbidden oxygen transitions of 5577 Å and 6300 Å are the dominant features in the dayside cusp, *Deehr et al.* [1980]. The lifetime of green O(¹S) is much shorter than the red O(¹D) emission: 0.74 seconds compared to approximately 110 seconds, *Chamberlain* [1961]. For reasons dealt with in the next section, the 5577 Å emission is generally regarded as being an indicator of higher energy precipitation particles. The 4278 Å emission is due to the (0,1) band of N₂⁺, and is also regarded as being an indicator of higher energy particles. The 4278 Å emission is difficult to interpret on the dayside under conditions where the tops of the arcs may be sunlit.

TABLE 2.2. Emissions Observed with MSP

Wavelength (\AA)	Emission Source	Transition	Lifetime (sec)
6300	[OI] ₂₁	$^3P_2 - ^1D_2$	110
5577	[OI] ₃₂	$^1D_2 - ^1S_0$	0.74
4278	N_2^+ 1N(0,1)	$B^2\Sigma_u^+ \rightarrow X^2\Sigma_g^+$	$< 10^{-6}$
7320 (doublet)	[OII] ₃₂	$^2D_{\frac{5}{2}} - ^2P_{\frac{3}{2}} \text{ or } \frac{1}{2}$	5
6563	H α	$2^2P^o - 3^2D$	$< 10^{-6}$

2.2 Use of Spectral Ratios for Cusp Observations

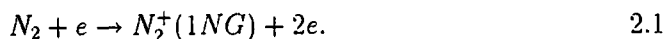
One of the most physically interesting uses of the spectral information collected by the MSP is to infer the energy and energy flux of the incoming particles that cause the emissions under observation. This technique relies upon taking ratios of the integrated field aligned emission rates of several different emissions as well as individual intensities. The inferred value of the energy and energy flux is subject to a number of assumptions, and understanding these assumptions, as well as the basic technique, is necessary in interpreting the results. In the end, I believe that these techniques give a result representative of the real energy and energy flux, but the accuracy of the absolute magnitude of the results is uncertain due to the large number of assumptions that go into the technique. Since no published uncertainty values are available, confidence limits on the resulting calculations can not be given.

There are two basic ideas behind the use of spectroscopic ratios in determining the energy and energy flux of incoming precipitation. The first is the basic fact that higher energy particles penetrate farther into the atmosphere, and the second

is that the actual intensity of emission for different transitions depends upon the altitude of the emission. The emission intensity also depends upon the altitude because the intensity depends on both the excitation and de-excitation processes.

As an example of the interplay between excitation and quenching, consider the 6300 Å emission from $[\text{OI}]_{21}$. *Rees and Roble* [1986] point out that there are at least five different processes that lead to the excitation of the $\text{O}(^1\text{D})$ excited state. In addition to excitation by direct impact of precipitating electrons, the $\text{O}(^1\text{D})$ state can be excited by the high energy tail of the thermal electrons since the excited state is only 1.96 eV above the ground level, [*Chamberlain* 1961]. This effect is important in the cusp where the electron temperature in the cusp can be above 3000 K, and cause significant increase in the 6300 Å emission, [*Rees and Roble* 1986]. In addition, there are de-excitation processes due to collisional quenching, which are particularly important for consideration in the case of the 6300 Å emission. Since the $^3\text{P}_2\text{-}^1\text{D}_2$ is an electric-quadrupole transition it has a low transition probability, (see *Chamberlain* [1961]), and the $\text{O}(^1\text{D})$ state thus has a relatively long time constant of about 110 seconds. At altitudes below approximately 180 km, collisional quenching by N_2 depopulates the excited state, resulting in very small amounts of 6300 Å emission, *Rees and Lucky* [1974]. The result of the energy dependent range and quenching effects is that most of the observed 6300 Å emission comes from higher altitudes, and corresponds to softer particle precipitation. The 6300 Å column integrated emission thus depends on the energy and the energy flux of the precipitating particles.

As a second example, consider the 4278 Å emission from N_2^+ . The process for direct electron impact ionization-excitation of N_2^+ is given by *Mende et al.* [1984].



Rees [1989] reports that since the ionization level of N_2 is 18.75 eV, excitation by the high energy tail of the thermal electron distribution will not be significant. Since the number density of N_2 drops by two orders of magnitude from 100 km to 140 km, see *Rees* [1989], the particles must be able to penetrate to these lower altitudes. Once the particles have enough energy to penetrate to where there are significant densities of N_2 the integrated column emission depends mainly upon the energy flux, and not the energy of the particles, *Rees and Lummerzheim* [1989].

Since the 4278 Å emission rate is almost independent of incoming particle energy, and the 6300 Å emission rate depends both on the energy and the energy flux, the ratio of these two emission rates is a measure of the characteristic energy of the particles, and the integrated 4278 Å emission rate is a measure of the energy flux of the particles. As mentioned before use of the 4278 Å emission in the cusp is debatable due to possible resonant scattering above 220 km. However another transition used in place of N_2^+ (0,1) band is the 1S transition resulting in 5577 Å emission. Such ratios have been used extensively: *Rees and Lucky* [1974] point out that *Eather and Mende* [1972] and *Gattinger and Vallance Jones* [1972] recorded spectroscopic ratios on the series of NASA flights and that *Eather and Mende* [1972] used these ratios to determine the existence of soft energy precipitation on the dayside of the auroral oval. Approximate analytic descriptions of the integrated column intensity using simulations with a range of input energy and energy flux regimes have been published. *Rees and Roble* [1986] give approximate formulae ([8] through [10] of their paper) for the integrated column emission rates of 6300 Å and 4278 Å, which are repeated here along with the equation for the approximate field-aligned column integrated emission rates due to the forbidden oxygen 5577 Å line, see *Rees et al.* [1988].

$$\frac{4\pi I(6300\text{\AA})\text{rayleighs}}{\text{erg}\cdot\text{cm}^{-2}\cdot\text{s}^{-1}} = 420\alpha^{-0.9}, \quad 0.1 < \alpha < 2.0\text{keV} \quad 2.2$$

$$\frac{4\pi I(4278\text{\AA})\text{rayleighs}}{\text{erg}\cdot\text{cm}^{-2}\cdot\text{s}^{-1}} = 213\alpha^{0.0735}, \quad 0.1 < \alpha < 2.0\text{keV} \quad 2.3$$

$$\frac{4\pi I(5577\text{\AA})\text{rayleighs}}{\text{erg}\cdot\text{cm}^{-2}\cdot\text{s}^{-1}} = 1,400\alpha^{-0.2}, \quad 0.1 < \alpha < 5.0\text{keV} \quad 2.4$$

$$\frac{4\pi I(6300\text{\AA})\text{rayleighs}}{4\pi I(4278\text{\AA})\text{rayleighs}} = 2.0\alpha^{-1}, \quad 0.1 < \alpha < 2.0\text{keV} \quad 2.5$$

$$\frac{4\pi I(6300\text{\AA})\text{rayleighs}}{4\pi I(5577\text{\AA})\text{rayleighs}} = 0.3\alpha^{-0.7}, \quad 0.1 < \alpha < 5.0\text{keV} \quad 2.6$$

where α represents the characteristic energy of an incoming beam of electrons with a Maxwellian energy distribution. Note that equations 2.2- 2.6 are only valid when integrating directly up the field line, and when the characteristic energy of the precipitating electrons is higher than 100 eV I have extrapolated equation 2.6 to energies less than 100 eV to investigate the precipitation energies in the cusp.

Note that the dependence on the energy is minimal in equation 2.3, while equation 2.2 shows the 6300 Å emission depends to a larger degree on the energy. Equation 2.4 shows that the 5577 Å emission is also less sensitive to the incoming particle energy and thus can be used in place of the 4278 Å emission, however a much less precise result will be achieved since the details of the 5577 Å emission are not yet fully understood,[*Rees et al* 1988]. Equation 2.6 was obtained by dividing equation 2.2 by equation 2.4. To the best of my knowledge, the uncertainties associated with using these analytic fits have not been published, and is the major drawback in using them. The investigation of how much uncertainty is present when using these analytic fits off the zenith is a separate question which is addressed in the next section.

2.3 Mapping of MSP scan angle to latitude

Mapping of MSP data to geographic or geomagnetic coordinates is important so that optical data can be compared to other data sets. There are two commonly used mapping techniques employed if data from only one station are available. The first method assumes a constant altitude for all emissions, and then maps scan angle to latitude. The second technique, described by *Eather et al.* [1976], assumes that all the emissions for one scan angle, or pixel, come from one point in space, and uses spectral ratios of that pixel to determine its altitude of emission. Each pixel is then mapped to its own latitude, and the results are then displayed for the entire pixel map. I will call this mapping technique the *Eather map* for the rest of this section.

Both techniques have their drawbacks; the flat map takes the arc and effectively projects it down onto the assumed emission height, see Figure 2.2. This results in an error in the inferred latitude from the station as well as a spread in the inferred latitudinal width of the emission. The *Eather map* assumes a particularly simple geometry, that is a long thin arc, with no arcs or background glow in front of or behind the arc, see the top panel of Figure 2.3. To quote *Eather et al.* [1976] about this assumption: “But on a synoptic basis, simple geometries are more the rule than the exception, so we believe that the approach is useful and superior to the obviously invalid assumption of height constancy.” The bottom panel of Figure 2.3 shows an extreme example of how this mapping technique can fail. If diffuse auroræ cover large amounts of latitude, or in this case two layers of emission cover large amounts of latitude, then the inferred emission altitude at one scan angle is incorrect. The latitude inferred from this incorrect altitude is equal to neither the latitude of the red or the blue emission along the line of sight of the MSP. The question of which method is better, or even how they compare requires knowledge

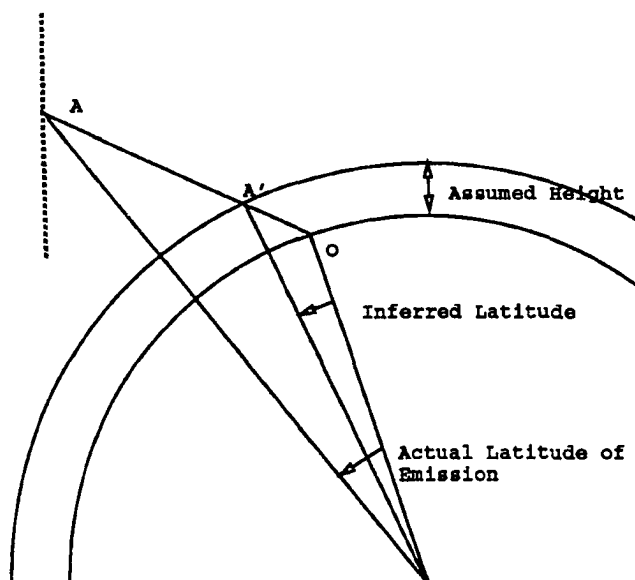


Figure 2.2. Geometry of the flat latitude map. Since the observer maps the emission at A to A' in the flat map, there will be a difference in the real emission latitude and that inferred from the mapping.

of the input so that the output can be compared to each other and reality. This section analyzes the two techniques using synthetic MSP data.

2.3.1 Manufacturing Synthetic MSP Data

Finding the amount of light measured by an MSP involves integrating the emission profile along the line of sight path of the optical instrument. The emission profile describes the number of photons per unit volume per second emitted as a function of altitude. Determining this emission profile is a research topic in itself; e.g. see [Rees and Lummerzheim 1989]. Briefly, this emission profile is determined by first solving for the ionization rate as a function of altitude given a particular

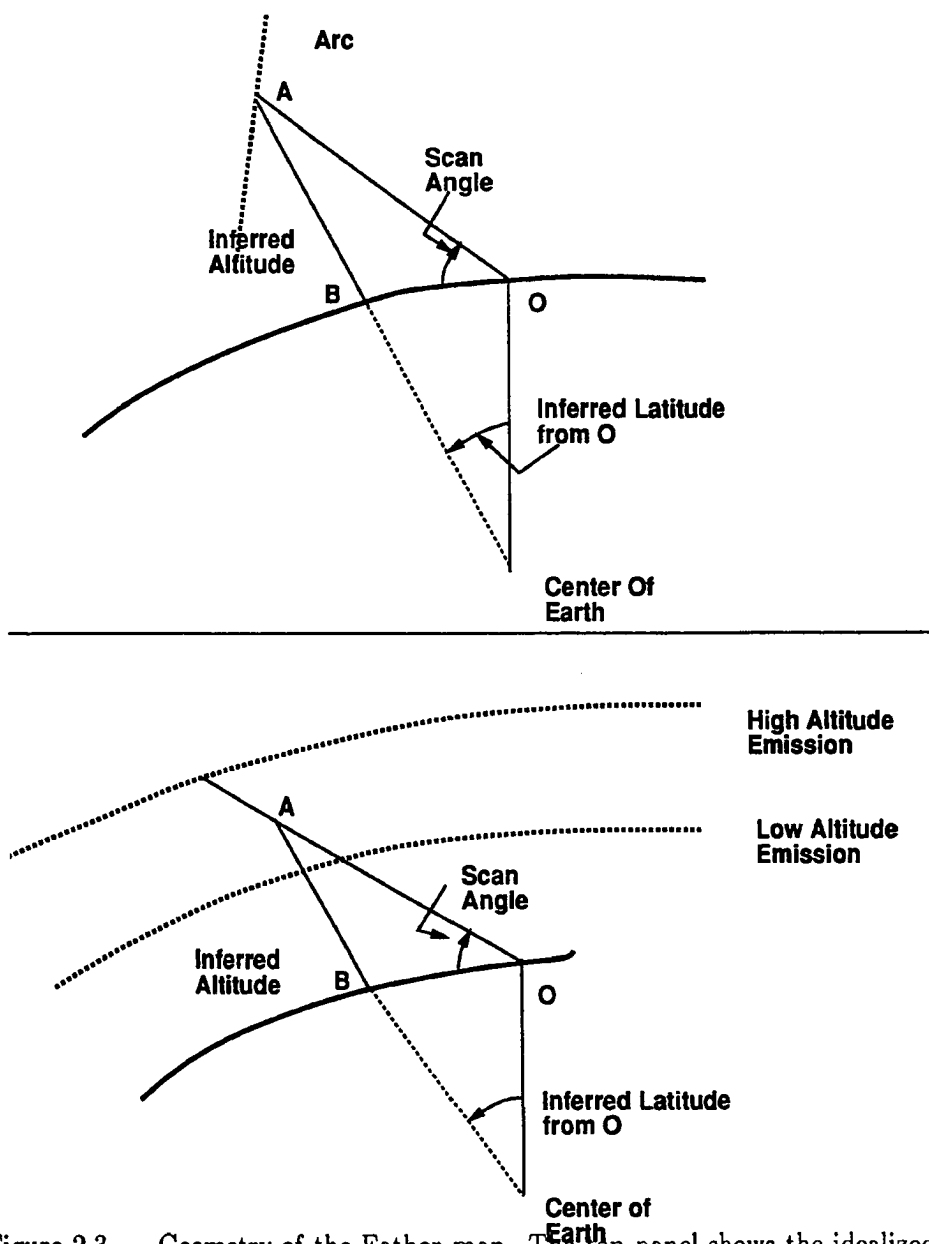


Figure 2.3. Geometry of the Eather map. The top panel shows the idealized view of the Eather map. If the height (AB) and the MSP scan angle are known then the difference in latitude from the station to the arc can be determined. The bottom panel shows an extreme example of how the method can fail. If two diffuse layers of emission exist, then along one scan angle the altitude inferred (AB) is equal to neither of the two emission altitudes and an error in latitude of the emission results.

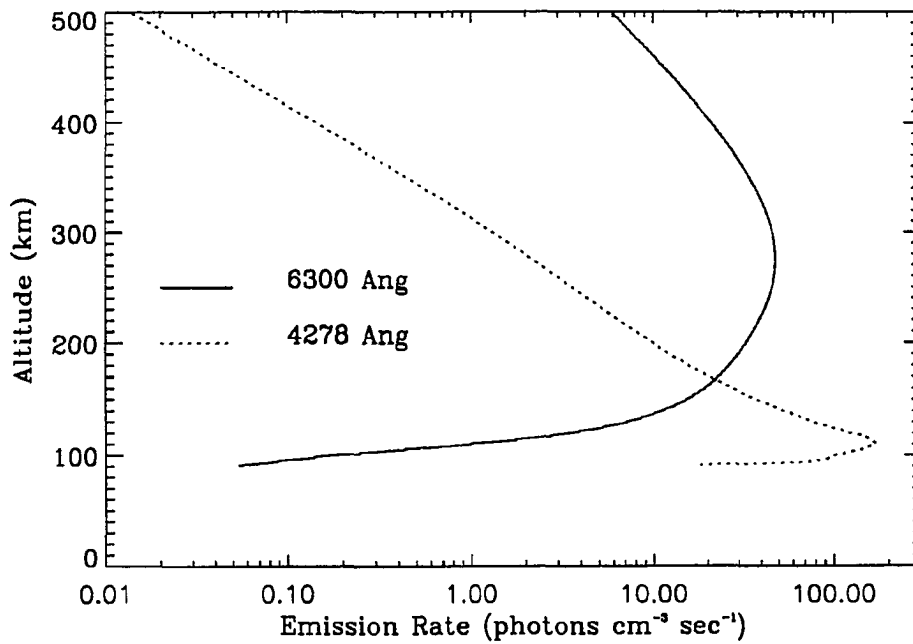


Figure 2.4. Emission Profile of 6300 Å from 1.3 keV particles and energy flux of $3.3 \text{ ergs} \cdot \text{cm}^{-2} \cdot \text{sec}^{-1}$.

energy distribution function of incoming particles. The ionization rate is turned into an excitation rate for a particular atomic or molecular state in a model atmosphere. This state is quenched by collisions as well as depopulated by optical radiation, and so the problem also requires detailed modeling of the chemistry in the upper atmosphere. The resulting emission profile is thus a complicated mixture of competing effects in both excitation and quenching processes. With these caveats once the emission profile is determined, the position of the emission in relation to the measuring station is known, and the altitude of the emission is known, then the integration along the line of sight is performed for each MSP scan angle. The emission profile for the forbidden oxygen 6300 Å line and the N_2^+ 4278

Å band resulting from a beam of electrons with a Maxwellian energy distribution of $n(E)dE = N_0 E \exp(-E/E_0) dE$ and a characteristic energy E_0 of 1.3 keV is given in Figure 2.4, (D. Lummerzheim University of Alaska, personal communication, 1993). Note that the 6300 Å line peaks at higher altitudes than the 4278 Å band. The 6300 Å emission line is also much broader in altitude than that of the 4278 Å band.

The MSP integrates all the light emitted along its viewing path that falls within its solid angle field of view. If the field of view is restricted so that the emitting object fills the field of view then a useful measure of the amount of light measured by the MSP is the Rayleigh, see *Chamberlain* [1961]. The Rayleigh is equal to 4π times the surface brightness if the emission is isotropic and no scattering or reradiation occurs along the path from the emission to the detector. To obtain the brightness in Rayleighs when looking along the field line we must integrate the emission profile in altitude and use the conversion factor 1 Rayleigh = 10^6 photons \cdot $\text{cm}^{-2} \cdot \text{sec}^{-1}$. The field aligned integrated brightness of the 6300 Å emission profile in Figure 2.4 is 1058 Rayleighs.

For the case where the observer is not looking up the field line, the emission profile must be integrated along the line of sight from the observer. This integral requires that either the emission profile be changed for each angle considered, or that a change of variable be performed in the integration. The latter seems to be the easier task considering the amount of work necessary for computing an emission profile in the first place, and is the tack I took in solving this problem. In principle, the emission profile is integrated over only the height of the emission profile intersected by the line of sight, and the change of variable takes care of the difference in path length along the line of sight compared to along the vertical.

Some initial assumptions must be made about the orientation of the emission before this change of variable can be performed. The model I use assumes an arc

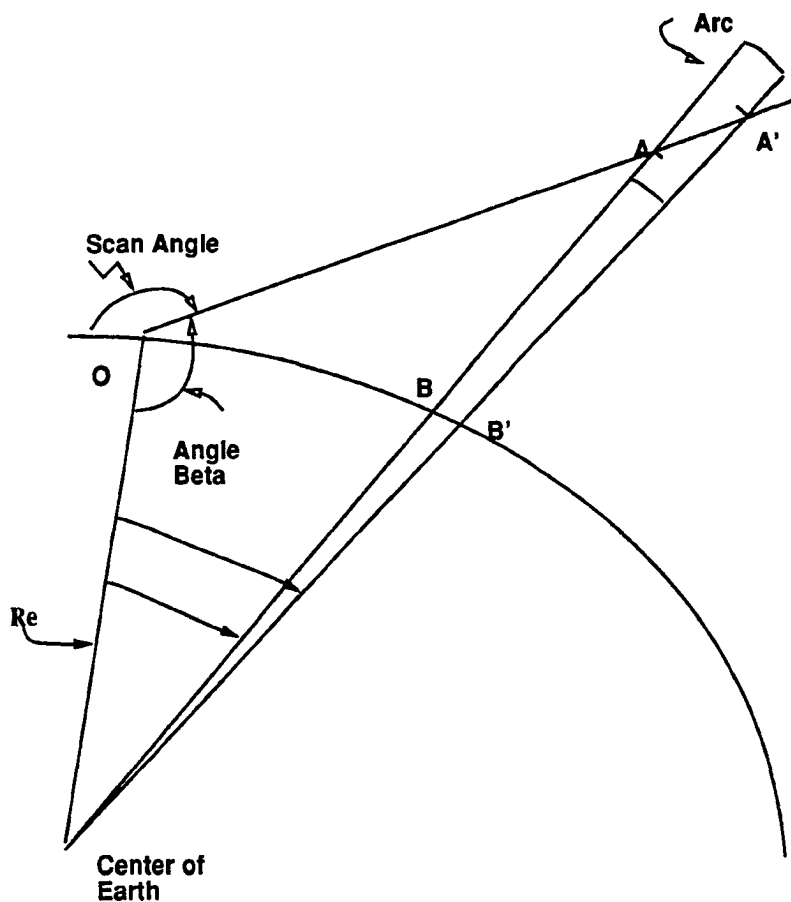


Figure 2.5. Geometry of integration along the line of sight for the MSP from an observer at point O. The line of sight first intersects the arc at a height z_{in} (AB), and then exits the arc at height z_{out} (A'B'). These heights set the limits on the integral over the emission profile to obtain the integrated intensity along any one scan angle.

that follows radials from the Earth's center rather than a dipole geometry, see Figure 2.5 for a schematic of the geometry in this situation. For any one position of this arc with respect to the station the intensity recorded by the MSP at any scan angle can be calculated using the integral shown below,

$$I(\beta) = \int_{z_{in}}^{z_{out}} \frac{n(z)dz}{\cos\gamma} \quad ; \quad \sin\gamma = \left(\frac{Re\sin\beta}{Re+z} \right) \quad 2.7$$

where Re is the radius of the Earth, and z is the height above the surface of the Earth to the integration point. Note that the scan angle is related to the angle β , but not equal to it. The difference in the latitude of the poleward and equatorward edge of the arc from the station's latitude are the angles λ_p and λ_e . The MSP scan angle is taken to be 0 degrees towards the pole, and 180 degrees towards the equator. The integration technique used is a modified trapezoidal rule with a variable step size to accommodate the altitudes supplied in the emission profile. The assumption of the arc following radials instead of dipole field lines is, admittedly, a simplification. For a case of dipole geometry, the z_{in} and z_{out} and angle β would have to be calculated separately, but the integral performed to obtain the surface brightness would remain the same as that shown in equation 2.7.

In addition to the emission profile shown in Figure 2.4 I have used a uniform emission profile over the entire region. This is caused by a low level uniform diffuse precipitation, and the emission profiles for 6300 Å and 4278 Å are shown in Figure 2.6 . This emission profile corresponds to an input of particles with a characteristic energy of 70 eV, and an energy flux of $0.03 \text{ ergs} \cdot \text{cm}^{-2} \cdot \text{sec}^{-1}$. This background was added to the arc when the integrated MSP scan was manufactured.

The result of the integrated line of sight response to a uniform background is shown for the 6300 Å emission in Figure 2.7. Here the intensity in Rayleighs is plotted versus the scan angle of the MSP. Note the increase in the intensity as the

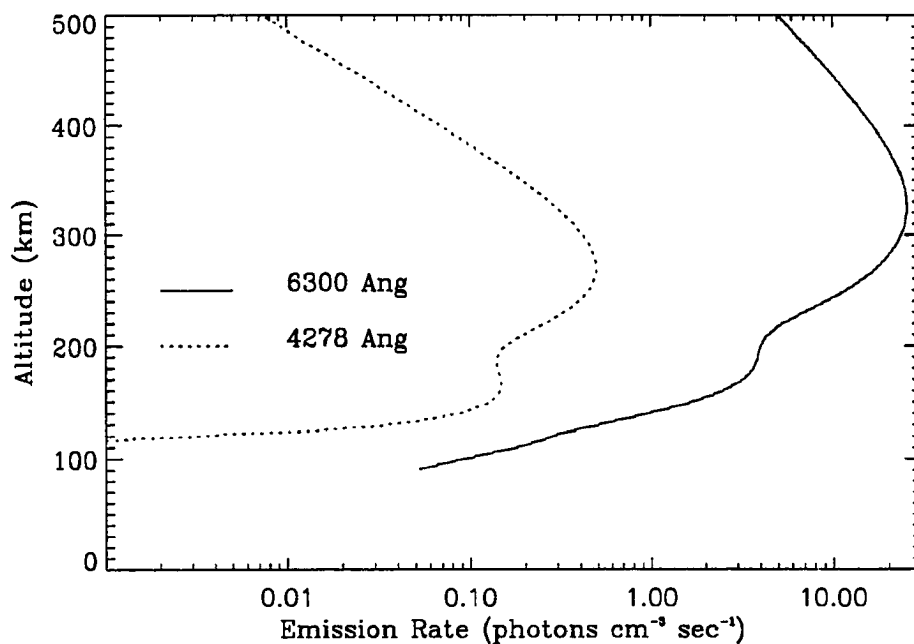


Figure 2.6. Background emission profiles for 6300 Å and 4278 Å from 70 eV particles with an energy flux of $0.03 \text{ ergs} \cdot \text{cm}^{-2} \cdot \text{sec}^{-1}$.

scan angle goes towards either horizon. This increase is due to the increased path length of integration.

When the arc intensity resulting from the emission profile of Figure 2.6 is superimposed onto this background, the complete MSP scan is shown in Figure 2.8. In Figure 2.8 the arc is 2.25 degrees poleward of the observing station. Note the peak in the 6300 Å scan does not occur at the same angle as the peak in the 4278 Å scan even though the arc is at the same latitude. This is due to the extended height of the arc; effectively the red is higher up the arc than the blue. Note that the shape of the peak intensities as a function of angle are different. Again, this is due to the difference in the 6300 Å and 4278 Å emission profiles.

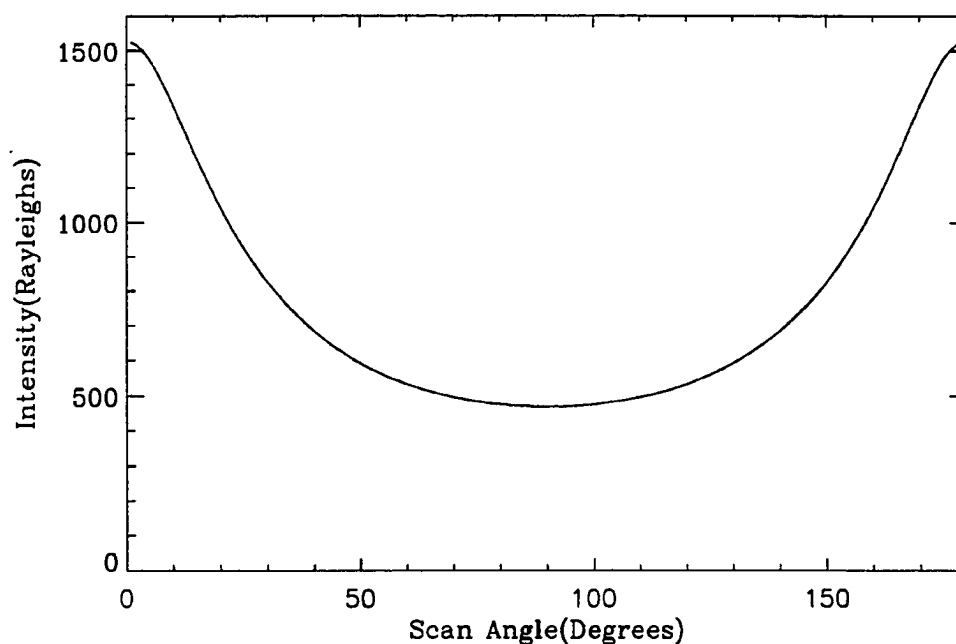


Figure 2.7. Background intensity versus scan angle.

2.3.2 Analysis of Synthetic MSP Data

To investigate how this output changes as an arc moves over the station, I have taken the output of this integration and stored it in a two dimensional array for each wavelength channel. As an input to the integration, I have used the modeled distribution shown in Figure 2.9. In this figure the upper panel shows the input energy of the incoming particles, and the lower panel shows the input energy flux as a function of latitude and time. As can be seen the width of the precipitation region was kept constant as the arc moved equatorward over the station. This input was used to generate the synthetic MSP scans as described in the previous section, and an image of the resulting 6300 Å emission is shown in the upper panel

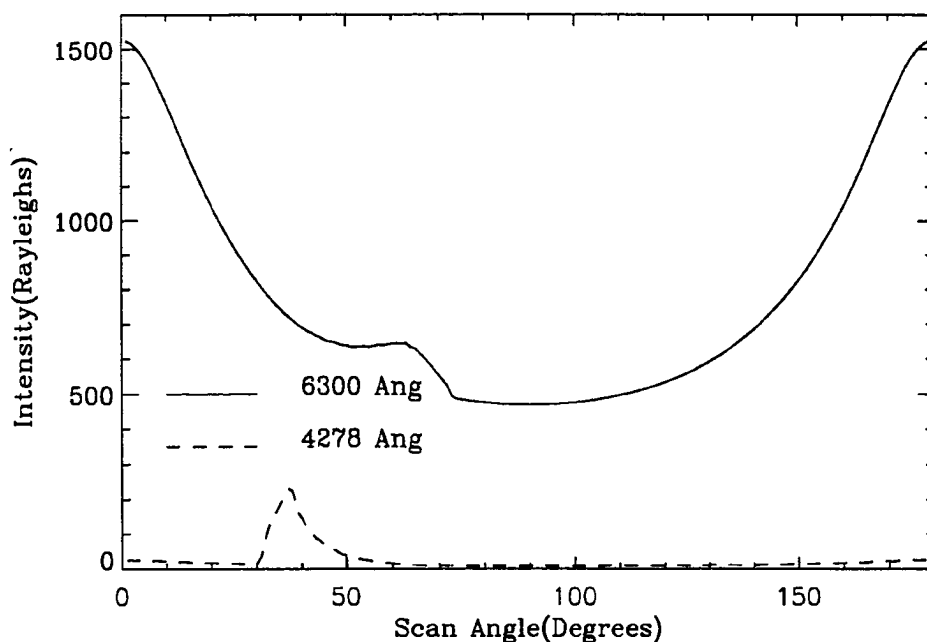


Figure 2.8. Background plus arc intensity versus scan angle for 6300 Å and 4278 Å. The arc is 1.25 degrees poleward of the station in this example.

of Figure 2.10, with the greyscale to the right showing the intensity in Rayleighs. As can be seen the apparent width of the intensity changes as the arc moves overhead, and this is due solely to the change in perspective. A similar image for the 4278 Å emission is shown in the lower portion of Figure 2.10. Note again the difference between the 4278 Å and the 6300 Å emissions are mainly due to the difference in the emission profiles. This series of figures demonstrates that large distortions occur when the MSP integrates all light along its line of sight and maps the intensity as a function of latitude to intensity as a function of scan angle.

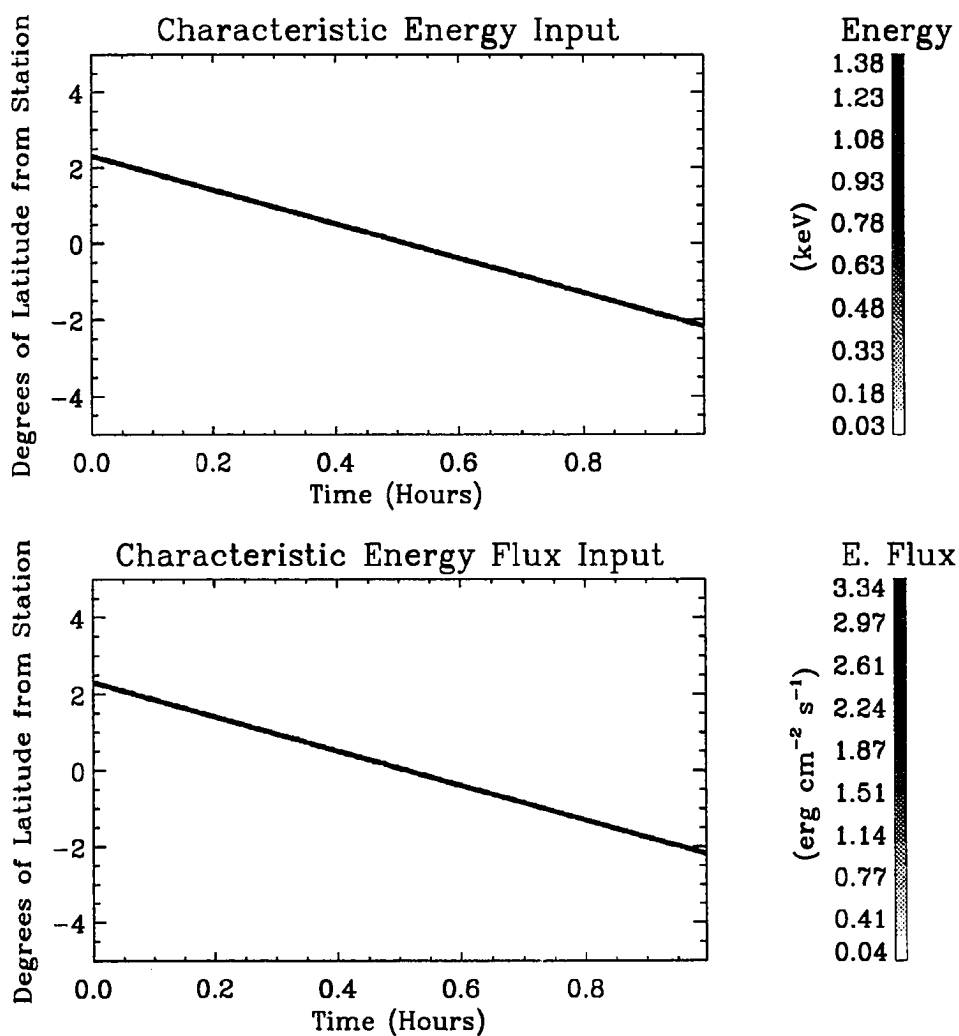


Figure 2.9. Map of actual characteristic energy and energy flux of precipitating particles used as input to synthetic MSP scans. The upper panel shows the energy of the incoming particles, while the lower panel shows the energy flux of the incoming particles. The modeled arc moves to the south at a constant rate of 4.5 degrees per hour. In both panels the abscissa is time in decimal hours, and the ordinate is degrees latitude from the station.

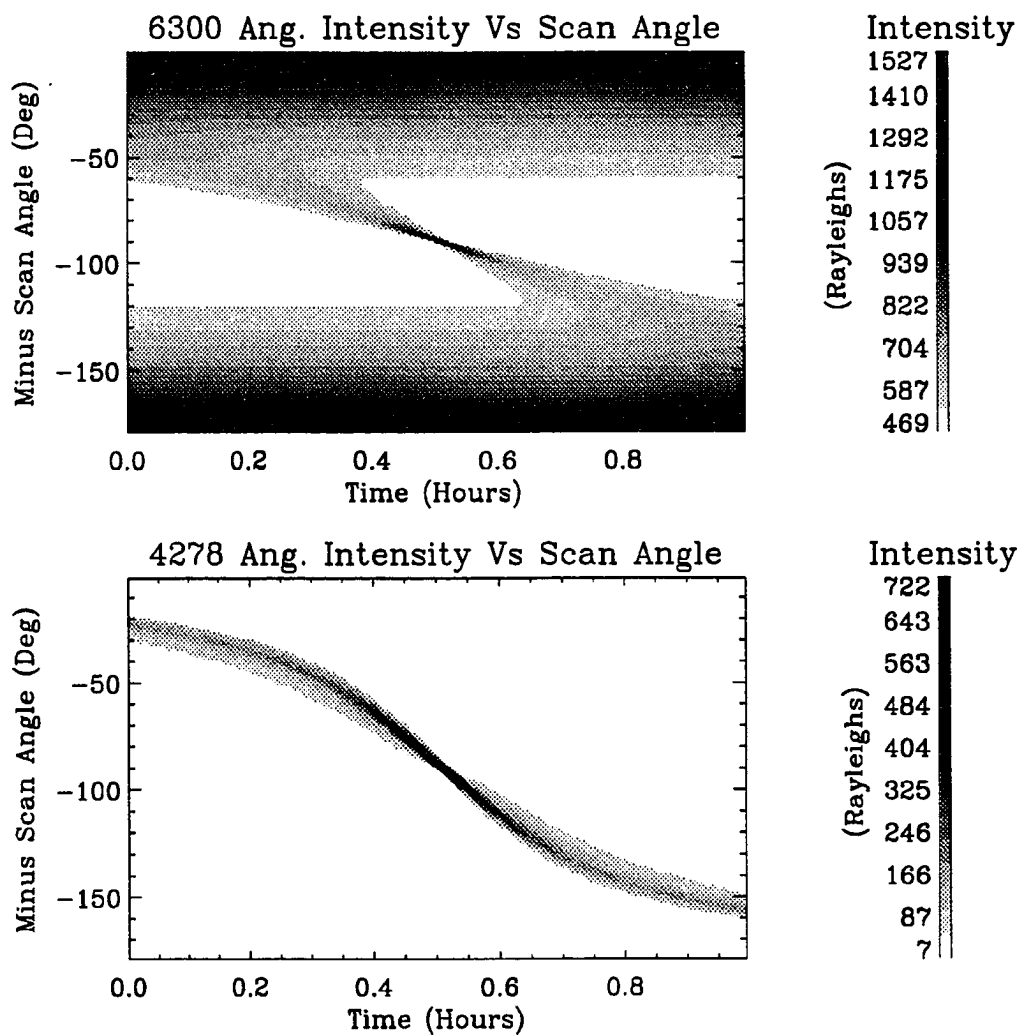


Figure 2.10. Keogram of 6300 Å and 4278 Å emission versus scan angle. The top portion of the figure is 6300 Å and the lower portion is 4278 Å. The ordinate in both images is scan angle, with 0 degrees as the top of the image being towards the pole. The abscissa values are time in decimal hours, and the image is built up of successive scans. The intensity scale in Rayleighs is shown to the right in the greyscale.

2.3.3 Flat Mapping Scan Angle to Latitude

The examples shown in Figure 2.10 are in the same form as actual raw data collected by the MSP: that is, the data are a function of scan angle, not latitude. As mentioned above, the two different techniques used to map the scan angle back to latitude are based on two different assumptions. The flat map is the easiest to explain. If a constant height is assumed for the emission, then a simple mapping to latitude is available and a uniformly sampled set of MSP scan angles results in a nonuniform sampling in latitude.

This mapping is demonstrated in Figure 2.11, which shows the 4278 Å emission mapped to 125 km and the 6300 Å emission mapped to 225 km. In both cases the uniform scan angle is mapped to a nonuniform latitude grid, which is subsequently interpolated onto a linear grid in latitude. Notice that the spiral shape seen in the 4278 Å plot of Figure 2.10 has been straightened due to the mapping to latitude. Note however in both instances that the inferred width becomes larger with increasing difference in latitude from the station. This is one of the undesirable artifacts of the mapping process.

The more interesting question, after you map the scan angle back to latitude, is: “What geophysical parameters can be obtained from such measurements?” In Section 2.2, the *Rees and Lucky* [1974] method of using the ratio of the 6300 to 4278 emission was described, which in principle, allows the calculation of the energy and integrated energy flux of the precipitating particles. If this ratio is made from the latitude representation, then the area of precipitation can be compared to that which was actually used.

The upper panel of Figure 2.12 shows the characteristic energy in keV for the case where the 4278 Å emission has been mapped to 125 km, and the 6300 Å emission has been mapped to 225 km by using equation 2.5. The lower panel of Figure 2.12 shows the energy flux in $\text{ergs} \cdot \text{cm}^{-2} \cdot \text{sec}^{-1}$ derived from equation

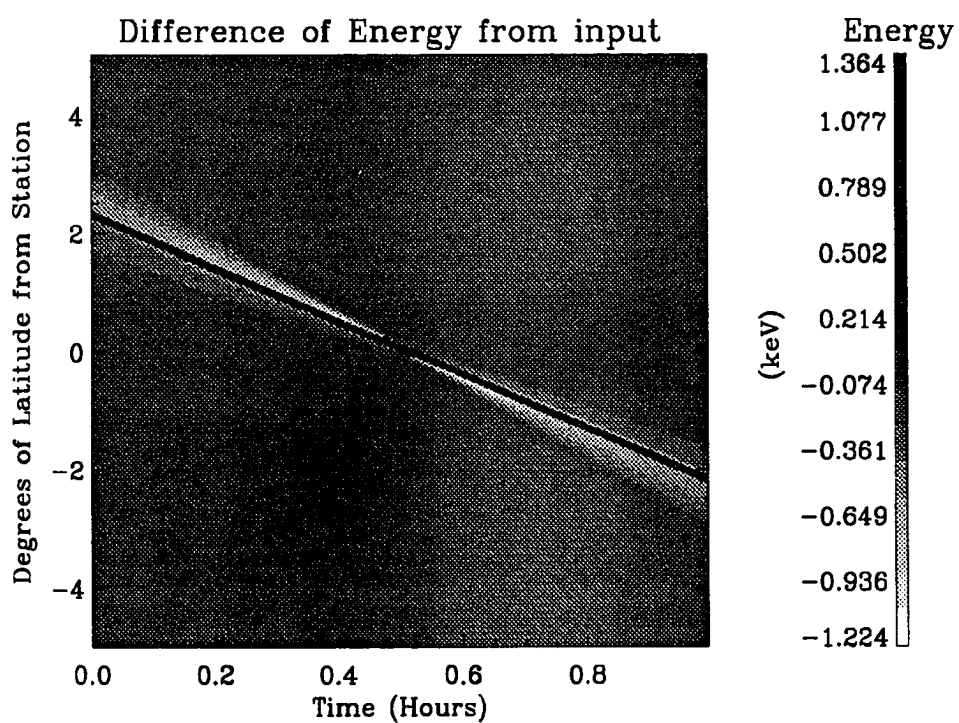


Figure 2.11. Flat map of 4278 Å emission mapped to 125 km, and 6300 Å emission mapped to 225 km. The upper panel is the 6300 Å emission, and the lower panel is the 4278 Å emission. In both panels the intensity is displayed versus latitude on the ordinate and time on the abscissa.

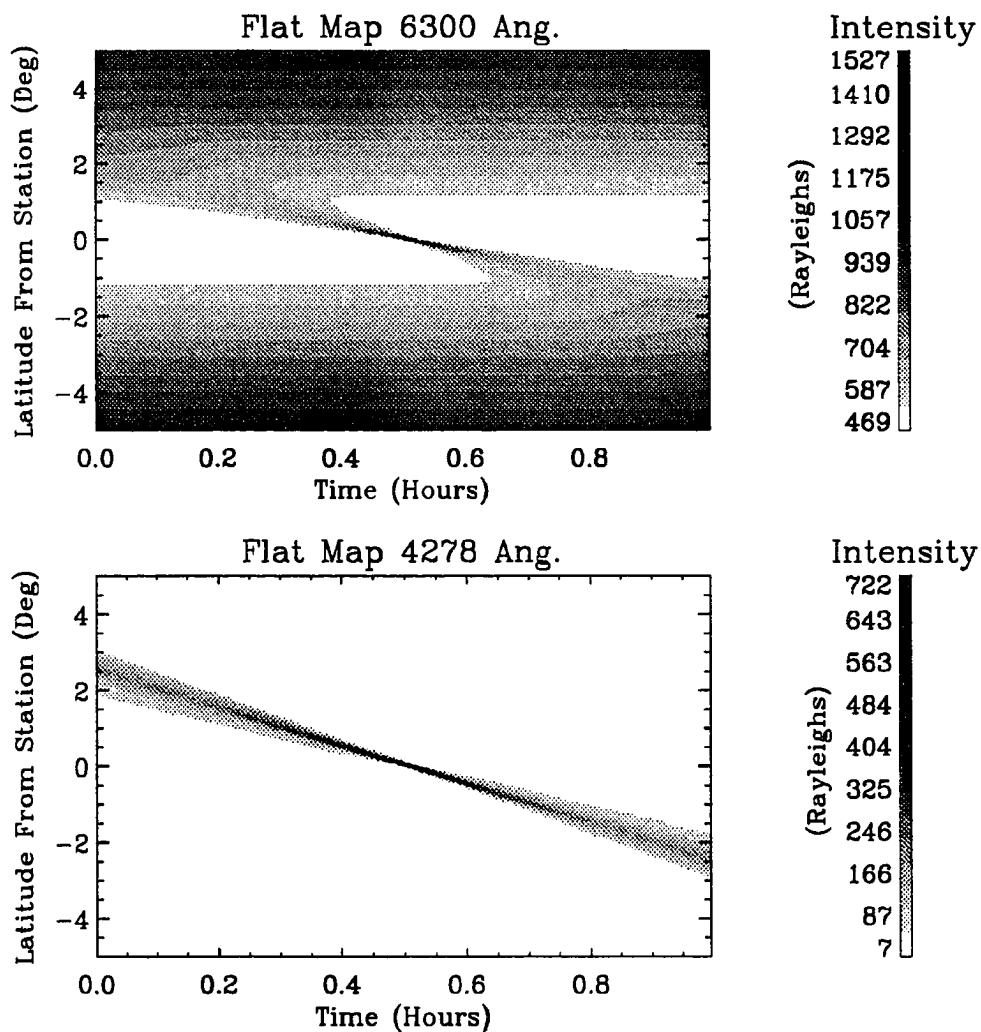


Figure 2.12. Map of characteristic energy and energy flux of precipitating particles inferred with 4278 Å mapped to 125 km and 6300 Å mapped to 225 km. The upper panel shows the inferred energy, and the lower panel shows the inferred energy flux using the flat mapping. The format is similar to Figure 2.11.

2.3 for the case where the 4278 Å emission has been mapped to 125 km. The use of equation 2.3 requires the characteristic energy to be known, however the dependence on this energy is minimal. Note that for both the energy and energy flux, the resulting map to latitude is different from the input. This is due to the distortions that come about due to the assumption of constant altitude.

Comparison to the real input data, shown in Figure 2.9 for the energy and the energy flux reveals that only when the arc is overhead is good agreement obtained with the actual input values. This makes sense physically because only when you are looking up the field line do you include all the emission in the integration. Looking at the arc from the side distorts the true integrated intensity, and thus distorts measurements that are inferred from ratios of these integrated intensities. Figure 2.13 shows the difference between the input and measured energy of precipitation for this example. Note that not only is the peak energy wrong in the inferred measurement for times when the arc is not overhead, but that the width of the precipitation region changes with the angle in degrees from the stations latitude. This effect is due to the fact that the arc is distributed in height, and is actually narrower than what is represented in the flat mapping. Attempting to correct for this problem is the idea that is the heart of the Eather mapping.

2.3.4 Eather Mapping of Scan Angle to Latitude

Eather et al. [1976] point out that *Rees and Lucky* [1974] showed that the ratio of the 6300 Å to 4278 Å emission profiles depends to a much larger extent on the altitude than the energy of the precipitating particles. This led Eather to propose using the 6300 Å to 4278 Å ratio in the MSP scan angle to determine the height for each individual scan angle, and then remap the entire scan angle to latitude.

An example of this method is shown in Figure 2.14. Again, in this example, the arc is 1.25 degrees poleward of the station. Here the red to blue ratio is used

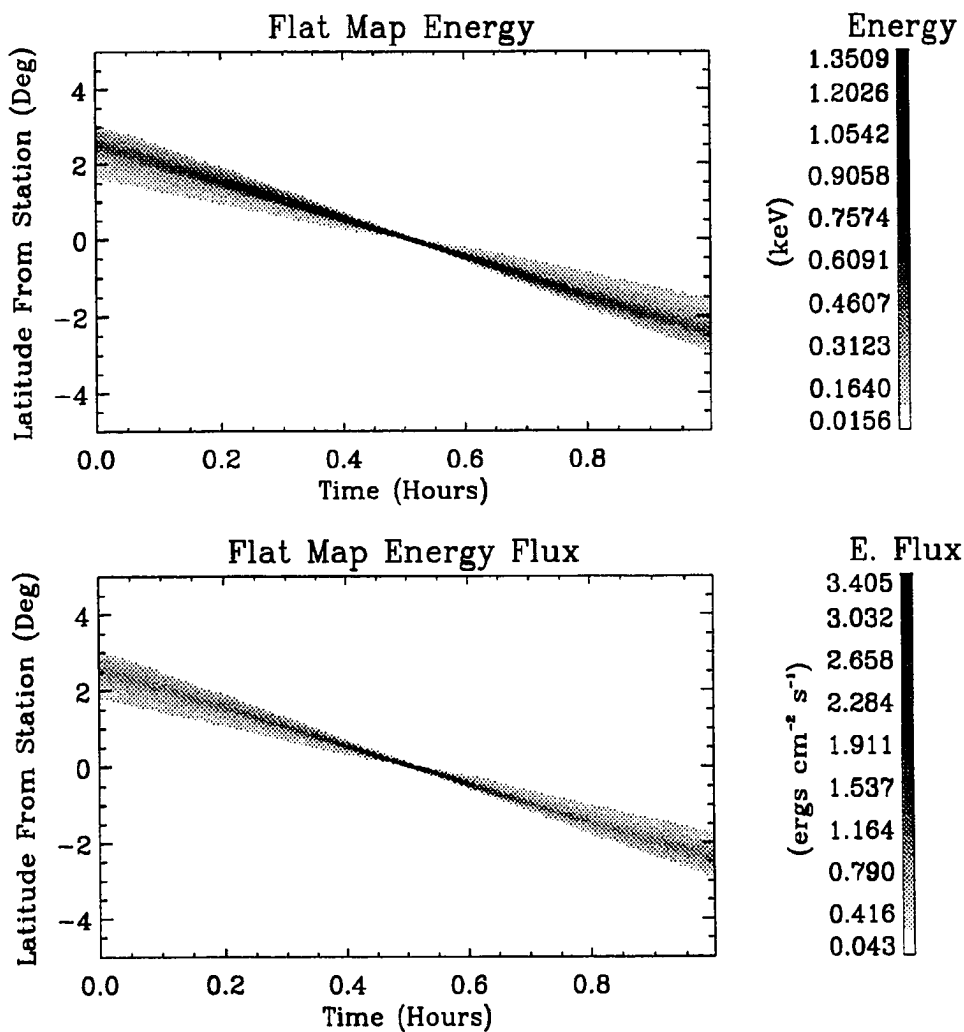


Figure 2.13. Difference of inferred characteristic energy of precipitating particles using the 4278 Å emission mapped to 125 km and the 6300 Å emission mapped to 225 km with the input characteristic energy. Note that only overhead is there relatively good agreement

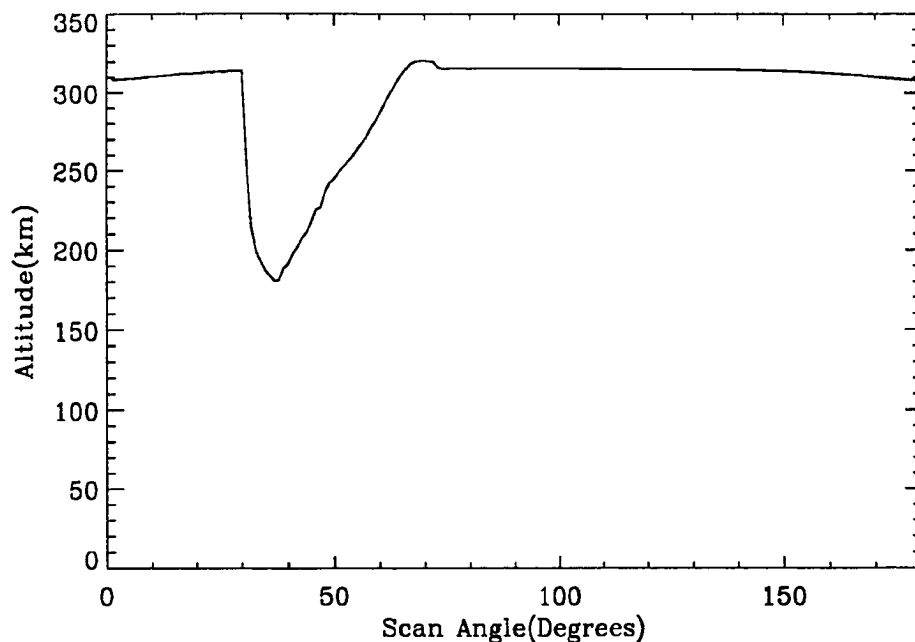


Figure 2.14. Inferred emission altitude for one scan using the red to blue ratio for each scan angle as an estimate of the altitude in that scan angle, this is called the Eather method. The arc is 1.25 degrees poleward of the station for this example. Note the uniform background is inferred to be at approximately 300 km while the bottom of the emission is at approximately 180 km.

to infer the altitude of the emission along the line of sight for each scan angle using the values from *Rees and Lucky* [1974]. Note that the uniform background is inferred to be at a constant height of approximately 300 km, and the lower border of the emission is at about 180 km. Figure 2.4 shows that the peak intensity of the 4278 Å emission is actually about 120 km rather than the 180 km estimated by the Eather method. The 180 km estimate is higher than the real height of the emission because the background 6300 Å emission integrated along the line of sight contaminates the ratio and thus affects the height estimate. Obviously

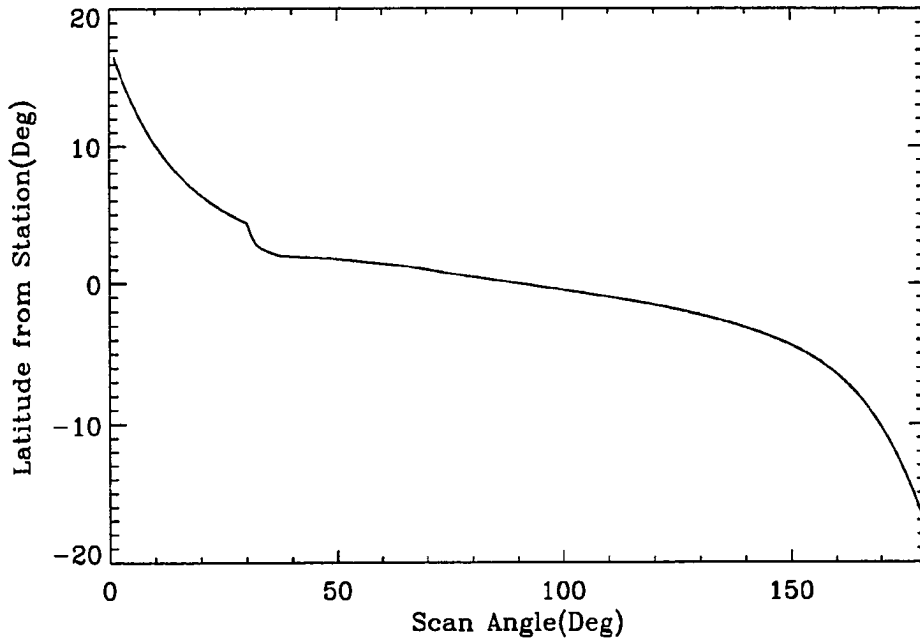


Figure 2.15. Inferred latitude for one scan using the Eather method. The arc is 1.25 degrees poleward of the station for this example.

the background and arc emissions are coming from different altitudes along the line of sight, and this violates the basic assumption behind the Eather mapping technique. Once the emission height is determined as in Figure 2.14, the latitude of the emission is calculated as before.

Figure 2.15 shows an example of the inferred latitudes of the emission versus scan angle. Since these latitudes are dependent upon the calculated height of emission, the latitudes are not necessarily monotonic with scan angle as they were with a constant height mapping. Thus the Eather mapping moves certain pixels

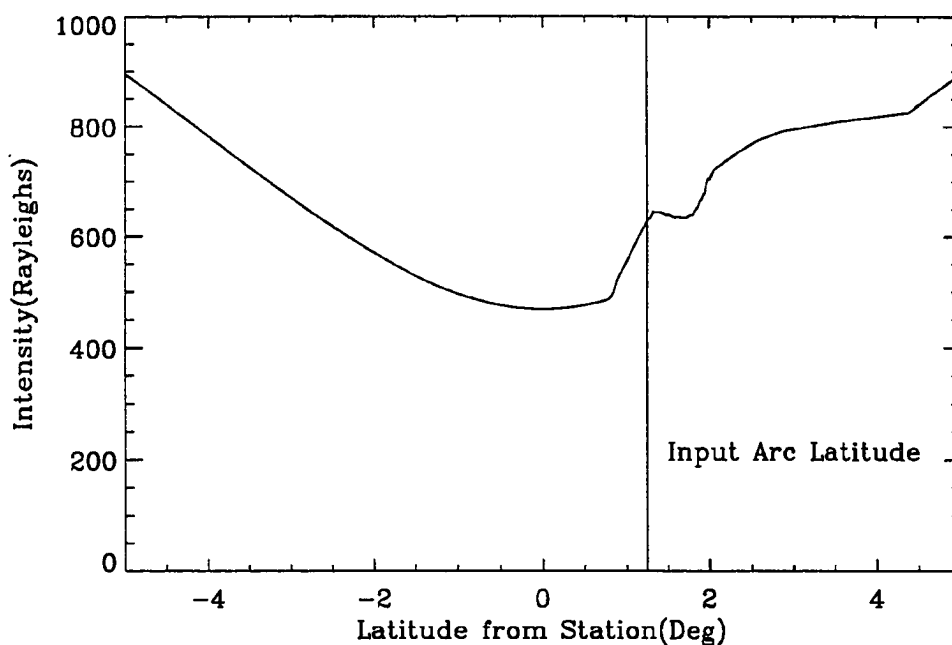


Figure 2.16. One 6300 Å scan mapped to latitude using the Eather method. The arc is 1.25 degrees poleward of the station for this example.

(scan angles) nonuniformly given the calculated height of emission. This has the desired effect of narrowing the distribution of emission over latitude.

The results of this mapping for the 6300 Å emission is shown in Figure 2.16 where the MSP intensity is mapped to latitude using the Eather mapping technique. The actual arc location is shown as the vertical line in Figure 2.16. Note that the background emission poleward of the station has also been remapped, and this causes the artificial increase in the intensity poleward of the arc.

Figure 2.17 plots both the flat map to 225 km and the Eather mapping of the 6300 Å line, again the actual arc location is shown as the vertical line in the figure. Note that the peak in the Eather mapping is closer to the actual location

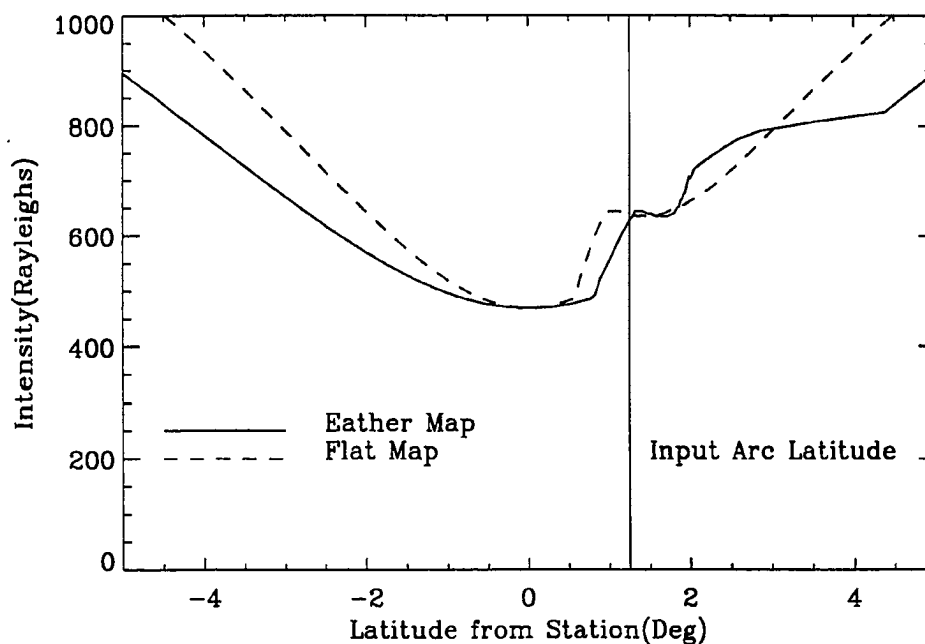


Figure 2.17. Comparison of Eather map and flat map for one 6300 Å scan. The arc is 1.25 degrees poleward of the station for this example, note that the inferred emission location for the Eather map is close to the actual latitude of emission.

of the arc compared to the flat mapping. This comes at the cost of the distortion in the background emission for those scan angles that the MSP line of sight does not intersect the arc.

The Eather map can be applied, scan by scan, and the entire two dimensional array again imaged to show the position of the mapped emissions. Figure 2.18 show images of the Eather map applied to the 4278 Å and 6300 Å emissions. The distortion in the 6300 Å emission at latitudes greater than the arc emission, and the mismatch of the arc latitude for the 4278 Å emission are both due to the

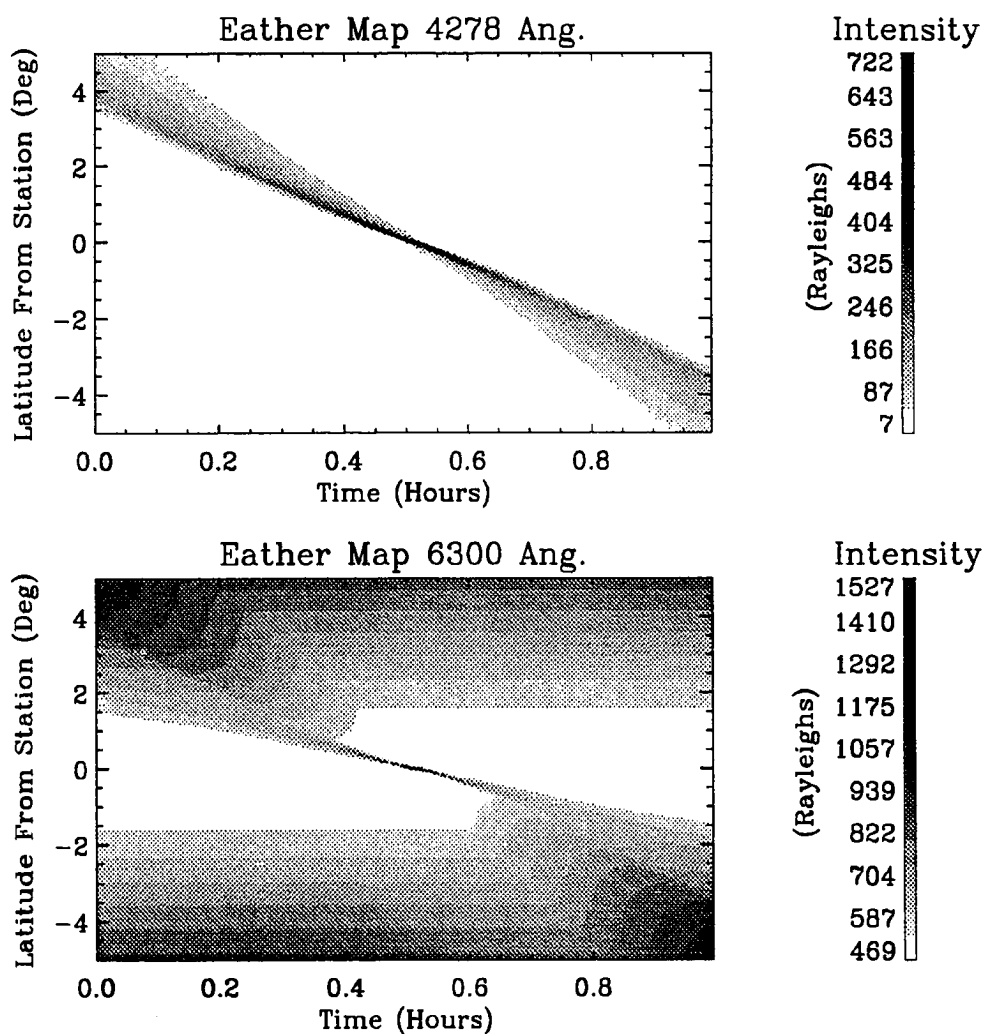


Figure 2.18. Keogram of the 4278 Å and 6300 Å emissions using the Eather map. The upper panel is 4278 Å, the lower panel is 6300 Å. Note that the latitude of the 4278 Å emission at 0 and 1 hours is larger than that in the flat map case. This is because the inferred altitude in the Eather map is higher than the 125 km used in the flat map case, due to the 6300 Å background emission.

height of the emission being improperly estimated. As noted before this improper estimation is due mainly to the large 6300 Å emission assumed in the model.

Taking these arrays and applying the *Rees and Roble* [1986] formulae results in characteristic energy and energy flux maps of the precipitating particles as inferred by the Eather map. These are displayed in Figure 2.19. Comparison to the real input energy and energy flux, shown in Figure 2.9, reveals that the large 6300 Å background in this example has made the altitude of emission too high. This causes scan angles with large blue contributions to be mapped to too large a latitude, resulting in the poor comparison to reality.

This is demonstrated in Figure 2.20, which shows the 6300 Å emission scan for the Eather map with the normal amount of background and a case where the background has been reduced by a factor of 20. Note that for the case where the background is reduced the arc is narrower, and the peak of the emission is closer to the actual arc position. This clearly shows the limitations of the Eather method: as the background becomes high, the method fails.

The above example points out the problems associated with using the Eather map. To the extent that you do not have emission from one point along the line of sight, the method will return poor estimates of the height, and hence latitude of the emission. One way around this problem might be to fit an analytic background curve to the experimental data to try to remove as much of the background contamination as possible. *Eather et al.* [1976] did fit airglow and extinction curves to the experimental 6300 Å and 5577 Å data to remove some of the background.

This discussion shows that the mapping of scan angle back to latitude always has inherent errors. These errors reflect the different assumptions that go into the two mapping techniques. The flat map would be appropriate for cases where there are two stratified layers of emission spread over a large range of latitude. The

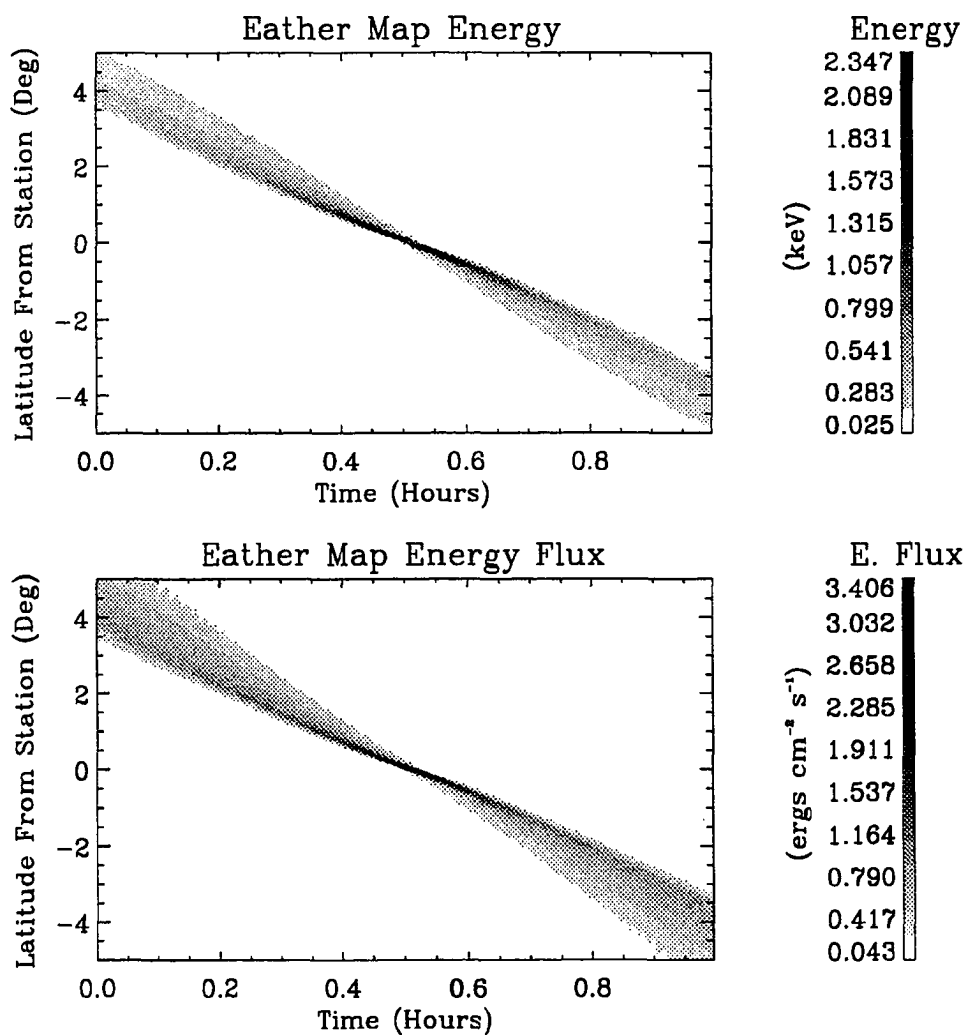


Figure 2.19. Plot of the inferred characteristic energy and energy flux of precipitating particles using the Eather map. The upper panel is the energy and the lower panel is the energy flux. Note that since the 4278 \AA has been mapped incorrectly the inferred energy and energy flux are also incorrect. There is fair agreement with the input data when the arc is directly overhead.

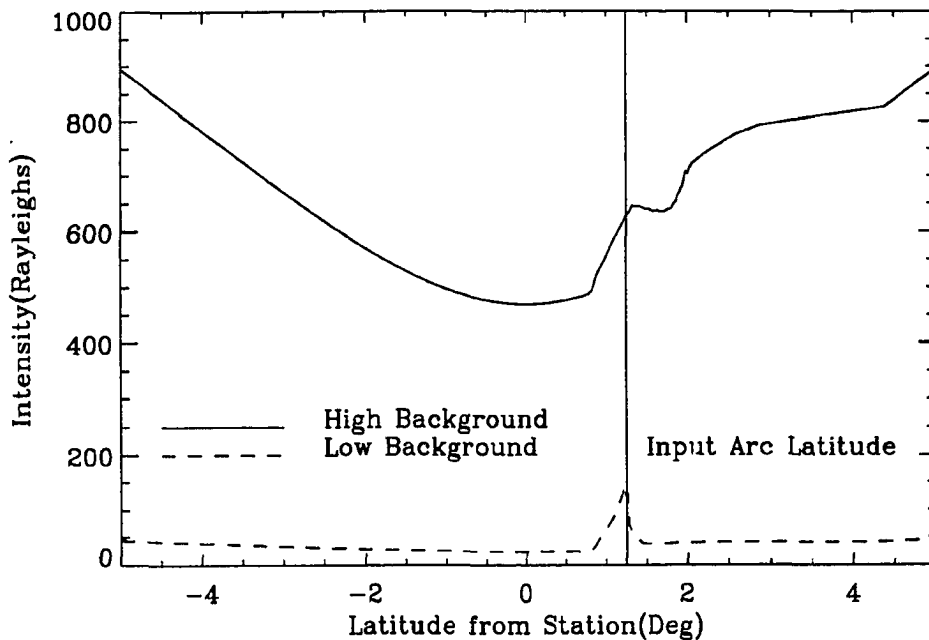


Figure 2.20. Comparison of Eather map of 6300 Å emission with high and low background. In the low background case the background has been reduced by a factor of 20. The arc is 1.25 degrees poleward of the station for this example, note that the inferred emission location for the low background case is closer to the actual latitude of emission.

Eather map is appropriate for thin arcs with a minimum of background. The next section shows how this type of analysis can be used on real data.

2.4 Ground based optical observations of the cusp

This section uses the mapping and analysis discussed earlier in the chapter to examine data taken from the cusp latitude station in Svalbard Norway. I will use the Eather mapping technique since the dayside auroral oval is characterized by very tall arcs, sometimes extending well past 400 km in altitude, see *Deehr*

et al. [1980]. The 6300 Å to 5577 Å spectroscopic ratio is used to determine the characteristic energy and energy flux since significant solar resonant contamination of the the 4278 Å band can occur in the sunlit tops of the tall dayside arcs, [*Deehr et al.* 1980].

The satellite particle precipitation measurements offer the most direct measure of the cusp at ionospheric altitudes, which is defined as the presence of sufficiently high fluxes of particles with magnetosheath characteristics at these altitudes. The major drawback to the satellite measurements is that data are only taken along the satellite path. Thus local time variations in the location of the cusp and boundary layers are necessarily inferred from statistical studies of many such passes. The ground station using optical observations has the advantage of good local time coverage since it rotates underneath the footprint of the cusp each day. The drawback to the ground station is that the energy and energy flux of the incoming electrons must be inferred from the optical observations, and thus the identification of regions similar to those in the satellite measurements is correspondingly less assured. This confusion is due to the fact that when the optical methods are used only the average energy and energy flux can be determined, while all energy dependence is lost in the measurement. In addition to this limitation the calculation of average energy and energy flux can be confused due to several factors. For instance the red line emission rate may be contaminated by the high energy tail of the very high temperature electrons that precipitate in the central cusp. Another problem encountered when using ground based optical data is that the Rees and Luckey optical method is applicable only to emissions caused by electron precipitation. While emissions from proton precipitation do exist, [*Eather and Mende* 1971], they are not included in the Rees and Lucky method. With these caveats in mind, the ground station measurements offer a good snapshot view of one days cusp data.

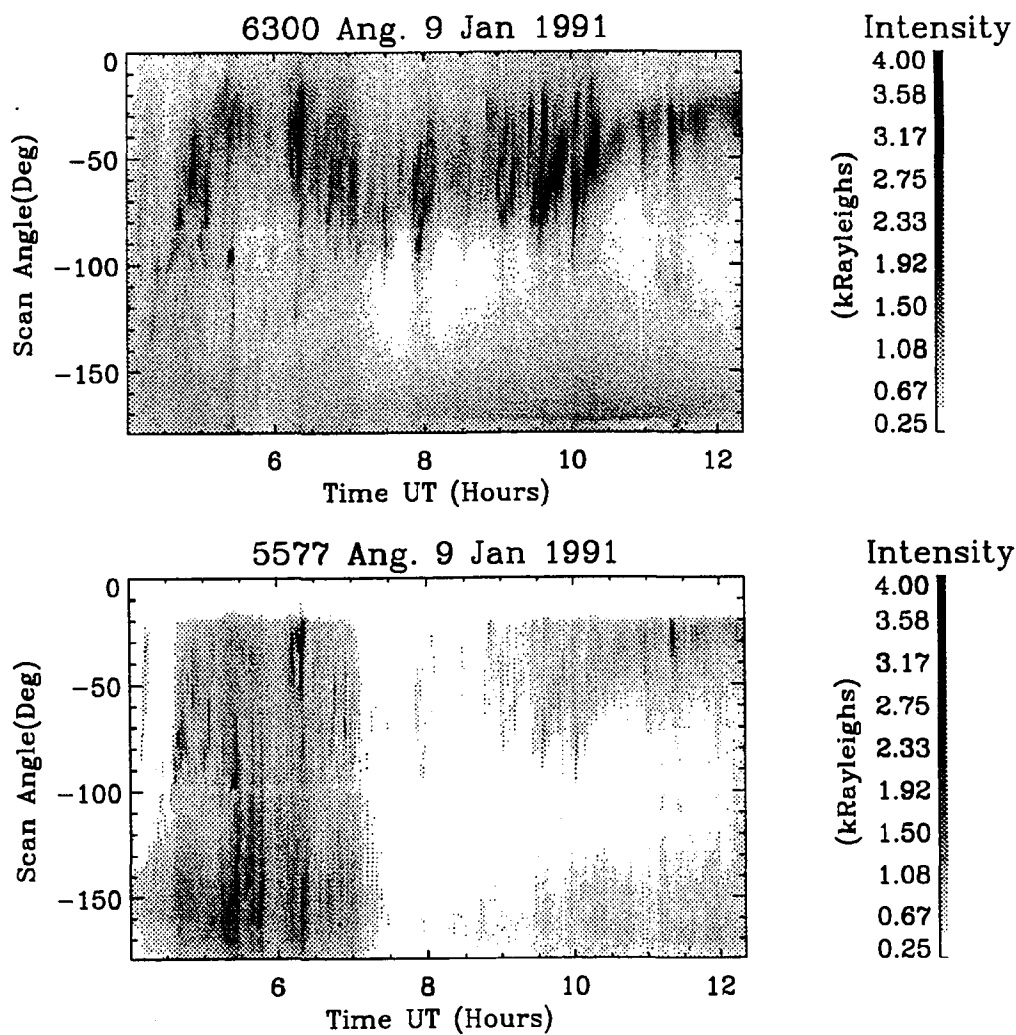


Figure 2.21. Keogram of 6300 Å and 5577 Å emission from 9 Jan 1991. The upper panel is the 6300 Å emission, while the lower panel is the 5577 Å emission. In both cases the intensity of emission is given in kRayleighs, and the Keogram lasts from approximately 0400 UT to 1215 UT. Magnetic noon occurs at 0900 UT. Note that the intense 6300 Å emission is predominately north of the station, while the 5577 Å emission is more uniformly distributed in latitude.

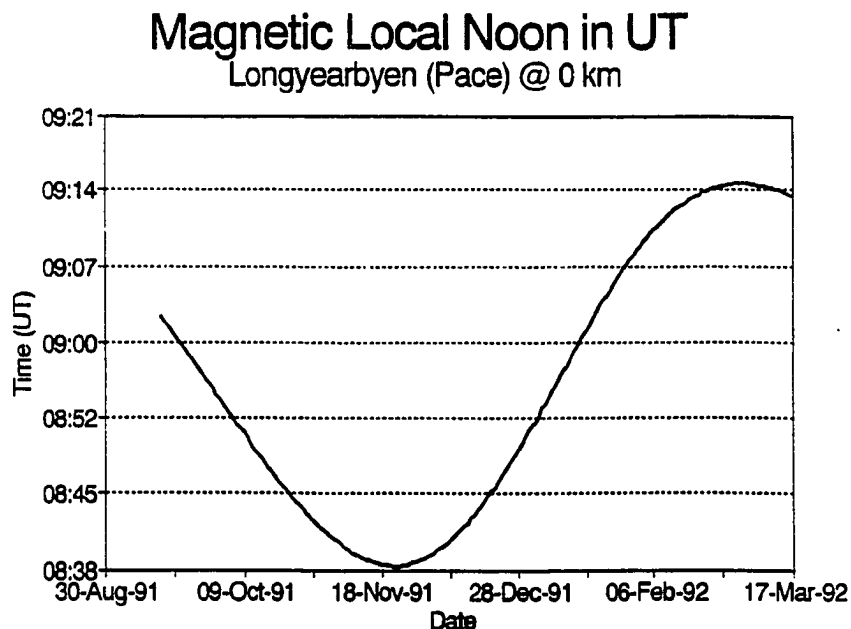


Figure 2.22. Universal time of magnetic local noon at Nordlysstasjonen from September 1990 to March 1991 according to the PACE coordinate system. The variation in time of local noon is approximately 30 minutes at this latitude due to the inclination of the Earth's equator with respect to the sun, and the slight eccentricity of Earth's orbit, [Baker and Wing 1989]. Note that during the time when optical observations are made, from late November to late January, that local magnetic noon occurs between 0830 to 0910 (UT).

Figure 2.21 shows the 6300 Å and 5577 Å emission for 9 January 1991, from approximately 0400 (UT) to 1215 (UT). The upper panel shows the 6300 Å emission, while the lower panel shows the 5577 Å emission. Magnetic noon occurs at approximately 0900 (UT) on this day. This is demonstrated in Figure 2.22 which shows the variation in universal time of local magnetic noon during the winter months. This variation is mainly due to the inclination of the Earth's equator

with respect to the Earth sun line, and the slight eccentricity of the Earth's orbit. Returning to Figure 2.21 we see that during this day the 6300 Å emission is mainly seen poleward of the station. An intensification in the emission is seen around 0930 to 1015 (UT) in scan angles poleward of the station. Note that the 5577 Å emission is more uniformly distributed in scan angle when compared to the 6300 Å data. There is a noticeable decrease in the 5577 Å emission after 0700 (UT) that lasts for approximately two hours. This decrease in the intensity of the green line is probably what led to the term "dayside gap" of *Dandekar and Pike* [1978]. Note that after 0930 (UT), the intensity of the 5577 Å emission increases again both poleward and equatorward of the station, with scan angles directly overhead continuing to show a minimum amount of emission. IMF data are not available since IMP-8 was inside the magnetopause at this time.

Figure 2.21 is mapped to latitude using the Eather mapping, and the characteristic energy and energy flux are found using the ratio of 6300 Å to 5577 Å emission as described in section 2.2. Figure 2.23 shows the inferred characteristic energy of the particle precipitation mapped to magnetic latitude from the station. Note that this figure covers ten degrees of the high latitude dayside from approximately 0400 to 1230 UT, or 0730 to 1600 MLT. This graphically demonstrates the ability of the MSP to give a snapshot of one day's passage underneath the dayside cusp region.

There are two important features in this figure. First note that between 0500 and 0700 UT there is a region of higher energy particles, with the highest energy precipitating particles in these local times on the equatorward side of the station. To a lesser extent this region of higher energy particles exists after magnetic noon, which is at approximately 0900 on this day. Second note that from 0700 to 1030 UT there exists a spatially confined region of extremely low energy precipitation. This region of low energy precipitation extends from magnetic latitudes 75 to

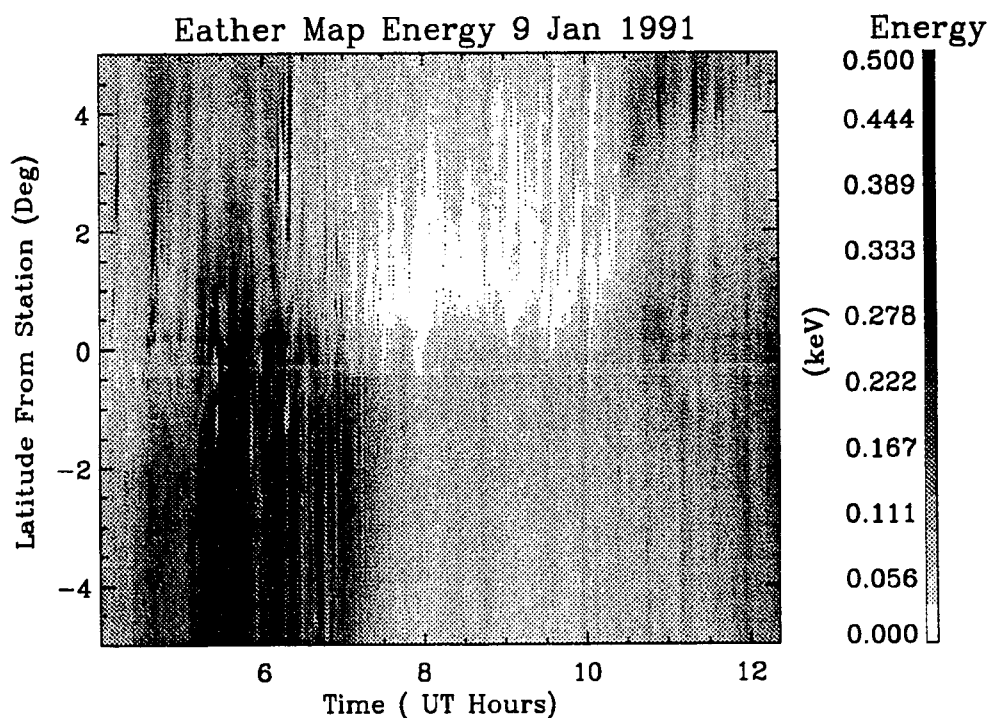


Figure 2.23. Inferred characteristic energy of precipitating particles for 9 Jan 1991 for magnetic latitude differences from the station of plus and minus five degrees. Note the broad latitude and local time distribution of higher energy particles both before and after magnetic noon at 0900 UT. Also note the very low energy particle precipitation region to the north of the station from approximately 0730 to 1030 UT. This region of very low energy particles is spatially confined to approximately 75 to 78 degrees magnetic latitude. The location and particle precipitation characteristics are consistent with cusp precipitation.

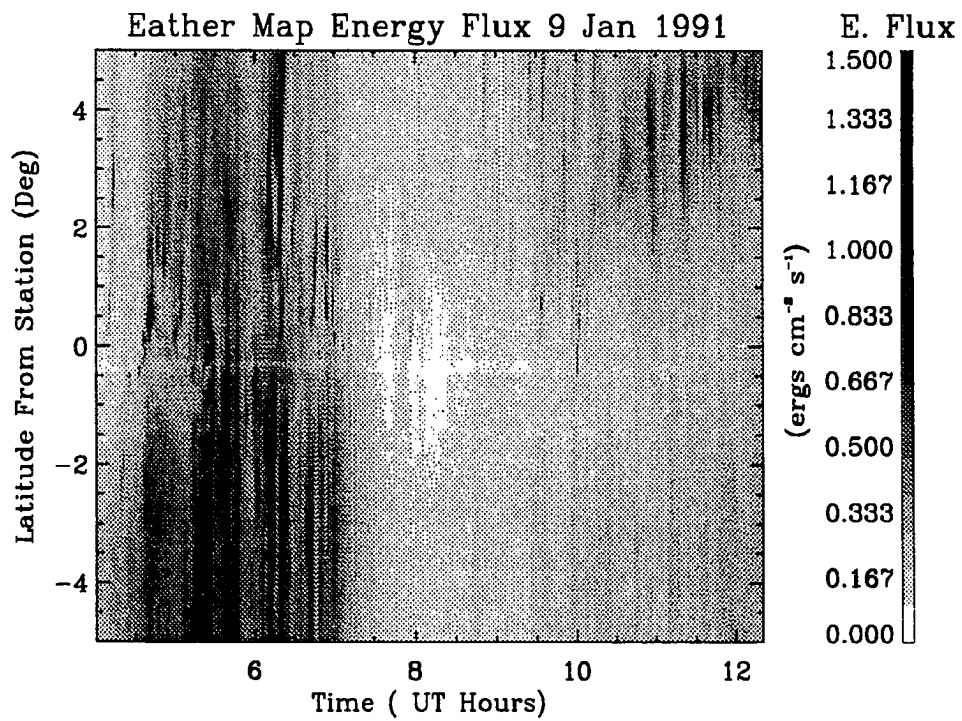


Figure 2.24. Inferred characteristic energy flux of precipitating particles for 9 Jan 1991 for magnetic latitude differences from the station of plus to minus five degrees. Note that this figure is derived from the 5577 Å emission, so it also shows a broad area of higher energy flux precipitation before and after local noon.

approximately 78 degrees. The upper latitude is in question since it is poleward of the zenith, and the last section clearly showed that even when the Eather map is used some residual uncertainty is associated with the results. It is important however that while the exact poleward edge of the region of low energy particles is in question, it clearly has such a poleward border. Using equation 2.4, Figure 2.24 shows a map of the the intensity of the energy flux derived from the 5577 Å emission. It shows that the region of higher energy particles before magnetic noon is also a region of significant energy flux. The region of very low energy particles discussed above is found to have a correspondingly low energy flux.

The maps of average energy and energy flux shown in Figure 2.24 and 2.23 are very suggestive. *Newell and Meng* [1992] shows the cusp in an average sense having a width of approximately 2.5 hours, centered around magnetic noon. The average latitudinal width of the cusp *Newell and Meng* [1992] give is approximately one degree. This description fits very well the observations made on the 9th of January 1991. In addition to this region of very low energy particles we see a region before and after magnetic noon with higher energy particles. *Newell and Meng* [1992] show that the region of structured precipitation on the dayside is most like the night side aurorae, which they call the boundary plasma sheet, extends around to almost 10 magnetic local time at 75 degrees latitude. Such a region fits very well with the higher energy particles seen before magnetic local noon on the 9th of January.

The one plasma region in the *Newell and Meng* [1992] work which is not obvious in the the 9 January 1991 data is the low latitude boundary layer (LLBL). The LLBL is thought to be the boundary layer on the magnetosphere side of the magnetopause. It consists of particles with both magnetosheath and magnetospheric properties. *Newell et al.* [1991c] note that the low latitude boundary layer region has precipitating electron energy and energy flux characteristics with values between that of the boundary plasma sheet and the cusp. The average electron

characteristic energy of the LLBL is typically below 200 eV, but there is significant spatial and temporal variation in the spectra. This reflects the thought that the LLBL is an admixture of the magnetosheath and magnetospheric plasma regions. In *Newell and Meng* [1992] the cusp has characteristic electron energies below 100 eV, and very large number fluxes. The boundary plasma sheet serves as the catch-all category in the soft energy precipitation regimes of *Newell et al.* [1991c]. The boundary plasma sheet is characterized by electrons with energies below 1 keV and with highly structured arc forms within it. Thus the LLBL has energies above those characteristic of the cusp, greater than 100 eV, and below those characteristic of the BPS.

This definition lies at the heart of the problem with optical identification of the LLBL. The BPS and cusp categories are sufficiently distinct that optical means can tell the difference between them. The question is where the LLBL fits into the picture when looking at the optical data. Only the characteristic energy and energy flux of the incoming particles are inferred using optical techniques. To identify the difference between the cusp and the LLBL the satellite particle measurements many times rely upon information about the ion energy and flux measurements. The cusp is characterized by a factor of 10 larger ion flux than the LLBL. Using the optical techniques described we cannot make this distinction. The same problem comes about with respect to the difference between the LLBL and the boundary plasma sheet. The LLBL can have structured arcs in it as well as the boundary plasma sheet, it simply has a lower average energy than the boundary plasma sheet. *Newell and Meng* [1991c] and *Sandholt* [1990] both point out the difficulties in making the distinction using optical techniques.

Figure 9 of *Newell et al.* [1991a] shows a schematic which is reproduced as Figure 2.25. This schematic shows the location of the the LLBL in relation to the central cusp and boundary plasma sheet. It serves as a transition region between

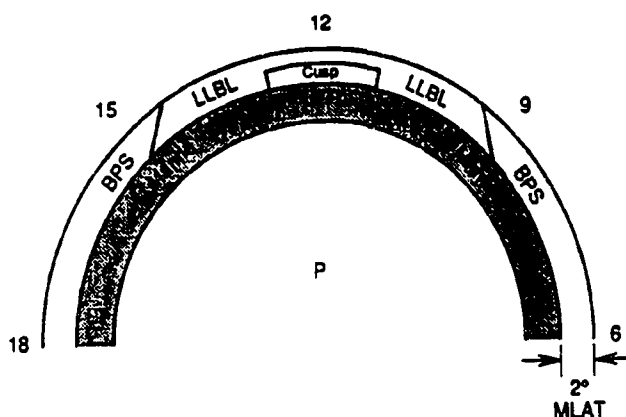


Fig. 9. A modification of the figure of Vasylunas based on our observations. The mantle forms a latitudinally narrow ring poleward of the other boundary layers.

Figure 2.25. Schematic of magnetospheric source of ionospheric precipitation from *Newell et al.* [1991a]. Note that the LLBL extends to earlier and later magnetic local times from the cusp. It is also equatorward of the cusp around magnetic noon, but at roughly equal latitudes at magnetic times before and after local noon.

the two regions, and is at similar latitudes as the cusp at magnetic times away from local magnetic noon. Again remember that this schematic is true only in a statistical sense. Comparison to any one days data is unknown at this time due to the sparse coverage of the dayside sector by satellite on any one day.

To summarize the results from the optical data shown in Figures 2.24 and 2.23 we make the following very tentative identifications. The central cusp is the region of very low energy precipitation lasting from 0730-1030 (UT), which corresponds from 1030-1330 magnetic local time. This region extends from just

poleward of the station to latitudes roughly 2-3 degrees poleward of the station. This region exhibits variable latitudinal width, but has a poleward edge to it. The boundary plasma sheet is identified as the region of higher energy particles, above characteristic energies of 0.4 keV in this case, extending from approximately 0500-0700 (UT) and being predominately found equatorward of the station.

Identifying characteristics of the LLBL is most open to question. It is tempting, and at least consistent with Figure 2.23 to view the LLBL at the region poleward of the station in the 0500-0700 (UT) times. Thus the BPS is equatorward of the LLBL and, and then drops out at 1000 magnetic local time. The LLBL would primarily extend at local magnetic times before and after magnetic noon in this picture. As stated these characteristics are consistent with that of the LLBL, but in my view inconclusive in this case. To be conclusive would require an overflight of a satellite which could delineate the LLBL from the boundary plasma sheet and central cusp. Until such events happen, and the comparison of optical and satellite identifications agree in a statistically valid way, we are forced to conclude that the identification LLBL using optical methods is not feasible in this instance.

The paradigm that I find useful is given by the schematic in Figure 2.25. As the station rotates in magnetic time underneath the footprint of the dayside auroral oval there is a transition from the boundary plasma sheet to the LLBL, into the central cusp, and then out through the LLBL and finally into the boundary plasma sheet on the afternoon side of the oval. If we are willing to accept the uncertainty associated with the location of the LLBL, then it seems that the optical data support this paradigm. The optical observations show that there is a transition from the region of higher energy particles, which are characteristic of the the dayside extension of the nightside auroral oval, to that of very low energy particles which characterize the cusp that are centered around magnetic noon. This transition in

the optical data is not unusual, as exemplified by the data collected 7 January 1992.

The optical data for 7 January 1992 are similar to that of 9 January 1991 in that a transition from higher energy to lower energy particles are visible. The data sets are different in that the transition comes earlier in the morning, and that the transition, while still clearly apparent is not as distinct as the data from 9 January 1991. This points out that daily variation in the dayside oval is an important feature in the real data.

The data presented for the 7 January 1992 case are similar in format to that shown in Figure 2.23. Figure 2.26 shows the characteristic energy data for the date of 7 January 1992. Note the region of higher energy particles poleward and equatorward of the station that lasts until almost 0900 UT. Within this region is an area of low energy particles that stretches from 0600-0830 UT and from approximately 2 degrees poleward of the station to 1 degree equatorward of the station. The energy in this region falls below the level of detectability (100eV) from 0830 to 0930, and then slowly increases back up to the 200 eV level from 0930 to 1030. From 1030 to 1400 this region continues to show alternating very low energy particles, interspersed with short time duration regions of higher energy particle precipitation. At 1200 UT a region of higher energy particles appear extending from about 1 degree equatorward of the station. Note the region from 1130 to 1330 UT that is in the zenith shows spatially small energetic injections of particles. Exact identification of this region as LLBL is not possible since there is not correlative DMSP satellite information for this time, however it is very consistent with the definition of the LLBL, and very similar to the LLBL optical data examined by *Sandholt and Newell* [1992].

Two other important parameters can be derived once the energy and energy flux have been determined. These parameters are the field aligned current density

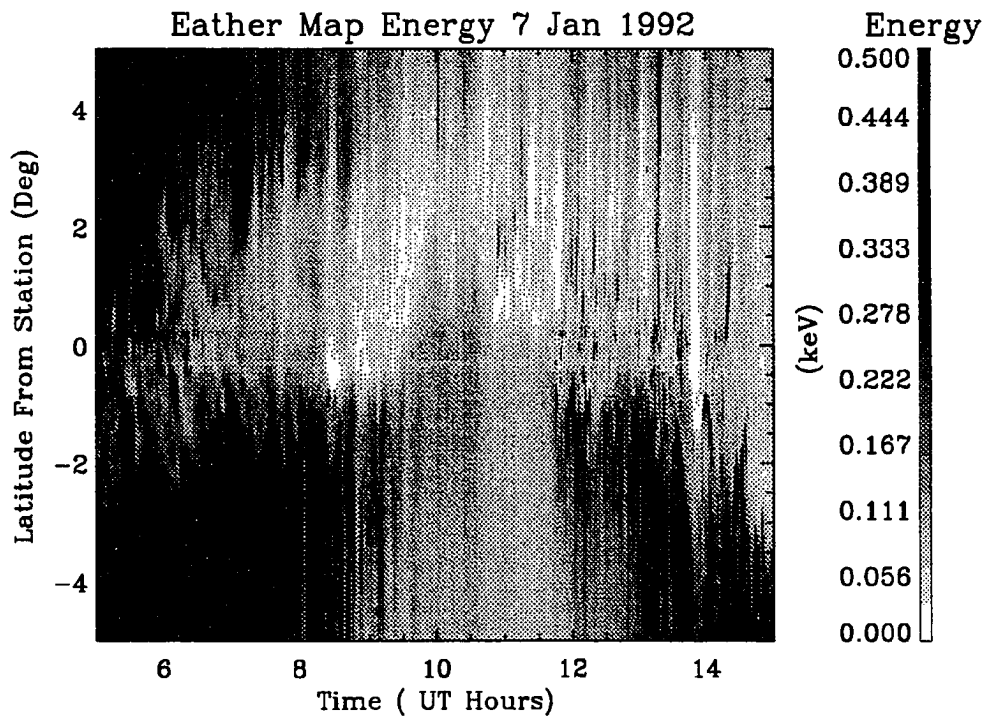


Figure 2.26. Inferred characteristic energy of precipitating particles for 7 Jan 1992. The energy is determined using the Eather mapped 6300 Å to 5577 Å ratio. See text for discussion.

of electrons above 100 eV and the height integrated conductivity of the ionosphere in the E region. The field aligned current density above 100 eV is derived from the average energy and energy flux information. The basic definition of the average energy for particles with an energy distribution function of $f(E)$ is;

$$\bar{E} = \frac{\int_{E_{min}}^{E_{max}} E f(E) dE}{\int_{E_{min}}^{E_{max}} f(E) dE}, \quad 2.8$$

where the integral in the denominator is the number flux (j), and the numerator is the energy flux (Φ_E) of the field aligned current. To obtain the current density, all that is required is to solve for this number flux, and multiply by the charge on an electron, i.e. $J = je$. Note that this derived upward field aligned current is not the total field aligned current. It is the component of the total current due to the number flux of downward flowing electrons. I have included energies with less than 100 eV in this calculation for the same reason that equation 2.6 was extrapolated to energies less than 100 eV. This downward flowing electron contribution to the total current will be offset by any return upwelling electrons, as well as any ions that add to the total field aligned current. Thus the component due to downward flowing electrons is only a partial measure of the total field aligned current.

With the caveats above in mind, Figure 2.27 shows the calculated component due to downward flowing electrons of the field aligned current density for 9 January 1991. Note first that the most intense current densities are $5 - 7 \mu\text{amps} \cdot \text{m}^{-2}$. This is a substantial fraction of typical substorm field aligned current densities, see *Armstrong et al.* [1975] and *Kamide et al.* [1989]. Also note that the most intense field aligned currents are on the equatorward side of the region of lowest energy precipitation. These intense field aligned currents only last a few minutes, and while the most intense portions are on the equatorward side of the cusp, the currents have a latitudinal distribution as well. These intensities are also in agreement with other observations of field aligned current densities in the cusp, see *Maynard et al.* [1991],

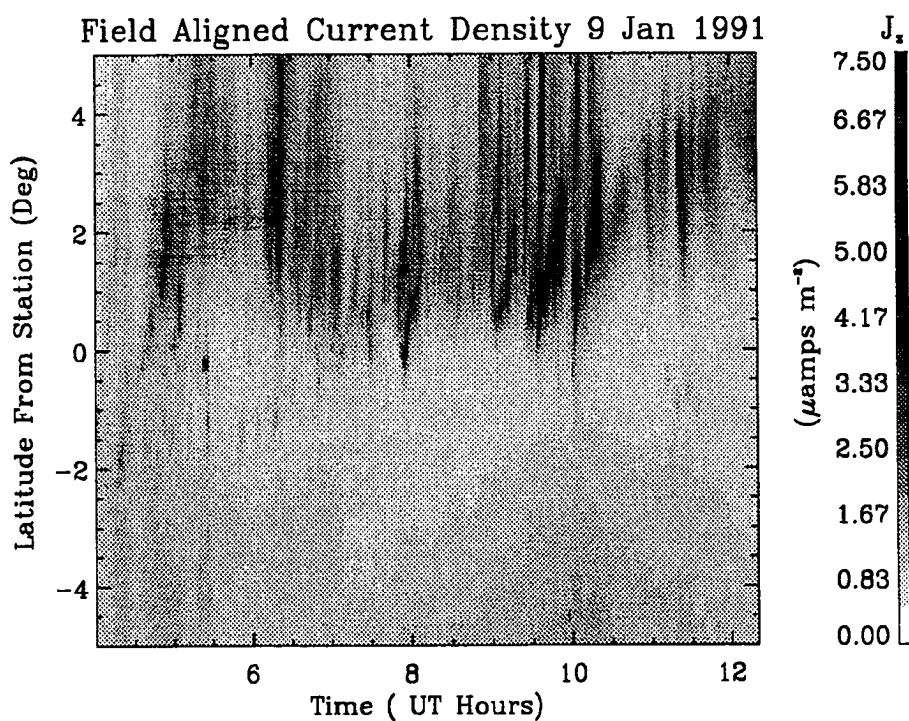


Figure 2.27. Inferred downward flowing electron component of the field aligned current density for 9 January 1991. Note that the most intense field aligned currents are seen on the equatorward side of the region that had the lowest energies. Also note the latitudinal extent of the current density in the the region of lowest energy.

and *Sandholt and Egeland* [1988]. *Maynard and Johnstone* [1974] directly measured the downward flowing electron number flux in the cusp using particle detectors on a two rockets launched out of Hall Beach, Northwest Territories Canada. This independent measure of the cusp electron number flux serves as a check on the observed values seen in Figure 2.27. *Maynard and Johnstone* [1974] infer field aligned current densities in a similar manner to that used in the optical measurements and find an intensity of $1.3 \mu \text{ amps} \cdot \text{m}^{-2}$. On the same series of rocket flights from Hall Beach, *Ledley and Farthing* [1974] report on the field aligned current density as deduced from onboard magnetometer measurements. *Ledley and Farthing* [1974] found that the field aligned current density had a horizontal scale size of 1 km, and peak intensities between 9×10^{-5} and $10^{-4} \text{ amps} \cdot \text{m}^{-2}$. Taken together these two papers indicate that the current density as inferred from the electron number flux is a major portion of the total field aligned current density in the cusp.

The field aligned current density for 7 January 1991 is shown in Figure 2.28. While the intensities are comparable in magnitude to those on the 9 January 1991 data, we see that the most intense currents are distributed over a larger time period on the 7 January 1992 data. Such intense field aligned currents are seen to be a common occurrence in the dayside ionosphere, and are an important observation in terms of the physical interpretation of what physical processes go on in the cusp. *Sandholt et al.* [1989b] also reported poleward moving enhanced regions of both red and green emission which was correlated with field aligned current densities in the few $\mu \text{amps} \cdot \text{m}^{-2}$. In this study *Sandholt et al.* [1989b] used magnetometer measurements from the DMSP satellite to determine the field aligned current densities. This topic will be presented in Chapter Four which discusses possible physical mechanisms of the observed magnetic and optical observations.

The height integrated conductivities can also be calculated using the results of *Robinson et al.* [1987]. In this work, the authors have a wide range in input

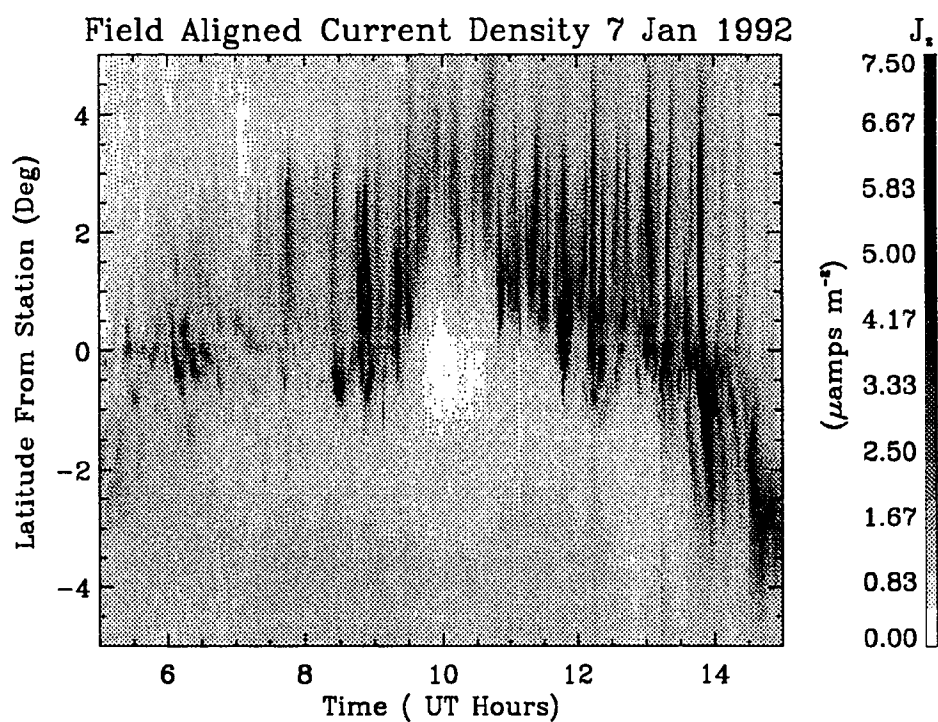


Figure 2.28. Inferred downward flowing electron component of the field aligned current density for 7 January 1992. Note that the intense field aligned currents are distributed over a larger time period when compared to the data for 9 January 1991.

energy and energy flux particle distributions on a model atmosphere. The ionization profile is determined by the range method of *Rees* [1963], and the the 1000 degree exosphere neutral atmosphere model of *Banks and Kockarts* [1973] is used to calculate the ion-neutral collision frequency. The resulting temperature, collision frequencies and electron densities are used to calculate the conductivities, see *Rees* [1989], and the height integrated conductance is then obtained. The resulting integrated conductance is parameterized with the average energy and energy flux, and the published parametric equations of *Robinson et al.* [1987] are;

$$\Sigma_P = \frac{40\bar{E}}{16 + \bar{E}^2} \Phi_E^{1/2}, \quad 2.9$$

$$\frac{\Sigma_H}{\Sigma_P} = 0.45\bar{E}^{0.85}, \quad 2.10$$

where Σ_P is the Pederson, and Σ_H is the Hall conductance in mhos, the average energy (\bar{E}) in keV, and the energy flux (Φ_E) in $\text{ergs} \cdot \text{cm}^{-2} \cdot \text{sec}^{-1}$.

Using the above relations, and the average energy and energy flux found for these days, the height integrated conductivities are shown for 7 January 1992 in Figure 2.30, and for 9 January 1991 in Figure 2.29. Notice in Figure 2.29 that large conductance gradients exist across the boundary between the areas of higher energy precipitation and lower energy precipitation. This is also seen in Figure 2.30. These large conductance gradients will cause a nonuniform ionospheric reflection coefficient to incident electric fields that map down from the magnetosphere, as well as a rotation angle of other than 90 degrees of the incident electric fields and the equivalent currents driven in the ionosphere, see *Glassmeier* [1984]. The values of the Pederson and Hall conductance are in rough agreement with those of *Hardy et al.* [1987].

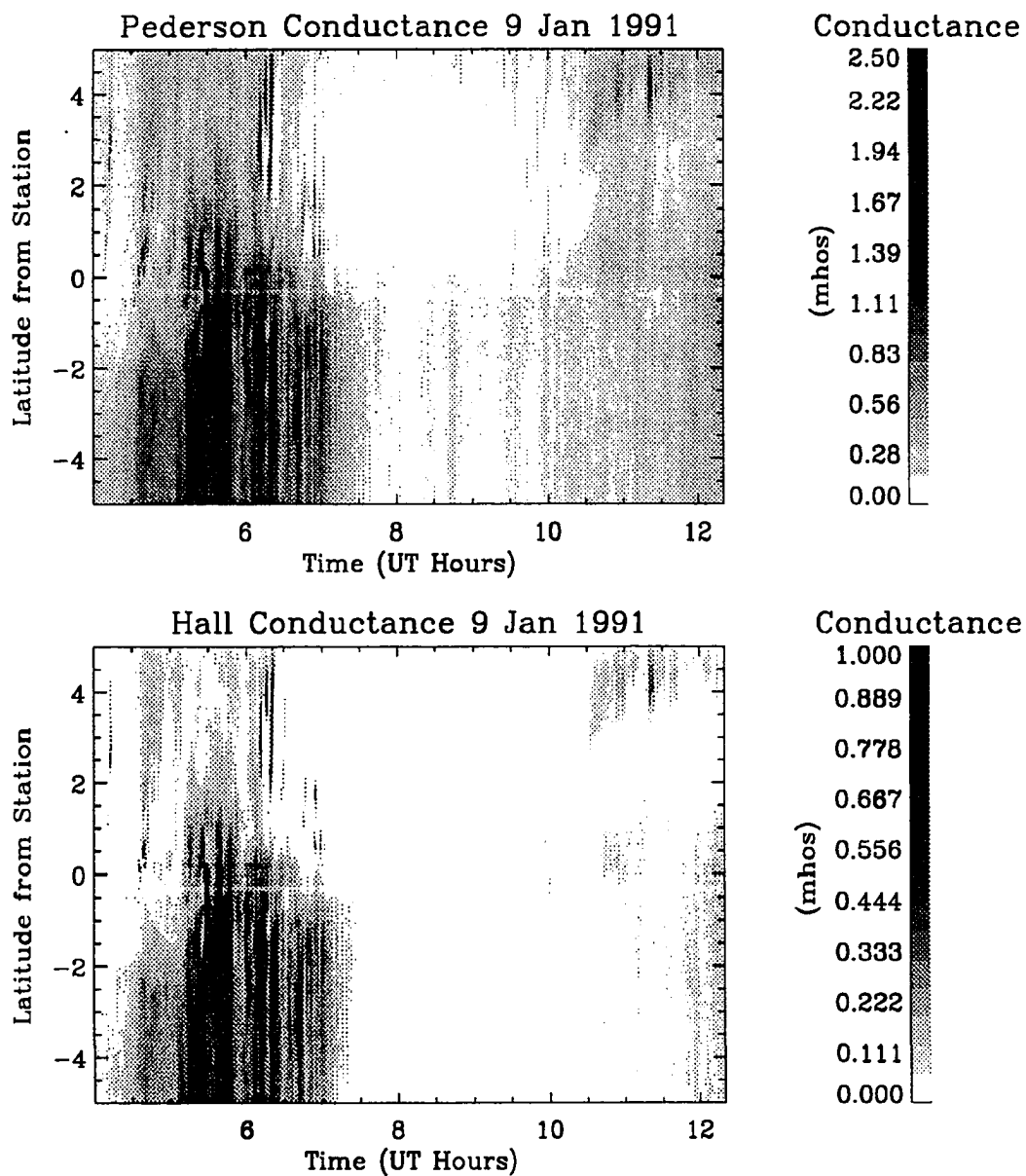


Figure 2.29. Inferred height Integrated Hall and Pederson Conductivity for 9 January 1991. The upper panel is the height integrated Pederson conductivity, and the lower panel is the Hall conductivity.

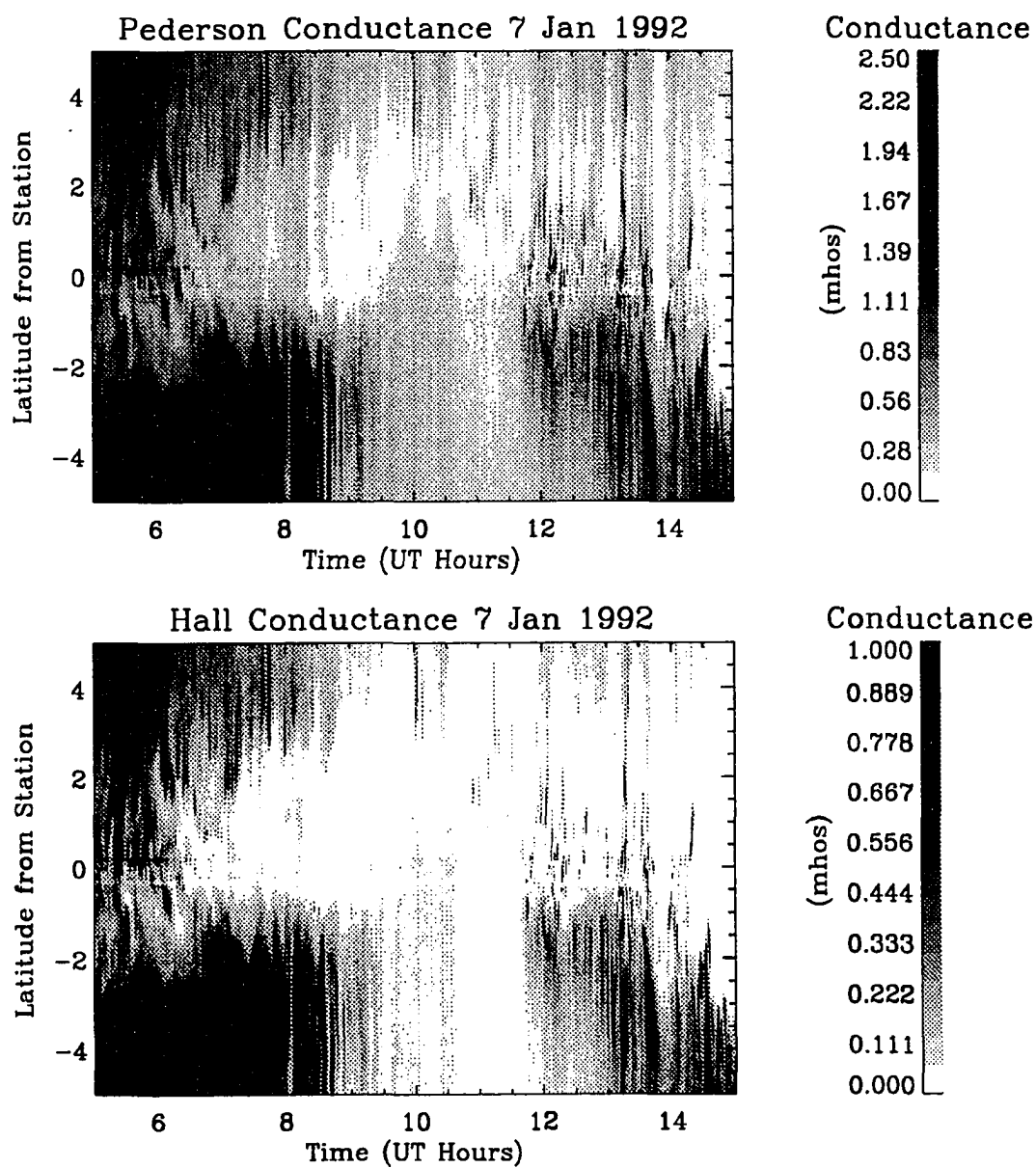


Figure 2.30. Inferred height Integrated Hall and Pederson Conductivity for 7 January 1992. The upper panel is the height integrated Pederson conductivity, and the lower panel is the Hall conductivity.

2.5 Identification of Boundary Regions and Central Cusp

The sequence of figures shown for the days of 9 January 1991 and 7 January 1992 shows that the transition from higher energy precipitation regions to low energy precipitation regions happens on a daily basis at high latitudes. While daily variations exist, the general feature can almost always be seen. Inspection of the red to green ratios as derived from the scan angle plots, not presented in this thesis, shows that the trend from regions with high energy to low energy and back to high energy is common. This conclusion is not new, as discussed in the introduction, [see particularly *Deehr et al.* 1980, *Sandholt et al.* 1989a, and *Eather et al.* 1979]. Using Figure 2.29 as a general guide, it seems appropriate to identify the time of the transition region between the dayside cusp and the remnants of the nightside oval as the period where both higher energy precipitating particles, and lower energy precipitation particles coexist at the same time. The energy I use to mark this transition is 400 eV. This energy is well above the minimum detectable by the Rees and Lucky technique, and seems to be a general feature in the data. Thus the transition region in the 9 January 1991 data set is from 0500-0700 UT; and the region lasts from 0500-0800 UT and 1200-1400 UT on the 7 January 1992 data set. Note that using a definite criterion, such as 400 eV, causes the absence of the post-magnetic noon transition region in the 9 January 1991 data set. While the energy of the precipitating particles increases from about 1030 UT onward, in this case it never reaches the threshold of 400 eV.

Since the LLBL is difficult to separate from the boundary plasma sheet and the cusp, I hesitate to label the transition region as the LLBL. Satellite data indicate that the LLBL exists in this region somewhere, we just do not yet know where it is when looking from the ground. I thus propose calling this region the boundary region as a compromise between where I think it maps to and my lack of ability to exactly pin down the location of the LLBL. Identifying the central cusp as the

region of extremely low energy particles, basically those particles below the 100 eV level, seems safer when looking at the data from 9 January 1991. Such regions in the 7 January 1992 data are sparser in nature, but still exist. Both these definitions are somewhat arbitrary, and looking at the actual data on a day to day basis seems to make the most sense.

This chapter has attempted to explain the basic optical observations and their use in identifying regions of dayside precipitation. In the next chapter, I show that the two regions identified in the optical data correlate with particular signatures in the magnetic field perturbations as measured by the induction coil magnetometers. This correspondence is important since the diurnal variations of the boundary regions and cusp position can then be described in a statistical sense using the magnetic observations.

CHAPTER 3

Magnetic observations of the cusp

One advantage gained when using ground-based magnetometers for cusp observations is that the seasonal and weather restrictions that limit optical observations do not apply to the magnetometer. However, the magnetometer signal is collected from the entire sky, and this limits the spatial resolution of the magnetometers. A second problem is that magnetometers measure magnetic fields, or the time rate of change of the magnetic field, and the interpretation of these measurements to obtain information about the ionosphere is difficult. To alleviate these problems I use the optical observations in conjunction with the magnetometer measurements. As shown in the last chapter, the identification of particular precipitation regions using the optics is a challenging prospect, and this challenge is magnified when applied to observations of the magnetic pulsations. My basic philosophy is to use the optical identification of different regions to look for signatures of these regions in the frequency-time spectrograms. As I will show, such signatures exist in the magnetometer data, and are a common occurrence in the spectrograms.

Two different types of magnetic field measurements are made at Nordlysstasjonen. Measurements of the vector magnetic field are made using fluxgate magnetometers, while induction magnetometers measure the time rate of change of the magnetic field. The data presented in this chapter are primarily induction magnetometer data, and will be displayed in frequency time spectrograms. See *Olson and Domke* [1985] for a complete description of the system. Note that the data collection period is 10 seconds, resulting in a Nyquist frequency of 50 mHz.

The first two sections of this chapter introduce the ULF pulsation spectra and compare these spectra to the optical observations. The result of the combined

observations are the magnetic signatures of the cusp and boundary region passage. The third section shows how these signatures are distributed in magnetic local time, and compares these distributions to satellite measurements of the locations of the cusp and low latitude boundary region (LLBL). In the final two sections of the chapter, I discuss how the magnetic pulsation data can be separated into three distinct categories. These categories are determined from the frequency time spectrograms spanning two years of magnetic pulsation data taken at Svalbard. I show that these categories correspond to different states of the interplanetary solar magnetic field during the time that the ground-based data were taken.

3.1 Introduction to magnetic pulsation observations of the cusp

Figure 3.1 shows the frequency time spectrogram of the magnetic ULF pulsations for 9 January 1991. In each panel, frequency in Hertz (Hz) is shown on the ordinate axis, with the Nyquist frequency of 50 mHz being the largest value displayed. The time axis, in Universal Time (UT) hours, runs along the abscissa of each panel, and the entire 24 hour period is shown. The power in each frequency-time bin is shown at fixed contours of 10 dB down from a relative maximum. The spectrograms were made by taking the fast fourier transform (FFT) of the data in the two spatially perpendicular induction coils and constructing the spectral matrix for each frequency estimate. The time window used in the spectrogram is one hour (360 points) wide, and has been offset by 15 minutes (90 points) for each new estimate. The resulting power spectra are smoothed three times in the frequency domain, resulting in approximately 12 equivalent degrees of freedom in the amplitude estimate, (J.V. Olson, personal communication, 1993). The frequency resolution is correspondingly three times the normal value of $1/3600$.

The lower panel of Figure 3.1 shows the total power deduced from both induction coils by taking the trace of the spectral matrix. The middle panel shows

the amount of power in the circular right-hand polarization state for this day, and the upper panel is amount of power in the circular left-hand polarization state, [see *Samson and Olson* 1981a,b]. The two top panels have been multiplied by the degree of polarization, see *Olson and Samson* [1979], and thus represent only polarized components of the signal; no unpolarized signal is left in these two panels. This explains why the noise floor on the two upper panels is reduced by approximately 10 dB in comparison to the lower panel. This format for frequency time spectrograms will remain unchanged throughout this chapter unless specifically noted in the figure caption.

In the bottom panel of Figure 3.1, note the broad-band increase in power before magnetic noon that lasts from 04:30 - 07:45 (UT) at all frequencies. The power at frequencies above 20 mHz falls by 10 dB from 07:45 - 09:45, and then increases again from 09:45 to 12:00. The power at frequencies below 20 mHz has a more complicated nature during the midday period from 07:00 - 10:00. Starting at approximately 07:00, the constant power contour labeled -30 dB is seen to rise in frequency to a maximum of about 3-6 mHz and then fall again after magnetic noon to lower frequencies. I will refer to this characteristic spectral feature as the "arch" because of its shape.

The upper two panels of Figure 3.1 show information concerning the polarization state of the signal. Notice that in the 1 - 5 mHz frequency band the broad band increase in power that lasts from 04:30 - 07:45 (UT) has a 10 dB increase in the right-hand circular polarization state before noon, and that the left-hand polarization state predominates after magnetic noon. The frequencies above 5 mHz do not show this strong asymmetry about magnetic noon. This asymmetry is consistent with the observations of *Samson et al.* [1971].

Summarizing, the two defining characteristics of the dayside pulsation spectrum are the broad frequency band increase in power before and after local magnetic

noon, and the unique spectral feature I have called the arch. Assuming for the moment that such occurrences are typical of the data, the question of how to interpret these two spectral characteristics is paramount. I have used the optical data to guide the interpretation of the magnetic pulsation data. This assumes that the two data sets both show some signature of the passage of the boundary region and cusp. Since I have identified the optical signature of the boundary region and cusp, I will look at the spectrograms at the times identified as boundary region and cusp to try to find the corresponding magnetic signatures of these features.

3.2 Identification of cusp and boundary region signature using ULF magnetic observations

Figure 3.2 shows the comparison of the optical and magnetic data for 9 January 1991. In Chapter 2, the periods from 04:30 - 07:45 and from 09:45 - 12:00 were identified as boundary regions. Note that during these times, the spectrogram shows a broad band increase in the power. This is accompanied by a narrow band, very intense low frequency tone at about 3 mHz. The period identified as the cusp using the optical data, lasting from 07:30 - 10:30 (UT) is concurrent with the arch in the magnetic data. This is a commonly observed association. When the higher energy particles inferred from the optical signal are detected, a broad-band increase in the magnetic pulsation spectrograms is seen. When the low energy particle precipitation is seen in the optical data the arch is seen in the spectrogram.

This comparison identifies the signatures of the boundary regions and cusp features in the magnetic pulsation spectrograms. This should not be interpreted as a causal link between the signatures observed in the magnetic perturbations and the actual cusp or boundary region. Since the magnetometers are a wide field of view instrument, it provides no information as to the location of the signal sources. *Thus when I refer to the magnetic signature of the cusp or boundary*

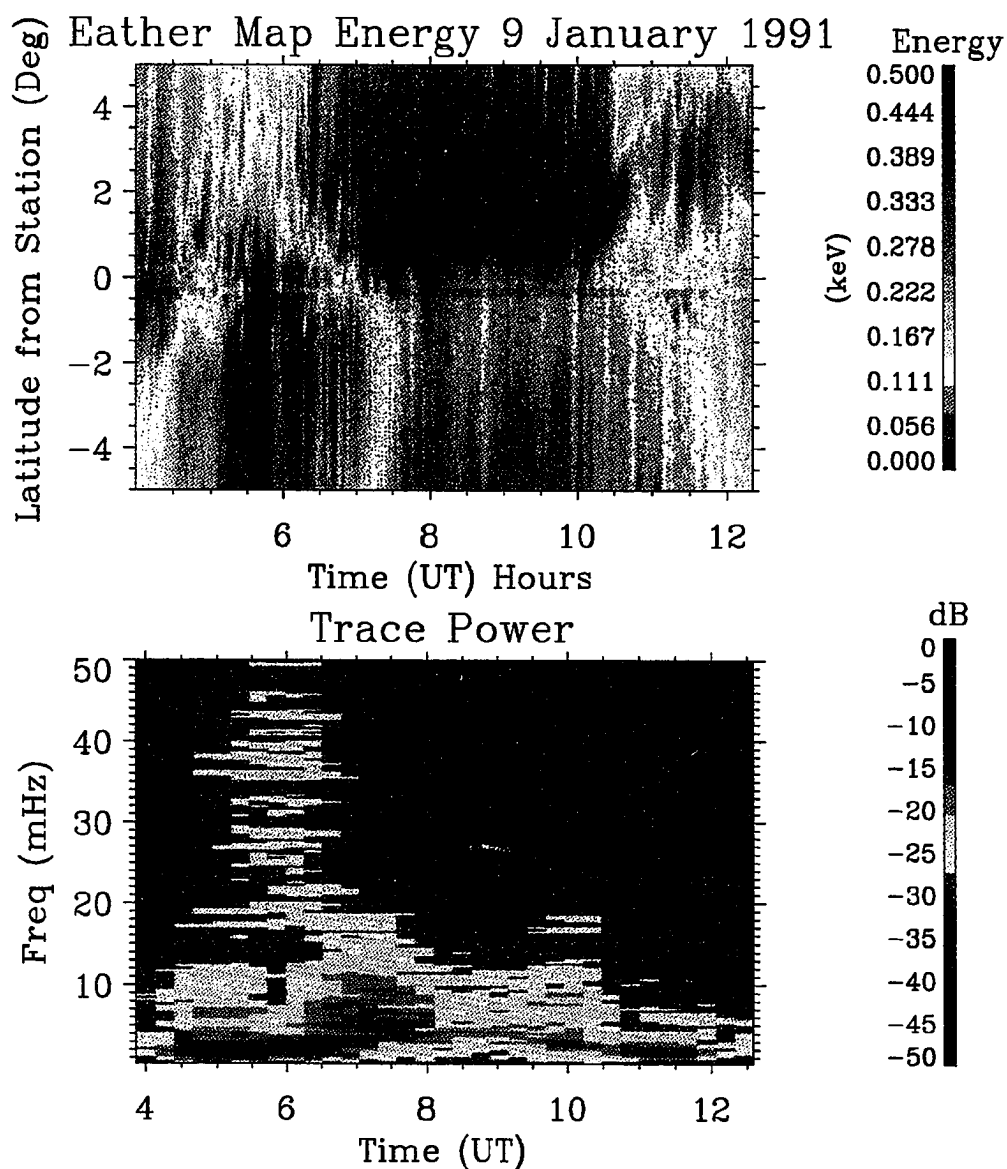


Figure 3.2. Comparison of the Optical MSP and Magnetic Pulsation data for 9 January 1991. The top panel shows the characteristic energy of the precipitating particles using the Eather mapping to latitude. This is the same as shown in Figure 2.23. The bottom panel shows the total power from the magnetic pulsation spectrogram for the same time period. The boundary regions identified in the optics are seen to happen at the same time as the broad band increase in the pulsation spectrogram. The cusp period identified using the optical data, lasting from 07:30 - 10:30 (UT) is concurrent with the arch in the magnetic data.

region, the reader should clearly understand that I mean a particular signature in the magnetic observations that were observed at the same time that I infer from the optical observations either the cusp or boundary region was in the field of view of the station. These signatures can however be used as a hypothesis for a statistical survey of the magnetic pulsation data. If the result of such a statistical study yields results that agree with other statistical studies of cusp and boundary region positions, such as satellite particle precipitation measurements for instance, then confidence in the hypothesis is increased. The next section looks at the results of such a statistical study.

3.3 Statistical occurrence of cusp and boundary region signatures

Induction magnetometer data from two years of observations at Svalbard have been included in this statistical study. Due to limitations in the data collection hardware, only 253 days yielded usable data during this two year period. In addition to these spectrograms, I produced an integrated version of the spectrogram which shows the amount of power in different spectral bands during each day's data. This makes identification of the times of boundary regions significantly easier as shown below. The four frequency bands used in this integrated spectrogram are;

Band 1: 0 - 1.6 mHz,

Band 2: 1.6 - 10 mHz (Pc5),

Band 3: 10 - 20 mHz,

Band 4: 20 - 50 mHz (Pc3).

Figure 3.3 shows the Pc-5 band integrated spectra from 9 January 1991 and shows both the total power and the circular left and right hand components of the polarized signal. Note that the boundary regions are clearly evident as an increase in the total power and are centered at approximately 06:00 and 11:25 (UT). The

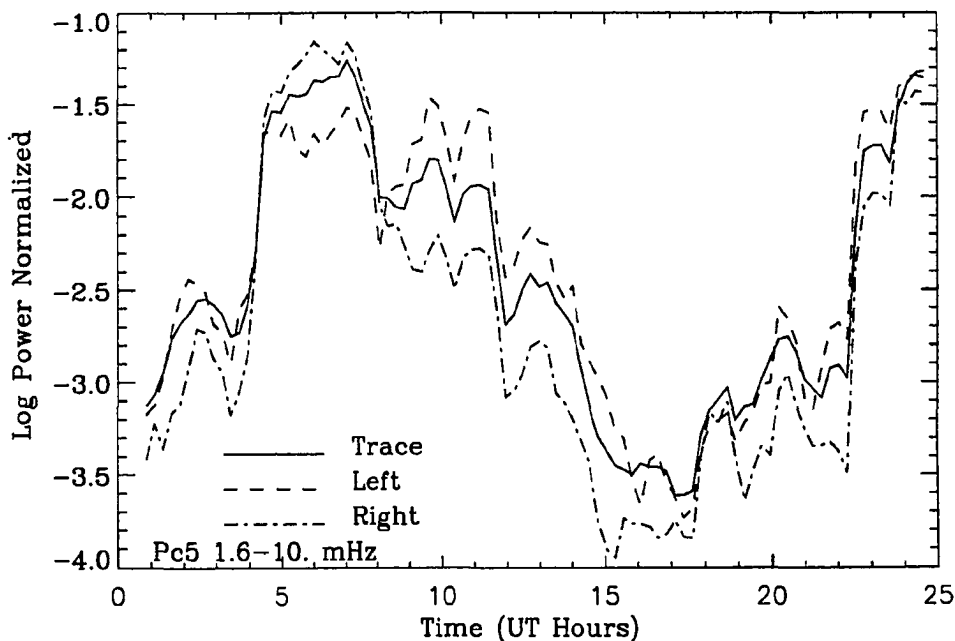


Figure 3.3. Pc-5 integrated spectra from 9 January 1991 showing both the total power and the circular left and right hand components of the polarized signal. Note that the boundary regions are evident as an increase in the total power and are centered at approximately 06:00 and 11:25 (UT). The area underneath each curve has been normalized to unity to allow comparison of spectral shape. Note that the prenoon boundary region is predominantly right handed, and the post noon boundary region is predominantly left handed.

area underneath each curve has been normalized to unity to allow comparison of spectral shape. The utility of this kind of integrated spectrogram is that it allows a particular time to be established for the boundary regions. The peak, or if highly asymmetric, the center, of the increased power region was chosen as the time of occurrence for the boundary region. The time of occurrence of the cusp was chosen to be the middle of the arch as observed in the frequency-time spectrograms. A visual inspection of the spectrograms was used to detect the arch, and hence cusp ,

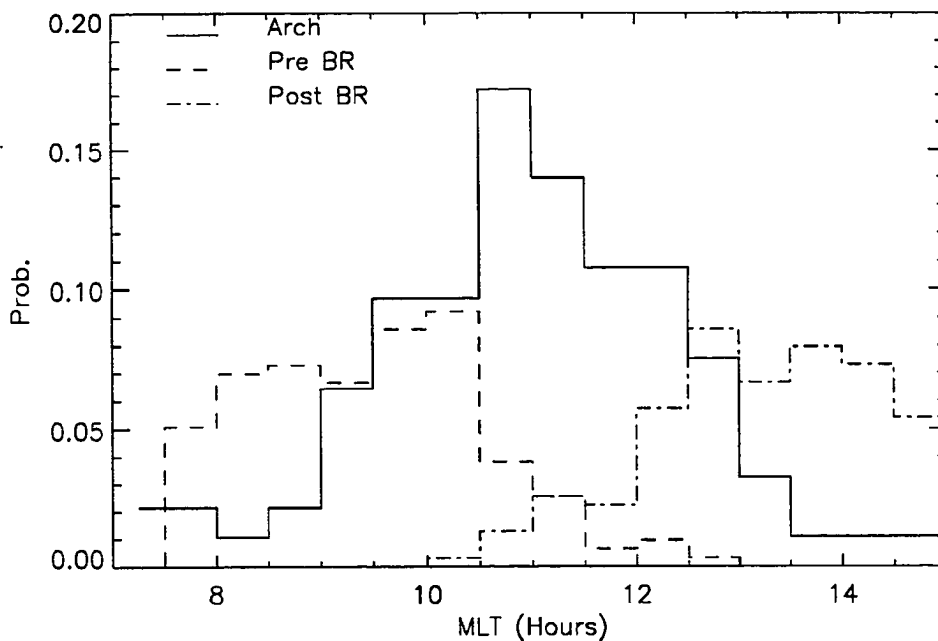


Figure 3.4. Probability of observing cusp and boundary region signatures versus magnetic local time. Note that the cusp probability distribution has only one peak, and this peak of the distribution is centered pre-magnetic local noon at 11:00 magnetic local time (MLT). The boundary layer probabilities are centered at 09:00 and 13:30 MLT

so it should be understood that not all of the cusp events might have been detected due to this visual inspection. In addition, the spectrograms were all produced with a threshold between levels of 10 db. Using a 3 db threshold for each level displayed on the spectrogram might result in more days showing the arch/cusp. Clearly an automated scheme for finding the arch would be an improvement in this regard.

3.3.1 Ground-based ULF signature of the boundary regions and cusp

Frequency-time spectrograms similar to Figure 3.2 were made for each day and visually inspected. For each day, I tabulated the UT time of the signature of the

boundary regions and arch/cusp. These UT times were transformed into magnetic local time using the PACE coordinate transforms. A histogram of the occurrences of these times produces a probability amplitude versus magnetic local time for the signatures of the boundary regions and cusp. Such a probability distribution is shown in Figure 3.4, where the bin width in MLT is 30 minutes. The total area underneath the boundary region and cusp curves is normalized to unity. Note in Figure 3.4 that the peak cusp probability is located before magnetic local noon at 11:00 magnetic local time (MLT). The centers of the boundary region probabilities are at 09:00 and 13:30 MLT. These times agree in principle with Figure 2.25.

The signatures identified as the boundary region and arch/cusp are a consistent occurrence in the data set, with the arch/cusp being seen 36 percent of the time, and the boundary regions are seen 65 percent of the time. The magnetic local times of the boundary regions agree fairly well with the satellite particle measurements seen in Figure 2.25. The cusp probability is located at magnetic times in between the two boundary regions but is offset from magnetic local noon towards the pre-noon hours. A detailed comparison of the ground-based observations of boundary region and cusp signatures with satellite particle precipitation data is the subject of the next subsection.

3.3.2 Comparison of ground based signature to satellite based signatures of the LLBL and cusp

Figure 3.5 shows the probability of observing the LLBL and cusp as obtained by DMSP particle precipitation, (P.T. Newell, Applied Physics Laboratory, personal communication, 1992). The upper panel of this figure shows the probability of observing the cusp in magnetic latitude versus magnetic local time (again using PACE coordinates). The lower panel shows the probability of observing the LLBL in the same format. In both cases, the total probability of detection has been

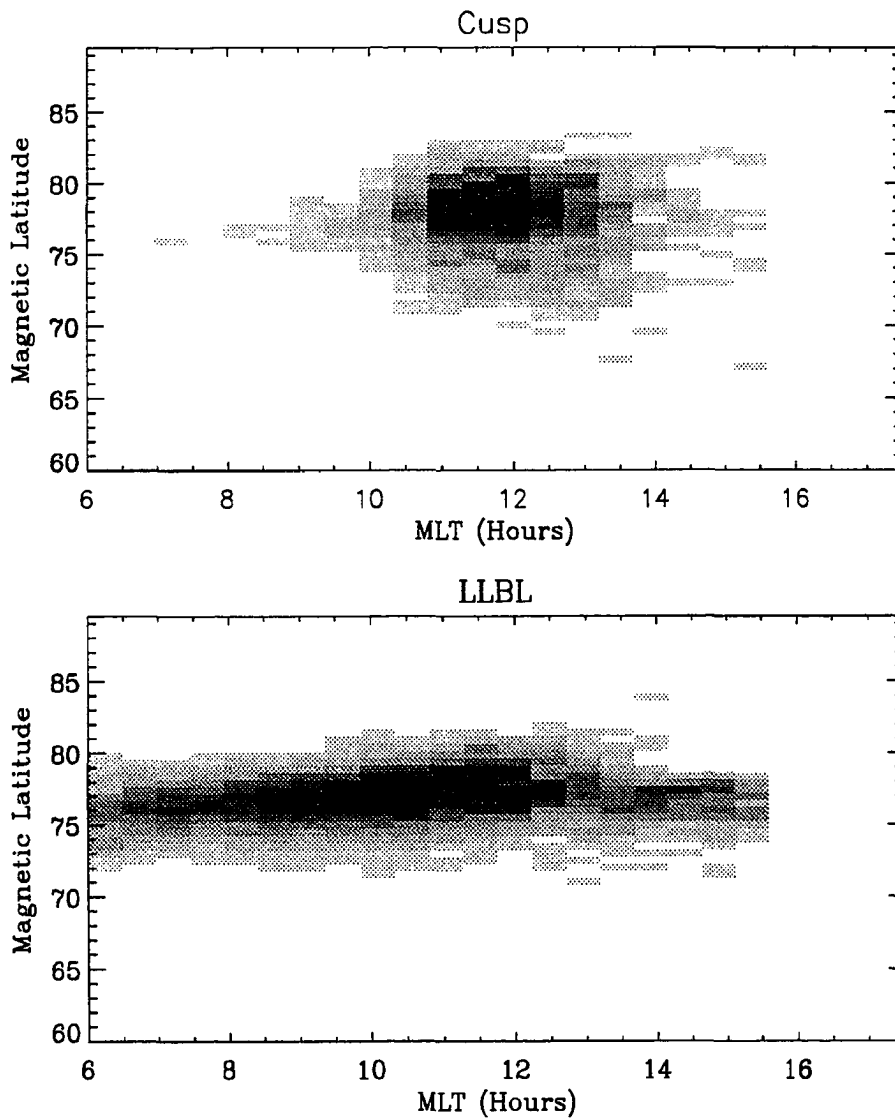


Figure 3.5. Probability distribution function in magnetic latitude versus magnetic time of the low latitude boundary region (LLBL) and cusp as observed by satellite measurement (courtesy of Dr P. Newell, APL). The darker regions have a higher probability of observation. The upper panel is the probability of detecting the cusp, and the lower panel is the probability of detecting the LLBL. A strong asymmetry about magnetic noon is evident in the probability of detecting the LLBL, while the probability of observing the cusp is seen to be approximately symmetric about magnetic local noon.

normalized to unity. Note that the LLBL probability is asymmetric with respect to magnetic local noon, while the cusp is symmetric with respect to magnetic local noon. The peak of the LLBL probability distribution is from 77-79 degrees latitude, and the corresponding latitude for the cusp is 78-80 degrees.

Figure 3.5 displays the probability distribution in both latitude and MLT. However, to compare the satellite observations to the magnetometer data requires that the probability distribution must be integrated in latitude so only the MLT dependence is left. This is because the magnetometer is a wide field of view instrument. To integrate the two dimensional particle precipitation data in latitude requires an assumption about the source geometry. The simplest geometry to analyze is that of a line current filament lying in a horizontal plane at some distance R from the station. The Biot-Savart law shows that the magnetic field at the station due to such a line filament is;

$$B = \frac{\mu_0 I}{2\pi R}. \quad 3.1$$

To integrate the latitude dimension out of Figure 3.5 we assume that the detected magnetic field comes from line filaments with the same probability distribution as given in Figure 3.5. Thus we obtain the probability of detection at the ground station versus magnetic time to be;

$$P(t)dt = \int_{Latitude} P(t, \theta) \cos(\theta - \theta_{station}) d\theta dt; \quad \theta = \text{degrees latitude}, \quad 3.2$$

where the $\cos(\theta - \theta_{station})$ term takes care of the weighting by inverse distance as prescribed in equation 3.1. The height of the line current is not included in this equation because the entire distribution is normalized to unity. Figure 3.6 shows the results of such an integration for the LLBL and the cusp. The station latitude used in equation 3.2 is 75 degrees magnetic, corresponding to the magnetic

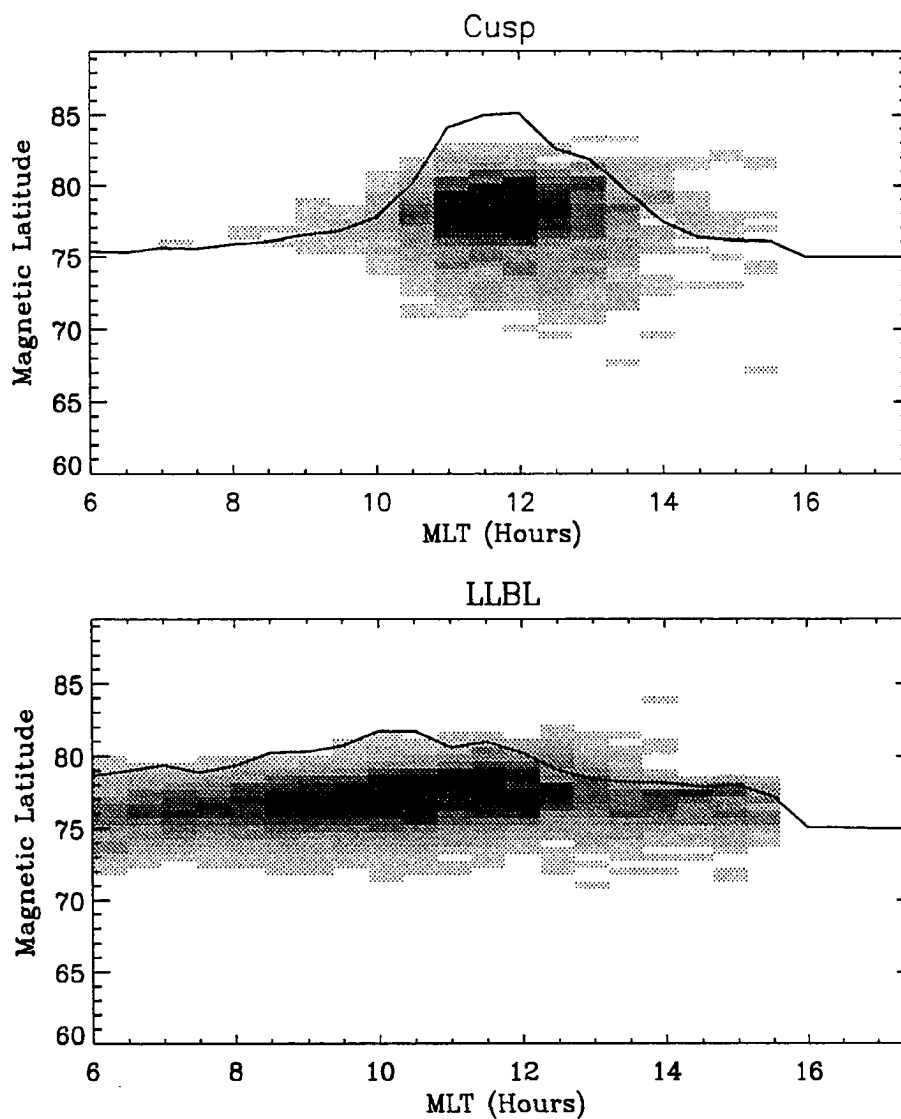


Figure 3.6. Latitude integrated probability distribution of LLBL and cusp. The distributions of Figure 3.5 have been integrated over latitude with an inverse distance weighting to account for an assumed line current distribution, see text for details. Note that the integrated probability distribution for the LLBL is strongly asymmetric about local magnetic noon, while the cusp is slightly asymmetric about magnetic noon.

latitude of the Svalbard. Note that the cusp probability distribution is slightly asymmetric about magnetic noon due to the integration over latitude, while the LLBL probability retains its basically asymmetric nature.

The ground-based and satellite based observations may now be directly compared. Figure 3.7 shows the probability of observing the ground-based signatures of the boundary regions and cusp along with the satellite based signatures of observing the LLBL and cusp. All the probabilities have been normalized to unity, and the satellite probabilities have been integrated over latitude as described in equation 3.2. Note that the shape and magnitude of the ground based signature of the cusp and the satellite-based signature of the cusp resemble each other, but the ground-based observations are offset pre-magnetic noon by about an hour. At this time this offset is not fully understood. It may represent a real offset in time of some current system with respect to the cusp, for example the high latitude DPY currents, [see *Friis-Christensen and Wilhelm, 1975*]. It may also represent a bias in the ground-based data due to the IMF state during the limited 253 days of data. This will be discussed late in Section 3.5

Inspection of Figure 3.7 shows the LLBL and boundary region probabilities do not greatly resemble each other in either shape or magnitude. It is interesting to note that the peak in the LLBL probability is roughly at the same local magnetic time as the peak in the ground based signature of the cusp. Thus we can see that the general comparison between the ground-based and satellite-based measurements is good for the cusp probabilities, while the comparison between the LLBL as defined by the satellite and the boundary regions as defined by the magnetic pulsations is not that good. This reflects the idea that the ground-based signatures of the boundary region are not correlated to the LLBL.

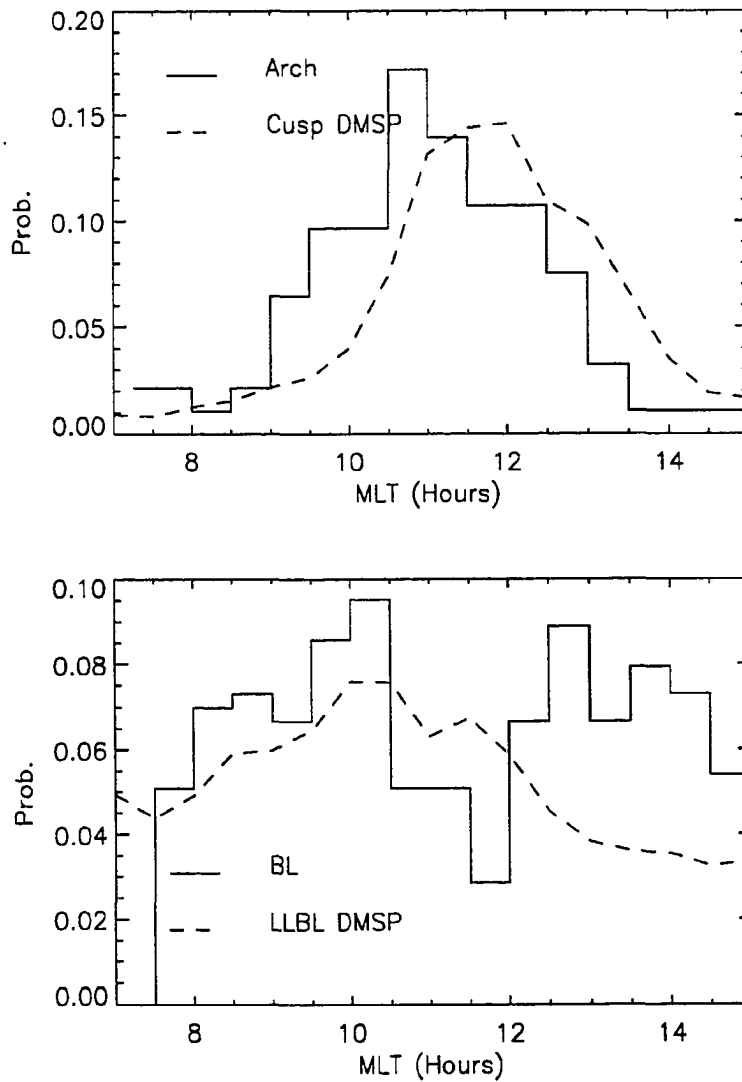


Figure 3.7. Comparison of ground based ULF signatures and satellite signatures of the boundary regions, cusp and LLBL. Note the satellite signatures have been integrated in latitude according to equation 3.2. The top panel shows the probabilities for the satellite and ground based cusp and the lower panel compares the LLBL and boundary regions. Note that the satellite and ground based signature of the cusp resemble each other in shape, but that the ground based signature of the cusp is offset by approximately one hour pre magnetic noon. The ground based signature of the boundary regions does not match well with the LLBL satellite signature.

3.4 Spectral categories observed in magnetic ULF observations

In addition to the ground-based signatures of the boundary regions and cusp, I have found that the observed spectra fall into five main spectral categories. The spectral shapes of these categories are defined below and the first three shown in Figures 3.8, 3.9 and 3.10.

Category 1: Distinct pre- and post- magnetic noon boundary layers with at least a 10 dB decrease in signal power above 20 mHz in the central cusp. An example is shown in Figure 3.8.

Category 2: No distinct boundary regions, but at least a 10 dB increase in signal power located around local magnetic noon. In some of these cases we see indications of one, but never both boundary regions. An example is shown in Figure 3.9.

Category 3: A combination of the above two features. Distinct pre- and post-magnetic noon boundary regions and significant signal power in the central cusp above 20 mHz. An example is shown in Figure 3.10.

Category 4: Extremely quiet, No significant increase in the signal power over the background level.

Category 5: Other, Those days which do not fit into the above four categories.

Table 3.1 shows the occurrence statistics for the five categories in the data set. As can be seen, categories 1 - 3 make up approximately 85 percent of the total data set. Because of this, I believe that the categories are representative of the entire data set seen during the winter cusp.

In addition to the basic statistic of the the times of the signatures of boundary region and cusp events I counted the actual number of arch/cusp events, and the

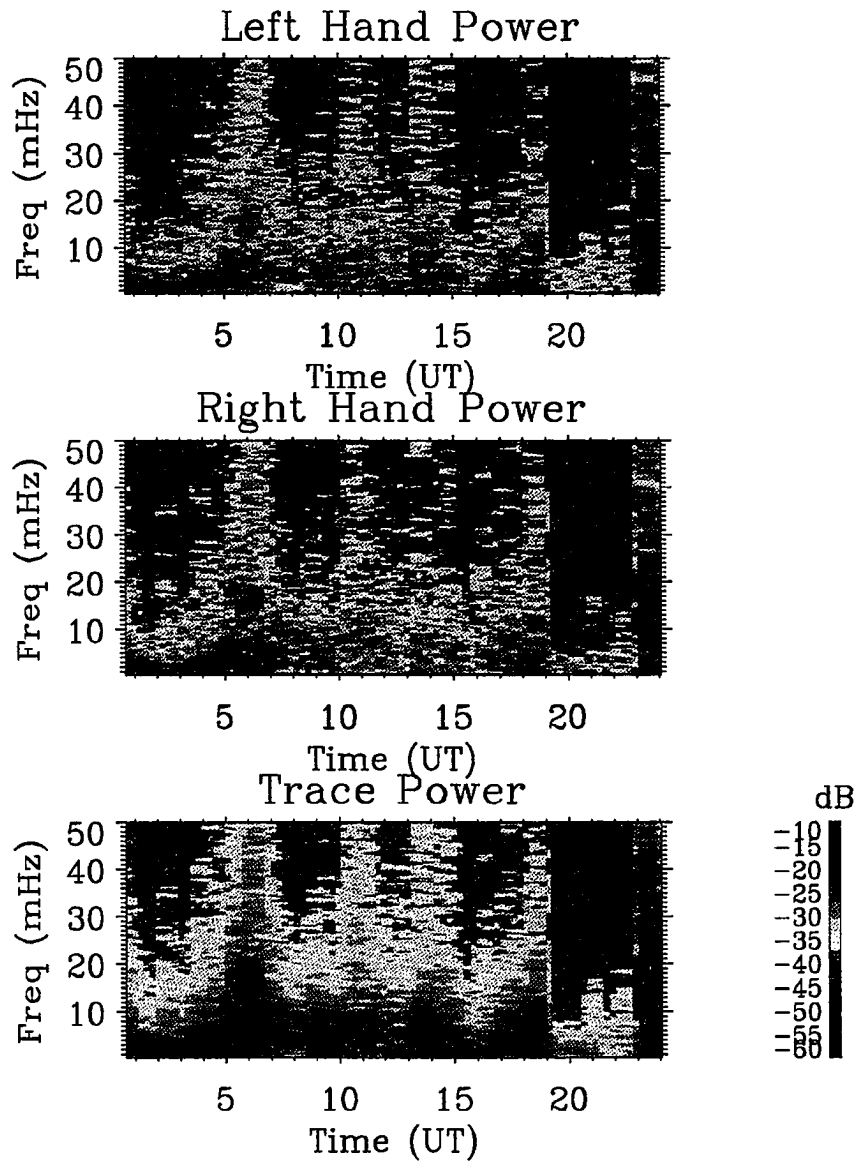


Figure 3.8. Example of Category 1 spectrogram taken at the winter cusp. The format is the same as in Figure 3.1. Notice that the boundary regions are prominent at 06:00 and 10:30 (UT) and there is a marked diminution in power at frequencies above 20 mHz between the boundary regions. The 9 January 1991 spectrogram fits into this category. The pre-magnetic noon boundary region is predominantly circularly right hand polarized.

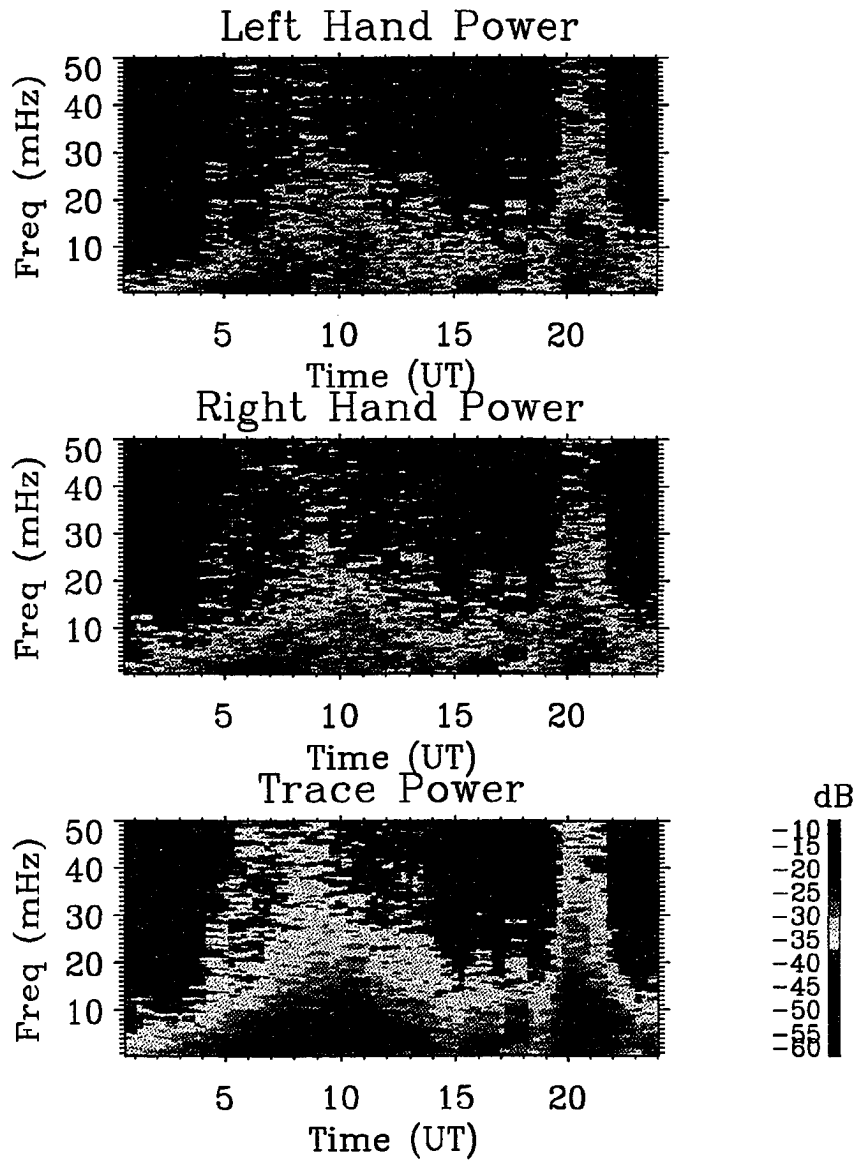


Figure 3.9. Example of Category 2 spectrogram taken at the winter cusp. The format is the same as in Figure 3.1. In this category no boundary regions are seen; rather a relative increase in the power at all frequencies is seen in the times around local magnetic noon. Again there is a dominance of circular right hand power in the spectra before magnetic noon.

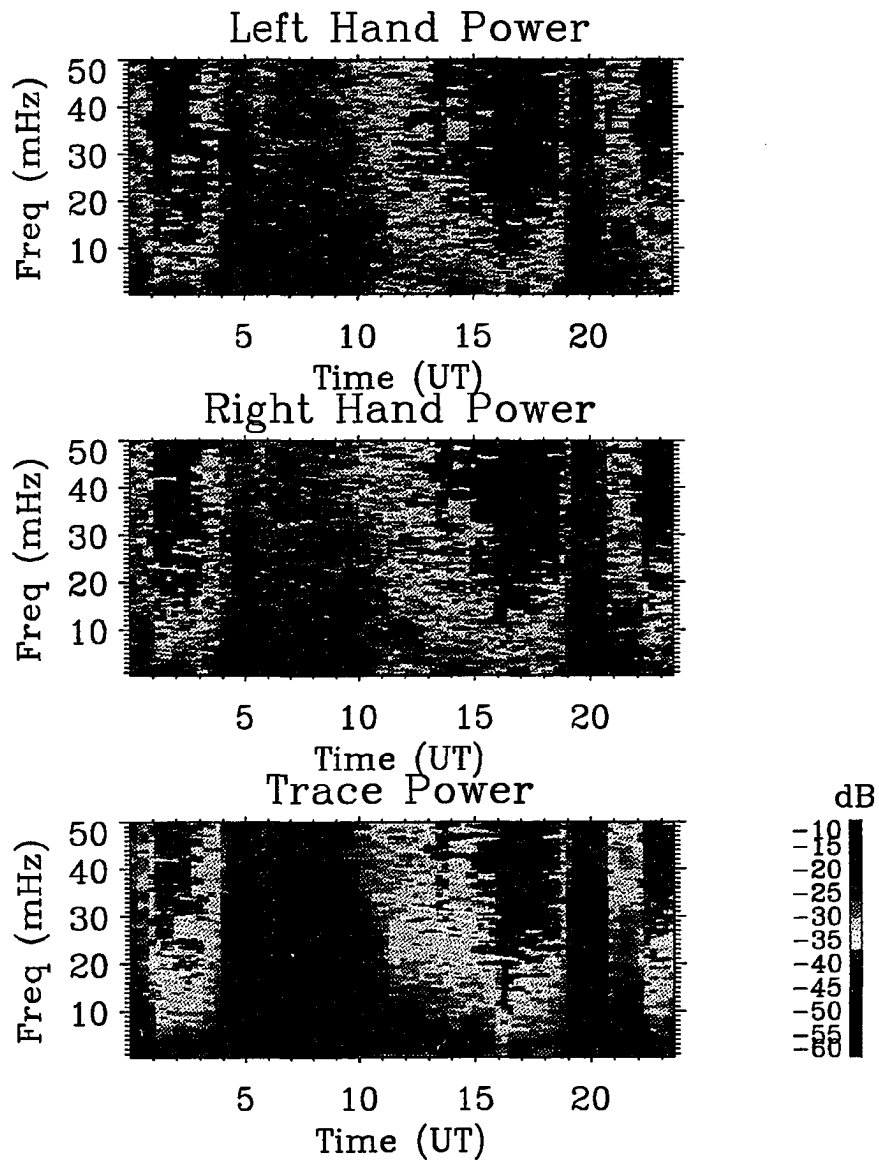


Figure 3.10. Example of Category 3 spectrogram taken at the winter cusp. The format is the same as in Figure 3.1. This category has features of both the previous categories. The boundary regions are observed in the spectrograms, but the higher frequency components retain broad band power during the times between the boundary regions.

TABLE 3.1. Occurrence Statistics of Spectral Categories

Category	Number	Percent of total
1	85	33
2	55	22
3	79	31
4	5	2
5	29	12

TABLE 3.2. Cusp signature and Pc3 Statistics, Percent Relative to Category

Category	Cusp	Pc3
1	48	55
2	30	42
3	44	78
Total	36	60

number of "Pc3" events. To be counted, the Pc3 event had to have signal power in the Pc3 band that was at least 10 dB above the ambient signal around it. Table 3.2 shows the occurrence of the cusp and "Pc3" type signals, again broken down by category. This table clearly demonstrates that these signals are common, with the cusp signature being seen approximately 40 percent of the time and the "Pc3" type event happening 60 percent of the time. Thus the 9 January 1991 event is not an isolated occurrence.

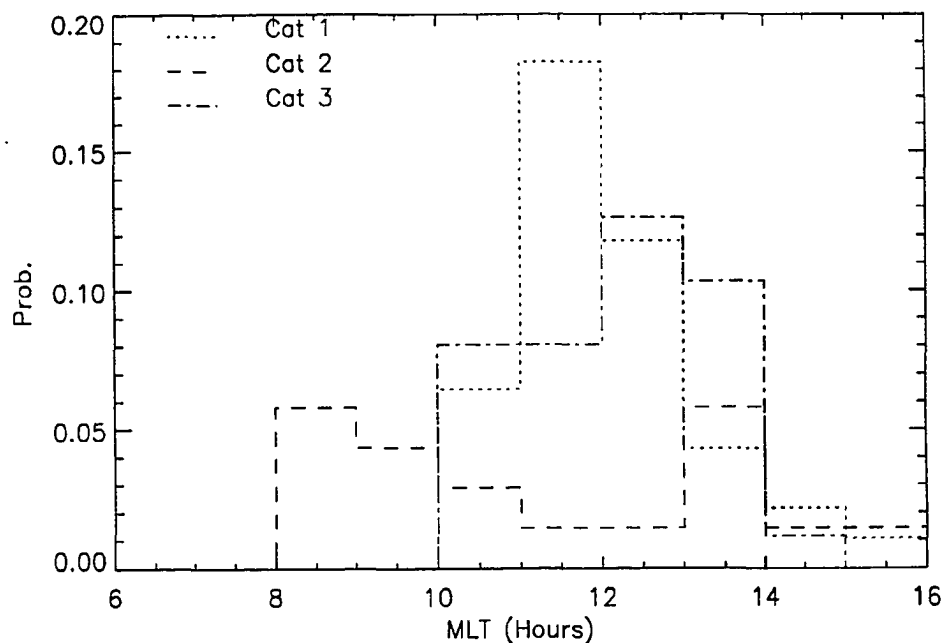


Figure 3.11. Distribution of cusp occurrences by spectral category. Note that category 2 is bimodal while categories 1 and 3 are single peaked. The area underneath each curve represents the relative contribution toward the total. The area underneath all three curves sums to unity.

To test if the probability of cusp occurrence shows any dependence on category type, the cusp occurrences are sorted by category and the occurrence probability plotted as a function of MLT. Figure 3.11 shows the results of this analysis. In this figure, we use the area underneath each category curve to represent the relative contribution to the total cusp distributions. In other words, the sum of the areas of the three categories is unity. Since there are fewer numbers in each category the bin width has been increased to 60 minutes. Note that Category 1 is narrow and single peaked, while Category 2 has a bimodal distribution, with a pre- and post-magnetic noon peak. Category 3 shows a single peak that is slightly wider in time

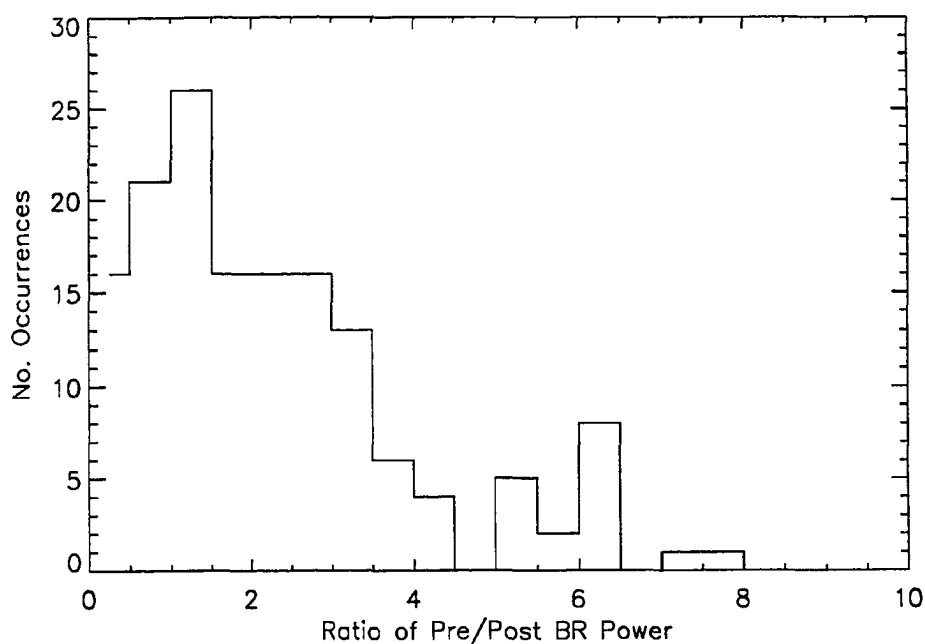


Figure 3.12. Ratio of the power in the pre-noon to post-noon boundary region. Note the peak of the distribution is above 1, thus the pre-noon boundary layer statistically has more power in the ULF fluctuations as observed at Svalbard.

than Category 1. Thus it seems that the temporal location of the cusp varies with category type, and to a lesser extent the width of the cusp varies with category type. For completeness, I also tabulated the occurrence statistics by category for the boundary region probability of occurrence, and find no particular differences between Category 1 and Category 3. Category 2 is not considered because by definition it does not have both boundary regions visible in the spectra.

One result of this study is that the power in the pre-noon boundary region is found to be larger than the power in the post-noon boundary region. This was evident in the single case of for 9 January 1991 as seen in Figure 3.1. To

demonstrate this statistically Figure 3.12 shows the probability distribution for the ratio of the pre- to post- noon boundary region power as obtained from the integrated spectra in the Pc5 band. When this ratio is larger than 1 the pre-noon boundary region has more power than the post-noon boundary region. Figure 3.12 shows that the pre-noon boundary region has more power in the perturbation magnetic field than the post-noon boundary region 90 percent of the time. Figure 3.12 also shows that the peak of the ratios distribution is between 1 and 2. Since there are a few very large ratios, the average of this distribution is 3.6 ± 8.6 . The pre-post noon asymmetry in pulsation amplitude has been predicted by several authors including *Lee and Olson* [1980] and *Lee et al.*[1981]. I believe this is the first time that such an asymmetry has been observed at cusp latitudes and described in terms of an actual difference in the ionospheric currents flowing in the boundary regions of the cusp.

3.5 IMF correlations with spectral categories seen in magnetic ULF observations

The categories established in the previous section are based on the general spectral shape seen during the dayside hours in MLT. To see if days in the same period have some measurable physical parameter in common, we turn to the solar wind interplanetary magnetic field (IMF) measurements during these days. Use of IMF correlations is traditional in cusp research, *Newell et al* [1989], but the assumptions behind such correlative studies deserves review.

Spreiter and Stahara [1985] show that the entire magnetopause streamline is defined by a spatially small streamline that comes through the bow shock within a small radius of the subsolar point. Thus a measurement of the IMF along this streamline should be representative of the IMF over the entire magnetopause. If

the exchange of energy, mass and momentum between the solar wind and the magnetosphere is dominated by magnetic reconnection, then this IMF orientation is obviously an important parameter to measure. For instance, *Crooker* [1979] believes that the locus of points on the magnetopause where the IMF is antiparallel to the dipole field is the location with maximum merging rate. The entire magnetopause is mapped to the cusps by the magnetic field topology, so it is logical to think that the ionospheric cusps are a location to look for direct IMF correlations. This line of reasoning is the basis for looking for IMF correlations with ground-based observations.

I think it is important to treat such studies on a statistical basis for the following reasons. First: the location of the measuring satellite is almost never along the subsolar streamline, thus a correlation with a measurement off this streamline requires the assumption that the coherence length of the IMF is the same size as the distance the satellite is off the earth sun line. *Le and Russell* [1992] show an example where this assumption is false. *Le and Russell* [1992] show that if the satellite is in the foreshock region as defined by *Greenstadt and Baum* [1986] then the IMF measurements are clearly different from that found at the subsolar point. Second: the bow shock modifies the IMF as it passes into the magnetosheath, and modeling of the exact nature of this modification is in its infancy, again see *Spreiter and Stahara* [1985]. The third reason is that to compare IMF data with ground-based data in a one-to-one correlation will require that the travel time for the IMF from the point of measurement to the ionosphere be known. Due to the problems reviewed above, the exact offset time would be difficult to calculate exactly, however an estimate is in order. The solar wind speed is known to normally be in the range of 300-800 km/sec, [*Parks* 1991], and the IMP-8 satellite used in this correlative study has an orbit that reaches upstream to about 30 earth radii (R_e). Picking a solar wind speed of 630 km/sec gives 6 R_e /minute. Even though the speed is

greatly decreased across the bow shock, and must include an Alfvén transit time to reach the ionosphere, a 15 minute offset time seems to be a good first estimate. This offset time has also been used by *Sandholt et al.* [1986b], *Rishbeth et al.* [1985] and *Lockwood et al.* [1986]. The offset time problem is alleviated if the IMF is treated on a statistical basis over several hours of time. This is because errors in the offset time of 15 - 30 minutes are small compared to the several hours over which the data are considered. The problems of coherence length of the measurement off the streamline, and modification of the magnetic field geometry by the bowshock seem more intractable, and I can only offer the hope that if a correlation is found then somehow these problems are alleviated and the analysis is worth the effort.

The magnetometer measurements used were supplied by NSSDC, and come from the IMP-8 satellite from the periods November 1990 through July 1991. The data were measured by a three axis magnetometer, and the data collection rate is one sample every 15.4 seconds. Of the 253 days used in the ground based study, only 36 overlap with the available IMP-8 data due to the spacecraft orbit. This still gives a representative look at all the categories described above, with the coverage by category given in Table 3.3.

The IMF data were binned into histogram format for each component magnitude in all three GSM coordinates with bin widths of 0.2 nT. The frequency of occurrence of these bins are collected for the periods under study. The times used in the frequency histogram were different for each category, but the criteria for choosing these times remains constant within each category. The time periods and the criteria for choosing them, are given in Table 3.4. In all cases the IMF times were offset by 15 minutes to account for the travel time from the measurement to the ionosphere.

Figure 3.13 shows the GSM component histogram for the entire data set. Note that the Bx component is bimodal, with the larger peak centered around + 3nT,

TABLE 3.3. IMF Coverage broken down by ground-based spectral category

Category	Number of days of IMF coverage
1	11
2	9
3	12
4	3
5	1
Total	36

TABLE 3.4. IMF time selection criteria for ground-based spectral category

Category	Criteria for Selecting Times
1	From pre-noon to post-noon boundary region
2	± 1 hour from time of maximum power
3	Same criteria for category 1
4	± 2 hours from magnetic noon
5	Same criteria for category 4

while the B_y component is strongly negative. This large negative B_y component is a possible reason why the ground-based probability of observation of the cusp is approximately one hour earlier than the satellite-based observation of the cusp, see Figure 3.7. *Newell et al.* [1989] show that a B_y negative component moves the cusp toward the dawn hours when B_z is negative. A similar trend is found by *Aparicio et al.* [1991] who find that the sign of B_y independent of B_z can move the

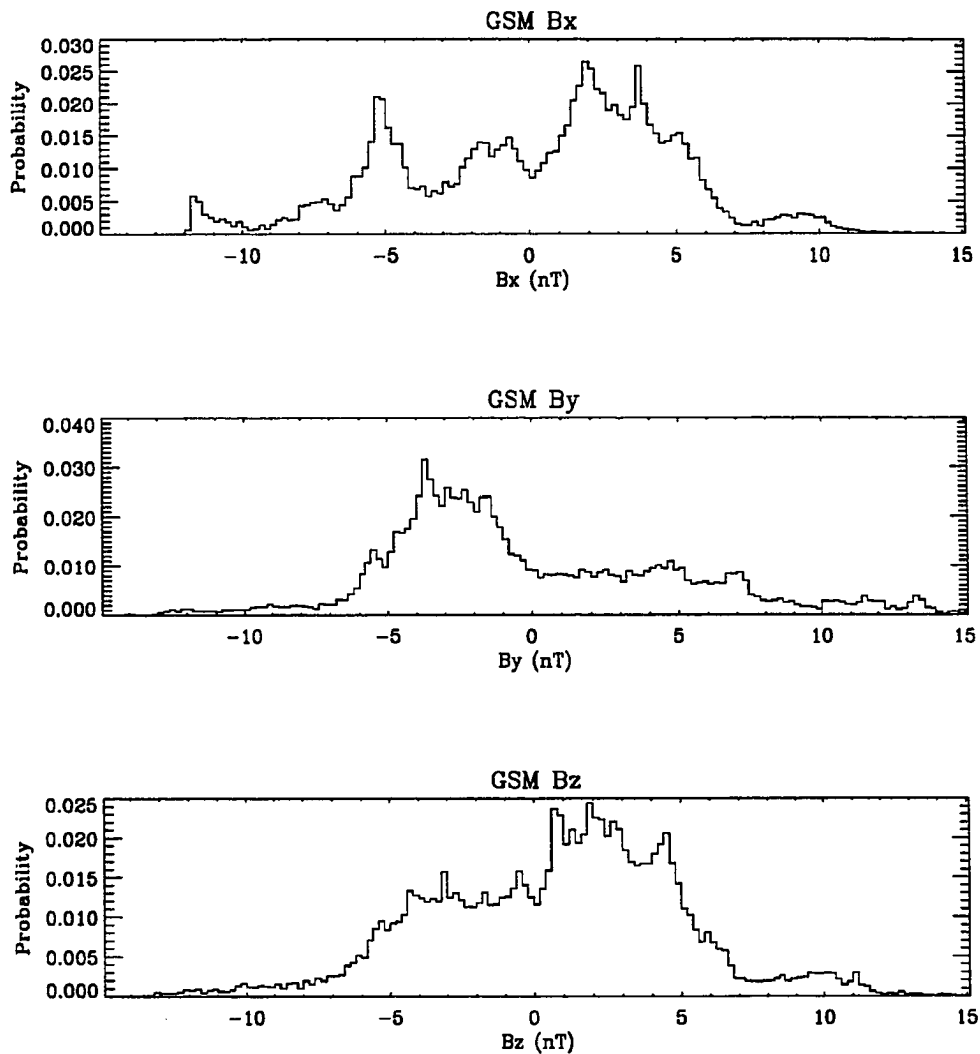


Figure 3.13. IMF GSM Component Histogram for all five categories. The top panel is the GSM X component, the middle panel is the GSM Y component, the bottom panel is the GSM Z component. Note that all three components show some level of occurrences between ± 5 nT. The Bx component is bimodal, with the larger peak centered around +3 nT. The By component is strongly negative, suggesting that during this period the earth is above the sun's current sheet. The Bz component is asymmetric about zero, and has a peak centered about +3 nT.

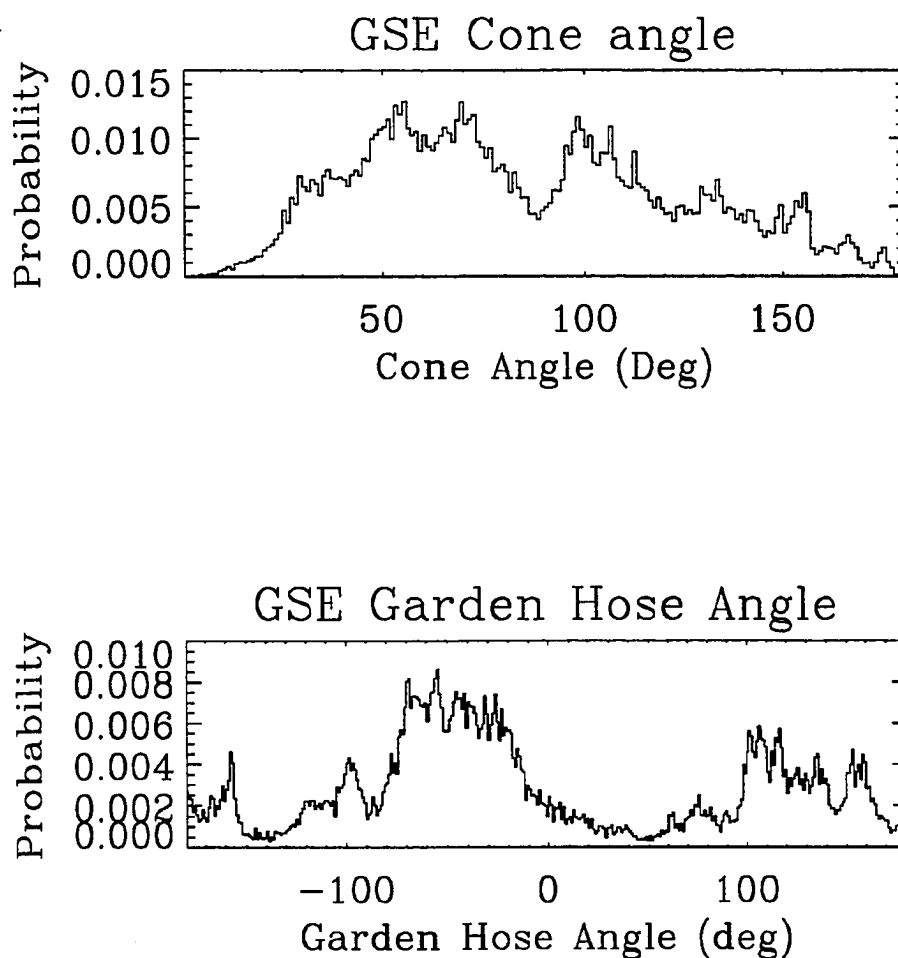


Figure 3.14. IMF GSE Angle Histogram for total data set. The upper panel shows the cone angle histogram for the entire data set, while the lower panel shows the “garden hose” angle in the GSE X-Y plane for the entire data set. Note that the garden hose angle histogram shows that this data set is centered around -50 degrees, with a smaller peak centered around +120 degrees. The relative size of the peaks shows that this period was dominated by a toward sector, which agrees very well with the GSM X and Y components shown in Figure 3.13.

cusp in magnetic local time. *Aparicio et al.* [1991] also find that the cusp moves to earlier MLT's for a negative B_y component. I interpret the large peaks centered around +2.5 nT in X and - 3. nT in Y as a manifestation of the Parker spiral for this period. This is confirmed in Figure 3.14 which shows the cone angle and the "garden hose" angle for the entire data set. The garden hose angle is simply the angle the IMF makes in the GSE X-Y plane as it crosses the Earth's orbit, [Parks, 1991]. The angle is measured counter clockwise positive from the plus X direction, so the large peak seen at -50 degrees corresponds to a period when the IMF is coming up from the ecliptic south, and heading towards the sun. This is consistent with the earth being above the IMF ecliptic current sheet. The cone angle is the angle between the GSE X axis and the magnetic field direction, θ_{xB} , and is defined as;

$$\theta_{xB} = \cos^{-1} \left(\frac{B_x}{|B|} \right). \quad 3.3$$

Figure 3.15 shows the IMF histogram for the days where the ground based ULF spectral category was 1. The B_x component is distributed in three large groups, and shows no real trends. The B_y component is dominated by magnitudes less than zero, or towards the dawn side of magnetopause. More interesting in Figure 3.15 is the B_z component. Note that the distribution in the B_z component is asymmetric about zero, with values larger than zero dominating values less than zero. This seems to indicate that the Category 1 days are the B_z north state of cusp ULF pulsations. The chief features of the category 1 days are the observation of the boundary regions and the relative decrease in power above 20 mHz for times between the boundary regions. If the B_z north state is accepted as the quiet state of the magnetosphere then the Category 1 spectra would seem to reflect this quiet state, and the other categories are then perturbations on this quiet state.

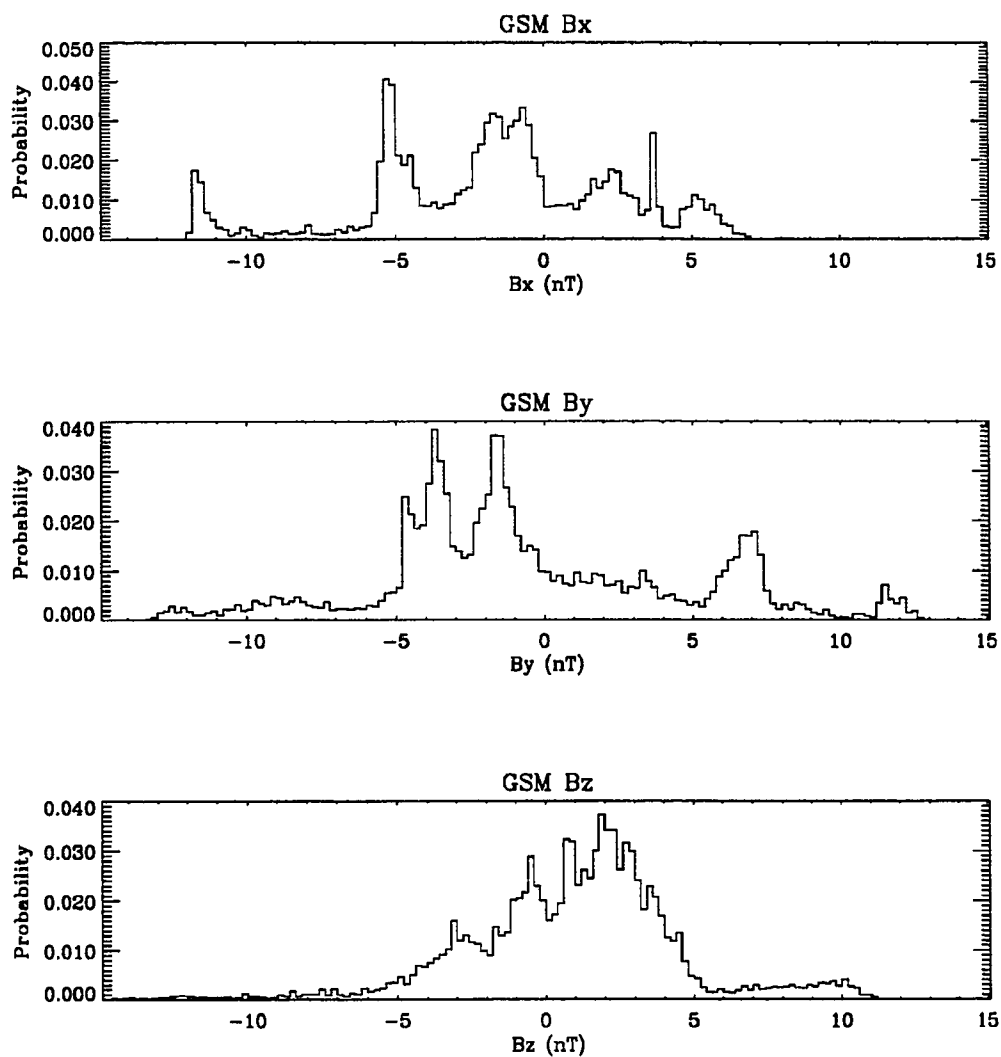


Figure 3.15. IMF GSM Component Histogram for Category 1. The format is the same as Figure 3.13. Note that for this category the GSM z component is asymmetric about zero, with the B_z greater than zero occurrences having a center value of approximately 2 nT.

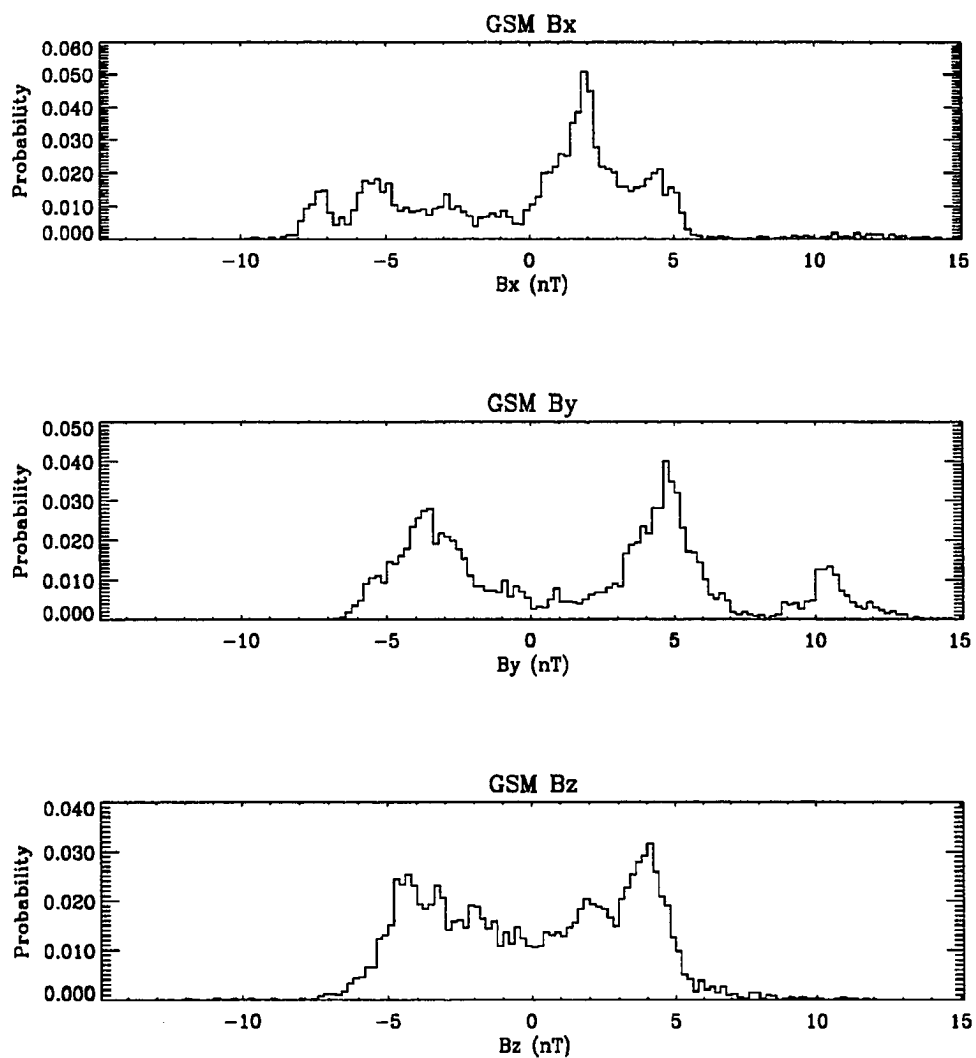


Figure 3.16. IMF GSM Component Histogram for Category 2. The format is the same as Figure 3.13. Note that the Bz component is bimodal, with two distinct peaks at roughly ± 4 nT. The By component is also bimodal and peaks at approximately +5 nT and -4 nT.

Figure 3.16 shows the component histogram for spectral Category 2. Note that the B_z and B_y component are bimodal, while the B_x component shows a single peak around $+2nT$. These are clearly times when the B_z and B_y components are within a certain range. The main feature in spectral Category 2 was that the boundary regions were not both present and that there was power above 20 mHz. The large B_y excursions could explain why both the boundary regions were not seen on these days. *Friis-Christensen et al.* [1985] show that the high latitude ionospheric currents in the cusp region, which they label the DPY currents, show a strong azimuthal variation with B_y . Thus the large B_y components associated with the Category 2 days cause an azimuthal shift in the ionospheric current system responsible for the pulsations and one or the other of the boundary regions are not present.

Figure 3.17 shows the GSM Category 3 histogram. The main difference between this and Category 1 is that the the Category 3 B_x component is single peaked around 4 nT. The main difference in the ground-based ULF spectrograms is that the Category 3 spectra have significant power in the frequencies above 20 mHz at times between the boundary regions. The explanation for this difference is found in Figure 3.18 which shows a histogram of the cone angle for each Category.

Figure 3.18 shows that the cone angles for Categories 2 and 3 are similar in that they have a relative minimum around 90-100 degrees, with relative maxima on either side of this minima. Category 1 on the other hand has a large peak that is centered around 100 degrees. As noted in the introduction *Greenstadt* [1972] showed that the bow shock is turbulent in the quasi-parallel shock geometry. The magnetosheath is seen to fill with ULF noise when in this geometry, see *Russell et al.* [1983], and *Luhmann et al.* [1986]. *Engebretson et al.* [1987] use satellite measurements in the magnetosheath and upstream of the bow shock to show that broad band compressional waves are detected in the 10-100 mHz frequency band near

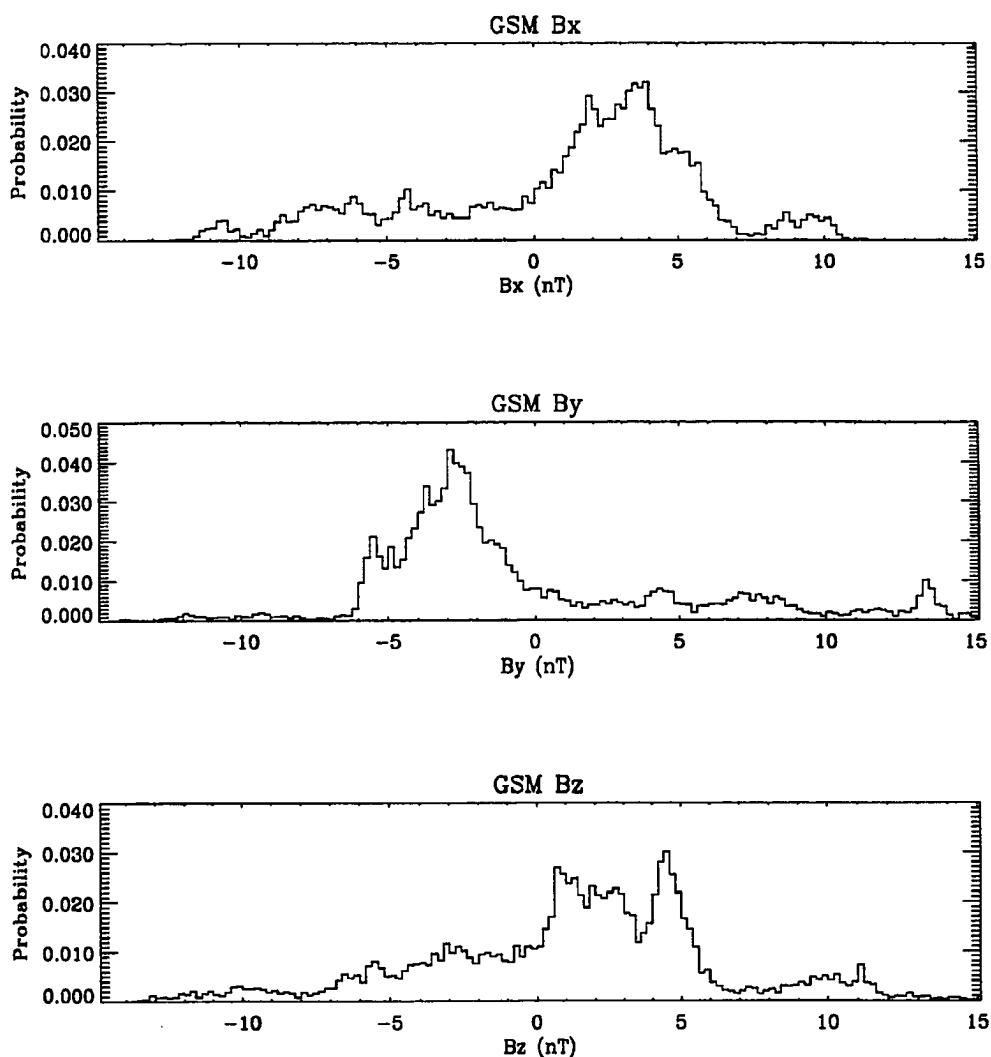


Figure 3.17. IMF GSM Component Histogram for Category 3. The format is the same as Figure 3.13. Note that all three components are single peaked. The Bz and Bx components are strongly positive, while the By component is strongly negative.

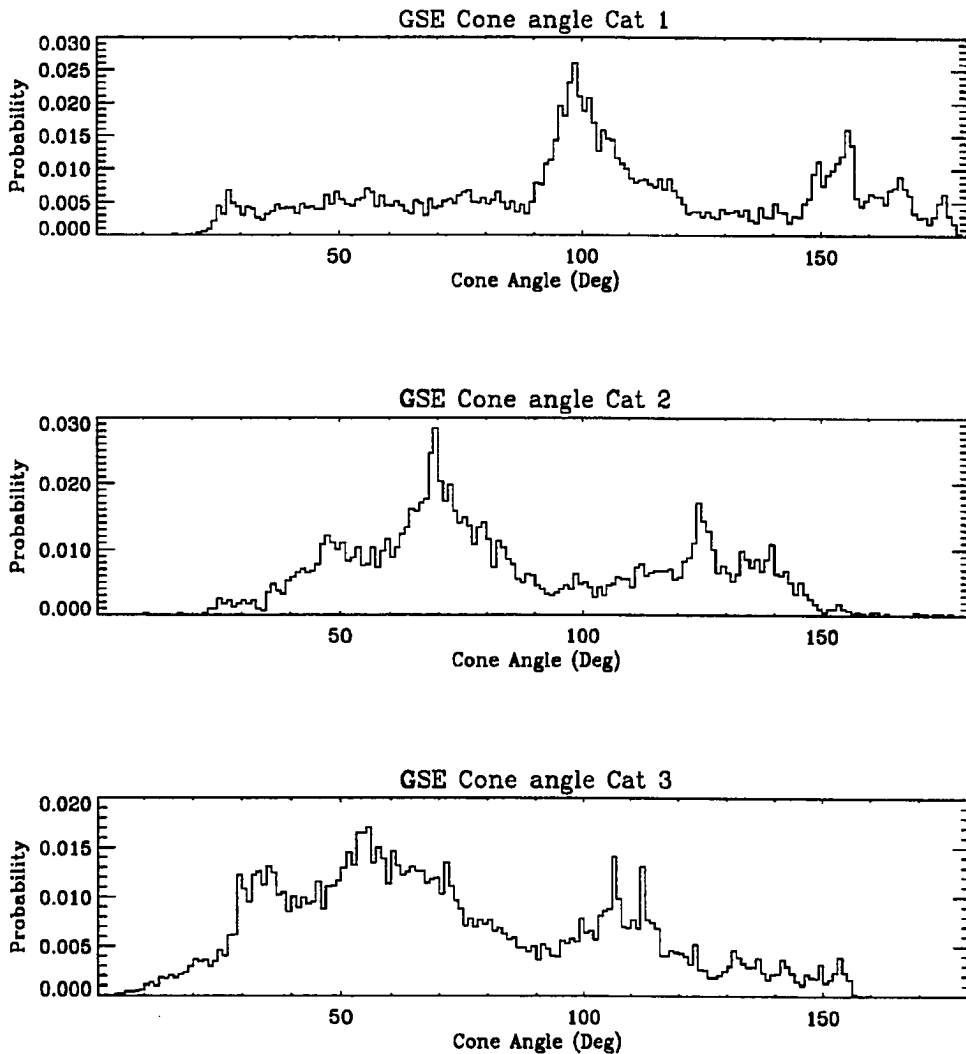


Figure 3.18. GSE IMF Angle Histogram for Categories 1-3. The cone angle for Categories 1-3 is shown in the upper, middle and lower panels respectively. The cone angle is the angle the magnetic field makes with the GSE X axis. Note that for Category 1 the main part of the distribution is centered about 100 degrees. For Categories 2 and 3 there is a relative minimum in the distribution of occurrences at 90-100 degrees. This makes Category 1 a quasi-perpendicular shock, and reduces the amount of wave activity produced in the upstream bowshock. Categories 2 and 3 are more quasi-parallel shocks, producing more wave activity, which results in the ULF Pc-3 power observed in the cusp.

magnetic local noon and are correlated to small cone angles in the IMF. *Engebretson et al.* [1987] attribute these broad band compressional waves to destabilization of the bow shock due to the quasi-parallel geometry of the magnetic field with respect to the bow shock. While the distribution of angles shown for Categories 2 and 3 would not for the most part be considered quasi-parallel at the nose of the bow shock, they are clearly more quasi-parallel than Category 1. It seems that the presence of broad band wave activity in the periods between the boundary regions correlates with intermediate cone angles in the IMF.

Figure 3.19 shows the GSM histogram for the Category 4 days. The ground-based ULF pulsations show very quiet spectra during these days. This is understood by the very large positive and negative values of the B_z component seen in Figure 3.19. These large B_z values move the dayside oval equatorward or poleward, and out of the field of view of the magnetometer. These days are very rare, Table 3.1 showing that they happen only 2 percent of the time. Figure 3.20 shows the histogram for the single Category 5 day that also has IMF data. The ground-based spectrogram resembles a confused Category 3. This is understood when looking at Figure 3.18, which shows the extreme variability in the B_z component. The IMF is unsteady enough during this time that the resulting spectrogram does not easily fit into the usual patterns observed. Table 3.1 shows that this type of spectrogram is observed 12 percent of the time.

3.6 Discussion

The signatures of the boundary regions and the arch/cusp make up a consistent way to order the data. Even if the source of the signatures described is not associated with the boundary regions or cusp, the data are still found to follow this pattern. I have shown that this pattern occurs on a daily basis, and the probability of finding the features identified as boundary region or cusp fall within a fairly

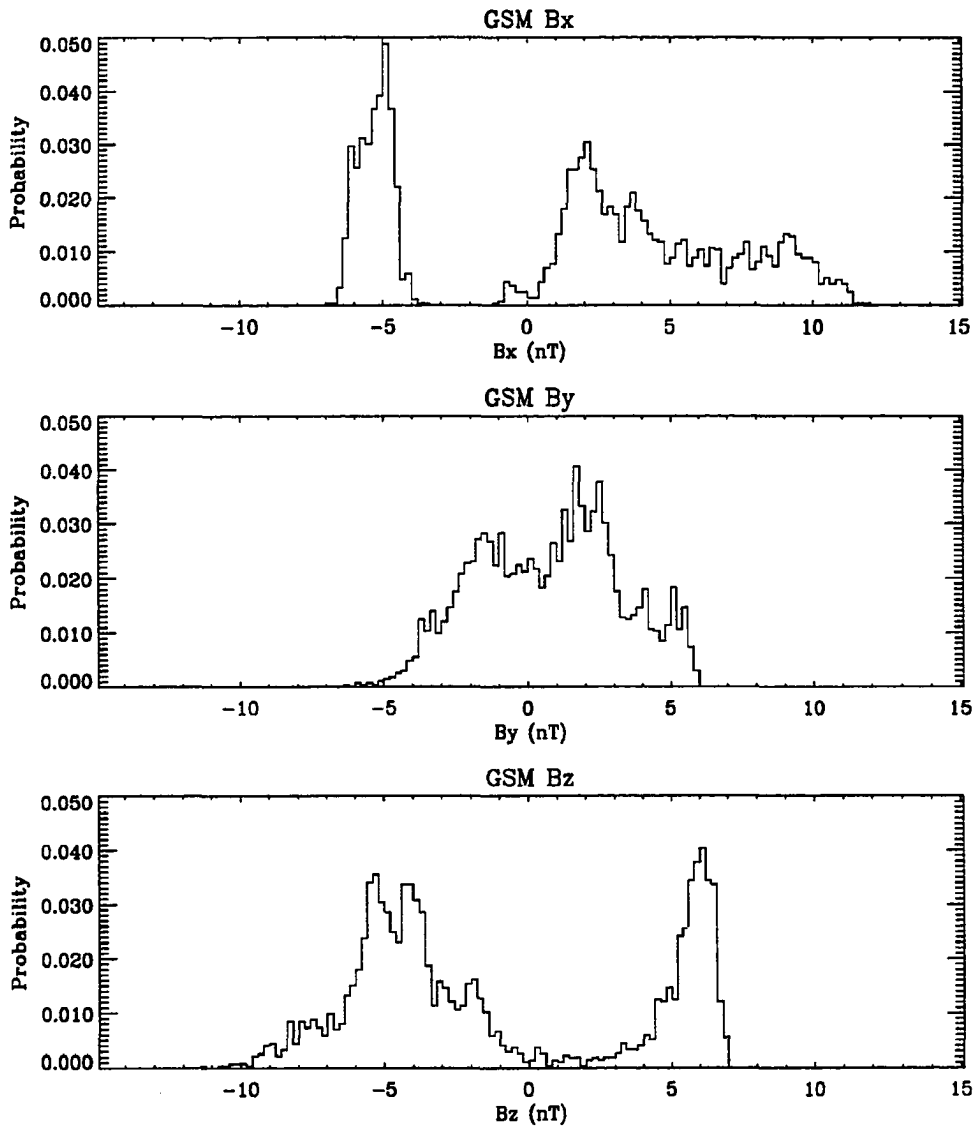


Figure 3.19. IMF GSM Component Histogram for Category 4. The format is the same as Figure 3.14. Note the extreme values of the B_z component. The ground-based ULF pulsation spectrograms show very little activity on Category 4 days. The large values of B_z move the cusp in latitude equatorward or poleward, and result in the quiet pulsation spectra on the ground.

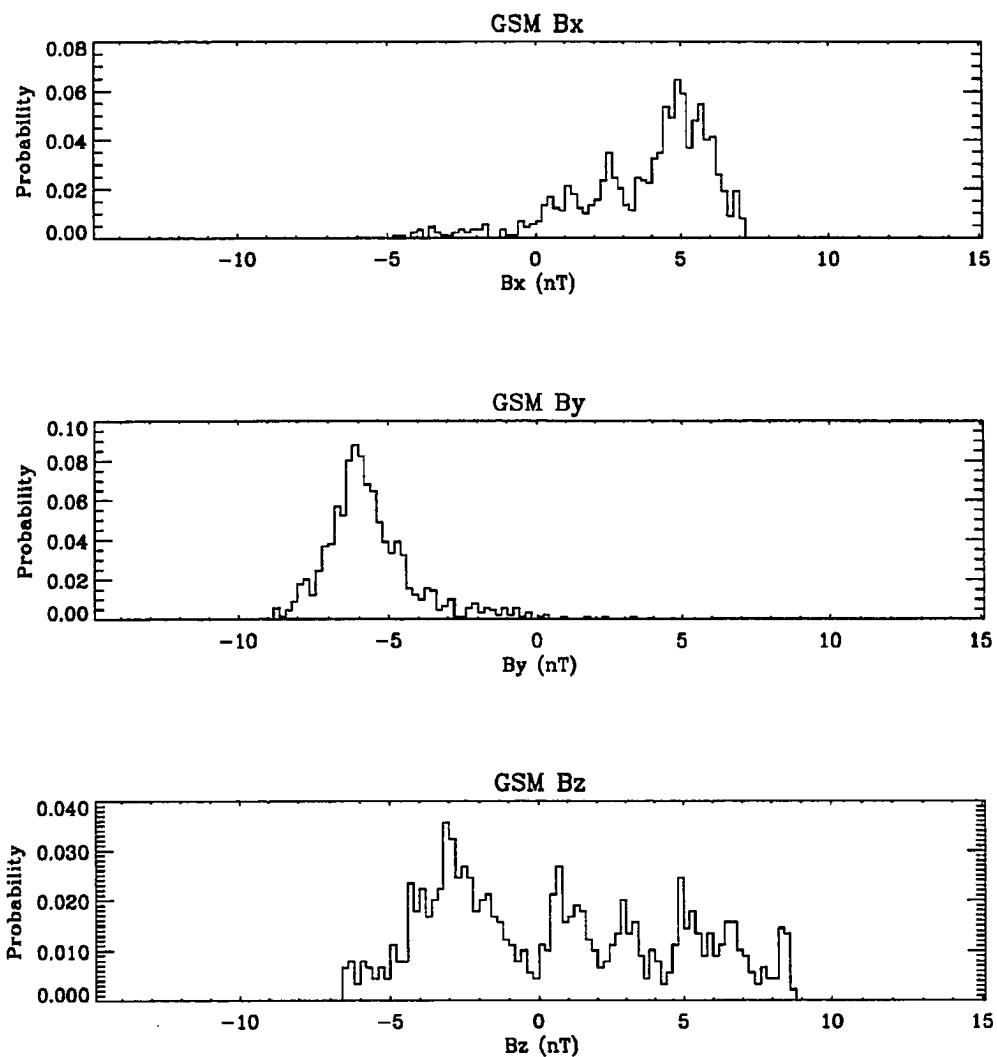


Figure 3.20. IMF GSM Component Histogram for Category 5. The format is the same as Figure 3.14. The groundbased ULF pulsation spectrogram for this day shows a distinct pre-noon boundary layer, and then a large amount of power at frequencies above 10mHz during the rest of the dayside hours. The IMF histogram shows that the Bz component was extremely variable for this day.

narrow window in MLT. This identification is useful when correlative studies are undertaken as exemplified by the IMF correlation presented earlier. Further, the probability distribution versus MLT of the arch/cusp is in rough agreement with the satellite data of *Newell and Meng* [1992].

In addition to the basic identification, I have shown that about 85 percent of the daily spectrograms fall into one of three categories. These categories represent different states of the current systems in the high latitude ionosphere, and by inference represent different states of the dayside magnetosphere. The following is a summary of these states based on the correlative IMF study.

Category 1 represents the quiet state of the dayside current system. The histogram of the GSM components, see Figure 3.17, shows that the B_z component is asymmetric and favors positive values. The cone angle is seen in Figure 3.18 to have a large maximum at 100 degrees. This makes a perpendicular bow shock which is unlikely to be accompanied by ULF noise in the Pc3 range, see *Greenstadt* [1972], *Russell et al.* [1983], and *Luhmann et al.* [1986]. The spectrogram for this category is characterized by a boundary region that is more intense in the morning than in the afternoon, and has a distinct minimum in power above 20 mHz in the central cusp.

Category 2 is thought to be an azimuthally rotated current system due to the large values of B_y in the GSM component histogram of Figure 3.18. *Friis-Christensen* [1985] show that the effects of B_y variations in the IMF are to cause an increase in the ionospheric currents on one side or the other of magnetic noon preferentially with the sign of B_y . Thus the relative increase in signal amplitude seen at our one station around local magnetic noon is seen as an azimuthal rotation due to the B_y effect.

Category 3 has power in the Pc3 frequency band near the cusp because the cone angle is small. This causes the bow shock to destabilize, see *Greenstadt* [1972], and

the magnetosheath to fill with compressional Pc3 wave activity, see *Engebretson et al.* [1987]. This causes Pc3 activity in the cusp, see *Engebretson et al.* [1990], and accounts for the increase in signal seen in the central cusp periods for this category.

It is interesting that no category was found with a predominately Bz south IMF, which would be expected for a state driven by reconnection. Analysis of the IMF data reveal that there is no statistical difference in the IMF between the days that have an arch and those days with no arch. If the arch is to be associate with reconnection at the dayside magnetopause then this observation seems to indicate that the amount of time the IMF Bz component is negative is not statistically important. However the arch may not be a direct result of reconnection, but rather the vibrating of the last closed field line on the magnetopause. I will return to these two possibilities in further detail in Chapter 4.

This chapter has shown that the ground-based ULF pulsation spectrograms are correlated with the optical data in a consistent manner, and that taken as an entire data set, give a broad description of the dayside morphology as seen at cusp latitudes. The three main spectral categories observed in the ULF pulsations are seen to have different IMF distributions. The next chapter turns from this morphological view of the dayside ULF spectrum and concentrates on specific quantitative measurements taken from the time series of individual days.

CHAPTER 4

Analysis of cusp magnetic observations

In this chapter, I will concentrate on the cusp magnetic spectrum and time series, and look at the possible sources of the magnetic perturbations. The morphological categories described in Chapter 3 are used to order the observations. This allows us to differentiate the signals observed during the boundary region passage from those which occur when the cusp was in the “field of view” of the magnetometer.

The first two sections of this chapter deal with the power spectrum of the cusp ULF perturbations. I find that the spectral amplitudes can be fitted using a power law dependence on the frequency, and the spectral index of this fit is found to vary with the solar depression angle. This analysis suggests that there exists a preferential geometry for transmission of higher frequency ULF perturbations during the course of the year with the summer cusp having larger high frequency amplitudes. The third section presents the magnetic perturbations in the time series format. The fourth section of the chapter covers the temporal coherence length of the observed magnetic pulsations in the boundary regions and central cusp. I will show that the boundary regions have large amplitude pulses, and these pulses are phase incoherent with each other. The central cusp is characterized by phase coherent pulses which form wave trains, and are separated by the appearance of intense field aligned currents on the equatorward edge of the cusp. The fifth section discusses the origin of the pulsations observed, and tries to put the observations into context of overall knowledge about the cusp. The sixth section is a summary of the important findings in this chapter.

4.1 Study of cusp ULF power spectra

In this section, I analyze the power spectra for 315 days spanning October 1990 to April 1992. This is the same data set used in Chapter 3, with an additional 62 days of data from February to April 1992. *Olson* [1986] first published the observed power spectra of the cusp ULF perturbations, and noted that the data between 1 mHz and 1 Hz are fit with a power law distribution of $f^{-2.6}$. This power law fit represents an ensemble average over 237 days taken at Cape Parry Canada centered around the summer of 1983. The rms fluctuation of the ULF perturbations was found to be 5.9 nT, yielding an rms current variation amplitude of 2.9×10^3 A. Assuming a resistance of the cusp ionosphere of a few ohms, *Olson* [1986] finds the joule heating in the ionospheric cusp to be on the order of 4×10^7 W.

I calculated the power spectral density for the entire data set, using the time periods as described in Table 3.4. Using the criteria outlined in Table 3.4 has the benefit of allowing the distinction between the boundary regions and cusp to be made, and is the major difference between this study and *Olson* [1986], who binned all 237 days into magnetic local time irrespective of variations of cusp location in magnetic time.

Figure 4.1 shows the power spectral density (psd) covering a six hour time span on 9 January 1991. The upper panel is derived from the induction coil magnetometer, while the lower panel is derived from the fluxgate magnetometer. In both panels, the psd is shown on a log-log graph, with the best fit line between frequencies of 1 and 50 mHz plotted over the actual psd. I will refer to the slope of this best fit line as the spectral index. Note that the slope of the fluxgate psd decreases towards zero above 10 mHz. This is an artifact of the instrument. This response can be compared to the induction coil magnetometer and shows that the induction coil magnetometers are more sensitive at higher frequencies. These

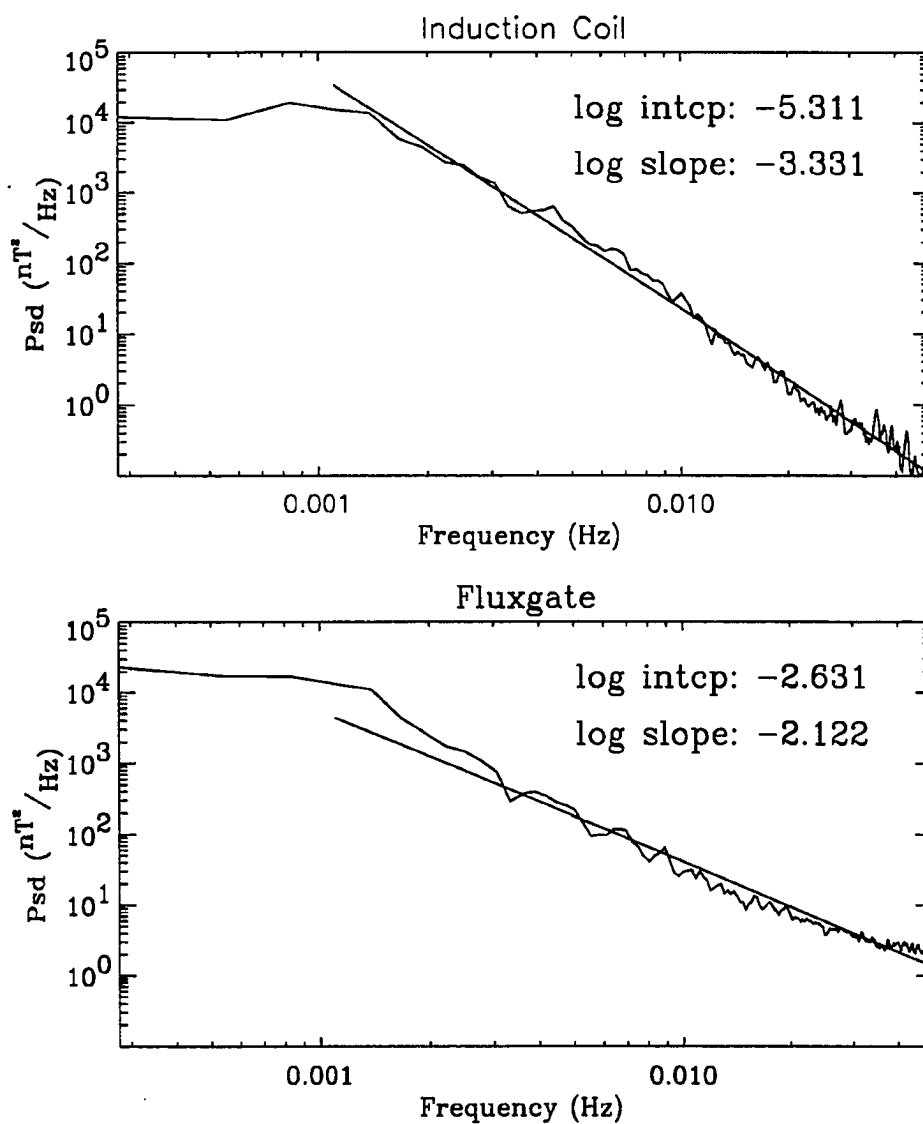


Figure 4.1. Example of power spectral density and power law fit for 9 January 1991. This power spectral density is the average of 6 hours worth of data lasting from 05:52 to 11:52 UT. The data are presented on a log-log scale, with the best fit line from 1 - 50 mHz shown plotted over the actual psd. The upper panel is derived from the induction coil magnetometer, and the lower panel is derived from the fluxgate magnetometer. Note the psd for the fluxgate magnetometer flattens at higher frequencies.

differences in the frequency response between the induction coil magnetometer and the fluxgate magnetometer led me to use the induction coil in all the studies that dealt with the psd of the magnetic fluctuations.

· Using Parseval's theorem, the total variance in the original time series data can be found by integrating over frequency in the psd, [(see *Jenkins and White* 1968)]. Such an integral results in a total variance in the 1 to 50 mHz range of 12.7 nT^2 or an rms variation of 3.55 nT. This is slightly less than *Olson* [1986], who found an rms variation of 5.9 nT. These field amplitudes are equivalent to that which would be produced by a line current of approximately 1800 Amps if the line current were 100 km away or 3400 Amps if the line current were 190 km away. These estimates are determined by using Equation 3.1. *Hardy et al.* [1987] gives a height integrated Pederson conductivity value on the noon-midnight meridian plane at 75 degrees magnetic latitude of 1.25 to 1.5 mhos. This conductivity is due to particle precipitation, since when the sun is below the horizon, particle precipitation is the dominant source of ionization. This conductivity corresponds to a resistance of 0.67 to 0.8 Ohms. Using this resistance and the above currents, we obtain a joule heating rate of 2.2×10^6 to 9.2×10^6 Watts, differing from that of *Olson* [1986] because *Olson* used a larger ionospheric resistance.

I computed the power spectral density of all 315 days of data and fitted a straight line to each day's psd. The variance and spectral index were determined for each day, along with the category of the day as described in Chapter 3. The solar depression angle was also computed, and used to order the data. The solar depression angle is defined as the solar zenith angle minus 90 degrees, where the solar zenith angle is the angle between the zenith and the line to the sun. Thus, the solar depression angle is positive when the sun is below the horizon, and negative when the sun is above the horizon. A sketch of the geometry is shown in Figure 4.2. The solar depression angle should have an effect on the magnetic fields because

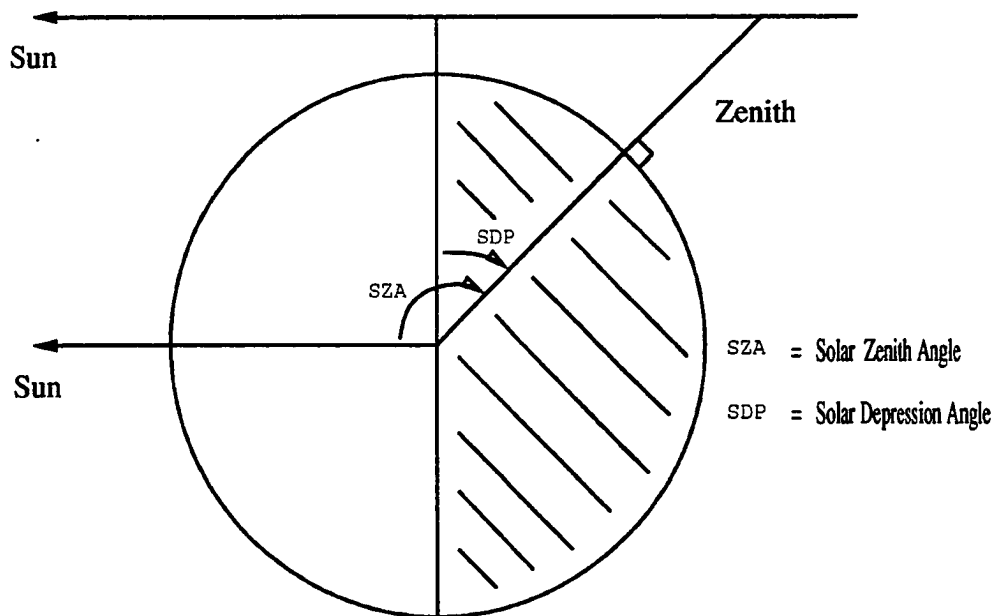


Figure 4.2. Geometry for relation between Solar Depression and Solar Zenith Angle. Note that when the sun is below the horizon the solar depression angle is positive, and when the sun is above the horizon the solar depression angle is negative.

the variation of solar EUV will have a significant impact on the ionization rate and hence electron number density and ionospheric conductivity. If the conductivity changes with solar depression angle, I expect a change in the currents, and thus the measured magnetic fields on the ground. In the following figures the spectral index and the variance for each day are shown versus solar depression angle

Figure 4.3 shows how the spectral index, variance and photoionization rate vary with solar depression angle for the entire data set. The top panel shows how the spectral index varies with solar depression angle. Each data point represents the best fit of one day's data. The data clearly fall around a straight line, and

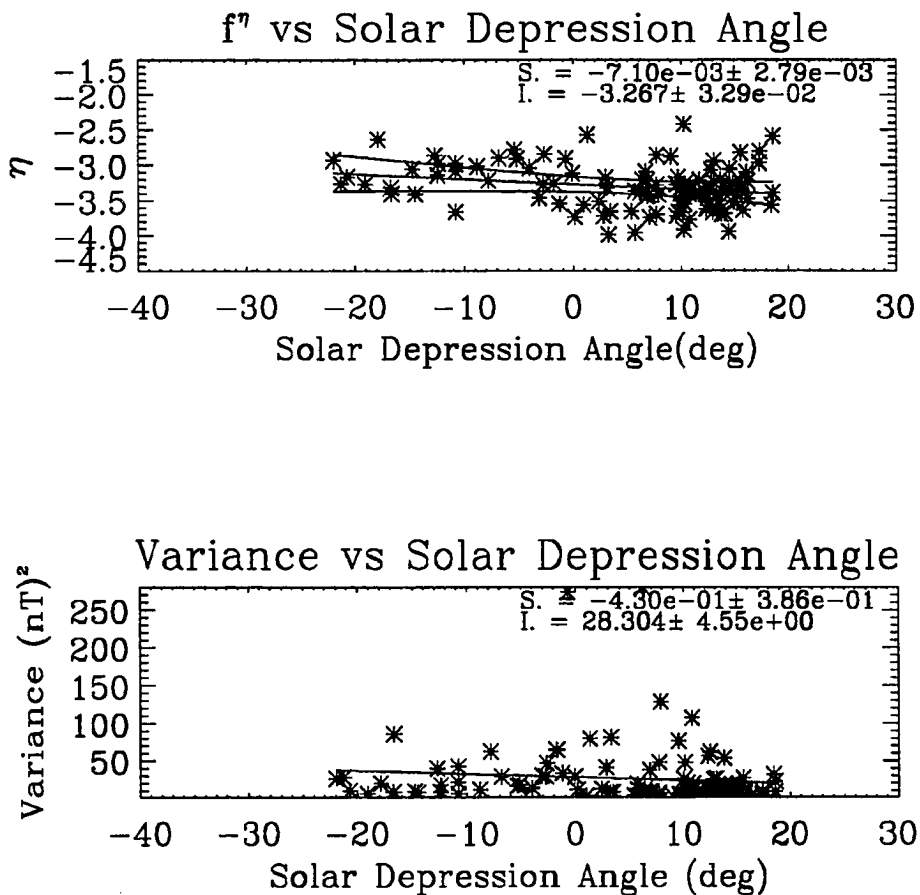


Figure 4.3. The top panel shows how the spectral index varies with solar depression angle. The best fit line and uncertainty bands associated with the best fit parameters are also shown. The middle panel shows the variance in the 1 - 50 mHz frequency band versus solar depression angle. Again the best fit line and fit parameters are shown. The lower panel shows the ratio of the photoionization rates at 105 and 120 km to the rate at 105 km and -40 degrees solar depression angle versus solar depression angle.

the ensemble has been fit with a line and the slope and intercept are shown along with the uncertainties in the slope and intercept. This best fit line, along with the uncertainty bars associated with the uncertainties in the fit parameters, and the fit parameters themselves, are also shown. I find the slope of this line, $S = -1.7 \times 10^{-2} \pm 1.7 \times 10^{-3}$, a statistically significant variation in the spectral index is seen with solar depression angle. The middle panel shows the variance in the 1 - 50 mHz frequency range of the induction coils versus solar depression angle. Again a variation with solar depression angle is seen. The intercept at 0 degrees solar depression angle is at approximately 36 nT^2 , in very good agreement with the average over 237 days reported by *Olson* [1986]. The lower panel shows the ratio of the photoionization rate at 105 and 120 km as a function of solar depression angle to the photoionization rate at 105 km and -40 degrees solar depression angle. These photoionization rates were calculated using equation 2.3.4 described in *Rees* [1989], with the MSISE-90 model atmosphere being used to calculate number densities of O, N₂, and O₂, see *Hedin* [1991]. This ratio shows that for solar depression angles larger than approximately -20 degrees the photoionization rate is less than half of what it was at -40 degrees. This is important because most of our data have solar depression angles greater than -20 degrees. Thus most our data are collected in periods when the contribution of ionization rate due to photoionization is the least.

Three important features of Figure 4.3 are that the spectral index, and the variance of the magnetic pulsations vary with solar depression angle, and that most of the data were taken when photoionization was at a relative minimum. The spectral index and variance are measures of the magnetic perturbations, which are proportional to the perturbations in the current density in the ionosphere as described by Ampere's law. *Fukushima* [1976] shows that for a uniform conductivity and vertical line currents, the magnetic perturbations measured on the ground are

due only to the Hall current since the perturbations due to the Pederson currents are canceled by the perturbations caused by the vertical line currents. *Hughes* [1974] also showed that the ionosphere serves to screen out micropulsation signals incident on it from the magnetosphere, while *Hughes and Southwood* [1976] showed that horizontal spatial variations in micropulsations incident on the ionosphere which were smaller than a scale height of the ionospheric height, approximately 120 km, were screened out from ground observations. *Glassmeier* [1984] extends this work for the case of nonuniform conductivity, and achieves the same basic result, with the modification that the Pederson currents are not totally screened when the conductivity is non-uniform. To first order then, the perturbations giving rise to the spectral index and variance can be modeled as perturbations in the Hall current density in the ionosphere.

These Hall current density perturbations can be written in a simplified Ohms law as;

$$\delta J_H = \sigma_H \delta E_{ion}, \quad 4.1$$

where δE_{ion} is the electric field amplitude in the ionosphere. To determine the spectral index of the power spectral density requires that the fourier transform of equation 4.1 be taken, and this leads to two possible results. If the conductivity is constant in time, then the changes in spectral index must be attributed to changes in the electric field source psd. If the conductivity is allowed to vary in time during the course of one day, then the result of the fourier transform will be a convolution in frequency. I have sorted the data by category as described in Chapter 3, with hopes that this will shed light on which of these two assumptions dominates the observations. Any changes in the spectral index due to conductivity changes should be seen in all three categories assuming that no differences due to the characteristic energy of the precipitating particles exist between the three different categories. In

chapter 3, I showed that the categories represent different IMF states at the bow shock, and by inference different states of the dayside magnetosphere. If changes in the spectral index appear in the one or two of the categories, but not all three, then the dominating influence will be changes in the electric field, which is a reflection of the electric field of the magnetosphere which is mapped down to the ionosphere.

Figures 4.4, 4.5, and 4.6 show the variation of the spectral index and variance versus solar depression angle for Categories 1,2, and 3 respectively. Note that the three figures have different scales on the ordinate. Note that the slope of the best fit line of the spectral index for Category 1 is statistically smaller than that of Category 2 and 3. This slope is also smaller than that found in the overall data set as shown in Figure 4.3. A similar trend is seen in the variances, but the effect is less pronounced. This is an important result that helps answer the question of whether the conductivity changes or electric field source changes are driving the change in spectral index.

I believe the evidence given shows that the changes in the ionospheric electric field, the $\delta \vec{E}_{ion}$ in equation 4.1, may be responsible for the changes seen in the spectral index with solar depression angle. As discussed in Chapter 3 the IMF correlations with Categories 2 and 3 showed cone angle distributions that indicated quasi-parallel shock geometries, while Category 1 was associated with a perpendicular shock geometry, see Figure 3.17. I interpret this as indicating that the source of the higher frequency ULF perturbations in the cusp is dominated by upstream wave activity caused in the bow shock when the IMF cone angle is in the configuration shown for Categories 2 and 3. This high frequency (20-50 mHz) noise observed within the cusp is increased when the solar depression angle is small, and the spectral index is reduced as well. The central cusp in Category 1 does not have a large component of high frequency (20 - 50 mHz) noise, and hence does not show the same variation in solar depression angle. I know of no apriori reason

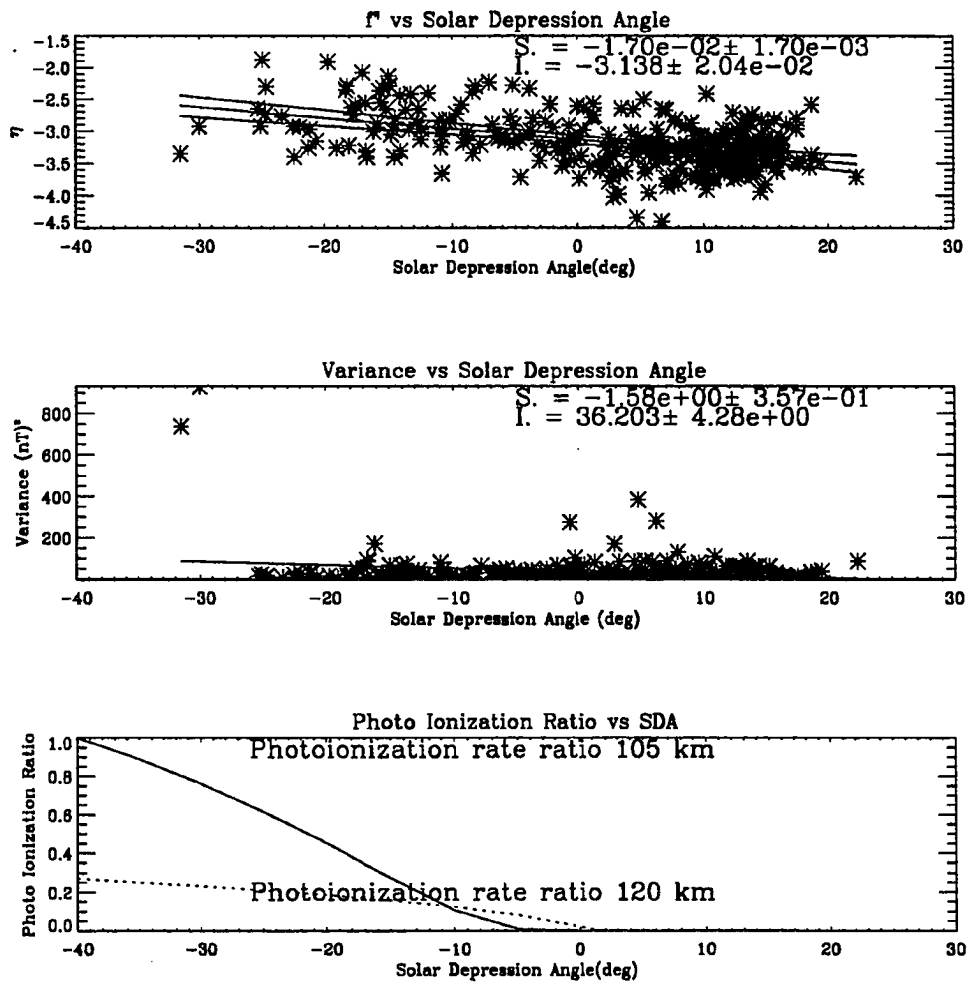


Figure 4.4. Spectral index, and variance versus solar depression angle for Category 1. The top panel is the spectral index versus solar depression angle, and the lower panel is the variance versus the solar depression angle. Note that the spectral index variation with solar depression angle is statistically less than that found for the entire data set. This is also true for the variance as a function of solar depression angle.

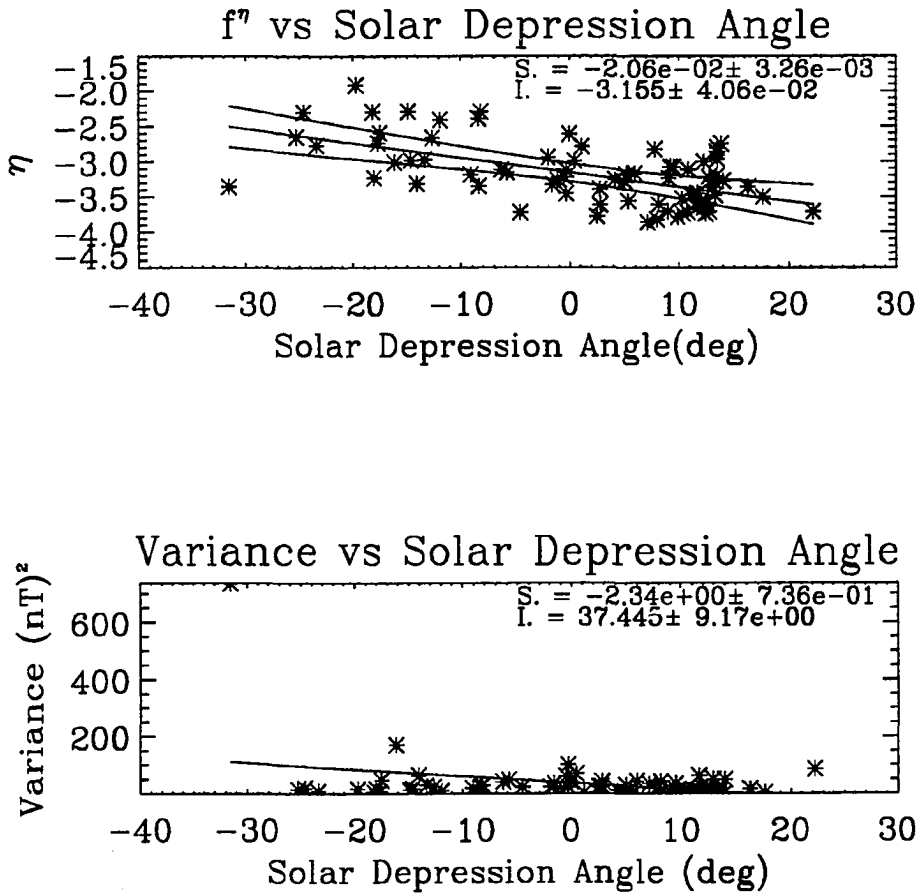


Figure 4.5. Spectral index, and variance versus solar depression angle for Category 2. The top panel is the spectral index versus solar depression angle, and the lower panel is the variance versus the solar depression angle. Note that the spectral index variation with solar depression angle is larger than that found for the entire data set. This is also true for the variance as a function of solar depression angle.

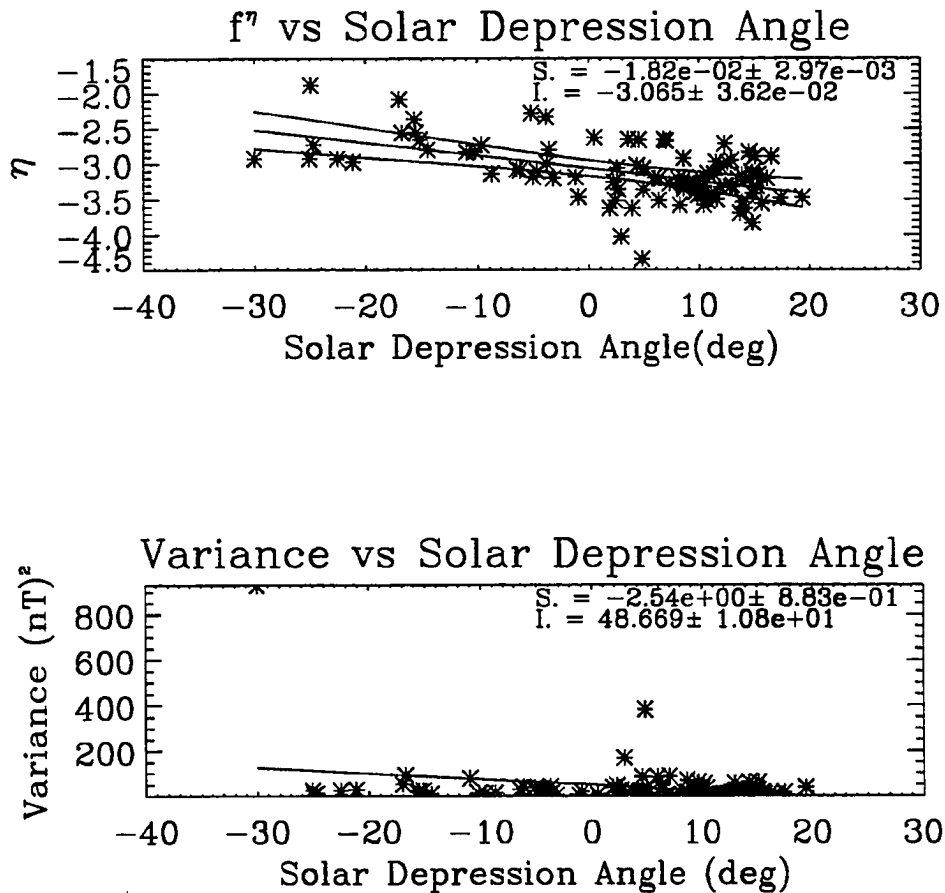


Figure 4.6. Spectral index, and variance versus solar depression angle for Category 3. The top panel is the spectral index versus solar depression angle, and the lower panel is the variance versus the solar depression angle. Note that the spectral index variation with solar depression angle is larger than that found for the entire data set. This is also true for the variance as a function of solar depression angle.

to believe that the time scale of conductivity changes with category. This would indicate that a significant effect in the spectral index due to conductivity changes should show the same general trends in all three categories. Since the Category 1 spectral index has a much smaller response to the solar depression angle when compared to Categories 2 and 3, I think that the changes seen in the spectral index are dominated by the power spectral density changes in the electric field in the ionosphere.

A physical model of the dependence of the spectral index with solar depression angle can be gained from looking at the mapping of the cusp field geometry with season, and assuming that the source of the higher frequency portion of the psd is upstream noise associated with instability in the subsolar region of the bow shock. Figure 4.7 shows the magnetic field line map of the magnetosphere using the Tsyganenko 1989 model, see *Tsyganenko* [1989]. This map is calculated for the winter solstice, and also shows the bow shock location, calculated via the empirical fits of *Slavin and Holzer* [1981]. As noted before, any noise generated in the subsolar portion of the bow shock dominates the source of the high frequency noise in the magnetosheath. This means differences in the propagation geometry through the magnetosheath and into the cusp will play an important role in the received spectra in the summer and winter cusp. In terms of magnetic field topology, the cusp is roughly the location where closure of magnetic field lines switches from the dayside to the nightside of the earth. Figure 4.7 clearly shows a difference of the summer and winter cusp with respect to the axis of the earth-sun line. The summer cusp has easier access to the the higher frequency noise generated in the bow shock, and thus its spectral index is reduced. This difference is mainly due to the orientation of the earth's rotation and dipole axes with respect to the solar ecliptic. In this explanation, the change in the spectral index is caused by the differing propagation paths that the high frequency noise must take to enter

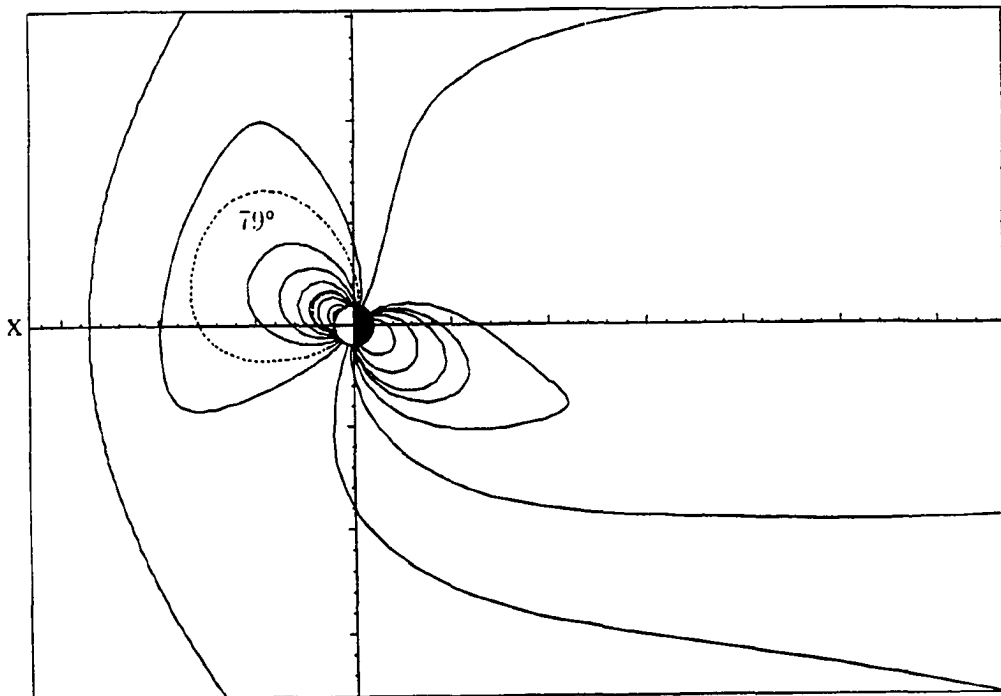


Figure 4.7. Topology of magnetic field and bow shock location for winter solstice in GSM coordinates. The magnetic field topology is calculated using the Tsyganenko field model, and the bow shock is calculated using the empirical fits of Slavin and Holzer. The dotted line is at 79 degrees magnetic latitude, and represents the average latitude of the cusp. Note that with respect to the earth sun line, the x axis, that the two cusp field geometries are very different. The summer cusp has easier access to the higher frequency noise generated in the bow shock, and thus has a reduced spectral index.

the cusp at ionospheric levels. This change in geometry is continuous during the year, and the effect roughly follows the solar depression angle. Thus the spectral index data are ordered by the solar depression angle not because of changes in the ionosphere, but by a geometry change in the magnetic field topology that follows the solar depression angle.

The variance of the ground magnetic perturbations is changing because the photoionization rate clearly changes with the solar depression angle. The Hall conductivity is proportional to the electron number density, see *Rees* [1989], and the number density is driven by the ionization rate. Thus as the ionization rate increases with smaller solar depression angle the conductivity increases, and hence the observed currents and magnetic fields change. If this explanation is accepted then a rough calculation of the change in conductivity between winter and summer solstice is available, and is the subject of the next section.

4.2 Estimation of cusp current system parameters

Given the assumptions detailed in the previous section, several cusp current system parameters can now be estimated. The magnetic perturbations are proportional to the perturbations in the current density, which is proportional to the conductivity. Since the variance in the magnetic field perturbations is proportional to the square of these perturbations, we obtain the conductance ratio;

$$\frac{\Sigma_{\theta_1}}{\Sigma_{\theta_2}} = \sqrt{\frac{\text{Var } \delta \vec{B}_{\theta_1}}{\text{Var } \delta \vec{B}_{\theta_2}}}, \quad 4.2$$

where

$$\text{Var } \delta \vec{B}_{\theta_1} = S\theta_1 + I, \quad 4.3$$

and

$$\text{Var } \delta \vec{B}_{\theta_2} = S\theta_2 + I. \quad 4.4$$

Here the slope (S) and intercept (I) are taken from the best fit parameters determined in Figure 4.3.

Using the solar depression angles of 13.9 and -32.7 degrees for the winter and summer solstice, respectively, we obtain a ratio of the conductivity changes between winter and summer of 2.5 ± 0.6 . This can be compared to other empirical estimates of dayside height integrated conductivity such as *Hardy et. al.* [1987], who calculates the conductivity due to precipitating particles. The conductivity due to precipitating particles can be combined with the solar ionization produced conductivity of *Robinson and Vondrak* [1984] by summing in quadrature, see *Wallis and Budzinski* [1981]. I used a solar 10.7 cm flux (S_a) of 200 ($10^{-22} \text{ W m}^{-2} \text{ Hz}^{-1}$) in the calculation of solar contribution to conductivity, and added a background of 1 mho for the case when the solar zenith angle was greater than 90 degrees. The solar contribution to the conductivity is;

$$\Sigma_p = 0.88(S_a \cos \chi)^{0.5}, \quad 4.5$$

while the contribution due to particle precipitation is taken from Figure 6 of *Hardy et. al* [1987], and is 1.75 - 2.0 mhos. This gives a total conductivity of 4.6 mhos at the summer solstice, and 2.23 mhos at the winter solstice, yielding a ratio of 2.1 in good agreement with my calculation based on magnetometer variance fits over the 315 days of data.

As noted earlier the variance can also be used to predict the current flowing in the ionospheric cusp region as a function of distance from the measurement location assuming the current is a line current. This results in the following; is;

$$I_{ion}(\text{amps}) = \frac{2\pi R\sqrt{S\theta + I}}{\mu_o}, \quad 4.6$$

where again S is the slope and I is the intercept from the variance best fits with solar depression angle shown in Figure 4.3, and R is the assumed distance to the current filament.

4.3 Time series of magnetic perturbations

The arch as described in Chapter 3 was found by looking at the spectrogram version of the data. The spectrograms were made from the induction coil data, and it is of interest to look at the fluxgate data during this time to see if any identifying characteristics in the time series can be seen.

Figure 4.8 shows an expanded version of the fluxgate and induction coil magnetometer signals for 9 January 1991 from 04:00 to 12:00 UT. In this figure the H induction coil, and the x component of the fluxgate are positive along magnetic north, and the D induction coil, and y component of the fluxgate are along magnetic east. The z component of the fluxgate is positive down. Magnetic north is 45 degrees west of geographic north.

Note that from 05:00-07:30 and 10:30 to 11:30 the induction coils show the largest pulsations, and this corresponds to the times identified as the boundary regions in the spectrograms. During the boundary regions the fluxgate magnetometers show large amplitude (approximately 40-50 nT) pulses. During the central cusp period from 7:30-10:30 there are small amplitude (approximately 3-5 nT) pulsations in the fluxgate data in all three components. These small amplitude oscillations are typical of the data observed during the arch on many days. While each day is unique, the time series shown is representative of the Category 1 data. I have found that in general the boundary layers are the easiest to spot in the time

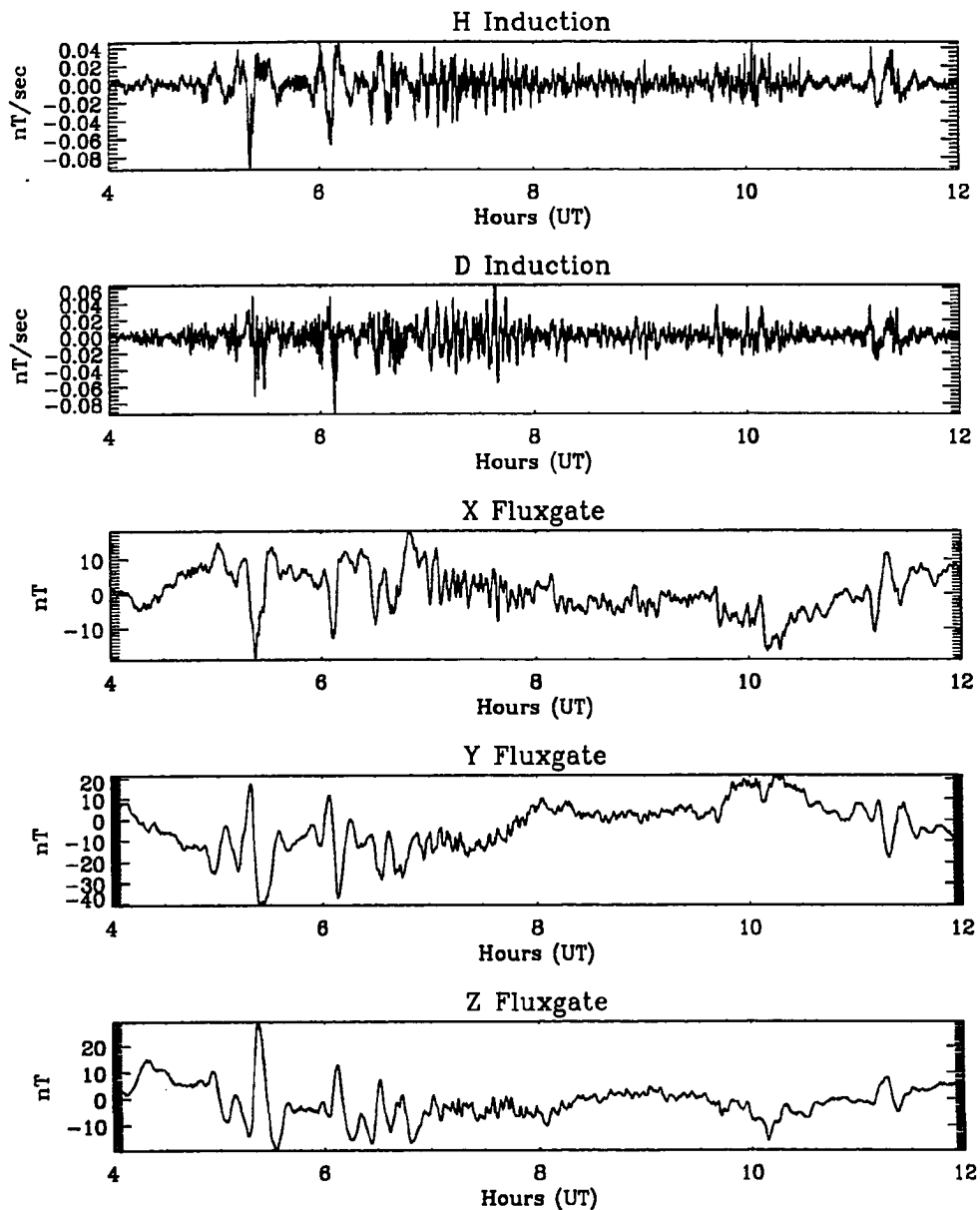


Figure 4.8. Time series for magnetometer on 9 January 1991. The top two panels are the H and D induction coils, the bottom three panels are the X, Y, Z fluxgate components respectively. Note the large amplitude pulses seen in the boundary region from 05:00-07:30 and from 10:30-11:30. Also note the small amplitude pulses from 07:30-10:30 UT

series of the magnetic data. The small amplitude pulses in the central cusp can typically be seen, but many times looking at the spectrogram is necessary to find the exact time of the arch.

Large amplitude pulses in the boundary regions are also seen by *Sakurai et al.* [1993] who show time series data taken on 4 November 1989 at Godhavn Greenland. While the fluxgate data are not shown in enough resolution to see the small oscillations during the central cusp period, the boundary regions are clearly visible in both the induction coil and fluxgate measurements. *Sakurai et al.* [1993] also report that the enhanced region of ULF wave activity seen at the cusp is accompanied by a negative excursion of the H (North-South) flux gate magnetic field. They interpret this to be the station passing underneath a westward directed current system in the ionosphere. This period corresponds to the boundary region passage at their station, and *Sakurai et al.* [1993] state that such negative deviations on the H component are recurrent in their data.

4.4 Temporal coherence length of cusp pulsations

In this section, I use the Hilbert transform to manufacture the analytic portion of the magnetometer signal and look at the instantaneous phase angle of these signals. I will show that the magnetic pulses seen in the boundary regions are phase incoherent from each other. This means that a large jump is seen in the instantaneous phase between each pulse. I show that the pulses in the central cusp region are phase coherent over approximately 5-10 periods, and that one train of coherent pulses ends and another begins in the central cusp when a downward electron flux appears on the equatorward side of the cusp. As described in Chapter 2 this downward electron flux can be considered the component of field aligned current carried by the electrons. In the rest of this chapter I will refer to such observations as field aligned currents, or FAC's. The difference between the pulses

in the boundary region and the central cusp is important when trying to decide on their possible sources.

Bracewell [1965] gives an excellent discussion of the use of the Hilbert transform to manufacture the analytic part of a signal that has a quasi-monochromatic signal in time, $f(t)$. The analytic part of the signal can be constructed as $\hat{f}(t) = f(t) - iF_{HI}(t)$, where;

$$F_{HI}(t) = \frac{1}{\pi} \int_{-\infty}^{+\infty} \frac{f(t')dt'}{t' - t}. \quad 4.7$$

This allows determination of the phase of the quasi-monochromatic part of the phase via $\Phi = \tan^{-1} \left(\text{imag}(\hat{f})/\text{real}(\hat{f}) \right)$. For a signal that is broad band, and not quasi-monochromatic, the reconstructed phase angle will have random jumps in it and this method will fail. However in our application I have shown in Chapter 3 that the arch is dominated by a narrow band tone at approximately 3-5 mHz, and that the boundary regions have a signal in the low Pc5 range that is 10 dB above the rest of the frequency spectrum.

I have used the Hilbert transform in the MATLAB package to perform such an analysis on the data from 9 January 1991. This Hilbert transform routine is based on the Kolmogorov method as described by [*Claerbout, 1976*]. Figure 4.9 shows the x component of the fluxgate for 9 January 1991. The upper panel shows the unfiltered data, while the middle panel shows the same data after having been passed through a low pass filter with a corner frequency of 6 mHz. The lower panel shows the phase using the analytic signal reconstructed from the Hilbert transform.

The low pass filter was applied to insure that the higher frequency components of the boundary regions did not cause random phase jumps in the Hilbert transform. The filter is a third order elliptical filter with 1 db of ripple in the passband, and the corner frequency 50 db down from the passband. The filter has been applied in the forward and backwards direction to insure causality in the data,

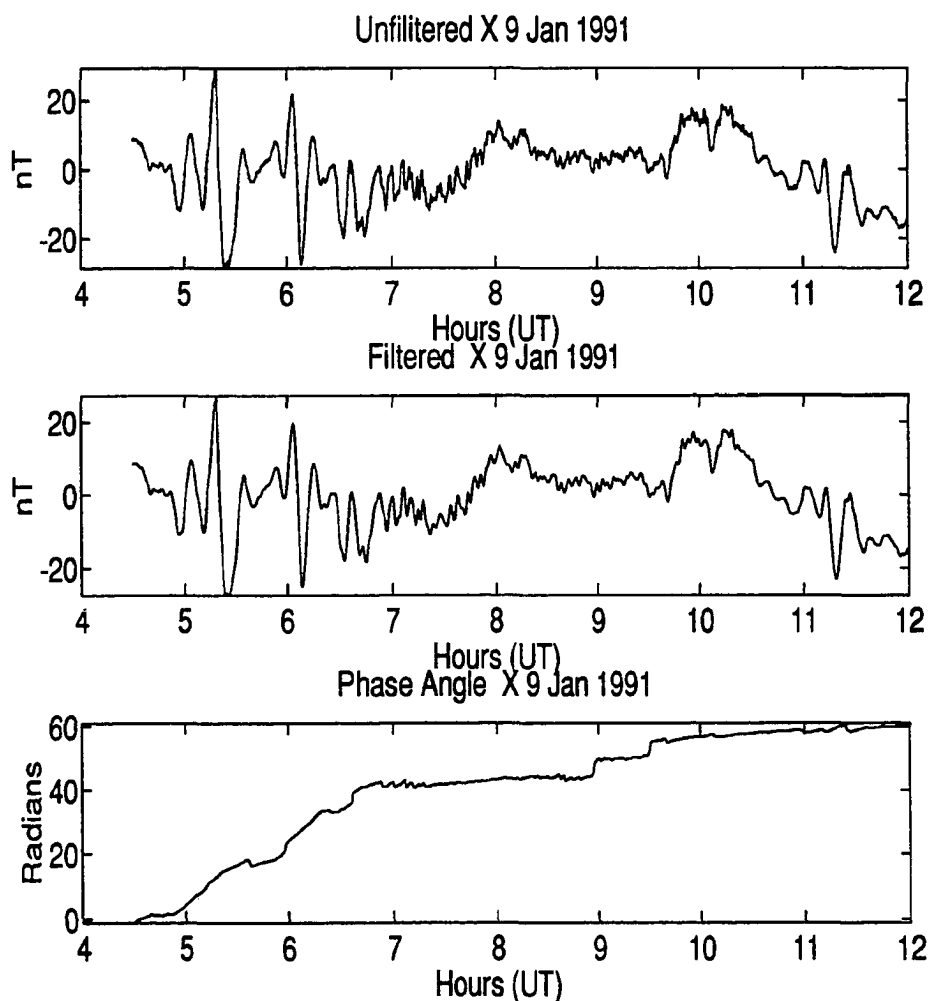


Figure 4.9. Fluxgate x component phase diagram, 9 January 1991. The top panel is the unfiltered x component of the fluxgate, the middle panel is the same data low pass filtered with a corner frequency of 6 mHz. The bottom panel is the phase angle of the filtered data, note the large phase jumps after each of the large pulses in the boundary region. Also note that the phase is very steady from 08:00 to 09:00, and then has intermittent phase jumps after that time.

resulting in an effective sixth order filter. Inspection of the filter characteristics in the frequency domain, not shown here, reveal that the filter has only very small phase variations with frequency.

Figure 4.9 shows that after each one of the large pulses in the 05:00 - 07:00 UT time period there is a jump in the phase angle. In particular, the pulse that ends at 05:30 shows a large phase jump. The next large pulse that starts at 06:00 is begun with a large phase jump, again showing the impulsive nature of the large amplitude pulses in the boundary region. Within the time period of the central cusp, 07:30-10:30 (UT), there are periods with stable phase separated by jumps in the phase angle. For instance in Figure 4.9 from roughly 07:30 - 08:30 UT the phase angle remains very stable, with no large jumps in the phase angle. During this period these pulses can be considered part of a phase coherent train of pulses, that have a coherence length of about 10 periods. This number was determined by counting the actual number of periods between the phase jumps. The large pulse seen at 11:00 again shows a phase jump, although not as dramatic as that in the prenoon boundary region. Thus the pulses in the central cusp form wave trains that suffer intermittent phase jumps, while the pulses in the boundary region are impulsive in nature.

Another example of the phase coherency of the central cusp is seen in Figure 4.10, which presents data from a Category 2 day. Remember the Category 2 days do not show prominent boundary region signatures, and the data from Figure 4.10 show that there are no large amplitude pulses which are impulsive in nature. The spectrogram for this day, not shown here, shows an arch centered at 06:00 UT. Notice that the period from 05:00 UT to 07:00 UT is filled with small amplitude (approximately 5 nT) pulses, that seem to come in phase coherent trains that last from 7-10 periods. The time period from 05:00 to 05:50 shows phase jumps, however the period starting at 05:50 and lasting to 6:45 does not show large jumps

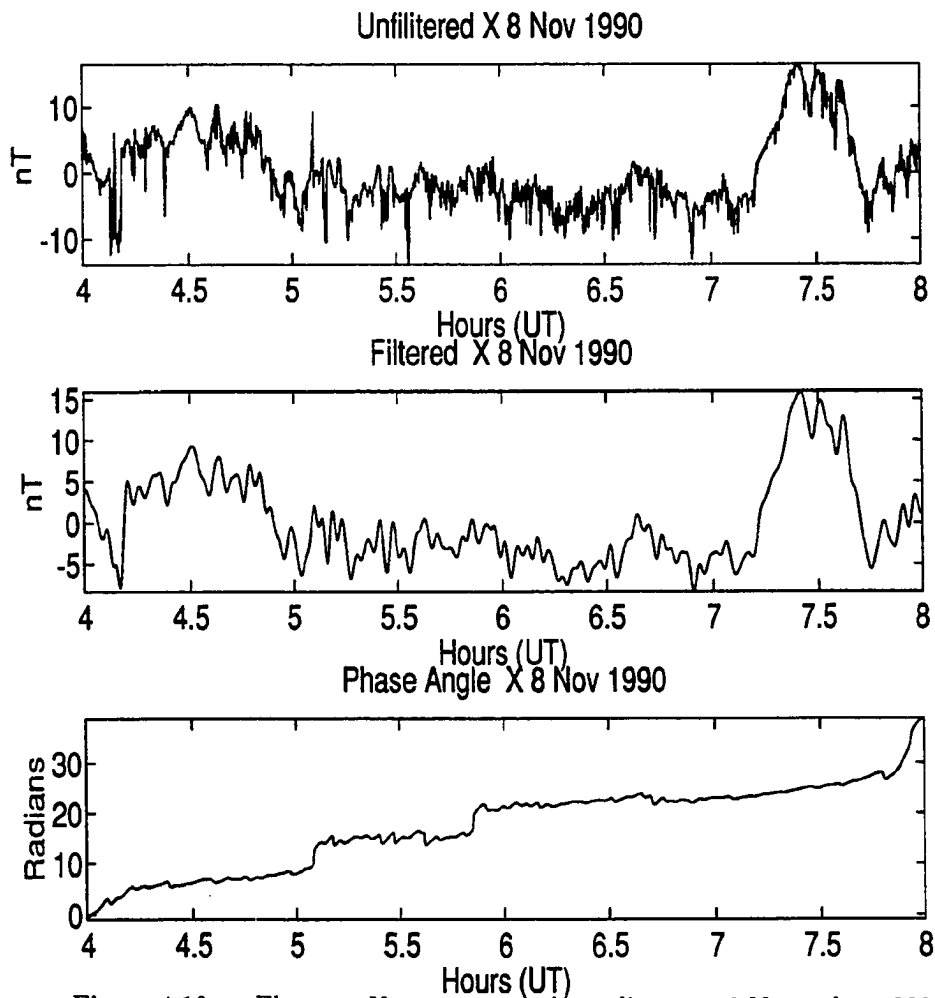


Figure 4.10. Fluxgate X component phase diagram, 8 November 1990. Similar format to Figure 4.9. This day is from Category 2, and the spectrogram shows an arch centered at 06:00 UT. Notice the lack of large amplitude pulses that characterize the boundary layers in Categories 1 and 3. Also notice the small amplitude pulses that have a constant phase from just before 06:00 UT and last to about 06:40 UT. Again these pulses form a phase coherent train that lasts 7-10 periods.

in the phase. This example shows that the pulses seen in the time series when the arch is evident in the spectrogram are consistent across different categories.

Figure 4.11 is the final example of the phase coherency of the pulses in the arch. The data for this example were measured on 22 December 1990, which was a Category 3 day. The spectrogram showed an arch centered at 08:30 UT on this day, with the pre-noon boundary region being much stronger than the post-noon boundary region. Notice the 20 nT pulse seen at 07:30, characteristic of the boundary regions. The phase angle is seen to jump at end of this pulse at 07:40. A smaller amplitude pulse lasting from 07:40 to about 07:50 also terminates in a small phase jump, and then the phase angle shows very steady growth with no phase jumps from 08:00 until just before 09:00. Small amplitude pulses forming a phase coherent train are seen during this entire period.

As seen in Figure 4.9, there is a jump in the phase angle of the x fluxgate at approximately 09:00 UT on 9 January 1991. This phase jump is associated with an intense field aligned current that appears at the equatorward edge of the cusp and moves poleward. Figure 4.12 shows the upward field aligned current (FAC), as derived from the downward flowing number flux of the electrons, for the periods 05:00- 11:00 UT on 9 January 1991. The upper panel is the usual two dimensional map in latitude versus time. The lower panel is a time series made from the data by integrating over latitude. The time series shows that, starting around 06:00 UT, the latitude integrated FAC increases, and shows variations in intensity until after 10:30 when it decrease back to ambient levels. One large spike is seen at 05:30 UT that is associated with a FAC directly over the station. The time series also shows a pronounced dip at 07:00 UT which is due to a data drop out. The large FAC's seen at 08:00, 09:00 and 09:30 all show evidence of poleward propagation. Since the MSP is a one-dimensional instrument such interpretations can be in error, but it is fair to say that regions of equal intensity are seen poleward at later times.

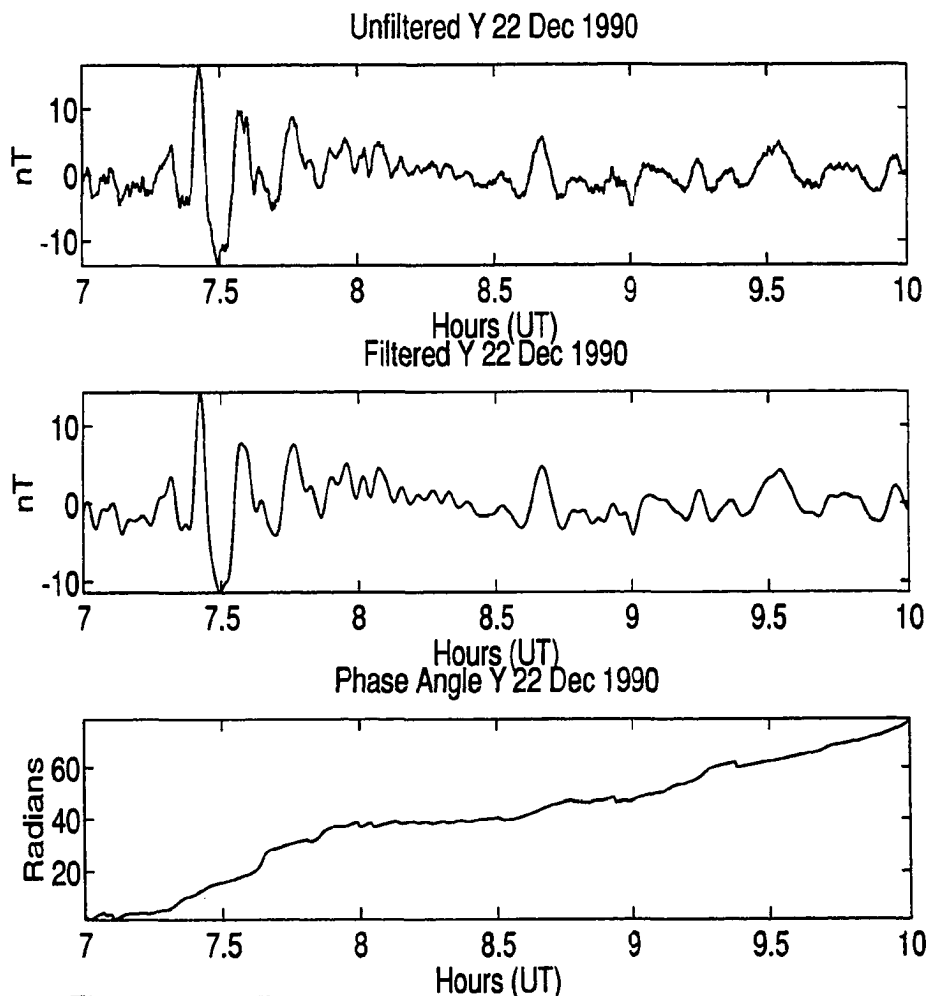


Figure 4.11. Fluxgate Y component phase diagram, 22 December 1990. Similar format to Figure 4.9. This day is from Category 3, and the spectrogram shows an arch centered at 08:30 UT. Notice the large amplitude pulse at 07:30 is terminated with a phase jump, and then the smaller pulses after it also show a small phase jump at approximately 07:50. The period of the arch, after 08:00 to just before 09:00, shows stable phase growth.

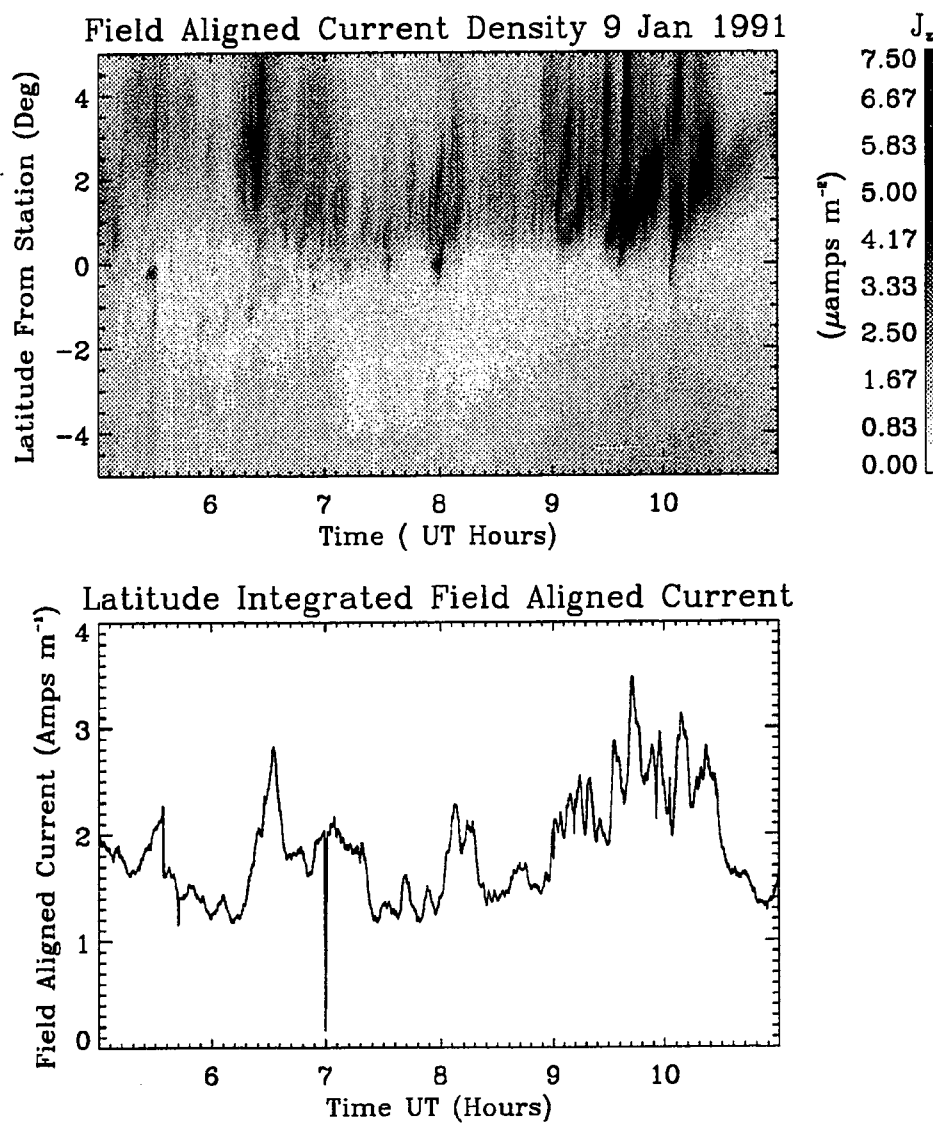


Figure 4.12. Inferred component of the field aligned current (FAC) carried by downward flowing electrons on 9 January 1991. The upper panel shows latitude versus UT hours over the period 05:00 - 11:00 UT. The lower panel is a time series of the same data with the latitudinal portion integrated out, the resulting units are *amps/m*. Notice there is a distinct equatorward boundary to the intense FAC at approximately 0.5 degrees north of the station. The dip in the time series at 07:00 and 11:00 UT is due to data drop out.

The phase jumps seen in the X component of the flux gate at 09:00 and 09:30 are seen to be associated with the large poleward propagating FAC's.

Figure 4.13 further demonstrates this correlation. In this figure the upper panel is the low pass filtered X component of the fluxgate, the next panel is the latitude integrated FAC, the next panel is the phase angle diagram for the X component, and the bottom panel is the phase angle diagram for the Y component of the fluxgate. Notice that the large amplitude pulse in the boundary region that ends in a phase jump at 05:30 is associated with a FAC directly over the station. The next large amplitude pulse that begins with a phase jump at 06:00 does not show any signs of an associated FAC. At 06:30 UT there is an increased FAC seen associated with the phase jumps in the X component. At 07:00 UT both the X and Y components show phase jumps, but there is only a slight increase in the FAC. It seems clear however that the phase jumps in the Y component at 08:00 UT are accompanied by a large FAC, and similarly for the X component at 09:00 and 09:30 UT.

That the boundary regions have phase incoherent pulses is not a new observation. *Olson* [1986] also referred to individual pulses seen in flux gate data taken at a cusp station in Cape Parry that were not coherent. Looking at *Olson* [1986] figures 8 and 11, it is clear that the pulses mentioned are in the pre-noon boundary region, and are of the large phase incoherent pulses presented in this section. *Olson* [1989] uses a combination of two stations at Sachs Harbor and Cape Parry to show that these pulses propagate poleward with velocities between 1-5 km/sec. As mentioned, *Sakurai et al.* [1993] also report impulsive pulses in the Pc5 frequency range during the boundary region period. *Sakurai et al.* [1993] also show data for the same day from an auroral latitude station at Syowa, and its conjugate station at Husafell. Their measurements indicate that while the Pc5 oscillations are impulsive at the cusp latitude station the auroral latitude stations show wave

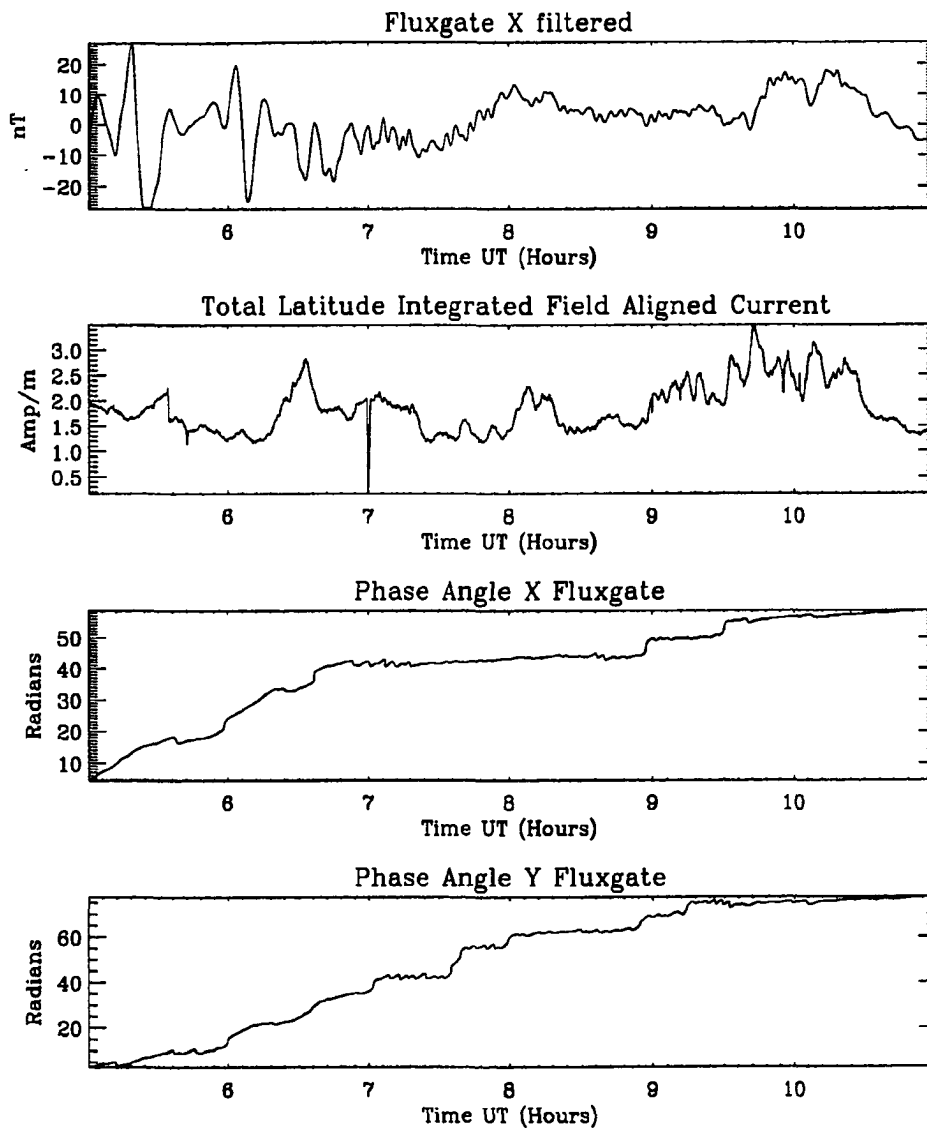


Figure 4.13. Comparison of Latitude Integrated FAC's and magnetometer phase jumps in the X and Y components of the fluxgate on 9 January 1991. The upper panel shows the filtered X component of the flux gate, the next panel the latitude integrated FAC, the next panel the phase diagram for the X component and the bottom panel the phase diagram for the Y component of the fluxgate. See text for discussion.

train like signatures that are consistent with field line resonances on closed field lines. From these observations *Sakurai et al.* [1993] conclude that “.. the Pc5 pulsations observed at Godhaven seem to have a signature of a source wave, while the pulsations observed in the auroral latitudes show continuous wave train with more enhanced power.” It seems then that the Pc5 oscillations are separable into two distinct classes, those seen in the boundary layers, and those seen in the central cusp. The possible physical sources of these two different classes are investigated in the next section.

4.5 Possible sources of cusp pulsations

This section investigates the physical sources that might explain the observations seen in the magnetometer data. I will investigate the pulsations seen in the boundary region first, and then those seen in the central cusp, since the two have different observables.

4.5.1 Boundary Region Phenomena

It seems appropriate before starting the search for physical sources of the boundary region pulsations to review the important observations already presented. The examples presented in the last section, and the work by *Olson* [1986,1989], *Lanzerotti et al.* [1986,1987,1991], *Lanzerotti* [1990] and *Sakurai et al.* [1993] lead me to conclude that the periods I call the boundary regions are characterized by large amplitude, impulsive pulses which are phase incoherent. These pulses are caused by filaments of ionospheric current of approximately 10^5 Amps that propagate poleward with velocities of 1-5 km/sec, [Olson, 1989]. Poleward propagation of these current filaments may be associated with the poleward propagating optical forms reported by *Vorobjev et al.* [1975], *Horowitz and Akasofu* [1977], *Sandholt et al.* [1986b], *Sandholt et al* [1989a;c], and *Fasel et al.* [1992]. Some of the poleward

propagating forms mentioned are in the boundary region, see *Fasel et al.* [1992], while some are in the cusp region, see *Sandholt et al.* [1989a,c]. I will deal in this section with those in the boundary regions.

These boundary region oscillations seem to be associated in time with field line resonances at auroral latitudes, *Sakurai et al.* [1993]. The oscillations are seen in the conjugate hemisphere at the same time, *Sakurai et al.* [1993], *Lanzerotti et al.* [1990] and *Lanzerotti et al.* [1991]. *Lanzerotti et al.* [1991] report field aligned currents associated with the very large amplitude oscillations (95 nT in the Z component) of approximately 2×10^{-7} amps·m⁻². This can be compared with the factor of 10 more intense field aligned current presented in the boundary regions seen on 9 January 1991, and presented earlier in Figure 4.11.

The other set of observations that pertain to the boundary region observations are the traveling vortices reported by *Friis-Christensen et al.* [1988], *McHenry et al.* [1990a], *McHenry et al.* [1990b], *Glassmeier et al.* [1989], *Glassmeier* [1992] and *Glassmeier and Heppner* [1992]. These observations, when taken as whole, indicate the existence of very large scale, 3000 km in longitude by 2000 km vortices with oppositely directed field aligned currents aligned on an east-west axis, which propagate tailward, *Glassmeier and Heppner* [1992]. The propagation velocity is approximately 5-10 km/sec measured in the ionosphere, *Glassmeier and Heppner* [1992]. The parallel currents associated with these vortices are found to be directed downward on the tailward side of the vortices, *Glassmeier* [1992]. Given this bewildering array of observational facts, it is not surprising that several different possible physical sources have been postulated for these pulsations. I will discuss four of the sources briefly and comment on the observational evidence supporting them. These sources are in order of their appearance in the text: 1. Kelvin-Helmholtz instability; 2. Solar wind pressure pulses; 3. Impulsive plasma penetration; and

4. Magnetic reconnection. A good review of the final three sources is given by *Glassmeier* [1992] in connection with traveling ionospheric vortices.

The Kelvin-Helmholtz instability is one of the first explanations of the observed reversal of ellipticity around magnetic noon in Pc5 observations, *Samson et al.* [1971], and *Rostoker et al.* [1972]. The Kelvin-Helmholtz instability occurs when a shear flow exists in a plasma such as the magnetopause boundary. The magnetosheath flow picks up speed as it proceeds away from the subsolar point, *Spreiter and Stahara* [1985], while the magnetopause and then the inner magnetosphere both have a slower flow rate. Thus *Lee et al.* [1981] show that the Kelvin-Helmholtz instability can exist both in the interface between the magnetosheath and the magnetopause, and on the inner boundary between the magnetopause and the magnetosphere. They also show that growth of the instability in the magnetopause is not only dependent upon the speed of the shear flow, but the relative orientation of the magnetic fields in the two plasma regions. The inner boundary between the magnetosphere and the inner boundary region is almost always unstable, and is insensitive to the orientation of the magnetic field in the magnetosheath. *Lee and Olson* [1980] show that the onset of the Kelvin-Helmholtz instability not only has a velocity threshold, [see *Southwood* 1968], but is controlled by the angle between the magnetic field in the magnetosheath and magnetosphere.

The Kelvin-Helmholtz instability can be linked to lower latitudes using the field line resonance model of *Southwood* [1974] and *Chen and Hasegawa* [1974]. In this model, the Kelvin-Helmholtz instability on the magnetopause can couple the energy of the surface wave into the inner magnetosphere, and the energy is transmitted to the ionosphere via a shear Alfvén wave. This model is successful at describing many of the observed features at auroral latitudes, specifically the tilt of the polarization ellipse in the morning and afternoon, as well as the reversal of the ellipticity about magnetic noon. In a similar idea, *Samson et al.* [1991] show

that a cavity mode can be set up between the ionosphere and the magnetosphere can be a source of low frequency oscillations.

The Kelvin-Helmholtz instability would seem to be a good candidate for describing the pulses seen in the boundary region away from local noon since the flow speed in the flanks is greater than at the subsolar point. However the Kelvin-Helmholtz instability does not describe why pulses would be seen to propagate poleward; rather we would expect them to show an azimuthal movement. While the instability has been shown to exist over a large scale size, (Wei and Lee, submitted to *J. Geophys. Res.*, March 1992), it does not predict the observed oppositely directed field aligned currents seen in the tailward moving twin vortices. Despite this, *McHenry et al* [1990a] use the Kelvin-Helmholtz instability as the source of the twin vortices.

Friis-Christensen et al. [1988], in the first report on twin ionospheric convecting vortices, linked the appearance of the vortices to a sudden change in the solar wind pressure. *Farrugia et al.* [1989] show magnetometer data from ISEE 1 and ISEE 2 that indicate an azimuthally propagating compression of the magnetosphere, and this is correlated with a twin vortex system. *Glassmeier* [1992] and *Glassmeier and Heppner* [1992] show convincing evidence that on a theoretical basis, a short duration change in the solar wind pressure can lead to a compression of the magnetopause, which can lead to a twin system of oppositely directed field aligned currents. These field aligned currents lie along the axis of propagation of the compression of the magnetopause, and will propagate tailward with the solar wind flow. These tailward propagating vortices might be the cause of the longitudinal phase variations reported by *Olson and Rostoker* [1978]. It is interesting to note that two of the large pulses seen in Figure 4.13 in the boundary region at 05:30 and 11:30 UT are associated with large upward field aligned currents. This might be evidence of the near field magnetic perturbations associated with twin convecting vortices. The field aligned current amplitude matches well with

that calculated by *Glassmeier and Heppner* [1992]. Thus it would seem that pressure changes in the solar wind can better explain the twin convecting vortices seen at cusp latitudes. *Sibeck* [1990] points out that pressure fluctuations in the solar wind can generate many of the same features that are associated with magnetic reconnection.

The next two possible sources of boundary region pulsations are magnetic reconnection and impulsive plasma penetration. In both cases, plasma containing mass and hence momentum is allowed to cross the magnetopause boundary. This transfer perturbs the closed field lines inside the magnetopause each time the event happens, and this perturbation causes the field lines to oscillate. Each of these oscillations is seen as an impulsive event on the outer field lines that thread the magnetopause, and hence maps to cusp latitudes. The lower latitude field lines respond via the field line resonance already described in the Kelvin-Helmholtz instability. In the field line resonance model it little matters what the source of the surface perturbation is, only that it exists.

Magnetic reconnection at the dayside magnetopause traces its roots back to *Dungey* [1961]. The interplanetary magnetic field interacts with the terrestrial magnetic field and field lines that were closed in the magnetosphere are now open to the solar wind. This magnetic merging between the IMF and the terrestrial field allows access to the magnetosphere of magnetosheath particles, and serves as a source of kinetic energy for the plasma due to the conversion of magnetic field energy, [*Parker*, 1957]. The steady-state version of reconnection presented by *Dungey* [1961] has been modified as observations started to appear, [*Russell and Elphic*, 1978,1979]. For an early review of this dynamic area, [see *Cowley* 1982].

Impulsive penetration is a competing view to reconnection that seems more controversial. *Heikkila et al.* [1989] point out an isolated instance where an impulsive event is seen to occur on closed field lines, which they think shows that it did not happen because of reconnection. In their view “... impulsive penetration of solar wind plasma on an interplanetary magnetic flux tube took place through the magnetopause,

ending up in the low latitude boundary region.” *Heikkila et al.* [1989] show that for impulsive penetration to happen, the MHD frozen in condition must not apply, and that the inductive term in Faraday’s law must play a significant role in the electrodynamics. It remains to be seen whether the idea will hold up, but the theory does point out that questioning the basic assumptions behind commonly accepted view points is often worth while.

In summary, the pulsations seen in the boundary region can have a variety of sources. The Kelvin-Helmholtz instability was an early explanation of ULF pulsations in the magnetosphere, and still seems a good candidate, especially when considering the time periods of the boundary regions. In Chapter 3 the statistical occurrences of the boundary regions were shown to be in the pre-noon and post-noon sectors. These magnetic local times would map to the flanks where the shear velocity is larger than the nose of the magnetopause. On theoretical grounds the solar wind pressure pulse idea seems to be able to explain most of the observed features of the twin convecting vortices, but the observational evidence of *McHenry et al.* [1990b] finds no correlation of the vortices with pressure variations in the solar wind. Magnetic reconnection as a source of impulsive events in the boundary regions is somewhat hard to understand given the MLT distribution of the pulsations. However *Friis-Christensen et al.* [1985] have shown that the IMF B_y can control the high latitude current systems. The pulsations seen during the boundary regions may simply be a reflection of the location of these ionospheric currents. Since the B_y control is presumably brought about by the interaction of the IMF with the terrestrial field via reconnection, the idea that reconnection can be the source for the boundary region pulsations is at least possible.

In conclusion, I divide the pulsations seen in the boundary layers into two different groups, with the tailward moving forms associated with the twin convecting vortices being obviously different from the poleward propagating forms of *Olson* [1989]. The work of *Sakurai et al.* [1993] point out that the impulsive events seen at cusp latitudes

are seen at auroral latitudes as wave trains due the field line resonance. This raises the tempting thought that the impulsive events seen in the boundary regions at cusp latitudes are the source of the lower latitude resonant wave trains. It seems that the boundary regions are a collection of impulsive events that have in common the magnetic local time of their occurrence.

4.5.2 Central Cusp Phenomena

Again I begin this section with a quick review of the important observations. The time period of the arch, which I take to be the central cusp, shows small amplitude pulses that form coherent wave trains for approximately 10 pulses. The frequency of these pulses can vary, but is typically seen to be approximately 5 mHz. The phase coherent wave trains are separated by the appearance of field aligned currents on the equatorward side of the cusp with intensities of a few μ amps \cdot m⁻². These field aligned currents propagate poleward. These phase coherent wave trains are found during the time the arch is seen on the spectrogram arches irrespective of which category is under observation. The statistical distribution of these events in magnetic local time was presented in Chapter 3. I can think of two different possible source mechanisms for such pulsations, first would be a field line oscillation on the last closed field lines just equatorward of the cusp, and the second is direct entry of the helical field associated with multiple X line reconnection on the dayside magnetopause.

A field line oscillation driven by some impulsive event could explain the phase coherent wave train of pulses that occasionally suffers a phase jump. In this picture the field line resonance is excited by either an intermittent pressure pulse or reconnection. The field line oscillates in phase at its resonant frequency until a new impulsive event re-excites it. If the re-excitation driving process is stochastic, the phase change will be random. The resonance period of high latitude field lines is on the order of 3-5 mHz, see *Rostoker et al.* [1972]. The model fails to describe why such oscillations are not seen

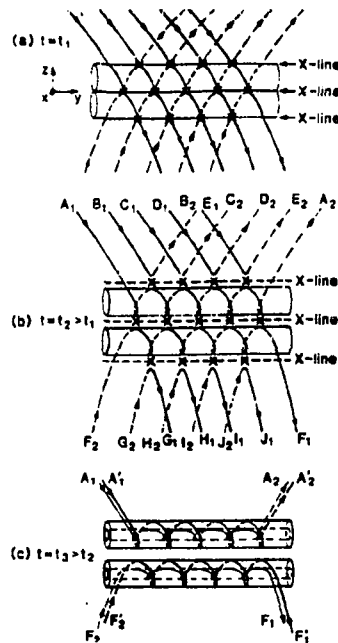


Figure 4.14. Multiple X Line Reconnection Geometry taken from Figure 1. of *Lee and Fu [1985]*. “(a) At time $t = t_1$, the field lines reconnect at the sites marked with an “X”. (b) At $t = t_2$, two helical lines A_1A_2 and F_2F_1 are formed. (c) At $t = t_3$, the helical lines A_1A_2 and F_2F_1 are wrapped by the newly formed field lines $A'_1A'_2$ and $F'_1F'_1$.”

in the data during the boundary regions, which seem to be rich in possible excitation mechanisms. As shown, the coherent wave trains are seen in the central cusp, not the boundary regions. However the major trouble with this model is that it fails to describe why the phase jumps seen in the data are associated with an intense FAC. One way out of this dilemma is to say that the excitation mechanism is sporadic multiple X line magnetic reconnection on the dayside.

This explanation is similar to that of *Lee et al. [1988]*, who extend the work of *Lee and Fu [1985]* pertaining to multiple X line reconnection. Figure 4.14 is a reproduction

of Figure 1 of *Lee and Fu* [1985]. Panel (a) of Figure 4.14 shows three lines of reconnection, called **X** lines from now on, lying in the Y-Z plane. The open field lines from the IMF are shown as solid, and the terrestrial field lines are shown in dotted lines. The field lines reconnect along the **X** lines at the points marked with an x in panel (a). At some later time t_2 the newly reconnected field lines will move due to the magnetic tension of the curved field geometry. This is shown in panel (b) of Figure 4.14, and now there are two tubes of flux that have moved away from each other. If $B_y \neq 0$ then a helical magnetic field exists inside the flux tube. This is caused because the central **X** line is assumed to be longer than the top and bottom **X** line so that the field line marked A_1 can come in from the IMF side and intersect the middle **X** line first. A similar line marked A_2 exists on the magnetopause side. This helical field line is referred to as a type W line because of its resemblance to the letter W. The lines B_1B_2 C_1C_2 D_1D_2 E_1E_2 all reconnect only once, and form a more conventional single **X** line reconnection shape, and are called type V lines due to their resemblance to the letter V. A similar series of events happens to the lower flux tube with F_2F_1 forming the type W lines, and G_2G_1 H_2H_1 I_2I_1 J_2J_1 lines forming the type V lines. In panel (c) we see a later time t_3 , here newly reconnected lines $A'_1A'_2$ are wrapped around the lines A_1A_2 and the flux tube continues to grow until the reconnection process halts. *Lee and Fu* [1985] maintain that this is similar to the nonlinear saturation of the tearing instability. In this manner flux tubes are generated that have an internal helical magnetic field, and are associated with single **X** line reconnection fields on the poleward sides. This geometry relies upon the $B_y \neq 0$ component, and also has the added advantage of automatically predicting parallel currents J_{\parallel} in conjunction with the helical field. The sign of B_y determines the direction of J_{\parallel} since for B_y positive the helix is right handed going into the magnetopause. The current must support this right handed helix, so $J_{\parallel} \cdot B_o > 0$. The sign of B_y also shows that J_{\parallel} will flow into the post-noon sector in the

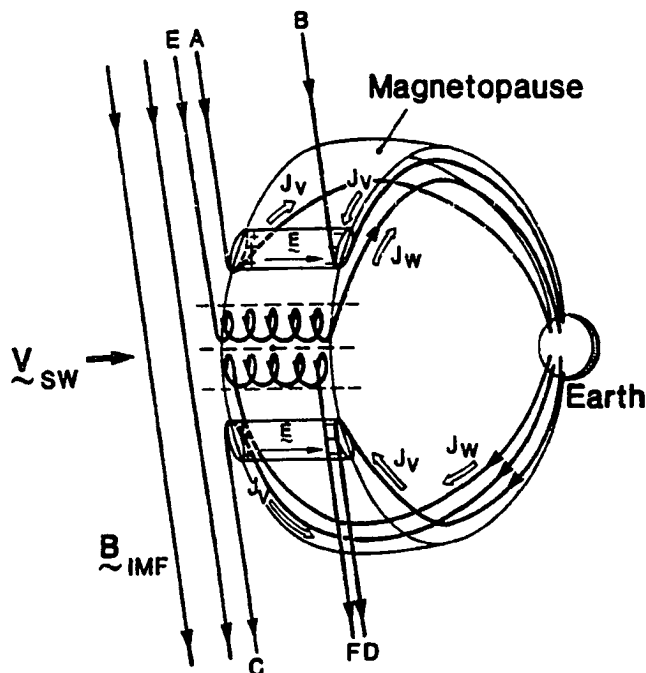


Figure 4.15. Field Aligned currents associated with multiple X line reconnection, take from Figure 2. of Lee *et al.* [1988]. "A perspective view of the three-dimensional magnetic field configuration associated with the multiple X line reconnection process on the dayside magnetopause. Field lines labeled with A,B,C and D are type V open field lines, and those labeled with type E and F are type W open field lines. The convection electric fields inside the elongated plasma clouds are denoted by E. The field aligned currents J_V are associated with elongated plasma clouds, while the field-aligned currents J_W are associated with the helical flux tubes."

northern hemisphere for $B_y > 0$ and out of the pre-noon sector for $B_y < 0$. This is due to the fact that in Figure 4.14 only the line at A_2 will have access to the magnetopause.

Figure 4.15 is reproduced from figure 2 of Lee *et al.* [1988]. It shows a three dimensional view of the multiple X line reconnection configuration already described. In addition to the parallel current associated with the type W line described in Figure 4.14, it has two parallel currents associated with the type V lines marked A and B. These parallel currents are driven by the polarization charge that is built up by the convection

electric field in the elongated plasma cloud that sits in the type V lines poleward of the flux tubes with helical magnetic field geometry. It should be noted that these field aligned currents will be insensitive to the sign of B_y , and will be symmetric when observed in opposite hemispheres. They are controlled by the direction of the convection electric field, and this is assumed to be dawn to dusk for B_z south conditions. The field aligned currents due to the type W lines will be asymmetric in opposite hemispheres, because the field aligned current must come out of the southern hemisphere and go into the northern hemisphere for $B_y > 0$.

The intensity of these field aligned currents is somewhat in question. *Glassmeier and Heppner* [1992] estimate the field aligned current density at the magnetopause due to reconnection at about 7.7×10^{-11} amps \cdot m $^{-2}$. This is at odds with a recent calculation by *Lin and Lee* [1993b] who calculate the field aligned current density at the magnetopause to be 1.4×10^{-8} amps \cdot m $^{-2}$. In both cases the authors then map this field aligned current density to the ionosphere assuming conservation of flux, and the densities are thus increased in the ionosphere by the ratio of the magnetic fields at the magnetopause and in the ionosphere. This increases both estimates by a factor of 1000. The difference between the two calculations is striking and demands resolution. It should be noted that *Glassmeier and Heppner* [1992] made estimates of the parallel current density based upon physical scaling laws, while *Lin and Lee* [1993a] used a resistive MHD code and a hybrid particle code to calculate the density. In the case of *Lin and Lee* [1993b], the field aligned current comes from the relaxation of twisted field lines caused by a rotational discontinuity on the inner magnetopause of reconnection. This is much the same as described by *Lee et al.* [1988] for the type J_W lines. It is unfortunate that the calculations differ by such a large amount. My observations of inferred field aligned currents in the cusp are on the order of 10^{-6} amps \cdot m $^{-2}$, which is

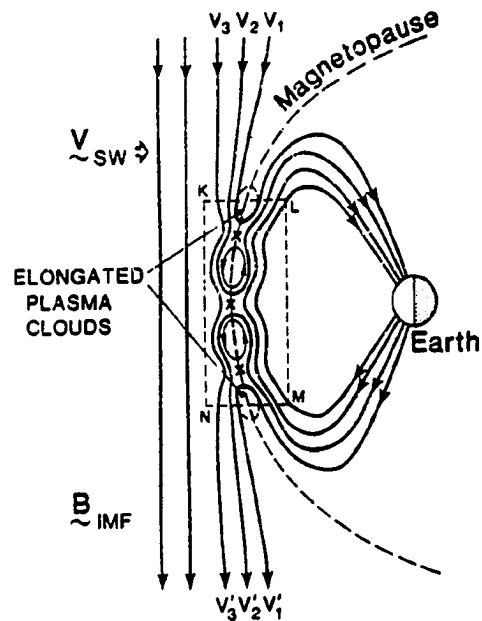


Figure 4.16. Geometry of ULF waves due to multiple X line reconnection, Figure 3 from *Lee et al.* [1988]. "The magnetic field configuration in the meridian plane. The elongated plasma clouds are located poleward to the magnetic islands. Closed field lines are compressed and distorted by the magnetic islands and elongated plasma clouds. The dashed area LMNK is the domain of the simulations in Figure 4. Field lines labeled with V_1 , V_1' , V_2 and V_2' , are type V open field lines."

two orders of magnitude larger than those of *Glassmeier and Heppner* [1992] and one order of magnitude smaller than those of *Lin and Lee* [1993b].

The intensity of the field aligned currents are now set aside and I return to the explanation given by *Lee et al.* [1988] to describe how multiple X line reconnection can cause ULF pulsations. Figure 4.16 is a reproduction of Figure 3 of *Lee et al.* [1988], and shows a meridional view of the multiple X line process. The elongated plasma clouds are shown poleward of the islands associated with the helical magnetic fields. *Lee et al.* [1988] believe that as the elongated clouds move poleward due to the Maxwell stress

in the type V lines labeled V_1 , V_2 and V_3 , the closed field lines are compressed. The compressions on one point of a closed field line are repeated every time an elongated cloud or magnetic island propagates past that point. Thus the fundamental frequency in the closed field line is given by the repetition rate of reconnection. *Lee et al.* [1988] use a repetition rate of 5-10 minutes, and quote *Daly et al.* [1984]; *Rijnbeek et al.* [1984] and *Saunders et al.* [1984]. This gives a fundamental frequency of 2-8 mHz. *Lockwood and Wild* [1993] have reviewed the question of the observed repetition rate of FTE's and find that there are really two intervals of interest. While the average repetition rate is about 8 minutes, the distribution is highly asymmetric, and the maximum probability of occurrence happens at approximately 3-5 minutes, with an extended tail that is centered at approximately 18 minutes. Using a 4 minute repetition rate yields a frequency of 4 mHz.

There are two major problems with the explanation as presented by *Lee et al.* [1988]. The assumption *Lee et al.* [1988] make is that the time between passage of an elongated plasma cloud or magnetic island past a fixed point on the closed field line represents a driving frequency for the field line. Figure 4.16 shows the actual configuration, there are multiple dimples on the field line spaced at a distance apart which is determined by the velocity and time between FTE occurrences. This entire chain of elongated plasma clouds and magnetic islands propagates poleward with the velocity of the plasma after reconnection. It is not at all clear what the response of the closed field lines to such a driving force will be. To represent this as a driving frequency given by the repetition rate seems overly simplified. No doubt the closed field line will respond to this compression, and the frequency of response may even be in the Pc5 range because the resonant frequency of the last closed field lines is in this range, *Lanzerotti and MacLennan* [1988]. The second problem which relates to the observations detailed above is that there seems no compelling reason to think that any oscillations that come about because of this type

of compression will be phase coherent for approximately 10 pulses and then suddenly suffer a phase jump.

An explanation that might explain the phase coherency is contained within the multiple X line reconnection configuration. As the type W helical field lines relax they will launch an Alfvén wave similar to that described by *Lin and Lee* [1993b]. As this Alfvén wave enters the ionosphere the wave field will cause horizontal currents to flow in the ionosphere, which can be detected on the ground. These oscillations will be phase coherent over the time that the wave field is incident in the local area of the station. Given that the radius of the flux tubes is approximately 1 RE, and conserving magnetic flux from the magnetopause to the ionosphere with a ratio of the fields being 10^3 , the radius of the flux tube in the ionosphere will be approximately 200 km. *Glassmeier* [1984] and *Hughes and Southwood* [1976] show that wave fields with a transverse size small compared to the height of the ionosphere will be highly damped on the ground due to the fact that the magnetic field below the ionosphere is due to the source free part of the ionospheric currents. The 200 km radius is larger than the approximately 100 km height of the ionosphere, so the fields can in principle be detectable on the ground. The existing flux tube propagates poleward and this explains the poleward propagation of the FAC. When a new reconnection event occurs a new Alfvén wave will be launched into the ionosphere. The phase will change because there is no relation between the phase angles of the two flux tubes, and will remain coherent over the time the next flux tube is in view.

While this explanation is attractive from the observational standpoint it has several drawbacks. First the frequencies of oscillation are unknown because the wave number is unknown. However using the observed frequency on the ground of 3-5 mHz, and an Alfvén speed at the magnetopause of approximately 100 km/sec, we can find the required wave number of approximately $3 \times 10^{-4} \text{ km}^{-1}$ which results in a wavelength of $2 \times 10^4 \text{ km}$. Such a length would be approximately one third the length of the total

flux tube of $10 R_E$, and while this wavelength is possible, it is not yet proven in either measurement or theory. The second problem is that the wave field amplitude on the ground has not yet been calculated.

We are left then with two ideas, both of which have problems explaining the observations. Both the ideas have the additional problem that the incoming particles will also divert into horizontal currents in the ionosphere and thus cause magnetic field perturbations on the ground. This signal must be sorted out from the incoming wave fields. This effect has not been accounted for in either model. In Appendix 1 I have formulated the electrodynamic problem of what happens when a field aligned current comes into an ionosphere with arbitrary height integrated conductivity. As shown in Appendix 1 this problem can be converted to an electrostatic potential problem and solved numerically assuming the conductances and field aligned currents are known. As shown in Chapter 2 while the conductances can be estimated using the optical data, only the upward field aligned currents are known. In addition to the problem of not knowing the downward field aligned currents the formulation offered in appendix 1 will be subject to the assumed boundary values of the potential on the border of the simulation. Such attempts are not new, *McHenry and Clauer* [1987], *Lanzerroti et al.* [1990] both calculate the field perturbations due to field aligned currents impinging on the ionosphere. However, in both cases, they assume a uniform conductance profile, which as shown in Chapter 2 is simply not realistic.

4.6 Summary

In this chapter I have shown that the observed magnetic perturbations offer a rich source of information. Analysis of the magnetic spectrum shows not only the diurnal cycle presented in Chapter 3, but a seasonal variation as well. This seasonal variation is ordered by the solar depression angle in the case of the total variance of the signals because of the change in conductivity due to solar EUV photoionization. The spectral

index variation with solar depression angle is due to the variation of the magnetic field geometry of the cusp with season. These waves are preferentially produced in the bow shock during quasi-parallel IMF conditions and propagate into the cusp. The summer and winter cusp have very different magnetic field geometries with respect to the bow shock, and the resulting penetration of the Pc3 waves into the summer cusp is relatively easier. This results in large amplitude high frequency components in the summer cusp spectrum, and thus the spectral index is less steep.

In addition to the spectral analysis, I have presented analysis of the time series of the fluxgate data that show the large amplitude (50 nT) boundary region pulses are phase incoherent, while the smaller amplitude (5 nT) pulses in the central cusp are phase coherent over 5-10 periods and then suffer a change in phase. This phase change is accompanied by the appearance of an intense field aligned current on the equatorward edge of the cusp. This correlation between the phase change and the appearance of the field aligned current is a clear indication that the pulsations seen are somehow associated with processes as yet undetermined that occur at the magnetopause.

The source mechanisms of the boundary region and central cusp pulsations have been reviewed. The boundary regions are a collection of impulsive events from several different sources. The Kelvin-Helmholtz instability, solar wind pressure variations, impulsive plasma penetration and magnetic reconnection have all been used to explain some portion of the signals seen. It seems sensible to separate the pulsations into two categories; first those events that have an azimuthal or tailward motion, and second those events that have a poleward motion, which may be connected to the poleward motion of auroral forms.

The best candidate for the central cusp pulsations seems to be some variation on the multiple X line reconnection idea. In this model the elongated plasma clouds and magnetic islands are formed at the FTE occurrence frequency. These plasma clouds and magnetic islands propagate poleward, and compress the last closed field lines that

thread the magnetopause. These field lines respond by launching Alfvén waves into the ionosphere, and the field aligned current associated with the waves is what is observed in the central cusp when the phase changes are seen. One main problem with this idea is the lack of understanding of what happens to the closed field lines as they are compressed by the poleward propagating islands. The second is that the time scale of the FTE occurrence is somehow turned into the frequency of the pulsations on the ground. The mechanism for this seems unclear at this time. The observational facts do seem clear however, intense field aligned currents on the equatorward edge of the cusp are associated with changes in the phase between wave trains of pulses. These pulses are small amplitude, and occur mainly in the 3-5 mHz frequency range.

CHAPTER 5

Review and recommendations for future work

The objective of this thesis is to understand the morphology and electro-dynamics of the cusp using ground based magnetic and optical observations. In this chapter I summarize the important findings and review how these fit with current thinking on the cusp. I will end this thesis with recommendations for future work.

5.1 Review

The cusp is defined in this thesis as the location of the most direct entry of magnetosheath particles into the ionosphere. The cusp as observed from the ground then offers a view of processes that happen at the dayside magnetosheath, and thus serves as a unique site for observations. The observations detailed in the thesis were carried out at Longyearbyen Norway on the island of Svalbard. This site allows optical observation of the cusp ionosphere for the two months around winter solstice, and these optical observations have served as a key to unlock the magnetic field measurements.

The optical emissions from the cusp ionosphere were observed with a meridian scanning photometer. This instrument is described in Chapter 2, along with a method to render the observations into geomagnetic coordinates and display latitude from the station and magnetic local time. The ratio of the intensity in the 6300 Å and 5577 Å emissions is used to determine the height of emission for this mapping. The remapped intensities are then used to calculate the characteristic energy of the incoming electrons that cause the emission along with the energy flux of these incoming particles.

I find that as the station rotates underneath the dayside ionosphere several different regions of energy and energy flux are sampled on a daily basis. The optical observations indicate that from approximately 08:30 to 10:30 magnetic local time (MLT) that the particles have a characteristic energy of 0.5 keV on the equatorward side of the station and a slightly smaller energy of 0.4 keV poleward of the station. From 10:30 through 13:30 MLT the energy of the particles is greatly reduced, and on one day a distinct region is seen where the energy is less than the resolution of the measurement which is 0.1 keV. As the station rotates into the afternoon sector the characteristic energy increases again to the 0.2-0.4 keV energy level. I interpret this very low energy region to be the cusp, and the higher energy regions to the side I call the boundary regions. No satellite data were available to collaborate the identification of these regions.

The measurement of the characteristic energy and energy flux allows the component of field aligned current density carried by electrons to be determined. I find that in the region identified as the cusp there are large field aligned currents with intensities of a few $\mu\text{amp} \cdot \text{m}^{-2}$. These field aligned currents are most intense on the equatorward side of the region identified as cusp, and the field aligned currents were observed to propagate poleward. During the interval of the cusp passage there were four such poleward moving field aligned currents with intensities over $1 \mu\text{amp} \cdot \text{m}^{-2}$. The regions identified as boundary regions had significantly less intense field aligned currents, and the two occasions when field aligned currents were seen in the boundary regions they were not observed to move poleward.

In addition to the field aligned currents, the measurements of characteristic energy and energy flux allow calculation of the height-integrated Pederson and Hall conductances. The Pederson conductance in the boundary layers was found to be 2.-2.5 mhos with large latitudinal and temporal gradients evident. The central cusp Pederson conductance was found to be very low, less than 0.2 mho. The Hall

conductances were found to be in the range of 1 mhos in the boundary regions, and 0.1 mho in the central cusp. The Hall conductance also showed gradients in both latitude and time.

The magnetic measurements are introduced in Chapter 3 and a correlation between the magnetic and optical measurements established. The boundary regions are found to have broad-band, large amplitude magnetic perturbations that are dominantly right-hand polarized pre-noon in the Pc5 band and left-hand polarized post noon. In the period between the boundary regions, a unique narrow band oscillation is observed with a center frequency of 3-5 mHz. This event is called the arch due to the resemblance the spectrogram to that of an arch. The post-noon boundary layer was again observed in the magnetic pulsations to have large broad band amplitude perturbations.

The spectrograms for 256 days were inspected, and sorted into three main categories. These categories were determined by spectral shape, and found to contain 85 percent of the data. The arch was observed on 36 percent of the days inspected. The occurrence statistics of the boundary regions and arches were collected and graphed versus magnetic local time. The boundary regions are consistently found to have maximum probability of occurrence away from local magnetic noon, with the center of the pre-noon boundary regions found to occur at 09:00 MLT, and the center of the post-noon boundary region found at 13:00 UT. The arch was found to have a maximum occurrence between the boundary regions with the peak falling at 10:30-11:00 MLT.

These occurrence statistics were compared to the statistics collected on the cusp and low latitude boundary regions by the DMSP satellite. The distribution of arches was found to resemble the distribution for the cusp, but as stated the peak was from 10:30-11:00 and the peak of the cusp distribution as determined by the DMSP particle precipitation data was 11:30-12:00 MLT. The boundary region

distribution distribution does not resemble the distribution of the low latitude boundary layer.

The distribution of arches was found to change for the different categories. This is explained by a study of interplanetary magnetic field orientation for each category. It was found that the first category represents a quiet B_z north state, while the second category was found to have large B_y variations. This causes the distribution of the arch for Category 2 to be bimodal, responding to the variation in B_y . The third category was found to have a quasi-parallel component in the IMF cone angle distribution which results in increased higher frequency Pc3 pulsations evident in the central cusp period. This is thought to be linked to the formation of upstream waves in the bow shock when the cone angle is small. Thus I find that division of the data into similar looking spectrograms has a physical basis. This identification of the boundary regions and central cusp in the magnetic data greatly facilitates performing statistical studies since the variation of the cusp in magnetic local time can now be accounted for.

Chapter four deals with the details of the cusp magnetic spectrum and analysis of the time series associated with pulsations in the boundary regions and central cusp. The ordering by Category described above was used to study the magnetic spectrum across the boundary regions and central cusp. I find that a power law distribution fit the power spectral density of the spectra. I fit 315 days of data taken over the two year interval of 1990 to 1992 with this power law distribution. I find the total variance of the magnetometer data changes with solar depression angle. As the solar depression angle becomes more negative, or as the sun comes above the horizon, the variance in the data increased. This is due to the increase in conductivity in the polar ionosphere due to the EUV photoionization of the sun. The data are well represented by a straight line fit, and I was able to determine the relative cusp conductivity in the summer compared to the fall. This ratio is

2.5 ± 0.6 , which is in agreement with conductivity estimates made from particle precipitation and solar contributions.

I find that the spectral index of the power law fit across the entire data set also changes with solar zenith angle. I find however that the Category 1 type data do not change spectral index with solar zenith angle, but that Category 2 and 3 data do change with solar zenith angle. Since the IMF study showed that Category 2 and 3 had a quasi-parallel component to the cone angle distribution, I believe this is not an effect of the sun, but rather due to the different propagation geometry between the summer and winter cusp with respect to the bow shock. The quasi-parallel geometry of the IMF causes the bow shock to destabilize and produce Pc3 band pulsations. These pulsations can propagate to the cusps, but the geometry for entry favors the summer cusp. This causes the summer cusp to have a larger amplitude high frequency component, and thus the apparent variation with solar angle.

The boundary region is found to be comprised of large amplitude pulses (40-50 nT) of varying periods. This is in agreement with the broad band nature of the spectrogram. The central cusp shows small amplitude (5 nT) perturbations that are very periodic in appearance, again in agreement with the narrow band nature of the spectrogram. Using an analytic reconstruction of the magnetic signals in the fluxgate magnetometer I find that the boundary region pulses are phase incoherent, while the pulses in the central cusp come in wave trains of phase coherent pulses. These trains of coherent pulses are separated by phase jumps and each train is seen to last 7-10 periods. The phase jumps between adjacent wave train in the central cusp are found to be associated with the appearance of an intense field aligned current of the equatorward edge of the cusp. These field aligned currents propagate poleward and the pulses in the wave train are coherent while one field

aligned current structure is in view. When the next field aligned current structure appears in the equatorward side of the cusp the phase again changes.

These poleward propagating field aligned currents which accompany the phase change in the magnetic perturbations are good candidates for the ionospheric footprint of a multiple X line reconnection event. As a flux tube propagates poleward the field aligned current in the ionosphere moves poleward, and either a wave field from the kinked magnetic field associated with the reconnection event or a closed field line oscillation driven by the passage of the flux tube causes the magnetic field perturbations on the ground. Both models have problems as detailed in Chapter 4, and it seems that much work remains to be accomplished in describing the details of these observations.

5.2 Recommendations for future work

Further work is required in both the optical and magnetic observations described in this thesis. The method used to reconstruct the optical meridian scanning photometer needs to have a background subtraction added. The study begun in this thesis to try to find out how to put error bars on the resulting energy and energy flux measurements needs to be continued. In particular the basic governing relations between the ratios of the 6300 Å and the 5577 Å emission to height need to be reevaluated. The relations used here were developed 20 years ago, and while they are useful, the field has progressed in its understanding over that time. In addition the latest relations between energy and energy flux and conductances should be incorporated into the optical data base.

In addition to these changes in method I suggest the entire optical data base should be put into energy and energy flux format. This will allow a check between the magnetic and optical data on a one to one basis. Since the magnetic categories have been shown to be the basis of different IMF magnetospheric states I venture

the prediction that a similar categorization will be found in the optical data if it is searched for. Use of the meridian scanning photometer to look for the expected field aligned currents associated with the traveling vortices in the boundary regions should also be investigated. In addition to the energy and energy flux data, a valid map of the high latitude conductances would be invaluable to the global modeling community. I think that this should have first priority in future work in the optical arena.

The magnetic pulsations are still a rich area for research. I did not look at the Pc3 band data other than to catalog its existence. A strong correlation between the Pc3 data and IMF cone angle exists, and the ground based cusp measurements will help define the details of this relationship. A network of stations on Svalbard would also be of utility to sort out the details of the poleward propagating filaments in the central cusp. The final area of research in this area must be theoretical. The observations are now in place, and a solid theory is lacking. The combined requirement for phase coherent wave trains associated with poleward propagating field aligned current structures seems to be a defining idea that can be turned into a physical model.

APPENDIX A1

Ground magnetic fields caused by field aligned currents

This appendix derives a method of calculating the ground magnetic field perturbation due to a field aligned current impinging on an ionosphere of known conductivity. A potential formulation of the problem is derived which must be solved numerically. From the potential the electric fields, and hence currents that flow in the ionosphere due to the field aligned currents can be deduced. The currents are used as inputs to the Biot-Savart law to calculate the magnetic fields on the ground.

A1.1 Assumptions and governing equations

The governing equations used are Faraday's law of induction,

$$\vec{\nabla} \times \vec{E} = -\frac{\partial \vec{B}}{\partial t} \quad (A.1)$$

Ohm's Law,

$$\vec{J} = \vec{\sigma} \cdot \vec{E} \quad (A.2)$$

and the current continuity equation,

$$\vec{\nabla} \cdot \vec{J} = -\frac{\partial \rho}{\partial t} \approx 0. \quad (A.3)$$

I will assume that the field aligned current density, $\vec{J}_z(x, y)$, and the height integrated Pederson and Hall conductances, $\Sigma_P(x, y)$ and $\Sigma_H(x, y)$, are known. I will also assume that the electric field in the horizontal plane is independent of

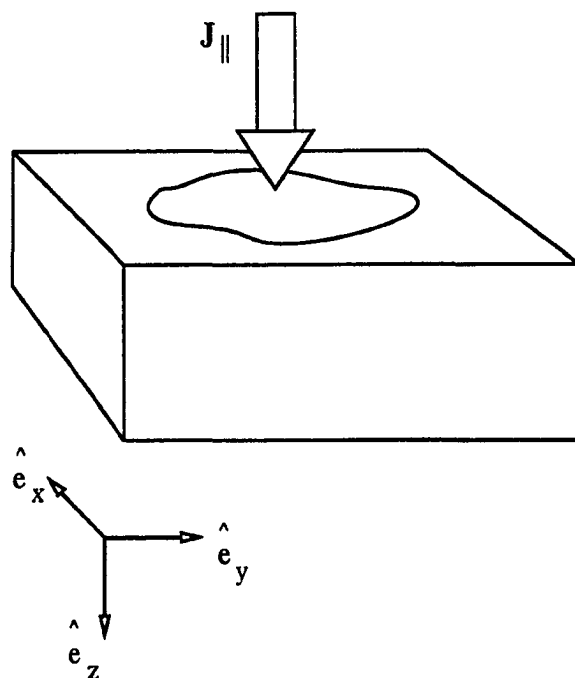


Figure A.1. Geometry for ionospheric slab with arbitrary conductance and field aligned current. Note that the coordinate system is right handed with x directed to magnetic north, y directed magnetic east, and z positive downwards along the field line.

height, that no electric field exists in the vertical direction, and that $\frac{\partial \rho}{\partial t} = 0$. The assumption that charge density does not change in time is justified because the time scales of interest are ULF periods and are very long, thus causing this term to be approximately zero. The geometry for the problem is shown in Figure A.1.

Assume that $\frac{\partial \vec{E}}{\partial t}$ is approximately 0 in the conducting ionosphere, (see *Glassmeier* [1984] for a discussion of this assumption), so equation A.1 can be written as:

$$\frac{\partial E_y}{\partial x} - \frac{\partial E_x}{\partial y} = 0. \quad (\text{A.4})$$

Rewriting equation A.3 we obtain,

$$-\frac{\partial J_z}{\partial z} = \frac{\partial J_x}{\partial x} + \frac{\partial J_y}{\partial y}. \quad (A.5)$$

and using Ohm's law;

$$\vec{J} = \vec{\sigma} \cdot \vec{E}, \quad \text{where} \quad \vec{\sigma} = \begin{pmatrix} \sigma_P & -\sigma_H & 0 \\ \sigma_H & \sigma_P & 0 \\ 0 & 0 & \sigma_0 \end{pmatrix}$$

where σ_P is the Pederson conductivity, σ_H is the Hall conductivity, and σ_0 is the field aligned conductivity, *Parks* [1991].

$$\begin{aligned} \vec{J}_x &= (\sigma_P E_x - \sigma_H E_y) \hat{e}_x \\ \vec{J}_y &= (\sigma_H E_x + \sigma_P E_y) \hat{e}_y \end{aligned} \quad (A.6)$$

A1.2 Derivation of Potential Equation

The objective of this section is to obtain a differential equation governing the electric scalar potential in the ionosphere that results from a field aligned current impinging on the ionosphere with a known spatial conductance. To obtain the conductance integrate equation A.3 over height and obtain;

$$-J_z = \frac{\partial}{\partial x} (\Sigma_P E_x - \Sigma_H E_y) + \frac{\partial}{\partial y} (\Sigma_H E_x - \Sigma_P E_y) \quad (A.7)$$

where $\Sigma_P = \int \sigma_P dz$ is the height integrated Pederson conductivity, and $\Sigma_H = \int \sigma_H dz$ is the height integrated Hall conductivity. Performing the partial differentiation yields eight terms which when collected by like coefficients yield:

$$-J_z = E_x \left(\frac{\partial \Sigma_P}{\partial x} + \frac{\partial \Sigma_H}{\partial y} \right) + E_y \left(-\frac{\partial \Sigma_P}{\partial y} - \frac{\partial \Sigma_H}{\partial x} \right) + \Sigma_P \left(\frac{\partial E_x}{\partial x} + \frac{\partial E_y}{\partial y} \right) + \Sigma_H \left(\frac{\partial E_x}{\partial y} - \frac{\partial E_y}{\partial x} \right) \quad (\text{A.8})$$

Since $\vec{\nabla} \times \vec{E} = 0$, \vec{E} can be derived from a scalar potential, $\vec{E} = -\nabla\phi$, and we then obtain the potential formulation of the problem;

$$\left(\frac{\partial^2 \phi}{\partial x^2} + \frac{\partial^2 \phi}{\partial y^2} \right) \Sigma_P(x, y) + \frac{\partial \phi}{\partial x} A(x, y) + \frac{\partial \phi}{\partial y} B(x, y) - J_z(x, y) = 0. \quad (\text{A.9})$$

where

$$\begin{aligned} A(x, y) &= \frac{\partial \Sigma_P}{\partial x} + \frac{\partial \Sigma_H}{\partial y} \\ B(x, y) &= -\frac{\partial \Sigma_P}{\partial y} - \frac{\partial \Sigma_H}{\partial x} \end{aligned} \quad (\text{A.10})$$

Note that since $A(x, y)$ and $B(x, y)$ are known, equation A.9 can be solved for the electrostatic potential $\phi(x, y)$. Once the potential solution is obtained the electric field in the horizontal plane can be reconstructed, and this used to obtain the surface currents flowing in the ionosphere.

A1.3 Determining the surface currents and the magnetic field

Once the electric field has been determined from the electric potential the surface currents are determined, and the Biot-Savart law is used to integrate the currents to determine the magnetic field on the ground. The surface currents are given by;

$$K_x = \int J_x dz = \Sigma_P E_x - \Sigma_H E_y \quad (\text{A.11})$$

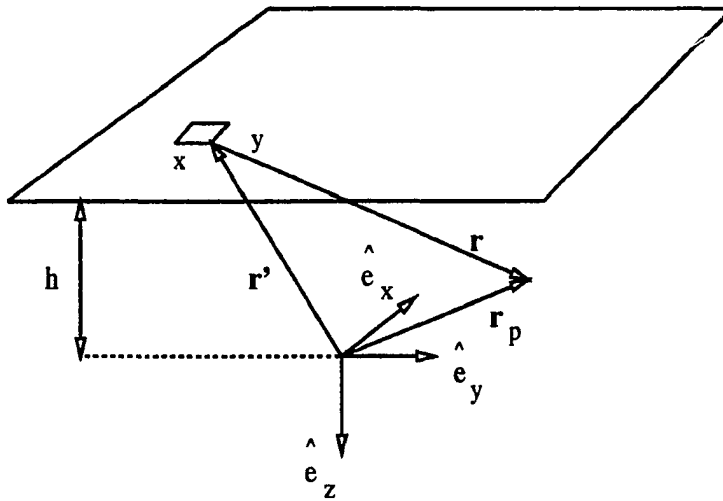


Figure A.2. Integration geometry for the Biot-Savart law. The vector \vec{r}' is the vector from the origin to the integration point, the vector \vec{r} is the vector from the integration point to the field point, which is at vector \vec{r}_p from the origin.

$$K_y = \int J_y dz = \Sigma_H E_x + \Sigma_P E_y \quad (A.12)$$

where the surface currents K_x and K_y have units of $\text{amps} \cdot \text{m}^{-1}$. The Biot-Savart law for surface and field aligned current densities is given in MKS units by *Griffiths* [1989];

$$d\vec{B} = \frac{\mu_0}{4\pi} \frac{\vec{J}(r') \times \vec{r} d^3 r'}{r^3} \quad (A.13)$$

$$d\vec{B} = \frac{\mu_0}{4\pi} \frac{\vec{K}(r') \times \vec{r} d^2 r'}{r^3} \quad (A.14)$$

where \vec{r}' is the vector to the integration point, and \vec{r} is the vector from the integration point to the field point, see Figure A.2 for the geometry. Using the vector relation that $\vec{r} = \vec{r}_p - \vec{r}'$, the Biot-Savart law gives for the surface currents;

$$\vec{B} = \frac{\mu_0}{4\pi} \Delta x \Delta y \left(\hat{e}_x \left(\frac{z_p - z'}{r^3} \right) K_y - \hat{e}_y \left(\frac{z_p - z'}{r^3} \right) K_x + \hat{e}_z \left(\left(\frac{y_p - y'}{r^3} \right) K_x - \left(\frac{x_p - x'}{r^3} \right) K_y \right) \right)$$

and that due to the field aligned current density J_z :

$$\vec{B} = \frac{\mu_0}{4\pi} \Delta x \Delta y \Delta z \left(-\hat{e}_x J_z \left(\frac{y_p - y'}{r^3} \right) + \hat{e}_y J_z \left(\frac{x_p - x'}{r^3} \right) \right).$$

Given that the ionosphere is at a height $-h$ above the ground, and that the field point r_p is at the origin the resulting perturbation magnetic field on the ground has components given by:

$$\begin{aligned} \Delta B_x &= \frac{\mu_0}{4\pi} \frac{\Delta x \Delta y}{r^3} \left(h K_y + y' J_z \Delta z \right) \\ \Delta B_y &= \frac{\mu_0}{4\pi} \frac{\Delta x \Delta y}{r^3} \left(-h K_x - x' J_z \Delta z \right) \\ \Delta B_z &= \frac{\mu_0}{4\pi} \frac{\Delta x \Delta y}{r^3} \left(x' K_y - y' K_x \right) \end{aligned} \quad (A.15)$$

APPENDIX A2

Emission height determination in the Eather map

This appendix details the determination of the emission height in the Eather mapping technique. As described in Chapter 2 this technique relies upon the determination of the height of emission for each scan angle. This determination is made by taking a ratio of two of the emissions at the same scan angle. I present in the following list the emission height and ratio of $6300 \text{ \AA} / 5577 \text{ \AA}$ and $6300 \text{ \AA} / 4278 \text{ \AA}$. These values were hand digitized from Figure 2 of *Rees and Luckey* [1974].

Ratios Used to determine emission height

Emission Height (km)	6300/5577	6300/4278
100	4. e-4	6. e-4
120	1.8 e-2	4.2e-2
140	6.3 e-2	0.35
160	0.16	1.3
180	0.32	3.
200	0.51	6.
220	0.8	10.
240	1.3	14.
260	2.1	25.
280	3.5	39.
300	5.3	53.
320	7.1	70.
340	8.1	110.

REFERENCES

- Aparicio, B., B. Thelin, and R. Lundin, The polar cusp from a particle point of view: A statistical study based on Viking data, J. Geophys. Res., 96,14,023, 1991.
- Armstrong, J.C., S. I. Akasofu, G. Rostoker, A comparison of satellite observations of birkeland currents with ground observations of visible aurora and ionospheric currents, J. Geophys. Res., 80,575,1975.
- Baker, K.B., and S. Wing, A new magnetic coordinate system for conjugate studies at high latitudes, J. Geophys. Res., 94,9139,1989.
- Banks, P.M. and G. Kockarts, Aeronomy, Academic, Orlando, Fla, 1973.
- Bol'shakova O.V. and V.A. Troitskaya, Dynamics of the day cusp, according to observations of long-period geomagnetic pulsations, Geomag. Aeron., 17,722,1977.
- Bol'shakova O.V. and V.A. Troitskaya, The relation of the high-latitude maximum of Pc3 intensity to the dayside cusp, Geomag. Aeron., 24,723,1984.
- Bracewell, R.M., The fourier transform and its applications, 381 pp.,McGraw-Hill, New York, 1965.
- Burch,J.L., Low energy fluxes at latitudes above the auroral zone, J. Geophys. Res., 73,3585,1968.
- Burch, J.L., J.D. Menietti, and J.N. Barfield, DE-1 observations of solar wind-magnetosphere coupling processes in the polar cusp, *Solar Wind-Magnetospheric Coupling*, edited by Y. Kamide and J.A. Slavin,pg 441,Terra Scientific Publishing Company, Tokyo, 1986.
- Burch, J.L., P.H. Reiff,R.A. Heelis,J.D. Winingham, W.B. Hanson,C. Gurgiolo,J.D. Menietti, R.A. Hoffman, and J.N. Barfield, Plasma injection and transport in the mid altitude polar cusp, Geophys. Res. Lett., 9,921,1982.
- Bythrow, P.F., R.A. Heelis, W.B. Hanson, R.A. Power, and R.A. Hoffman, Observational evidence for a boundary layer source of the region 1 field-aligned currents, J. Geophys. Res., 86,5577,1981.

- Bythrow, P.F., T.A. Potemra, R.E. Erlandson, L.J. Zanetti, and D.M. Klumppar, Birkeland currents and charged particles in the high-latitude prenoon region: A new interpretation, J. Geophys. Res., 93, 9791,1988.
- Carbary, J.F., and C.I. Meng, Correlation of cusp latitude with Bz and AE(12) using nearly one year's data, J. Geophys. Res., 91,10,047,1986.
- Chamberlain, J.W., Physics of the aurora and airglow,704 pp.,Academic, New York and London, 1961.
- Chapman, S., and V.C.A. Ferraro, Terrestrial magnetism and atmospheric electricity, J. Geophys. Res., 36,77,1931.
- Chen L. and A. Hasegawa, A theory of long-period magnetic pulsations, 1. Steady state excitation of field line resonance, J. Geophys. Res., 79,1024,1974.
- Claerbout, J.F., Fundamentals of geophysical data processing, 274 pp., McGraw-Hill, New York, 1976.
- Cogger, L.L., J.S. Murphree, S. Ismail and C.D. Anger, Characteristics of Dayside 5577 Aand 3914 A Aurora, Geophys. Res. Lett., 4,413,1977.
- Cowley, S.W.H., The causes of convection in the Earth's magnetosphere: A review of developments during the IMS, Rev. Geophys. and Space Physics, 20,531,1982.
- Crooker, N.U., Dayside merging and cusp geometry, J. Geophys. Res., 84, 951,1979.
- Daly, P.W., M.A. Saunders, R.P. Rijnbeek, N. Sckopke, and C.T. Russell, The distribution of reconnection geometry in flux transfer events using energetic ion plasma and magnetic data, J. Geophys. Res., 89,3438,1984.
- Dandekar, B.S., Relationship between the IMF, the midday gap, and auroral substorm activity, J. Geophys. Res., 84,4413,1979.
- Dandekar, B.S. and C.P. Pike, The midday, discreet auroral gap, J. Geophys. Res., 83,4227, 1978.
- D'Angelo, N., Ultralow frequency fluctuations at the polar cusp Boundaries, J. Geophys. Res., 78,1206,1973.

- D'Angelo, N., Bahnsen A., and H. Rosenbauer, Wave and particle measurements at the polar cusp, J. Geophys. Res., 97,3129,1974
- Deehr, C.S., G.G. Sivjee, A. Egeland, K. Henriksen, P.E. Sandholt, R. Smith, P. Sweeney, C. Duncan, and J. Gilmer, Ground-based observations of F region aurora associated with the magnetospheric cusp, J. Geophys. Res., 85, 2185, 1980.
- Dungey, J.W., Interplanetary magnetic field and the auroral zones, Physical Review Letters, 6, 47,1961.
- Eather, R.H., Latitudinal distribution of auroral and airglow emissions: The soft zone, J. Geophys. Res., 74,153, 1969.
- Eather, R.H., and S.B. Mende, Airborne observations of auroral precipitation patterns, J. Geophys. Res., 76,1746,1971.
- Eather, R.H. and D.L. Reasoner, Spectrophotometry of faint light sources with a tilting-filter photometer', Applied Optics, 8,227,1969.
- Eather, R.H., S.B. Mende and R.J.R. Judge, Plasma injection at synchronous orbit and spatial and temporal auroral morphology, J. Geophys. Res., 81,2805, 1976.
- Eather, R.H., S.B. Mende, and E.J. Weber, Dayside aurora and relevance to substorm current systems and dayside merging, J. Geophys. Res., 84,3339, 1979.
- Engbretson M.J., C.I. Meng, R.L. Arnoldy and L.J. Cahill, Pc3 pulsations observed near the south polar cusp, J. Geophys. Res., 91,8909,1986
- Engbretson M.J., L.J. Zanetti, T.A. Potemra, W. Baumjohann, H. Luhr, and M.H. Acuna, Simultaneous Observations of Pc3-4 Pulsations in the solar wind and in the earth's magnetosphere, J. Geophys. Res., 92,10,053, 1987.
- Engbretson, M.J., B.J. Anderson, L.J. Cahill, Jr., R.L. Arnoldy, P.T. Newell, C.I. Meng, L.J. Zanetti, and T.A. Potemra, A multipoint case study of high-latitude daytime ULF pulsations, J. Geophys. Res., 94, 17,143,1989.
- Engbretson, M.J., B.J. Anderson, L.J. Cahill, Jr., R.L. Arnoldy, T.J. Rosenberg, D.L. Carpenter, W.B. Gail, and R.H. Eather, Ionospheric signatures of cusp latitude Pc 3 pulsations, J. Geophys. Res., 95,2447,1990.

- Engbretson M.J., L.J. Cahill, Jr., R.L. Arnoldy, B.J. Anderson, T.J. Rosenberg, D.L. Carpenter, U.S. Inan, and R.H. Eather, The role of the ionosphere in coupling upstream ULF wave power into the dayside magnetosphere, J. Geophys. Res., 96, 1527, 1991.
- Engbretson M.J., W. Lin, W. Baumjohann, H. Luehr, B.J. Anderson, L.J. Zanetti, T.A. Potemra, R.L. McPherron, and M.G. Kivelson, A comparison of ULF fluctuations in the Solar wind, magnetosheath, and dayside magnetosphere 1. Magnetosheath morphology, J. Geophys. Res., 96, 3441, 1991.
- Erlanson, R.E., R. Pottelette, T.A. Potemra, L.J. Zanetti, A. Bahsen, R. Lundin, and M. Hamelin, Impulsive electrostatic waves and field-aligned currents observed in the entry layer, Geophys. Res. Lett., 14, 431, 1987.
- Erlanson, R.E., L.J. Zanetti, T.A. Potemra, and P.F. Bythrow, IMF By dependence of region 1 Birkeland currents near noon, J. Geophys. Res., 93, 9804, 1988.
- Farrugia, C.J., M.P. Freeman, S.W.H. Cowley, D.J. Southwood, M. Lockwood, and A. Etemadi, Pressure-driven magnetopause motions and attendant response on the ground, Planet. Space Sci., 37, 589, 1989.
- Fasel G.J., J.I. Minow, R.W. Smith, C.S. Deehr, and L.C. Lee, Multiple brightenings of transient dayside auroral forms during oval expansion, Geophys. Res. Lett., 12, 2429, 1992.
- Feldstein Y.I. and A.N. Zaitzev, Quiet and disturbed solar-daily variations of the magnetic field at high latitudes during the IGY, Tellus XX, 20, 338, 1968.
- Frank, L.A., Plasma in the Earth's polar magnetosphere, J. Geophys. Res., 76, 5202, 1971.
- Frank, L.A., and K.L. Ackerson, Observations of charged particle precipitation into the auroral zone, J. Geophys. Res., 76, 3612, 1971.
- Fredricks R.W. and C.T. Russell, Ion cyclotron waves observed in the polar cusps, J. Geophys. Res., 78, 2917, 1973.
- Fredricks R.W., Scarf F.L. and C.T. Russell, Field-aligned currents, plasma waves, and anomalous resistivity in the Disturbed Polar Cusp, J. Geophys. Res., 78, 2133, 1973.

- Friis-Christensen, E., and J. Wilhelm, Polar cap currents for different directions of the interplanetary magnetic field in the Y-Z plane, J. Geophys. Res., 80,1248, 1975.
- Friis-Christensen, E., Y. Kamide, A.D. Richmond, and S. Matsushita, Interplanetary magnetic field control of high-latitude electric fields and currents determined from the Greenland magnetometer array, J. Geophys. Res., 90, 1325, 1985.
- Friis-Christensen E., M.A. McHenry, C.R. Clauer, S. Vennerstrom, Ionospheric traveling convection vortices observed near the polar cleft: A triggered response to sudden changes in the solar wind, Geophys. Res. Lett., 15,253,1988.
- Fukushima, N., Generalized theorem for no ground magnetic effect of vertical currents connected with Pederson currents in the uniform-conductivity ionosphere, Report on Ionosphere and Space Research in Japan,30,35,1976.
- Glassmeier,K.H., On the influences of ionospheres with non-uniform conductivity on hydromagnetic waves, Journal of Geophysics, 54,125,1984.
- Glassmeier, K.H., ULF Pulsations in the polar cusp and cap, *Electromagnetic Coupling in the Polar Clefts and Caps* Edited by P.E. Sandholt and A. Egeland, Kluwer Academic Press, pg 167, 1989.
- Glassmeier,K.H., Traveling magnetospheric convection twin-vortices: observations and theory, Ann. Geophysicae, 10,547,1992.
- Glassmeier K. H. and C. Heppner, Traveling magnetospheric convection twin vortices: Another case study, global characteristics, and a model, J. Geophys. Res., 97,3977,1992.
- Glassmeier K., M. Honisch, J. Untied, Ground-based and satellite observations of traveling magnetospheric convection twin vortices, J. Geophys. Res., 94,2520, 1989.
- Greenstadt, E.W., Field-determined oscillation in the magnetosheath as a possible source of medium-period daytime micropulsations, paper presented at Solar-Terrestrial Relations Symposium, University of Calgary, Calgary, Alta., Canada, Aug 28 to Sept.,1,1972.
- Greenstadt,E.W., and L.M. Baum, Earth's compressional foreshock boundary revisited: observations by ISEE-1 magnetometer, J. Geophys. Res., 91, 9001, 1986.

- Griffiths, D.J., Introduction to electrodynamics; Second Edition, 532 pp., Prentice Hall, Englewood Cliffs, 1989.
- Hansen H.J.m B.J Fraser, F.W. Menk, YD. Hu, P.T. Newell, C.T. Meng, and R.J. Morris, High-latitude Pc 1 bursts arising in the dayside boundary layer region, J. Geophys. Res., 97,3993, 1992.
- Hardy, D.A., M.S. Gussenhoven, R. Raistrick, and W. J. McNeil, Statistical and Functional Representations of the Pattern of Auroral Energy Flux, Number Flux, and Conductivity, J. Geophys. Res., 92,12,275, 1987.
- Hedin, A.E., Extensions of the MSIS Thermosphere Model into the Middle and Lower Atmosphere, J. Geophys. Res., 96, 1159, 1991.
- Heikkila W.J. and J.D. Winningham, Penetration of magnetosheath plasma to low altitudes through the dayside magnetospheric cusps, J. Geophys. Res., 76,883,1971
- Heikkila, W.J., Winningham J.D., Eather R.H., and S.I. Akasofu, Auroral emission and particle precipitation in the noon sector, J. Geophys. Res., 77, 4100,1972.
- Heikkila, W.J., T.S. Jorgensen, L.J. Lanzerotti, and C.G. MacLennan, A transient auroral event on the dayside, J. Geophys. Res., 94, 15,291, 1989.
- Horowitz, J.L., and S.-I. Akasofu, The response of the dayside aurora to sharp northward and southward transitions in the interplanetary magnetic field and to magnetospheric substorms, J. Geophys. Res., 82,2723,1977.
- Hughes, W.J., The effect of the atmosphere and ionosphere on long period magnetospheric micropulsations, Planet. Space Sci., 22,1157,1974.
- Hughes, W.J., and D.J. Southwood, The Screening of Micropulsation Signals by the Atmosphere and Ionosphere, J. Geophys. Res., 81, 3234, 1976.
- Iijima, T., and T.A. Potemra, The amplitude distribution of field-aligned currents at northern high latitudes observed by Triad, J. Geophys. Res., 81,2165,1976a.
- Iijima, T., and T.A. Potemra, Field-aligned currents in the dayside cusp observed by Triad, J. Geophys. Res., 81, 5971, 1976b.

- Jenkins, G.M., and D.G. White, Spectral Analysis and its Applications, 525pp., Holden-Day, San Francisco, 1968.
- Kamide, Y., Y. Ishihara, T.L. Killeen, J.D. Craven, L.A. Frank, and R.A. Heelis, Combining electric field and auroral observations from DE 1 and 2 with ground magnetometer records to estimate ionospheric electromagnetic quantities, J. Geophys. Res., 94,6723,1989.
- Kleymenova N.G., O.V. Bol'shakova, V.A. Troitskaya and E. Friis-Kristensen, Long-period geomagnetic fluctuations and the polar chorus at latitudes corresponding to the daytime polar cusp, Geomag. Aeron., 22,580,1982.
- Kremser, G., and R. Lundin, Average Spatial Distributions of energetic particles in the midaltitude cusp/cleft region observed by Viking, J. Geophys. Res., 95,5753, 1990.
- Lanzerotti, L.J. and C.G. MacLennan, Hydromagnetic waves associated with possible flux transfer events, Astrophysics and Space Science, bf 144,279,1988.
- Lanzerotti L.J., C.G. MacLennan, L.V. Medford, and D.L. Carpenter, Study of a QP/GP event at very high latitudes, J. Geophys. Res., 91,375,1986
- Lanzerotti L.J., R.D. Hunsucker, D. Rice, C.G. MacLennan, L.V. Medford, and A. Wolfe, Studies of a cusp-region hydromagnetic wave event with magnetometers and incoherent scatter radar, Annales Geophysicae, 5A,479,1987.
- Lanzerotti L.J., A. Wolfe, N. Trivedi, C.G. MacLennan, and L.V. Medford, Magnetic impulse events at high latitudes: Magnetopause and boundary layer processes, J. Geophys. Res., 95,97,1990
- Lanzerotti L.J., R.M. Konik, A. Wolfe, D. Venkatesan, and C.G. MacLennan, Cusp latitude magnetic impulse events 1. Occurrence statistics, J. Geophys. Res., 96, 14009,1991.
- Lin, Y. and L.C. Lee, Structure of the dayside reconnection layer in resistive MHD and hybrid models, J. Geophys. Res., 98,3919,1993a.
- Lin Y., and L.C. Lee, Generation of region 1 and mantle-field aligned currents by the secondary rotational discontinuity, submitted to Proceedings for the Chapman Conference.

To be published in AGU Monograph "Solar Wind Sources of Magnetospheric ULF Waves", May 1993b.

Le, G. and C.T. Russell, Observations of the magnetic fluctuation enhancement in the Earth's foreshock region, Geophys. Res. Lett., 17, 905, 1992.

Ledley, B.G. and W.H. Farthing, Field-aligned current observations in the polar cusp ionosphere, J. Geophys. Res., 79,3124.,1974.

Lee, L.C. and John V. Olson, Kelvin-Helmholtz instability and the variation of geomagnetic pulsation activity, Geophys. Res. Lett., 7,777,1980.

Lee, L.C., and Z.F. Fu, A Theory of magnetic flux transfer at the Earth's magnetopause, Geophys. Res. Lett., 12,105,1985.

Lee, L.C., Albano R.K. and J.R. Kan, Kelvin-Helmholtz in the magnetopause -boundary layer region, J. Geophys. Res., 86,541,1981.

Lee L.C., Y. Shi, and L. J. Lanzerotti, A mechanism for the generation of cusp region hydromagnetic waves, J. Geophys. Res., 93, 7578,1988.

Lockwood, M., and M.N. Wild, On the quasi-periodic nature of magnetopause flux transfer events, J. Geophys. Res., 98,5935,1993.

Lockwood, M., A.P. van Eyken, B.J.I. Bromage, D.M. Willis, and S.W.H. Crowley, Eastward propagation of a plasma convection enhancement following a southward turning of the interplanetary magnetic field, Geophys. Res. Lett., , 13,72,1986.

Luhmann, J.G., C.T. Russell, and R.C. Elphic, Spatial distributions of magnetic field fluctuations in the dayside magnetosheath, J. Geophys. Res., 91, 1711,1986.

Maynard, N.C., and A.D. Johnstone, High-latitude day side electric field and particle measurements, J. Geophys. Res., 79,3111,1974.

Maynard, N.C., T.L. Aggson, E.M. Basinska, W.J. Burke, P. Craven, W.K. Peterson, M. Subiura, and D.R. Weimer, Magnetospheric Boundary Dynamics: DE 1 and DE 2 Observations Near the Magnetopause and Cusp, J. Geophys. Res., 96,3505,1991.

- P.N. Mayaud, Derivation, Meaning and Use of Geomagnetic Indices, geophysical monograph 22, 154 pp., American Geophysical Union, Washington, D.C., 1980.
- McDiarmid, I.B., J.R. Burrows, and M.D. Wilson, Solar Particles and the dayside limit of closed field lines, J. Geophys. Res., 77,1103,1972.
- McDiarmid, I.B., J.R. Burrows, and E.E. Budzinski, Average characteristics of magnetospheric electrons (150 eV to 200 eV) at 1400 km, J. Geophys. Res., 80, 73,1975.
- McDiarmid, I.B., J.R. Burrows, and E.E. Budzinski, Particle properties in the dayside cleft, J. Geophys. Res., 81,221,1976.
- McHarg, M.G., and J.V. Olson, Correlated optical and ULF magnetic observations of the winter cusp--boundary layer system, Geophys. Res. Lett., 19,17, 1992.
- McHenry, M.A., C.R. Clauer, Modeled ground magnetic signatures of flux transfer events, J. Geophys. Res., 92,11,231,1987.
- McHenry M.A., C R. Clauer, E. Friis-Christensen, P.T. Newell, J.D. Kelly, Ground observations of magnetospheric boundary layer phenomena, J. Geophys. Res., 95,14995,1990a.
- McHenry M.A., C.R. Clauer, E. Friis-Christensen, Relationship of solar wind parameters to continuous, dayside, high latitude traveling ionospheric convection vortices, J. Geophys. Res., 95,15007,1990b.
- Mende, S.B., R.H. Eather, M.H. Rees, R.R. Vondrak, and R.M. Robinson, Optical mapping of ionospheric conductance, J. Geophys. Res., 89,1755,1984.
- Meng, C.I., Electron precipitation in the midday auroral oval, J. Geophys. Res., 86,2149,1981.
- Meng, C.I., Case studies of the storm time variation of the polar cusp, J. Geophys. Res., 88,137, 1983.
- Meng, C.I., and R. Lundin, Auroral Morphology of the Midday Oval, J. Geophys. Res., 91,1572,1986.
- Newell, P.T., and C.I. Meng, The cusp and the cleft/boundary layer: Low altitude identification and statistical local time variation, J. Geophys. Res., 93,14549,1988a.

- Newell, P.T. and C.I. Meng, Hemispherical Asymmetry in Cusp Precipitation Near Solstices, J. Geophys. Res., 93,2643,1988b.
- Newell, P.T., and C.I. Meng, On quantifying the distinctions between the cusp and the cleft/LLBL, *Electromagnetic Coupling in the Polar Clefts and Caps* Edited by P.E. Sandholt and A. Egeland, Kluwer Academic Press, pg 87, 1989a.
- Newell, P.T., and C.I. Meng, Dipole Tilt effects on the latitude of the Cusp and the cleft/low-latitude boundary layer, J. Geophys. Res., 94,6949,1989b.
- Newell, P.T. and C.I. Meng, Mapping the dayside ionosphere to the magnetosphere according to particle precipitation characteristics, Geophys. Res. Lett., 19,609, 1992.
- Newell, P.T., C.I. Meng, D.S. Sibeck and R. Lepping, Some low-altitude dependencies on the interplanetary magnetic field, J. Geophys. Res., 94,8921,1989.
- Newell, P.T., W.J. Burke, C.I. Meng, E.R. Sanchez, and M.E. Greenspan, Identification of the plasma mantle at low altitude, J. Geophys. Res., 96, 35,1991a.
- Newell, P.T., S. Wing, C.I. Meng, and V. Sigillito The auroral oval position, structure, and intensity of precipitation from 1984 onward: an automated on-line data base, J. Geophys. Res., 96, 5877,1991b.
- Newell, P.T., W.J. Burke, E.R. Sanchez, C.I. Meng, M.E. Greenspan, and C.R. Clauer, The low-latitude boundary layer and the boundary plasma sheet at low altitude: Preenoon precipitation regions and convection reversal boundaries, J. Geophys. Res., 96,21013,1991c.
- Newell, P.T., C.I. Meng, and R.E. Huffman, Determining the source region of auroral emissions in the prenoon oval using coordinated POLAR BEAR UV-imaging and DMSP particle measurements, J. Geophys. Res., 97,12,245,1992.
- Olson, J. V., ULF signatures of the polar cusp, J. Geophys. Res., 91,10055,1986.
- Olson, J.V., Poleward propagation of pulsations near the cusp, Planet. Space Sci., 37,775,1989.
- Olson, J. V., and Gordon Rostoker, Longitudinal phase variations of Pc 4-5 micropulsations, J. Geophys. Res., 83,2481,1978.

- Olson J.V. and J.C. Samson, On the detection of the polarization states of PC micropulsations, Geophys. Res. Lett., 6,413,1979.
- Olson, J.V. and R. Domke, Instrument to measure the polarization state of waves, Rev. Sci. Instrum., 56(2),278, 1985.
- Parker, E.N., Sweet's mechanism for merging magnetic fields in conducting fluids, J. Geophys. Res., 62, 509, 1957.
- Parks, George, K., Physics of Space Plasmas,538 pp, Addison-Wesley Publishing Company, Redwood City, CA, 1991.
- Potemra, T.A., L.J. Zanetti, R.E. Erlandson, P.F. Bythrow, G. Gustafsson, M.H. Acuna, and R. Lundin, Observations of large-scale birkeland currents with Viking, J. Geophys. Res., 14,419, 1987.
- Rees, M.H., Auroral Ionization and Excitation by Incident Energetic Electrons, Planet. Space Sci., 11,1209,1963.
- Rees, M.H., Physics and chemistry of the upper atmosphere ,289 pp.,Cambridge University Press, Cambridge,1989.
- Rees, M.H. and D. Lucky, Auroral eletrons and spectroscopic ratios, J. Geophys. Res., 79,5181,1974.
- Rees, M.H. and D. Lummerzheim, Characteristics of auroral electron precipitation derived from optical spectroscopy, J. Geophys. Res., bf 94,6799, 1989.
- Rees, M.H. and R.G. Roble, Excitation of O(¹D) atoms in aurorae and emission of the [OI] 6300-A line, Can. J. Phys., 64,1608, 1986.
- Rees, M.H., D. Lummerzheim, R.G. Roble, J.D. Winningham, J.D. Craven, and L.A. Frank, Auroral energy deposition rate, characteristic electron energy, and ionospheric parameters derived from Dynamics Explorer 1 images, J. Geophys. Res., 93,12,841,1988.
- Reiff,P.H., T.W. Hill, and J.L. Burch, Solar wind plasma injection at the dayside magnetospheric cusp, J. Geophys. Res., bf 82,479,1977.

- Rijnbeek, R.P., S.W.H. Cowley, D.J. Southwood, and C.T. Russell, A survey of dayside flux transfer events observed by ISEE 1 and ISEE 2 magnetometers, J. Geophys. Res., 89, 786,1984.
- Rishbeth, H, P.R. Smith, S.W. Cowley, D.M. Willis, A.P. van Eyken, B.J.I. Bromage, and S.R. Crothers, Ionospheric response to changes in the interplanetary magnetic field observed by EISCAT and AMPTE-UKS, Nature, 318, 451, 1985.
- Robinson, R.M. and R.R. Vondrak, Measurements of E Region Ionization and Conductivity Produced by Solar Illumination at High Latitudes, J. Geophys. Res., 89,3951,1984.
- Robinson, R.M., R.R. Vondrak, K. Miller, T. Dabbs, and D. Hardy, On Calculating Ionospheric Conductances from the flux and energy of precipitating electrons, J. Geophys. Res., 92, 2565, 1987.
- Rogers, E.H. and D.F. Nelson, Auroral Photography from a satellite, Science, 183,951,1974.
- Rostoker, E. H. , Samson, J.C., and Y. Higuchi, Occurrence of Pc4,5 micropulsations activity at the polar cusp, J. Geophys. Res., 77, 4700, 1972.
- Russell, C.T., and R.C. Elphic, Initial ISEE magnetometer results: magnetopause observations, Space Sci. Rev., 22,681,1978.
- Russell, C.T., and R.C. Elphic, ISEE observations of flux transfer events at the dayside magnetopause, Geophys. Res. Lett., 6, 33,1979.
- Russell C.T., Chappell C.R., Montgomery M.D., Neugebauer M. and F.L. Scarf, Ogo 5 observations of the polar cusp on November 1,1968, J. Geophys. Res., 76,6743,1971.
- Russell, C.T., J.G. Luhmann, T.J. Odera, W.F. Stuart, The rate of occurrence of dayside Pc 3,4 Pulsations: The L- value dependence of the imf cone angle effect, Geophys. Res. Lett., 10,663,1983.
- Sakurai, T., Y. Tonegawa, K. Kato, K. Makita, M. Ejiri, H. Yamagishi, and N. Sato, ULF waves and magnetic field characteristics in the polar cusp observed at Godhavn, Proc. NIPR Symp. Upper Atmos. Phys. 6, 103,1993.

- Samson J.C. and J.V. Olson, Generalized Stokes Vectors and Generalized Power Spectra for Second-Order Stationary Vector Processes, SIAM Journal of Applied Mathematics 40,137,1981a.
- Samson J.C. and J.V. Olson, Data-adaptive polarization filters for multichannel geophysical data, Geophysics 46,1423,1981b.
- Samson J.C., Jacobs J.A. and G. Rostoker, Latitude dependent characteristics of long-period geomagnetic micropulsations, J. Geophys. Res., 76,3675,1971.
- Samson J.C., R.A. Greenwald, J.M. Ruohoniemi, T.J. Hughes and D.D. Wallis, Magnetometer and radar observations of magnetohydrodynamic cavity modes in the Earth's magnetosphere, Can. J. Phys., 69,929,1991.
- Sandholt P.E., Dayside auroral activity and magnetospheric boundary Layer phenomena, J. Geomag. Geoelectr., 42,711,1990
- Sandholt, P.E., and A. Egeland, Auroral and magnetic variations in the polar cusp and cleft - signatures of magnetopause boundary-layer dynamics, Astrophysics and Space Science, 144, 144,1988.
- Sandholt P.E. and P.T. Newell, Ground and satellite observations of an auroral event at the cusp/cleft equatorward boundary, J. Geophys. Res., 97,8685,1992.
- Sandholt, P.E., A. Egeland, B. Lybakk, C.S. Deehr, G.G. Sivjee, and G.J. Romick, Effects of the interplanetary magnetic field and magnetospheric substorm variations on the dayside aurora, Planet. Space Sci., 31,1345, 1983.
- Sandholt, P.E., A. Egeland, J.A. Holtet, B. Lybakk, K. Svenes, S. Asheim, and C.S. Deehr, Large- and small-scale dynamics of the polar cusp, J. Geophys. Res., 90,4407,1985.
- Sandholt, P.E., A. Egeland, B. Lybakk, On the spatial relationship between auroral emissions and magnetic signatures of plasma convection in the midday polar cusp and cap ionospheres during negative and positive IMF Bz: A case study, J. Geophys. Res., 91,12,108,1986.
- Sandholt, P.E., C.S. Deehr, A. Egeland, B. Lybakk, R. Vireck, and G.J. Romick, Signatures in the dayside aurora of plasma transfer from the magnetosheath, J. Geophys. Res., 91,10,063,1986.

- Sandholt, P.E., B. Jacobsen, B. Lybekk, A. Egeland, C.I. Meng, P.T. Newell, F.J. Rich, and E.J. Weber, Structure and dynamics in the polar cleft: Coordinated satellite and ground-based observations in the prenoon sector, J. Geophys. Res., 94, 8928, 1989a.
- Sandholt, P.E., B. Jacobsen, B. Lybekk, A. Egeland, P.F. Login, timed out after 240 seconds. Bythrov
Electrodynamics of the polar cusp ionosphere, A case study, J. Geophys. Res., 94, 6713, 1989b.
- Sandholt, P.E., B.L. Lybekk, A. Egeland, R. Nakamura, and T. Oguti, Midday auroral breakup, J. Geomag. Geoelectr., 41, 371, 1989c.
- Saunders, M.A., C.T. Russell, and N. Sckopke, Flux transfer events: Scale size and interior structure, Geophys. Res. Lett., 11, 131, 1984.
- Scarf F.L., Fredricks R.W., Green I.M. and C.T. Russell, Plasma waves in the dayside polar cusp, J. Geophys. Res., 77, 2274, 1972.
- Shelly, E.G., R.D. Sharp, and R.G. Johnson, He⁺⁺ and H⁺ flux measurements in the dayside cusp, J. Geophys. Res., 81, 2363, 1976.
- Shepherd, G.D., Dayside cleft aurora and its ionospheric effects, Rev. Geophys. and Space Physics, 17, 2017, 1979.
- Shepherd, G.G., and F.W. Thirkettle, Magnetospheric dayside cusp: A topside view of it 6300 A atomic oxygen emission, Science, 180, 737, 1973.
- Shepherd, G.G., J.H. Whitteker, J.D. Winningham, J.H. Hoffman, E.J. Maier, L.H. Brace, J.R. Burrows, and L.L. Cogger, The topside magnetospheric cleft ionosphere observed from the Isis 2 spacecraft, J. Geophys. Res., 81, 6092, 1976.
- Sibeck, D.G., A model for the transient magnetospheric response of sudden solar wind dynamic pressure variations, J. Geophys. Res., 95, 3755, 1990.
- Sivjee, G.G., Optical emissions from the mid-day aurora, J. Atmos. Terres., Physics, 38, 533, 1976.
- Sivjee, G.G. and B. Hultqvist, Particle and optical measurements in the magnetic noon sector of the auroral oval, Planet. Space Sci., 23, 1597, 1975.

- Sivjee, G.G., G.J. Romick, and C.S. Deehr, Optical Signatures of some magnetospheric processes on the dayside, Geophys. Res. Lett., 9, 676,1982.
- Slavin, J. A. and R.E. Holzer, Solar Wind Flow about the Terrestrial Planets 1. Modeling Bow Shock Position and Shape, J. Geophys. Res., 86, 11401,1981.
- Snyder, A.L. and S.I. Akasofu, Auroal Oval Photographs from the DMSP 8531 and 10533 Satellites, J. Geophys. Res., 81, 1799,1976.
- Southwood D.J., The Hydromagnetic Stability of the Magnetospheric Boundary, Planet. Space Sci., 16,587,1968.
- Southwood D.J., Some features of field line resonances in the magnetosphere, Planet. Space Sci., 22,483,1974.
- Spreiter J.R., and S.S. Stahara, Magnetohydrodynamic and Gasdynamic Theories for Planetary Bow Waves, in Collisionless Shocks in the Heliosphere: Review in Current Research, edited by Bruce T. Tsurutani and Robert G. Stone, 301 pp, Geophysical Monograph 35, Washington D.C., 1985.
- Spreiter J.R., and A.L. Summers, On conditions near the neutral points on the magnetosphere boundary, Planet. Space Sci., 15,787,1967.
- Stamnes, K, M.H. Rees, B.A. Emery, and R.G. Roble, Modelling of cusp aurora: The relative impact of solar EUV radiation and soft electron recipitation, in The Polar Cusp, edited by J.A. Holtet, and A. Egeland, 422 pp, NATO ASI Series, D. Reidel Publishing Co., Dordrecht,1985.
- Starkov, G.V., Analytical representation of the equatorial boundary of the oval auroral zone, Geomag. Aeron., 9,614, 1969.
- Stasiewicz K., Polar cusp topology and position as a function of interplanetary magnetic field and magnetic activity: comparison of model with Viking and other observations, J. Geophys. Res., 15,789,1991.
- Sugiura, M. and T.A. Potemra, Net field-aligned currnets observed by Triad, J. Geophys. Res., 81,2155,1976.

- Troitskaya V.A., ULF wave investigations in the dayside cusp, *Magnetospheric and Ionospheric Plasmas*, Advances in Space Research, Volume 5, Number 4, Edited by E.R. Schmerling, S.W.H. Cowley and P.H. Reiff, Pergamon Press, 1985
- Troitskaya V.A. and O.V. Bolshakova, Diurnal latitude variations of the location of the dayside cusp, Planet. Space Sci., 25,1167,1977.
- Tsurutani B.T., E.J. Smith, R.M. Thorne, R.R. Anderson, D.A. Gurnett, G.K. Parks, C.S. Lin, and C.T. Russell, Wave-particle interactions at the magnetopause: Contributions to the dayside aurora, Geophys. Res. Lett., 8,183,1981.
- Tsyganenko N.A., Global quantitative models of the geomagnetic field in the cislunar magnetosphere for different disturbance levels, Planet. Space Sci., 35,1347,1987.
- Tsyganenko N.A., A magnetospheric magnetic field model with a warped tail current sheet, Planet. Space Sci., 37,5,1989.
- Vorobjev, V.G., G. Gustafsson, G.V. Starkov, Y.I. Feldstein, and N.F. Shernina, Dynamics of day and night aurora during substorms, Planet. Space Sci., 23, 269, 1975.
- Wallis, D.D., and E.E. Budzinski, Empirical Models of Height Integrated Conductivity, J. Geophys. Res., 86, 125,1981.
- Zmuda A.J., Armstrong J.C. and F.T. Heuring, Characteristics of transverse disturbances observed at 1100 kilometers in the auroral oval, J. Geophys. Res., 75,4757,1970.